Development and Implications of ISOL Target-Materials with High-Carbon content for Short-Lived Radioactive Isotope Beam Production

by

Marla Stephanie Cervantes Smith
B.Sc., Universidad Autonoma de Yucatan, 2013
M.Sc., University of Victoria, 2016

A Dissertation Submitted in Partial Fulfillment of the
Requirements for the Degree of

DOCTOR OF PHILOSOPHY

in the Department of Physics and Astronomy

Development and Implications of ISOL Target-Materials with High-Carbon content for Short-Lived Radioactive Isotope Beam Production

by

Marla Stephanie Cervantes Smith
B.Sc., Universidad Autonoma de Yucatan, 2013
M.Sc., University of Victoria, 2016

Supervisory Committee

Dr. Alexander Gottberg, Co-Supervisor
(Department of Physics and Astronomy)

Dr. Dean Karlen, Co-Supervisor
(Department of Physics and Astronomy)

Dr. Robert Kowalewski, Departmental Member
(Department of Physics and Astronomy)

Dr. David Berg, Outside Member
(Department of Chemistry)

ABSTRACT

In the Isotope Separation On-Line (ISOL) method, a high-energy particle beam strikes a target, inducing nuclear reactions that produce isotopes. After releasing from the target by diffusion, the isotopes are ionized, and separated by mass. ISAC, TRIUMF's ISOL facility, delivers RIBs to experiments on nuclear astrophysics, nuclear physics, particle physics, and material science. The Advanced Rare IsotopE Laboratory (ARIEL) is under construction to expand TRIUMF's scientific capabilities with the development of two additional ISOL target systems for TRIUMF. This expansion entails a greater demand for target material, promoting the research and development of new targets tailored for enhanced isotope release and improved resilience under high-power beam irradiation. This work presents the research and development towards reducing several limitations of the current ISOL-target paradigm. A new method for synthesizing UC_x targets has been developed. Now UC_x targets are synthesized eight times faster than before while complying with the required micrometric particle size and high open porosity to promote isotope release. The reduction in production time complies with ARIEL's future target material demand, and it has relieved personnel and equipment, allowing the development of a novel graphite-composite target. Both targets have been characterized and submitted online for isotope delivery to experiments. Their performance has been studied and related to microstructure and thermal properties. Both targets are now established and regularly operated at ISAC-TRIUMF and will be used in ARIEL. Furthermore, temperature investigations of both targets, have resulted in an analytical and a finite element model to predict their temperature during operation. Moreover, to further improve the performance of the targets, the implications of operating target materials with high carbon content have been investigated. Strategies are proposed for further learning about carbon penetration, the resulting target ovens' corrosion, and its prevention.

Contents

List of Tables

List of Figures

ACKNOWLEDGEMENTS

I want to express my deep gratitude to the University of Victoria for giving me the opportunity to pursue a graduate career in physics. I am thankful for having Dean Karlen as my academic supervisor, as well as my kind supervisor committee members. A special thanks goes out to my supervisor at TRIUMF, Alexander Gottberg, for his guidance and friendship.

I am also grateful to all of the past and present members of the Target and Ion Sources group whose continuous efforts and foundational work made this research possible. A special thanks goes to Anders Mjos for helping and inspiring me.

Also, I would like to acknowledge the contributions of all the participants in the Graphite-composite target online development; your cooperation was key to the success of this measurement campaign.

The members of TRIUMF's Machine and Scintillator shops have played an essential role, and I want to recognize their hard work, which enabled several experiments from this work. A special thanks goes to Jaroslaw Zielinski, whose enthusiasm and engagement in my work kept me motivated.

I am also grateful to Heli Eunike and Jacob Kabel for their training and understanding, having them as allies at MEML was a privilege.

Thank you to the Tantalum Collaboration Group, João Pedro Ramos, Michele Ballan, Donald Houngbo, and Vasileios Samothrakis. Discussing ideas with them not only helped me set up experiments but also made me feel like a true scientist. A special thanks to João for his mentorship.

I would also like to thank Ricardo Dos Santos, Luca Egoriti, Mia Au, Ferran Boix, and Trian Groumoutis for your support and friendship, which are invaluable to me.

Moreover, I want to express my gratitude to Pauline Fouquet-Mètivier, Aaron Schmidt, and Darwin Ortiz. It was easier to cope with the long days in the lab with them by my side.

Also, it is necessary to acknowledge the help provided by The Centre for Academic Communication at UVic, especially Odivi and Emily, who provided crucial assistance in wrapping up this dissertation.

Last but not least, I want to thank my family. Without them, I would not be where I am today.

Fernando Maldonado, thank you for believing in me.

DEDICATION

I dedicate this dissertation to myself.

Introduction

TRIUMF, Canada's Particle Accelerator Centre, started by delivering protons to particle physics experiments in 1968. Thirty years later, TRIUMF expanded its scientific capabilities with the commissioning of the Isotope Separator and ACcelerator (ISAC) [1], a facility that delivers Radioactive Isotope Beams (RIB) by applying the ISOL (Isotope Separation On-Line) method.

In the ISOL method, a high-energy particle beam impinges on a thick target, inducing nuclear reactions that produce isotopes, which escape the target bulk by thermally induced diffusion. Once on the target surface, the isotopes are absorbed and desorbed until they reach an ion source that strips them of an electron, allowing their electrostatic acceleration, and their separation by mass in a dipole magnet. Finally, a RIB of the requested isotope is delivered to an experiment [2]. Nuclear astrophysics, particle and nuclear physics, nuclear medicine, biology, and material science are disciplines benefiting from radioactive isotopes [3].

The Advanced Rare IsotopE Laboratory (ARIEL) is under construction at TRIUMF, and it will be adding two new ISOL target stations to the two currently operated at ISAC. Once ARIEL is fully operational, an estimated 9000 RIB hours will be available to experimental users at TRIUMF each year [4]. ARIEL will achieve its full potential through research and development in target materials, overcoming present limitations of RIB species availability, intensity, and purity.

The RIB availability refers to the isotopes produced in a target material provided to an experiment as an ion beam. Different target materials produce different isotopes; the higher the mass number of the target, the richer the isotope assortment obtained. On the other hand, the RIB intensity refers to the RIB's isotope delivery rate, which increases when irradiating the target with a more intense driver beam, and when increasing the number of target-material nuclei; however, both strategies are limited by the target capacity to dissipate the heat deposited by the driver beam. The RIB intensity's greatest limitation is the isotope release efficiency that describes the probability of the isotope reaching the ion source before its nuclear decay, chemical absorption, or other forms of losses; the isotope release efficiency can be as low as $10^{-4}\%$ [5]. Both, the RIB intensity and the isotope availability are limited by

the isotope release efficiency, so the ISOL target materials are engineered to withstand high temperatures, and have high density while simultaneously maintaining a tailored porosity and microstructure to favour isotope production, and promote diffusion and effusion.

The construction of ARIEL is expanding TRIUMF's radioisotope beam program, and it is seeking to increase the current and future targets' isotope release efficiencies by studying and improving the material's micro and nano structure. Before this work, the routinely operated ISAC targets consisted of Ta, SiC, ZrC, TiC, and UC_x [6]. However, the production of ISAC targets, especially of UC_x, had monopolized ISAC human and infrastructure resources, preventing the development of new materials and the investigation of the current ones.

Since lanthanum is a chemical homologue of uranium [7], LaC_2/C targets have been developed in this work as a rehearsal for synthesizing UC_x. Due to their sensitivity to oxygen, LaC_2/C targets can not be irradiated in ISAC, but they will be used in ARIEL to produce neutron-deficient barium and cesium with no isobaric contamination. A new method to synthesize UC_x targets has been conceived from this work, resulting in an eight-fold reduction in production time [8], increasing the number of available targets, and allowing the development of a graphite-composite target dedicated to the production of beryllium and lithium. This new target is a low Z material that lessens ISAC's radioactive inventory and can be irradiated with higher proton beam intensity than its high Z material counterparts (i.e. ZrC and UC_x). The graphite-composite target forms part of the routine ISAC and ARIEL target collection.

All the targets developed in this work have a high carbon content. They are submitted online in tantalum ovens to resistively heat them to 2000 °C to promote isotope diffusion and effusion. However, the formation of tantalum carbides above 1300 °C [9] embrittles the ovens, changing their electrical and thermal properties, reducing their lifetime, and ultimately diminishing the target performance. Current and new strategies to prevent the ovens' embrittlement have been investigated in this work. Furthermore, an analytical and a finite element model have been developed to better predict the target material temperature during irradiation and achieve optimal target operation to provide more intense RIBs to experiments.

The first chapter of this thesis describes the physical mechanisms for the isotope production and release on ISOL targets. Also, the first chapter provides an overview of established ISAC target materials, as well as this work's successfully developed and operated new target materials. The second chapter presents the isotope production rates expected from the induced nuclear reactions considering the target materials' micromorphology. The chapter further describes the target materials' characterization and the synthesis' methodology influencing the targets' micromorphology. The third chapter introduces the carbon embrittlement investigations of the ISAC target ovens, the entailed limitations on the target's

operation, and the expected impact on the isotope production rate. Furthermore, the chapter describes the strategies investigated to mitigate carbon penetration in target ovens. The fourth chapter presents the isotope yields achieved with the carbon and UC_x targets, as well as the analytical models that describe their temperature and allow the estimation of the isotopes' release efficiencies. Finally, the fifth chapter compiles the conclusions obtained through this work.

Chapter 1

ISOL targetry

The target material limits the RIB intensity and therefore the capability of an ISOL facility. From all the steps in the ISOL method, the isotope release from the target material has often the lowest efficiency (Fig. 1.1). Since the release of the isotopes is governed by diffusion, the target materials are developed with reduced particle size, increased porosity, and the ability to withstand high temperatures; all with the objective of promoting isotope diffusion, and consequently increasing the release efficiency.

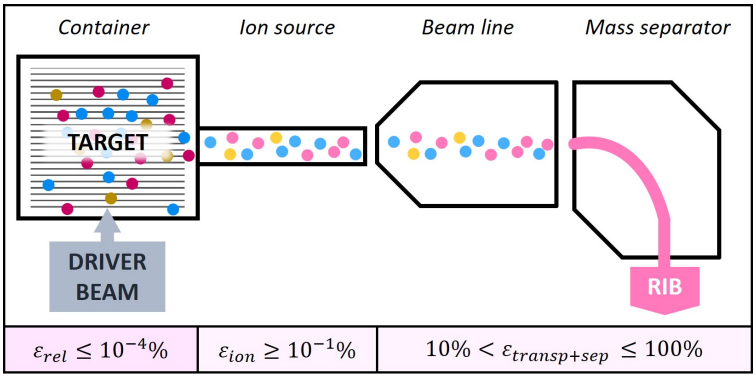

Figure 1.1: Diagram of the ISOL method. The steps of the ISOL method are subject to different efficiencies, but the target release efficiency (ε_{rel}), with values as low as $10^{-4}\%$ or less [5], is often the lowest.

This chapter presents the ISOL figures of merit that are addressed through target material research and development. Moreover, it describes the material's micromorphology contribution to the isotope release efficiency and the related isotopes diffusion mechanisms. Furthermore, this chapter introduces the targets used at ISAC, as well as the new targets developed in this work.

1.1 ISOL figures of merit

Isotope availability, RIB purity, and RIB intensity are important figures of merit of any ISOL facility [10]. Isotope availability refers to the collection of isotope species that can be delivered, while the RIB purity is given by the selectivity of separation of the extracted species [11]. Furthermore, the RIB intensity refers to the rate of isotopes of the same kind that are available for an experiment at the end of the production and transport chain.

Isotope availability is achieved by having a varied collection of target materials in relation to the available driver beam. From the targets studied for this work, the one that produces the larger isotope assortment is uranium carbide (UC_x) (Fig. 1.2a), followed by lanthanum carbide (LaC_2) (Fig. 1.2b), and finally by graphite (Fig. 1.2c).

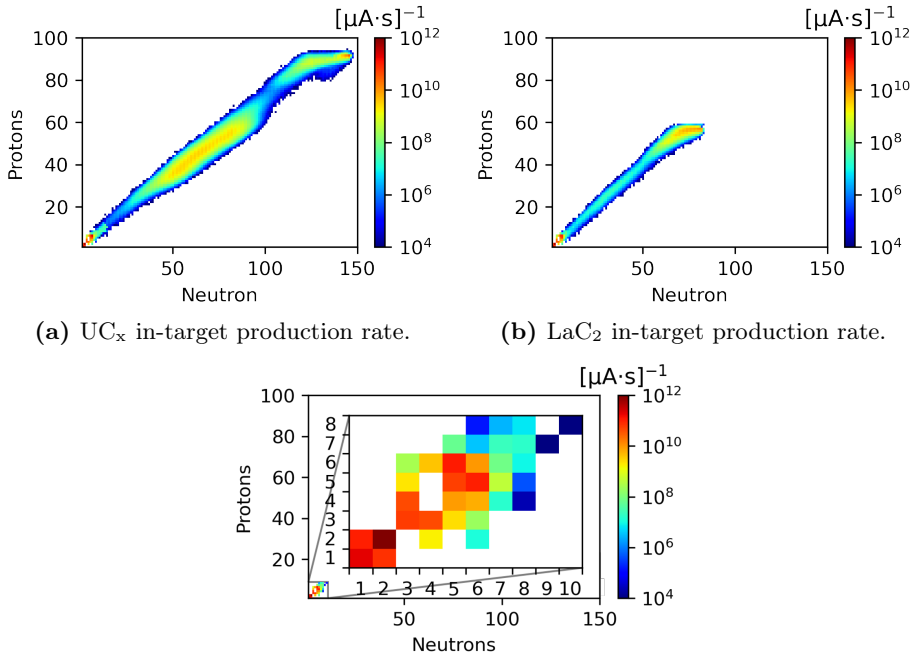

(a) UC_x in-target production rate.

(b) LaC_2 in-target production rate.

(c) Graphite in-target production rate.

Figure 1.2: Simulated isotope production rates for three composite target materials ((c) is zoomed in for better visualization). These FLUKA simulations' results correspond to 10 cm long targets impinged with 480 MeV proton beam; the isotope production rates are normalized per μA (simulations'details in Chapter 4).

A requisite for the production of an isotope is for the target material to be heavier than the desired isotope. The nuclear reactions in a target material irradiated with a high energy driver beam produce a variety of isotopes lighter than the target material. Fission products have a mass number (A) centred around $A_{target}/2$, spallation products are $\geq (2/3)A_{target}$, and fragmentation products have a mass number of $(1/3)A_{target}$ [12]. Thus, different target materials produce different isotopes, and the higher the mass number of the target material, the richer the isotope assortment that the target produces.

A target material is selected for an experiment depending on the isotope of interest. However, the target material with the largest isotope assortment is not always picked. For example, UC_x can produce ^{8}Li among many other isotopes, but a graphite target would be a more convenient candidate to deliver that isotope because, in contrast with UC_x, this target does not produce ^{227}Ac or ^{209}Po; having these alpha-emitter isotopes entails additional authorizations for the target's manipulation and disposal after its operation.

Another condition for selecting target materials is to have disparate physical and chemical properties between them and the desired isotopes. The isotope and the target material must not create refractory compounds with volatilizing temperatures above the evaporation temperature of the target material such that the isotope can easily diffuse and volatilize without compromising the material integrity [10]. Often, the disparity between target and isotope properties is not met, so some produced isotopes are not released from the target; hence, they cannot be made available to the experiments [5].

Besides isotope availability, RIB purity plays a key role on the experiments using the RIBs. The primary process determining the RIB purity is the separation by mass of the species. However, the dipole magnet resolution is sometimes not enough to separate isobars from the RIB [13]. Due to differences in their ionization mechanisms (Appendix C), using different ion sources can improve chemical selectivity [14] to potentially reduce isobaric contamination and contribute to RIB purity. Furthermore, by adding vapours into the target–ion source region, the desired species can be ionized and transported as a molecule [13].

The next challenge after producing the isotope of interest is obtaining it in high quantities. The RIB intensity of the desired isotope (i) depends linearly on the cross section (σ_i), the intensity of the irradiating driver beam (ϕ), the number of target nuclei being irradiated (N_{target}), and the overall ISOL efficiency (ε) (Eq. 1.1) [10]:

$$I_{rib} = \sigma_i \cdot N_{target} \cdot \phi \cdot \varepsilon. \tag{1.1}$$

The cross section is an intrinsic property of each nuclear reaction. Therefore, to obtain a higher I_{rib} an appropriate target nucleus and driver beam combination must be chosen. For instance, both LaC_2 and UC_x targets can produce isotopes of barium and cesium, but their corresponding neutron deficient isotopes are produced in several orders of magnitudes higher with a LaC_2 target than with a UC_x one (Fig. 1.3).

Higher RIB intensities are also obtained by irradiating the target with a more intense driver beam. However, the driver beam deposits power in the target material, increasing its temperature; thus, the driver beam intensity is limited by the capacity of the target to dissipate the power deposited. To exemplify this situation, assume that an experiment is requesting ^{8}Li, between a graphite, a UC_x or a LaC_2 target, graphite is a good choice because it has a higher RIB intensity (Fig. 1.4), but the ratio is within a factor of ten.

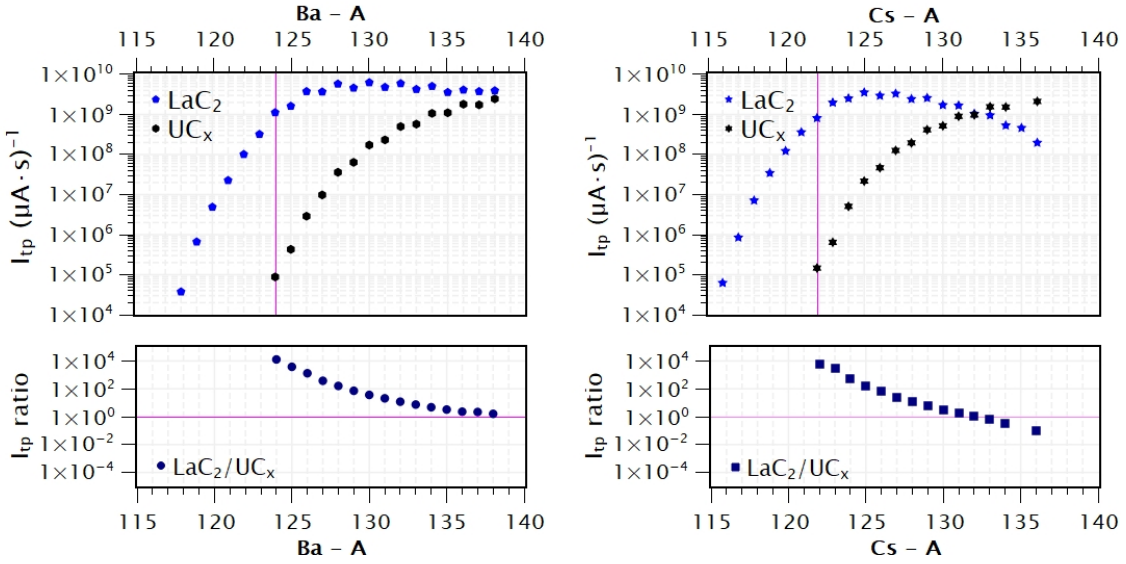

(a) Barium isotopes I_{tp} **(b)** Cesium isotopes I_{tp}

Figure 1.3: Simulated in-target production rates of barium and cesium from LaC_2 and UC_x targets. A LaC_2 target produces neutron deficient Ba and Cs isotopes by several orders of magnitude higher than a UC_x target, so a LaC_2 target is more suitable to produce these isotopes. Simulation results correspond to 10 cm long targets impinged with 480 MeV proton beam simulated in FLUKA (FLUKA simulation details can be found in Chapter 4).

However, the graphite target is a low-Z material, so it has a lower power deposition and it can withstand higher beam intensities than the LaC_2 and UC_x targets, allowing the ^{8}Li intensity from the graphite target to surpass the other two.

Increasing the number of target nuclei (N_{target}) by densifying the target material is an option to increase the RIB intensity. In the ceramic industry, sintering is the established process for eliminating porosity and increasing density [16]; however, sintering is avoided when synthesizing ISOL materials because open porosity is important for the effusion of isotopes. An alternative to increase the target nuclei is by increasing the target's thickness. The target's thickness refers to the length of target material that the proton beam sees in its path; to increase this length, the target container is loaded with thicker targets. In the case of the UC_x target, the amount of uranium allowed for irradiation is limited by the Canadian Nuclear Safety Commission (CNSC), so the target thickness is also limited; the rest of the targets are limited to the capacity of their containers and the thermal gradients associated to the power deposited through the target's thickness.

The selection of the targets is also influenced by their residual dose. Besides producing the desired isotope in adequate amounts, the residual dose rate associated to the target radioactivity is considered when choosing a target material. At the End of Bombardment (EoB), the targets are radioactive because the proton irradiation induces nuclear reactions, producing radioactive species that stay in the target material and its container. As time

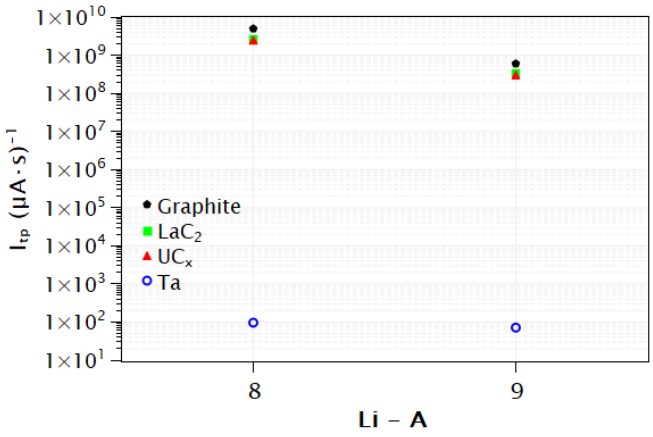

Figure 1.4: Comparison of the production rate (I_{tp}) of ^{8}Li and ^{9}Li (I_{tp}) of graphite, LaC_2, UC_x and tantalum targets obtained with simulations. The lowest production of ^{8}Li and ^{9}Li corresponds to the tantalum target, and the highest to the graphite target; however, the lithium production is in the same order of magnitude than the corresponding I_{tp} of the LaC_2 and UC_x targets. Nevertheless, a graphite target allows higher driver intensity than the other two targets, so it has the potential to deliver a RIB intensity higher than LaC_2 and UC_x targets in direct proportionality with the driver beam intensity (Eq. 1.1). Simulation results correspond to 10 cm long graphite, UC_x, and LaC_2 targets impinged with 480 MeV proton beam simulated in FLUKA (Chapter 4); tantalum's lithium-I_{tp} were obtained from ISAC simulation data base [15] for a target of 50 mmol/cm^2 impinged with 480 MeV proton beam also simulated in FLUKA.

passes, the radioactive isotopes decay and the residual dose rate reduces. To avoid exposing personnel to hazardous equivalent dose rates, the targets are remotely operated after EoB, and transferred to hot cells where they are stored until their activity is low enough for safe disposal.

The targets' associated residual dose rate is proportional to its isotope production. Thus, it is higher when irradiating with more intense beam currents, and for targets that produce a larger isotope assortment. Another factor contributing to the targets' residual dose is the duration of its irradiation campaign; a target irradiated for longer at high proton beam current has a higher net charge (μA·h). At comparable average net charges (Table 1.1), the graphite target has lower residual dose than tantalum (Fig. 1.5); considering that the graphite target has a higher production of ^{8}Li and ^{9}Li than a tantalum target (Fig. 1.4), then graphite targets are a better option to deliver these light isotopes. On the other hand, the graphite target has a higher average net charge in comparison with the UC_x target (Table 1.1) and its residual dose is within the upper limit of that of the UC_x targets. However, the UC_x targets have a comparable production rate of ^{8}Li and ^{9}Li (Fig. 1.4), and on average, it is routinely irradiated at lower proton currents (Table 1.1), so there is not much room to increase its production of these isotopes. Therefore, the graphite target is still a good option to deliver ^{8}Li and ^{9}Li even though it has a higher residual dose than UC_x targets.

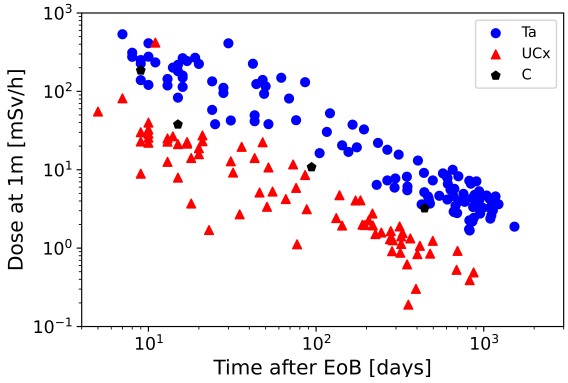

Figure 1.5: Residual dose of tantalum, UC_x, and graphite targets measured after End of Bombardment (EoB) 1 m away from the targets.

Table 1.1: Average registered proton beam current and net charge during the irradiation of UC_x, LaC_2, and graphite composite targets with a proton beam energy of 480 MeV at ISAC [17].

	Average	
Target material	**Proton current (μA)**	**Net charge (10^4·μA·h)**
Graphite	81	2.07
Tantalum	55	2.37
UC_x	17	0.37

Beyond producing isotopes, releasing them is critical for the RIB intensity. The overall ISOL efficiency (ε), comprises all the processes the isotopes undergo since they are produced until they are delivered to an experiment (Fig. 1.1). While the efficiency of separation and transport ranges from 10 to 100%, the ionization and release efficiencies can be as low as 10^{-1}% and 10^{-4}%, respectively [5]. To produce exotic isotope beams, the release time of the isotope must be lower, or in the same order of magnitude as its half-life (a few tens of milliseconds in the case of exotic isotopes) [18]; therefore, increasing the release efficiency enables the delivery of more exotic isotopes. Investigating the release efficiency and the research and development of target materials guarantees opportunities for the constant improvement of the RIB intensity and availability of any ISOL facility.

1.1.1 Release efficiency quality factors

Once an isotope is produced in the target, it has to escape from the material by bulk, grain-boundary, and surface diffusion. When the isotope reaches the grain's surface, it can be adsorbed back to the grain, or desorb and effuse through the target material pores (Fig. 1.6). The diffusion-effusion process continues until the isotopes effuse from the target material and find their way out of the target container towards the ion source [2].

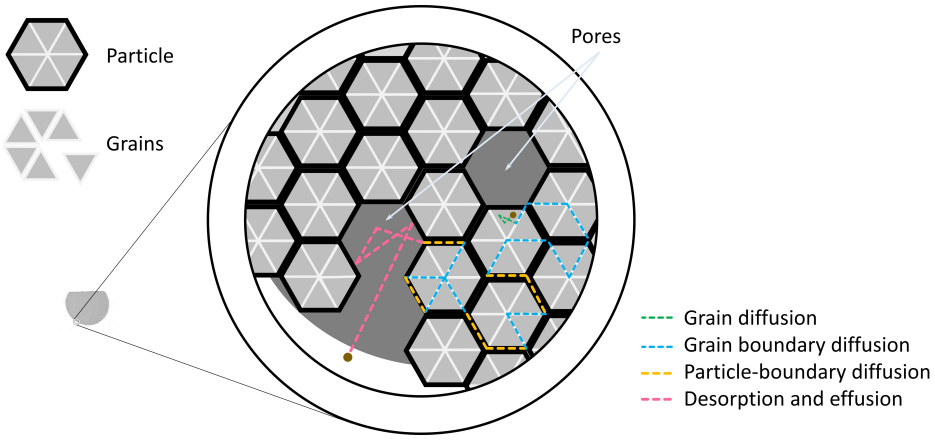

Figure 1.6: Depiction of the path an isotope follows to escape the target material bulk. The isotope randomly diffuses in a grain and neighbouring boundaries of grains and particles. When reaching a pore, the isotope desorbs or adsorbs from the pore's surface. The isotope diffuses and effuses until it releases from the target material [2].

The overall efficiency ε is given by:

$$\varepsilon = \frac{I_{obs}}{I_{tp}}, \tag{1.2}$$

where I_{obs} is the isotope yield delivered to experiments, and I_{tp} refers to the total isotope production rate in the target. The overall efficiency comprises all the process the isotopes go through from their production to their delivery to experiments (Fig. 1.1). ε is less than one because some isotopes are either not ionized, or they decay at some point between their production and delivery. With efficiencies between 10% and 100% [5], delays due to transport and separation are negligible, and even though the ionization release can be as low as 10^{-1}% [5], the efficiency of the isotopes to release from the target material (ε_{rel}) dominates the overall efficiency because ε_{rel} can be as low as 10^{-4}% or less [5].

The release efficiency (ε_{rel}) and the time to release an isotope (t) of decay time λ are related with the expression Eq. 1.3 [19]:

$$\varepsilon_{rel} = \int_0^{\infty} e^{-\lambda t} P(t) dt, \tag{1.3}$$

where $e^{-\lambda t}$ is the probability that the release time (t) is shorter than the decay time of the isotope (λ), and $P(t)$ is the probability that an isotope will be released within time t after its production:

$$P(t) = \int_{t=0}^{t} p(t') dt'; \tag{1.4}$$

in Eq. 1.4, $p(t')$ is the isotope release distribution, which in turn is obtained with Fick's second law.

The isotope diffusion from the particles is described by Fick's second law [20]:

$$\frac{\partial C}{\partial t} = \nabla \cdot (D \nabla C). \tag{1.5}$$

According to Eq. 1.5, the time evolution of the isotope concentration C is equal to the spatial variation of the concentration in proportion to the diffusion coefficient D. Assuming that the target material is composed by spherical particles of uniform radius r, and that it has an homogeneous isotope concentration, the solution of the Fick's second law is the cumulative distribution $(F(t'))$ [21]:

$$F(t') = 1 - \frac{6}{\pi^2} \sum_{n=1}^{\infty} \frac{1}{n^2} e^{-n^2 \pi^2 D t'/r^2}, \tag{1.6}$$

corresponding to the total amount of diffusing isotopes leaving a particle. In Eq. 1.6, t' is the diffusion time, and n is the summation index of the $(F(t'))$ distribution series. Differentiating Eq. 1.6 with respect to t', provides the diffusion time distribution from a spherical particle:

$$p(t') = \frac{6\pi^2 D}{\pi^2 r^2} \sum_{n=1}^{\infty} e^{-(n^2 \pi^2 D/r^2)t'}, \tag{1.7}$$

where the first term of the summation $(n = 1)$ has the dominant contribution such that Eq. 1.7 can be expressed as:

$$p(t') = \frac{6\pi^2 D}{\pi^2 r^2} e^{-(\pi^2 D/r^2)t'}. \tag{1.8}$$

Collecting the diffusion coefficient D, the radius r, and π in a diffusion parameter μ gives:

$$\mu = \pi^2 D/r^2, \tag{1.9}$$

that simplifies Eq. 1.8 to:

$$p(t') = \frac{6\mu}{\pi^2} e^{-\mu t'}. \tag{1.10}$$

Substituting the distribution of diffusion times $p(t')$ (Eq. 1.10) in Eq. 1.4 and integrating from 0 to t gives:

$$P(t) = \int_{t=0}^{t} \frac{6\mu}{\pi^2} e^{-\mu t'} dt' = \frac{6}{\pi^2} \left(1 - e^{-\mu t}\right). \tag{1.11}$$

Then, an expression for the release efficiency given by diffusion is obtained when substituting Eq. 1.11 in Eq. 1.3 and integrating:

$$\varepsilon_{rel} = \frac{6}{\pi^2} \int_0^{\infty} e^{-\lambda t} \left(1 - e^{-\mu t}\right) dt = \frac{6}{\pi^2 \lambda} \left(\frac{1}{1 + \frac{\lambda}{\mu}}\right). \tag{1.12}$$

Note from Eq. 1.12 that the release efficiency increases as λ/μ becomes much smaller than

one. When substituting Eq. 1.9 in λ/μ

$$\frac{\lambda}{\mu} = \frac{\lambda}{\pi^2}\frac{r^2}{D}, \tag{1.13}$$

it becomes evident that to maximize the release efficiency, the particle radius r should be small, and the diffusion coefficient D must be large.

To achieve small particle size, most ISAC targets are composed of slip casting micrometric powders. In facilities like ISOLDE and SPES, targets with nanometric particle size have been synthesized and irradiated, resulting in higher yield intensities than their micrometric counterparts [18, 22]. The synthesis of nanometric materials, however, requires special precautions and equipment currently unavailable in the ISAC facilities, but forthcoming in the ARIEL laboratories.

The ratio λ/μ also decreases by increasing the diffusion coefficient, which in turn increases with temperature. To approximate the influence of the temperature on the isotope release, the Arrhenius behaviour of diffusion is used (Eq. 1.14):

$$D = D_0 \cdot e^{-Q/RT}, \tag{1.14}$$

where D_0 is a pre-exponential factor, Q is the activation energy, R is the gas constant 8.31 J·(K·mol)$^{-1}$, and T is the temperature [20]. Inserting the Arrhenius behaviour of the diffusion in Eq. 1.9 gives:

$$\mu = \mu_0 e^{-Q/RT}, \tag{1.15}$$

where $\mu_0 = \pi^2 D_0/r^2$. Substituting Eq. 1.15 in Eq. 1.12 gives an expression for the release efficiency due to diffusion as a function of the target temperature:

$$\varepsilon_{rel} = \frac{6}{\pi^2\lambda}\left(1 + \frac{\lambda}{\mu_0 e^{-Q/RT}}\right)^{-1}. \tag{1.16}$$

Once the isotopes diffuse to the particles' surface, they must desorb from it and effuse through the pores. The open pores that connect the bulk to the surface, are paths for the isotopes to escape from the material. During their journey through the pores, the isotope collides with the pore walls, and depending on the temperature and the target-isotope combination, the isotope either scatters and follows a random trajectory until finding an exit, or it will reside in the pore wall until it is desorbed and able to keep flying until colliding with a pore wall again. Both process cause a delay in the effusion of the isotopes.

The effusion delay ($\bar{t}_c$) due to the mere collisions with the pore walls is given by [23]

$$\bar{t}_c = \frac{L^2}{4\rho\bar{v}}. \tag{1.17}$$

$\bar{t}_c$ depends on the length to pass through the pore (L), the radius of the pore (ρ), and the

average velocity of the isotope ($\bar{v}$). The isotope average velocity is given by [24]:

$$\bar{v} = \sqrt{\frac{8k_BT}{\pi m}}, \tag{1.18}$$

where k_B is the Boltzmann constant, T is the temperature, and m is the mass of the isotope. Increasing the temperature, increases the average velocity which in turn reduces the delay due to effusion. The same effect is obtained by reducing the length and increasing the radius of the pores.

The lingering due to adsorption $\bar{t}_s$ is governed by the sticking time τ_s [23]

$$\bar{t}_s = \frac{L^2\tau_s}{8\rho^2}, \tag{1.19}$$

and as the delay due to collisions, $\bar{t}_s$ also depends on the geometry of the pores. The sticking time τ_s is described by the Frenkel equation:

$$\tau_s = \tau_0 e^{-\Delta H_a/k_bT}, \tag{1.20}$$

where τ_0 is the time for single lattice vibration ($\sim 10^{-3} - 10^{-5}$ s) [10], ΔH_a is the adsorption activation energy, and T is the absolute temperature. The Frenkel equation indicates that the sticking time reduces as the activation energy decreases and the temperature T increases. For adsorption values typical of ISOL ($\Delta H_a \lesssim 3.5\ eV$), the sticking time is negligible at high temperatures [19].

The target materials are carefully chosen for the isotope of interest and the target material to have discordant chemical properties such that the desorption activation energy between them is low; however, this is not always achieved. To promote desorption, the targets are kept at high temperatures, so the sticking time of the effusing isotopes is low and their average velocity is high.

A high operational temperature not only enhances the isotope diffusion and effusion, but also contributes to the deterioration of the target material. Even when a certain temperature is chosen where no melting nor sublimation occurs, the material may still sinter [18]. Sintering promotes the growth of target material particles and eventually fuses the grains and particles together forming a monolith with low or no porosity. Often, target materials are synthesized with high-temperature resistant backbones, such as carbon powder, foils, or fibres; the target material is dispersed in the backbone avoiding the contact between the target material particles thus obstructing their sintering [6, 25, 26].

Typical ISOL targets consist of refractory metals (e.g. tantalum foils at TRIUMF) and refractory carbides (e.g. ZrC, TiC at TRIUMF and CERN [6, 27]). The carbide targets are often manufactured by pressing powders into pellets, or slip casting carbide

powders over graphite foils, such as at TRIUMF. This technique delivers thin target material composite foils with micrometric particle size and high porosity, thus providing increased isotope release.

1.2 ISAC slip cast composite targets

In 1998, powder pressed pellets were irradiated at ISAC [28]. The maximum operational driver beam current was restricted by the limited contact between the pellets and the target container; while the target oven had an internal diameter of 18.3 mm (Fig. 1.7b), the pellets diameter was only 16 mm, so there was not enough contact between the pellets and the container to dissipate the power deposited by the driver beam [29].

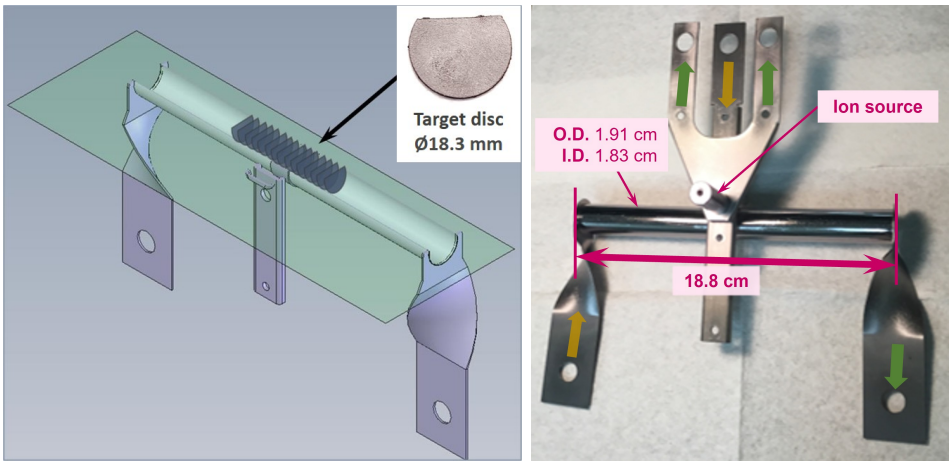

(a) Target material stacked in oven. **(b)** Target oven.

Figure 1.7: An average of 200 discs constitute an ISAC target (Fig. 1.7a). The discs are stacked in an oven and heated by passing current through the oven legs and walls (Fig. 1.7b); the ion source is also resistively heated using the supply legs on the top (see green and yellow arrows in Fig. 1.7b).

In 2002, targets made by slip cast composite discs were implemented at ISAC to substitute the pellets [29]. An ISAC slip cast composite target consist of about 200 D-shaped discs of a 200 µm thick material slip cast over 13 µm thick exfoliated graphite foil (Fig. 1.7a). The discs are stacked in a target oven made out of tantalum that is resistively heated to keep the discs evenly hot during irradiation and consequently enhance isotope release (Fig. 1.7b). ISAC's collection of routinely operated slip-cast composite targets includes silicon carbide (SiC), titanium carbide (TiC), zirconium carbide (ZrC), graphite and UC_x (Fig. 1.8) [30]; the graphite and UC_x targets have been developed as part of the project presented here.

The slip casting method to produce targets consists of mixing powder of the desired target material with binders and plastizers in a slurry and spread it thin on an exfoliated graphite foil of 0.13 mm thickness (Fig.2.1c). The resulting cast is flexible, and can be easily cut in any desired shape (Fig. 1.8). Preceding irradiation, the discs are resistively

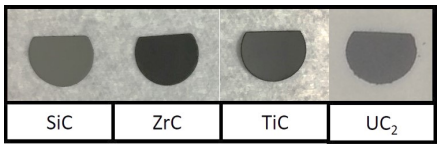

Figure 1.8: ISAC composite target material discs. These discs are 18.3 mm in diameter; they consist of a graphite foil 0.13 mm thick with a slip cast layer of the material. Except for the ZrC with an average thickness of 0.12 mm, the rest of the material thicknesses ranges from 0.18 to 0.26 mm.

heated under vacuum to outgass the plastizciers and binders from the slurry, and promote the adherence of the composite to the graphite foil [31].

The slip cast method delivers a thin layer of highly porous material suitable for isotope diffusion and effusion [32], but with the drawback of being fragile. The fragility of the slip cast material is compensated by the graphite foil that acts as an anchor and structural stabilizer. Moreover, it is believed that the graphite foil improves the thermal conductivity of the slip cast material [6] predominantly in the in-plane direction [33] (Table 1.2) such that most of the target heat conduction should occur between the graphite foils rim and the target oven wall. No studies in the thermal conductivity of the ISAC target materials have been done so far. However, testing infrastructure is presently under development [34] and when commissioned, it will allow systematic investigations on the heat conductivity of any new or already established target material.

Table 1.2: Graphite foil thermal conductivity reported by supplier (Ceramat) [35].

Direction	**Thermal conductivity (W/m-K)**
In-plane	140
Through-plane	5

1.3 ARIEL targets

ISAC has two target stations but only one operates at any given moment in time. To further expand its scientific capabilities, TRIUMF is developing ARIEL (Advanced Rare IsotopE Laboratory); this new facility will have the capability to deliver two RIBs simultaneously in addition to the operating one from ISAC [4]. This extended effort, is combined with a research and development campaign on target materials, aiming at understanding and improving their release properties in order to match the demanded exotic isotope beam production, as well as to cope with the increased power deposition and different geometry of the ARIEL Electron Target station East (AETE). For this work, three composite target materials were developed: graphite, LaC_2 and UC_x.

Until 2020, ISAC did not have a dedicated target for the delivery of beryllium and lithium isotopes. The lightest target that produced these isotopes was the SiC, but the

majority of the nuclear production of these isotopes comes from the carbon in this target. Also tantalum, ZrC, and even UC_x targets have been used to produce these light isotopes.

A slip-cast composite graphite target has been developed for the production of the highly demanded beryllium and lithium isotopes. Producing these light isotopes with a low Z target material alleviates the radioactive inventory that is produced by TRIUMF through lower inventory of exhausted gases and targets. Moreover, low-Z materials like carbon have smaller stopping power for protons, so they have less heat dissipation challenges as compared to high-Z materials. Therefore,the graphite composite target can be irradiated with larger proton beam currents, contributing to a more intense RIB. As part of its development, the graphite target material has been characterized by X-Ray Diffraction (XRD) and Scanning Electron Microscopy (SEM). Three graphite targets have been successfully irradiated, and this target is now routinely offered as part of the ISAC collection. The graphite composite target's ^{7}Be release has been analyzed offline and has proved superior as compared to alternative carbon target materials.

A LaC_2/C target material has been developed as a chemical surrogate of UC_2/C to investigate the methodology and material characterization. LaC_2/C can not be irradiated in ISAC because the facility does not have the capabilities to handle strongly pyrophoric materials; however, ARIEL foresees the necessary infrastructure to allow the operation of LaC_2/C targets. This target will be used for the production of neutron deficient barium and cesium isotopes, that combined with the adequate ion source will deliver these species with significantly reduced isobaric contamination and improved yields; so far, those isotopes have only been delivered with UC_x and ThO targets respectively. ThO targets are not part of ISAC's standard target repertoire because their operation and disposal are challenging [36]. UC_x and ThO targets deliver Cs only on the neutron rich side and the yields are subject to isobaric contamination. In contrast, LaC_2 is not a radioactive material like UC_x or ThO, so handling their precursors and setting this material online does not require special precautions, or licensing as a radiaoctive material.

A modified methodology was developed to accelerate the production rate of UC_x slip cast composite targets. Since the most requested target material is the UC_x and synthesizing them used to take up to eight weeks, the production of these targets was binding ISAC and ARIEL workforce and resources, preventing the research and development of new target materials. With the new method, a target is synthesized in eight days (Section 2.3). The resulting target material has also been characterized by XRD and SEM. Furthermore, the UC_x targets synthesized with this new accelerated method have been irradiated and their resulting RIBs (Section 4.8) have been successfully used in several experiments. The UC_x targets synthesized with the new method have now become the baseline for targets at ISAC.

Chapter 2

Target material synthesis and characterization

Three new composite targets have been developed in this study: LaC_2, UC_x, and graphite. To continue using the available infrastructure, each of the new target materials has been produced by slip casting; additionally, LaC_2 pressed pellets have been developed. The slip casting method to produce targets consists of mixing target material powder with water-based binders and plasticizers to form a slurry that is cast on a graphite foil (Fig. 2.1c). When the cast is dry, it is cut into D-shaped foils that are heated under vacuum.

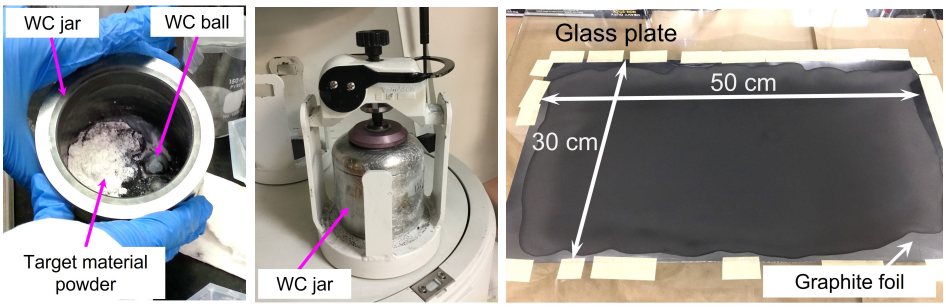

(a) Jar and balls **(b)** Planetary ball mill **(c)** Slip cast

Figure 2.1: Target material slip casting preparation. Powder of the desired target material is combined with graphite, plasticizers, and solvents in a WC jar with eight WC balls (a); the powders are mixed in a slurry with a planetary ball mill (b). The slurry is slip cast over a graphite foil (c).

The slurries are mixed with a planetary ball mill (Pulverisette 5) in tungsten carbide (WC) jars, always using eight WC balls of 20 mm diameter (Fig. 2.1a and 2.1b). All the slurries are slip cast on 130 µm thick exfoliated ≥99.8% pure graphite foil from Ceramaterials [35]. In preparation for casting the slurry, a 50×30 cm graphite foil is fixed to a glass plate; then, the slurry is poured at the centre of the foil and spread by manually tilting the plate in a rotatory movement (Fig. 2.1c). After a day, when the cast is dry, the foil is removed from the plate and cut into 1 inch wide strips. D-shaped discs of 18.3 mm diameter are

obtained by feeding the strips into a rotatory die cutter (Fig. 2.2). The discs are weighed and their thickness is measured with a micrometer. To remove the slurry binders, the discs are loaded conventionally in a target oven (Fig. 1.7) and heated under vacuum.

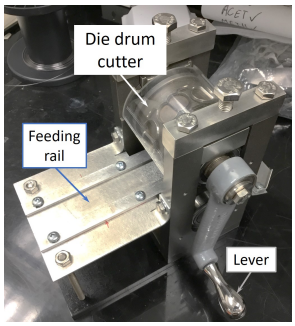

Figure 2.2: Rotatory die cutter used to cut D-shaped target discs. One strip 1" wide is positioned in the feeding rail. Turning the lever feds the strip in the cutter and punches discs from the strip. The discs and the reminder of the strip are collected in the opposite side of the cutter.

The discs' thermal treatment is carried out under vacuum in one of two furnaces (Fig. 2.3). One furnace is used for actinide materials and the other for non-actinide ones. Both furnaces have one roughing pump and one turbo molecular pump that allows them to reach a pressure of 1×10^{-7} Torr. Also, both furnaces have two power supplies, one supplying current to the target oven body, and the other to its ion source (Fig. 1.7b). Heating the target oven body promotes the evaporation of target material's binders and, in the case of UC_x and LaC_2/C targets, the carbothermal reduction of the target material precursors; both of these processes generate pores in the target materials. On the other hand, keeping the ion source hot prevents the condensation of impurities on its surface such that it stays clean in preparation for online use. The power supplies and pumping system of both evaporators are controlled with EPICS (Experimental Physics and Industrial Control System) [37].

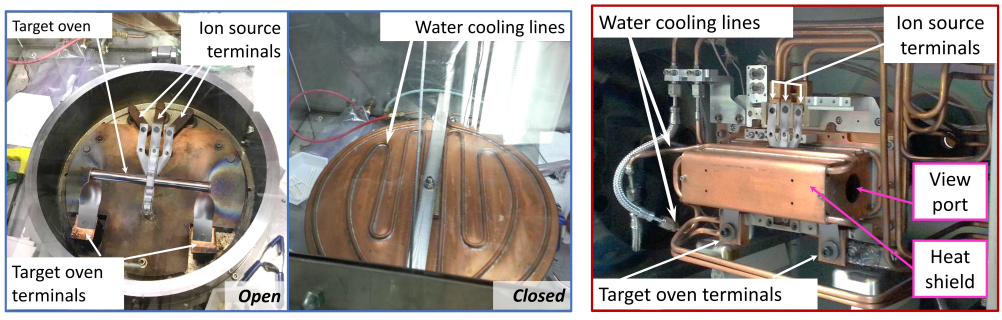

(a) Actinide materials furnace **(b)** Non-actinide materials furnace

Figure 2.3: Furnaces used for thermally treating target materials. Beside their shape, the furnaces differ in that the actinide material furnace (a) is enclosed in a glove box. Furthermore, the non-actinide furnace (b) has a view port for temperature measurements. To thermally treat a target material, the material is loaded in a target oven and installed on the terminals of a furnace; then, the furnace is set under vacuum, and the oven is resistively heated, heating the material inside of it.

Both furnaces include cooling lines but the non-actinide is the only one with a view-port where the temperature is measured with a two colour pyrometer operating in the range of 1000 to 3000°C (Fig. 2.3b and Fig. 2.3a). Another difference between the furnaces is that the actinide one is connected to a glove box to prevent spreading radioactive contamination and to control oxidation of the air sensitive UC_2. Both furnaces exhausts are coupled to nuclear ventilation.

2.1 Material characterization methodology

The target discs density, porosity, and microstructure were studied to identify the influence of the heat treatment on them, and ultimately, to correlate the targets characteristics with their isotope release.

In the following sections, slip cast material will refer to the material that is deposited onto the graphite foil (i.e. graphite, UO_2/C, UC_x, $La(OH)_3$/C, or LaC_2). And composite or target discs, to the slip cast material and graphite foil combined (Fig. 2.4).

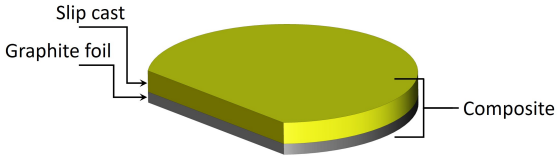

Figure 2.4: Diagram of a target disc. The slip cast is the material deposited on the graphite foil; together, the graphite foil and slip cast are called "composite" or "target disc".

2.1.1 Target material density and porosity

The bulk density of a slip cast material is calculated with Eq. 2.1:

$$\rho_{bulk} = \frac{m_{sc}}{V_g}, \tag{2.1}$$

where m_{sc} is the mass of the composite minus the mass of the graphite foil, and V_g is the geometrical volume

$$V_g = t_{sc} \cdot a_{seg} \tag{2.2}$$

that is given by the slip cast material thickness (t_{sc}) and the area of the disc (a_{seg}). The slip cast thickness (t_{sc}) across the cast varies because the slurries are slip cast manually. Therefore, several discs are measured with a micrometer to obtain an average t_{sc}. The diameter of the target material discs is determined by the die cutter, so it does not fluctuate as the cast thickness; nevertheless, the diameter (d) and height (h) (Fig. 2.5) of several discs are measured with a caliper. The area of the discs (a_{seg}) is estimated with the formula for

the area of a circle segment:

$$a_{seg} = r^2 \arccos\left(\frac{r-h}{r}\right) - (r-h)\sqrt{2rh-h^2} \tag{2.3}$$

where $r = d/2$.

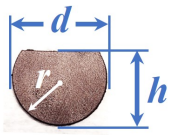

Figure 2.5: Target material disc. The height h and diameter d of the discs are measured with a caliper (the radius is $r = d/2$), allowing to calculate the total area of the discs segment a_{seg}.

Open pores in the target material not only affect its density but also become relevant for isotope release [10]. Open porosity describes those pores within the material bulk that, unlike closed pores, make an open path from the pore to the surface, promoting isotope effusion [38]. The volume of the open pores (V_{op}) is the difference between the geometric (V_g) (Eq. 2.2) and apparent volume (V_a):

$$V_{op} = V_g - V_a. \tag{2.4}$$

The apparent volume (V_a) includes the volume of the slip cast and that of the closed pores (Fig. 2.6); V_a is measured with a gas pycnometer. The slip cast apparent density (ρ_a) is the ratio between the slip cast mass (m_{sc}) and the apparent volume:

$$\rho_a = \frac{m_{sc}}{V_a}. \tag{2.5}$$

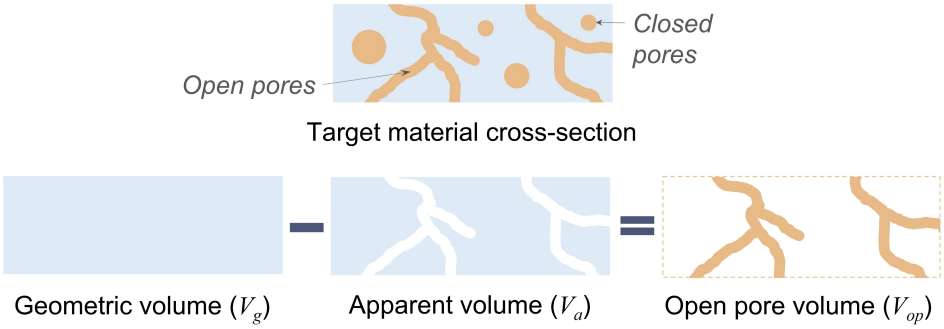

Figure 2.6: Schematics of cross section of a target material sample. The circles represent closed pores, and the paths depict open pores that connect the interior of the sample to its surface.

The open porosity fraction is calculated using the ratio of the open and geometric volume:

$$P_{op} = \frac{V_{op}}{V_g}. \tag{2.6}$$

The total porosity (P_{tot}) is calculated with the bulk density (ρ_{bulk}) (Eq. 2.1) and the theoretical density (ρ_{th}) of the slip cast material [16]:

$$P_{tot} = \left(1 - \frac{\rho_{bulk}}{\rho_{th}}\right). \tag{2.7}$$

The theoretical density corresponds to a slip cast with no pores, and it can be found in the literature for several materials (e.g. [39]). For the graphite slip cast, the theoretical density of carbon 2.25 g/cm^3[40] was used to calculate the slip cast's total porosity. In contrast, the UO_2, $La(OH)_3$, UC_x and LaC_2 slip casts have excess graphite, so their theoretical density ($\rho_{th_{sc}}$) was estimated with Eq. 2.8:

$$\rho_{th_{comp}} = \frac{1}{\frac{C_x}{\rho_{th_x}} + \frac{C_{graphite}}{\rho_{th_{graphite}}}}, \tag{2.8}$$

where $\rho_{th_{graphite}}$ is the theoretical density of graphite, and ρ_{th_x} the theoretical density of $La(OH)_3$, UO_2, LaC_2 or UC_2 accordingly; $C_{graphite}$ is the mass concentration of graphite in the slip cast (Eq. 2.9):

$$C_{graphite} = \left(\frac{m_{graphite}}{m_{graphite} + m_{sc}}\right), \tag{2.9}$$

and C_x is the mass concentration of $La(OH)_3$, LaC_2, UO_2, or UC_x in the slip cast (Eq. 2.10):

$$C_{graphite} + C_x = 1. \tag{2.10}$$

The concentration of the slip cast material C_x before carbothermal reduction is calculated using the stoichiometry of the educts in the $La(OH)_3$ (Eq. 2.11a) or UO_2 (Eq. 2.12) slurries; assuming that the chemical reactions are complete after carbothermal reduction, the C_x of the slip cast materials is calculated with their mass and the expected stoichiometry of the UC_x (Eq. 2.12) or LaC_2 (Eq. 2.11c) products. The stoichiometries of the $La(OH)_3$, UO_2, LaC_2, and UC_x/C are outlined in Sections 2.2 and 2.3.

Since all our composite targets consist of slip cast materials attached to a graphite foil (Fig. 2.4), characterizing the later is essential to distinguish its properties from those of the slip cast. Thus, the slip cast apparent volume can be distinguished from that of the graphite foil even if it is not separated from it during pycnometry analysis.

Samples of graphite foil were prepared to obtain their density and porosity. Discs of 0.55±0.01 cm diameter were cut with a hammer driven punch, and their thickness and mass were measured. The resulting bulk density of 1.15±0.04 g/cm^3 (Table 2.1) is in agreement with the one reported by the vendor of 1.12 g/cm^3 [35]. Furthermore, these graphite foil samples were submitted to pycnometry to measure their apparent volume and calculate their apparent density (Eq. 2.5). Also, the total, closed, and open porosity of the graphite foils were calculated (using a theoretical density of 2.25 g/cm^3 [40]).

The values from the characterization of the graphite foils are compiled in Table 2.1. The apparent volume of the graphite foils is subtracted from the composite's apparent volume when characterizing all the slip casts mentioned in the following sections. Also, with the high open porosity of the graphite foils it would be expected for them to have an excellent isotope release, but it was found in this work that it was not the case for releasing ^{7}Be (Section 4.1).

Table 2.1: Characteristics of the graphite foils used as backing foil in ISAC composite targets.

Characteristic	**Value**
Thickness (mm)	0.129 ± 0.004
Bulk density (g/cm^3)	1.15 ± 0.04
Apparent density (g/cm^3)	2.03 ± 0.01
Total porosity	0.49 ± 0.02
Open porosity	0.44 ± 0.01
Closed porosity	0.05 ± 0.02

2.1.2 Scanning electron microscopy

A Scanning Electron Microscope (SEM) produces a micrograph by scanning the surface of a sample with an electron beam, and by detecting reflected or emitted electrons in backscattered direction. Scanning electron microscopy was used to analyze the slip casts of the target discs. The surface and cross sections of two samples per target were analyzed to observe their particle distribution, size, and morphology. Micrographs of the slip cast before and after thermal treatment were compared to diagnose the influence of the thermal treatment in the slip cast microstructure.

The SEMs were operated in two modes: Backscattering Electrons (BSE), Secondary Electrons (SE). In the BSE mode, the electrons detected are those scattered due to Coulomb interactions with the nucleus of the sample, and their energy is close to the incident electron beam energy [41]. Chemical composition contrast in the sample is visible depending on the atomic number of the compounds present [42]; thus, BSE allowed the observation of the compounds distribution through the slip casts. Secondary electrons (SE) on the other hand, are outer shell electrons emitted from the surface of the sample [41]. Compared with BSE, SE delivers images with greater topographical detail, so the surface morphology of the target materials synthesized in this work was observed with SE.

Some of the SEMs used in this work have a spectrometer to detect X-rays and carry out Energy-Dispersive X-ray Spectroscopy (EDS). Characteristic X-rays are emitted when the beam's electrons knocks out inner-shell atomic electrons [41]. With EDS, the elemental composition and in some cases impurities of the target materials were studied.

In addition to SE and BSE, the electron beam also produces specimen current which consists of the absorbed electrons that do not escape the sample. When the sample is

not grounded the specimen builds up a negative charge that discharges when it reaches a critical point. Due to their high carbon content, the target material analyzed in this work were already conductive; to minimize specimen charge up, the target-material samples were attached with carbon tape to an aluminum SEM stub (Fig. 2.7). The samples were attached to the stubs with their slip cast facing up allowing the scanning of the slip cast surface. The stubs were tilted in the SEM to observe the samples' cross section except for the graphite slip cast sample. The graphite samples' cross section was not analyzed because its adherence to the stub was weak, and tilting the stub entailed the risk of dropping the powdery sample in the SEM; nevertheless, its surface was analyzed.

To prevent their oxidation, LaC_2 and UC_x samples were prepared in a glove box under argon atmosphere. However, during their installation in the SEM, the samples were briefly exposed to atmospheric conditions such that their surface absorbed oxygen; this modified the morphology of the LaC_2 samples, and prevented the reliable determination of oxygen content in the UC_x samples.

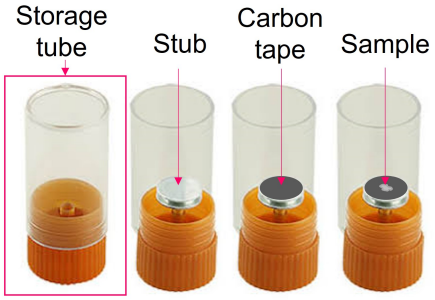

Figure 2.7: Slip cast sample on SEM stub. The slip cast samples were adhered to a standard SEM stub (12.7 mm diameter) with double-sided carbon tape. The samples were transported to the SEM in single pin mount storage tubes. Samples sensitive to air (UC_x and LaC_2) were prepared under argon atmosphere in a glove box; the storage tube would keep the sample under argon during transportation (∼20 min), but the sample would be exposed to air when placed in the SEM for a few seconds or minutes.

The SEM micrographs of each target material are included in the their respective subsections (2.2.2, 2.3.1, 2.4.1). The displayed SEM micrographs were selected to be representative of the morphology of each sample, and were used to estimate the average particle size of the slip casts (Appendix A.5).

BSE micrographs of UO_2 casts are displayed in this work because the distribution of the compunds in the slip cast is an indicator of the potential particle size during heat treatment (Fig. 2.32 and 2.40). After heat treatment, observing the morphology of the particles is more relevant than the contrast against compounds, and since the morphology is displayed with more detail with SE than with BSE, SE micrographs of UC_x and LaC_2 slip casts are included in the following sections to display the slip casts particle size and shape (Section 2.3.1 and 2.3.2).

The EDS results of selected samples of graphite and UC_x are included in Sections 2.4 and 2.3. The intention of those is to showcase the presence or absence of impurities in the given samples. The complete phase composition of the target materials was studied with X-ray powder diffraction (XRD).

2.1.3 X-ray powder diffraction

X-ray diffraction (XRD) is a technique to study the phase composition of materials. A single axis X-Ray Diffractometer (XRD) was used to determine the average bulk composition of our target materials. The XRD was equipped with a 2 kW X-ray copper generator with a monochromator and a scintillation counter detector [43]. The samples were analyzed with 40 kV and 40 mA at a starting angle of 3° and stopping angle of 90°, at a scan speed of 1°/min. The detection limit of XRD ranges from 0.1 to 1 wt%, so crystalline phases below this concentration can typically not be detected with this technique (Table 2.2) [16].

Table 2.2: Limitations of the X-Ray Diffraction technique. Data reproduced from [16].

Feature	**XRD limitations**
Common state of specimen	Solid
Detection limit (ppm)	$10^3 - 10^4$
Angular precision (%)	$0.2 - 0.5$
Angular accuracy (%)	$0.5 - 5$

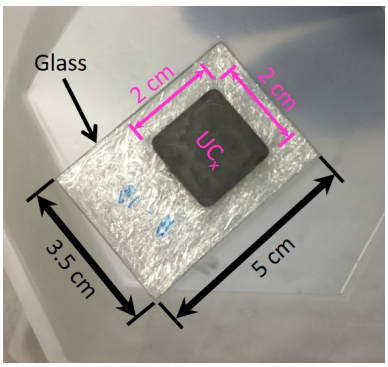

Figure 2.8: UC_x sample prepared for XRD analyzes. The glass is wrapped with cling foil to protect the material from oxygen. The wrapping also prevents the spread of contamination by containing the UC_x powder. This methodology was used to prepare LaC_2/C samples as well. Graphite samples were not wrapped with cling foil.

The sample preparation for XRD powder analysis of our target material consists of scrapping off the slip cast from the backing graphite foil and grinding it manually in an agate mortar. Then the powder is compacted on a zero diffraction XRD plate of 0.2 mm depression (Fig. 2.8). Since the graphite target does not oxidize when exposed to air, samples of this material do not require additional preparation. In contrast, the UC_x and LaC_2 samples are wrapped with transparent cling wrap to prevent the material to enter in contact

with oxygen during transportation and analysis at UBC-MEML [43] (Fig. 2.8). While the graphite samples were prepared in a fume hood, the UC_x and LaC_2 samples are prepared in a glovebox under argon.

The target material composition was investigated with XRD. The results were especially important to confirm the carbothermal reduction completion of the UC_x and LaC_2 materials that are synthesized in-house. Also, XRD analysis revealed impurities that were in crystalline form and above the concentration limit of 1 wt%. The XRD patterns were analyzed with Match! [44], this software compares experimental patterns with reference patterns from the Crystallography Open Database (COD) [45].

2.2 LaC_2 target synthesis

All ISAC target material carbide composites are made out of commercially available carbide compounds, except for the UC_x target that is synthesized in-house by carbothermal reduction of isotopically U-235 depleted UO_2 powder. LaC_2 target material has been developed in this work as a rehearsal for the development of UC_x targets because lanthanum is a chemical homologue for uranium [7], but is not a radioactive element such that special authorizations are not required to handle it.

LaC_2 targets allow delivering neutron-deficient barium and cesium RIBs (Fig. 1.3). Even though ISAC does not have the means to irradiate materials that are sensitive to air as LaC_2, ARIEL will employ hermetic target vessels, allowing the online operation of LaC_2 targets. Developing LaC_2 pellets and slip casting in this work proves that we have the capabilities to synthesize LaC_2 with our current infrastructure, methods and resources.

According to the La:C phase diagram (Fig. 2.9) [46], a minimum molar concentration of 67% carbon (C) has to be combined with lanthanum (La) to synthesize LaC_2 [7]. At this carbon concentration and above, α-LaC_2 is obtained below 1060 °C, and β-LaC_2 phase is obtained over it (Fig. 2.9); the former is a body central tetragonal crystal structure, and the latter is a body centred cubic crystal structure. Ideally, a target material would be multiphasic to prevent particle growth [16], a mechanisms that leads to isotope release declining (Eq. 1.12 and 1.18). However, the two LaC_2 phases could not coexist at the conventional operational temperature that ranges from 1700 °C to 2300 °C because the β-LaC_2 phase prevails above 1060 °C.

Cesium (Cs) and barium (Ba), the elements of interest extracted from the LaC_2 target, vaporize at 17 °C and 387 °C respectively [47] at the operational pressure of 10^{-6} Torr [48]. Even though the temperatures to vaporize Cs and Ba are low, operating the target at higher temperatures promotes their diffusion and release (Eq. 1.14). The limiting temperature of the LaC_2 target is given by its vapour pressure; LaC_2 starts vaporizing above 1720 °C [49] at the operational pressure of 10^{-6} Torr [48] (Fig. 2.10).

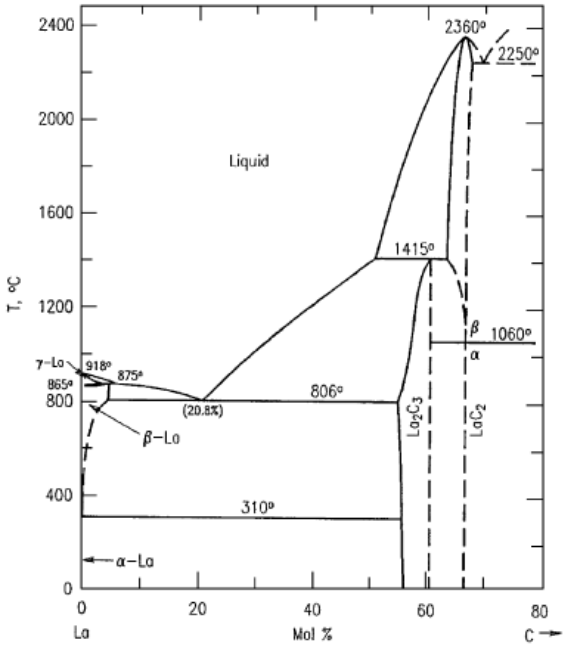

Figure 2.9: La:C phase diagram from [46].

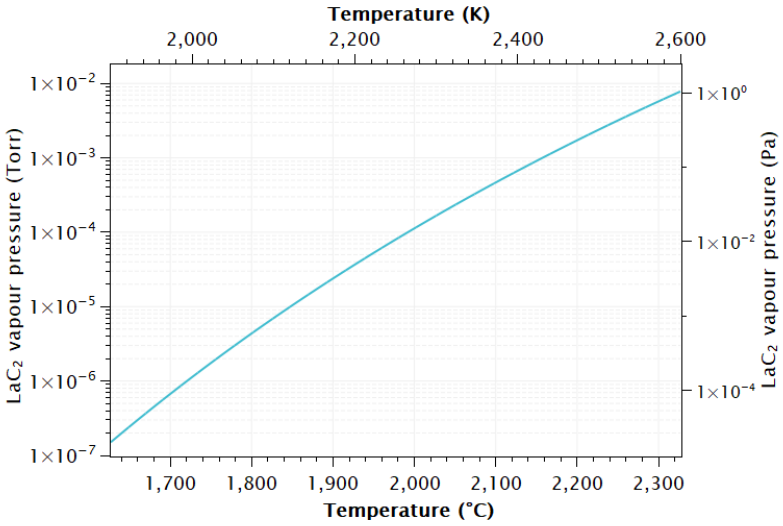

Figure 2.10: LaC_2 vapour pressure. Curve plotted in accordance with LaC_2 vapour pressure function from [49].

To synthesize LaC_2 target material, La was mixed with C in a proportion of 15% mol and 85% mol respectively (Eq. 2.11). The resulting mixture had more graphite than the minimum necessary to obtain LaC_2 (Fig. 2.9); in this way, the carbothermal reduction was more likely to be completed, and the material ended up with excess carbon to prevent particle sintering and growth [16], and led to improving the material thermal conductivity [6]. This graphite-lanthanum proportion has proven successful for LaC_2 synthesis at RISP and SPES [50, 7] when following the methodology developed at CERN [51].

La_2O_3 has been used as a precursor to synthesize LaC_2 targets first at CERN and then at INFN and TRIUMF [52, 7, 53, 32]. However, superficial hydration of La_2O_3 into LaOOH was observed during synthesis at INFN [7]; furthermore, Ravn et. al. [52] report outgassing and target material loss during operation of LaC_2 targets synthesized with oxides. $La(OH)_3$, on the other hand, is more stable than La_2O_3, it is not supposed to oxidize at ambient temperature, and it is expected to promote higher porosity because it is suggested to outgas more during the heating treatment to synthesize LaC_2.

For this work, $La(OH)_3$ and graphite were used as precursors for the synthesis of LaC_2/C pellets (Section 2.2.1) and LaC_2/C slip cast discs (Section 2.2.2). The $La(OH)_3$ powder had a mean particle size of 20 µm and it was 99.95% pure. The graphite powder was ≥44 µm (-325 mesh) 99.9995% pure. Both powders were supplied by Alfa Aesar [54, 55]. The additional plasticizers and solvents used in the slip cast are listed in Table 2.5 (their specification are reported in the Appendix A.1). On the other hand, the pellets did not contain any other substance besides $La(OH)_3$ and graphite.

The $La(OH)_3$/C discs and pellets were thermally treated to carbothermally reduce their $La(OH)_3$. To be able to monitor the temperature during the heating treatment, both, pellets and discs were heated in the non-actinide furnace (Fig. 2.3b) under vacuum. The pressure was also monitored, but the values weighed to the furnace chamber, so they might differ from the local pressure in the testing container.

The pressure ranged from 5×10^{-7} Torr to 4×10^{-5} Torr during the thermal treatments of the pellets and discs. The pellets were heated aiming at 1700 °C, which would be the maximum operational temperature of a LaC_2 target given that the vaporization temperature of this material is 1720 °C at 10^{-6} Torr [49]. Heating the target material just below its vaporization temperature promotes the outgassing of impurities in the material that would otherwise be released during operation. Even though the LaC_2 pellets were not going to be irradiated online, thermally treating them at 1700 °gives information about the endurance of the synthesized LaC_2/C.

The $La(OH)_3$ discs were heated aiming at 1800 °C, 100 °C hotter than the pellets. The higher temperature attempts to compensate for the improved thermal dissipation (not yet quantified) that is expected from their backing graphite foil [6]. Neither the pellets nor the discs lost more mass than expected due to the carbothermal reduction (Table 2.3 and 2.6), suggesting that LaC_2 did not vaporize during their heating treatment.

Besides carbothermally reducing the $La(OH)_3$, the thermal treatment evaporates moisture from the pellets, and, in case of the discs, it also evaporates plasticizers and other substance (Table 2.5) in the slip cast. The formation of open pores in the pellets and discs is promoted by the evaporation of their water and binders, as well as the release of CO and H_2O due to the carbothermal reduction. Between pellets and discs, the discs had higher total porosity (Table 2.7). This was expected because the discs had additional outgassing due

to evaporation of binders and plasticizers in the slip cast. Neither the pellets nor the discs were submitted to pycnometry because LaC_2 is prone to oxidation, so their open porosity is unknown. Nevertheless, the discs' open porosity is higher than that of the pellets, suggesting an advantage for isotope effusion over the pellets. The synthesis and characterization of the LaC_2/C discs and pellets is detailed in the sections below.

2.2.1 LaC_2 pellet synthesis

Pressing pellets is the established production methodology among the ISOL community. The resulting material have shown effective performance in this format [56]. For ARIEL, pellets synthesis should be revisited (Section 1.2) to take advantage of this quick and clean method of producing targets. For this work, LaC_2 pellets were synthesized by milling $La(OH)_3$ and graphite powders together, then the mixed powder was pressed into pellets and submitted to carbothermal reduction. This methodology can also be followed to produce UC_x pellets for ARIEL and ISAC by using UO_2 instead of $La(OH)_3$, but first, safety procedures have to be implemented to prevent contamination.

$La(OH)_3$ and graphite were milled in a planetary ball mill both dry and in suspension. 20 g of $La(OH)_3$, and 7 g of graphite were dry-milled for one minute six times at 60 RPM. On the other hand, the same amount of $La(OH)_3$ and graphite, were suspension-milled with 40 ml of isopropanol (IPA) under the same conditions; the resulting mixture was left in a fume hood for three days until the IPA evaporated and the mixture was dry.

Dry milling was ineffective in reducing the average particle size. The $La(OH)_3$ average particle size remained 20 µm after dry milling it. In contrast, suspension milling reduced the $La(OH)_3$ average particle size to 10 µm. The average particle size of the $La(OH)_3$ was estimated measuring the diameter of particles in a line across their respective micrographs (Fig. 2.11) (Appendix A.5).

Pellets of both mixtures were uniaxially pressed with a hydraulic press of 50 tons capacity in a 13 mm diameter die of 10 tons capacity. For each pellet, the die was loaded with 0.5 g of $La(OH)_3$/C mixture. Darker and thinner pellets resulted from pressing suspension-milled powder (Fig. 2.12), suggesting that these pellets were more compacted because their $La(OH)_3$ and graphite powders were smaller, and more homogeneously mixed.

Different forces were applied to form $La(OH)_3$/C pellets. The higher the force the thinner the pellets. Even though the same amount of powder was used for all pellets, those made with the suspension-milled $La(OH)_3$/C were consistently thinner than the pellets made with dry-milled $La(OH)_3$/C, indicating that the suspension-milled powder allowed more compaction, and hence denser pellets with lower total porosity (Eq. 2.7) (Fig. 2.13).

Suspension-milled $La(OH)_3$/C powder was chosen over dry-milled $La(OH)_3$/C because it delivered pellets with superior structural stability. In order to obtain 1 mm thick pellets, 0.33 g of $La(OH)_3$/C powder was loaded in a 13 mm die and pressed with a force of 10 tf

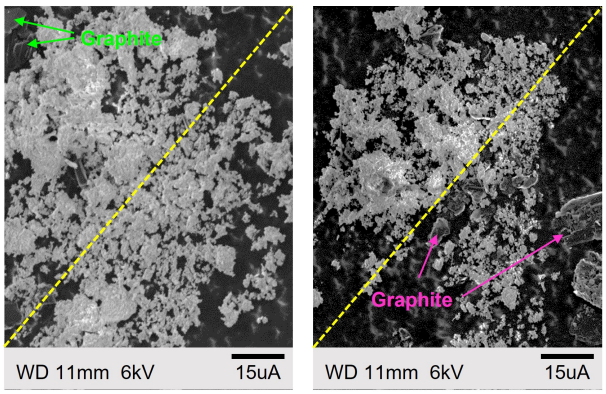

(a) Dry-milled **(b)** Suspension-milled

Figure 2.11: SEM micrographs of $La(OH)_3$/C used to press pellets. White powder is $La(OH)_3$; dark large particles are graphite. Suspension milled $La(OH)_3$ (b) exhibits smaller average particles as compared to dry-milled $La(OH)_3$ (a). The average particle size of the $La(OH)_3$ was estimated measuring the diameter of its particles in a line across their respective micrographs like the yellow one in (a) and (b).

(a) Dry milled **(b)** Suspension milled

Figure 2.12: Pellets made with $La(OH)_3$/C mixtures dry and suspension-milled. The suspension-milled pellets (b) were darker and thinner than the dry-milled ones (a), suggesting a more homogeneous mix of the $La(OH)_3$ and graphite powders.

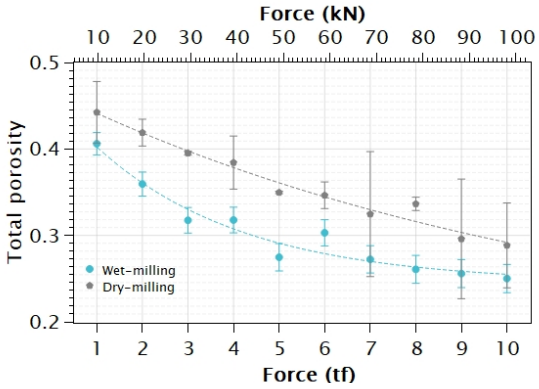

Figure 2.13: Contrast between the total porosity of $La(OH)_3$/C pellets pressed with suspension and dry-milled $La(OH)_3$/C powder. Suspension-milling delivered smaller $La(OH)_3$ particle size than dry-milling. Finer particles allowed more compact and dense pellets with lower porosity.

(98 kN) with a hydraulic press. Since these pellets were not going to be irradiated, they did not need to be loaded in a target oven (Fig. 1.7b). Instead, the pellets were carbothermally reduced by resistively heating a tantalum boat where they were loaded (Fig. 2.14b). To set

the 13 mm diameter pellets in the 19.05 mm diameter boat, the pellets were introduced in a 19 mm diameter graphite testing-container of 24 mm length (Fig. 2.14a).

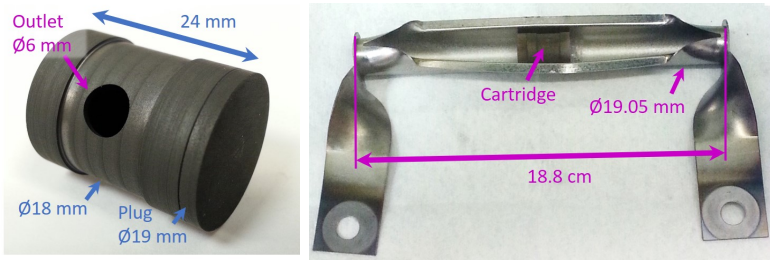

(a) Testing container **(b)** Tantalum boat

Figure 2.14: Testing container and tantalum boat for the carbothermal reduction of $La(OH)_3$ pellets. Five $La(OH)_3$ pellets were loaded in a testing container (a), and set in a tantalum boat (b) to resistively heat them in the non-actinide furnace.

The thermal treatment of the $La(OH)_3$ pellets lasted twenty five hours (Fig. 2.15a). An automatic current ramp of 0.5 A/min was set to 300 A. The automatic mode was programmed to pause the current ramp when the pressure reached a vacuum limit of 0.03 mTorr, and to reduced it to 0 A if the pressure reached the limit of 0.04 mTorr. The pressure was rising at the beginning of the thermal treatment, so from 40 A to 100 A, the current ramp was intermittently interrupted automatically (Fig. 2.15b). Above 100 A, the 0.5 A/min current ramp was continuous until 300 A when it was manually stopped to prevent the pressure to rise overnight. After 8 hours, the 0.5 A/min current ramp was set to 420 A (≈1700 °C). The pellets remained at this conditions for 1 hour until the current suddenly tripped to 0 A due to a technical failure; after that, the pellets were not returned to 420 A.

During the target materials thermal treatment, the pressure peaks matching with a temperature give an insight of the carbothermal reduction reactions. However, none of the furnaces are equipped with a Residual Gas Analyzer (RGA) to identify the gases released during heating treatments. Moreover, only pressure increments that occur above 1000 °C can be matched with a temperature because the pyrometer is limited to a 1000 °C to 3000 °C range. Nevertheless, the order of occurrence of the peaks are still an indication of the evaporation of organics or the release of carbothermal reduction gasses.

During the thermal treatment of the $La(OH)_3/C$ pellets, two ranges of pressure peaks were observed (Fig. 2.15). The first peaks most likely corresponds to the water that the pellet retained from moisture in the environment, and to the water released from the decomposition reaction of $La(OH)_3$ and LaOOH at $\sim$ 330 °C and ∼490 °C, respectively [57] (Eq. 2.11a and Eq. 2.11b). The second region most likely correspond to the CO released due to the carbothermal reduction of the La_2O_3 and the synthesis of LaC_2 (Eq. 2.11c); this reaction is expected to start at 1200 °C [7], and it seems to be matching with the pellets' thermal treatment. Note that there are two peaks in the second region, this is because the ramping

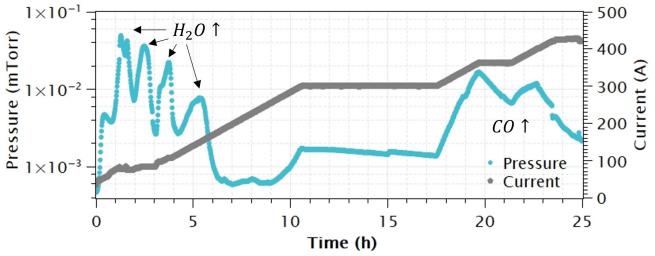

(a) Evolution of the $La(OH)_3$ pellets thermal treatment.

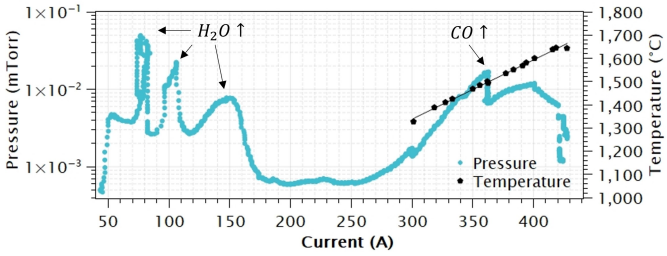

(b) Temperature and pressure corresponding to the current supplied for resistively heating the $La(OH)_3$/C pellets.

Figure 2.15: Heat treatment of five $La(OH)_3$ pellets. The treatment lasted around 25 hours (a). First, water was released due to the decomposition reaction of $La(OH)_3$ into La_2O_3. The pressure remained below $\approx 2\times10^{-3}$ Torr for about eleven hours until it rose again indicating the carbohtermal reduction of La_2O_3, that started around 1200 °C (b). To fully carbothermal reduce the target, it was held for 1 hour at 420 A corresponding to ≈1700 °C (b).

was interrupted by the vacuum limit, resulting in the splitting of the peak corresponding to the release of CO (Fig. 2.15a and 2.15b).

$$2La(OH)_3 + 11C \rightarrow 2LaOOH + 11C + 2H_2O \uparrow \tag{2.11a}$$

$$2LaOOH + 11C \rightarrow La_2O_3 + 11C + H_2O \uparrow \tag{2.11b}$$

$$La_2O_3 + 11C \rightarrow 2LaC_2 + 4C + 3CO \uparrow \tag{2.11c}$$

The characterization of the LaC_2 pellets was limited to their macroscopic appearance, linear dimensions, bulk density, and total porosity. This material was not subject to pycnomtrey nor XRD analysis due to its oxidation promptness when exposed to air. The LaC_2/C pellets were stored, and characterized in a glove box under argon atmosphere. The most noticeable characteristic of the LaC_2/C pellets was their colour; instead of dark grey (Fig. 2.16a), they became golden as a result of their thermal treatment (Fig. 2.16b). Like Greenwood and Osborn [58] observed when synthesizing LaC_2, after carbothermal reduction, the $La(OH)_3$/C pellets (Fig. 2.18a) changed from grey to yellow-ochre (Fig. 2.18b) suggesting the synthesis of LaC_2. Another indication of the pellets carbothermal reduction was their mass lost of 27.7 %, matching with the 27% mass lost expected (Eq. 2.11). Furthermore, the diameter of the resulting LaC_2/C pellets shrank, their bulk density (Eq. 2.8)

reduced and their total porosity (Eq. 2.7) increased (Table 2.3) (the LaC_2/C pellets' total porosity was calculated with LaC_2 and C theoretical densities of 5.29 g/cm^3 [59] and 2.25 g/cm^3 [40], respectively).

(a) $La(OH)_3$/C pellets **(b)** LaC_2/C pellets

Figure 2.16: LaC_2/C pellets synthesized in-house (b). Before carbothermal reduction, these pellets were dark grey (a).

Table 2.3: Characteristics of pellets before ($La(OH)_3$/C) and after carbothermal reduction (LaC_2/C).

Characteristic	**$La(OH)_3$/C**	**LaC_2/C**
Mass (g)	0.36±0.01	0.26±0.01
Diameter (cm)	1.29±0.01	1.15±0.01
Thickness (cm)	0.099±0.004	0.115±0.010
Bulk density (g/cm^3)	2.82±0.15	2.17±0.22
Total porosity	0.19±0.01	0.52±0.02

Compared with the LaC_2 pellets developed at RISP [50], the pellets synthesized in this work have a lower total porosity; nevertheless, their total porosity is close to the mean reported for SPESs' pellets [53] (Table 2.4). Further experiments in the thermal treatment, milling, and pressing methods could lead to higher porosity; for example, heating the material faster might contribute to the formation of open pores while avoiding particle growth of $La(OH)_3$ [16]. As the LaC_2 pellets' high porosity and small particle size would be effective for isotope release, those characteristics will also enhance the pellets' propensity to oxidation since oxygen diffusion through the bulk will also be facilitated. The development of improved LaC_2 pellets would require special precautions and infrastructure currently unavailable; nevertheless, the ARIEL facilities are expected to include the capabilities necessary to continue with the LaC_2 pellets' research and development.

Table 2.4: Comparison of the total porosity of the LaC_2/C pellets synthesized in house with pellets developed at RISP [50] and SPES [53].

LaC_2/C	Total porosity (%)
This work	52±2
RISP [50]	68 to 71
SPES [53]	24 to 70

2.2.2 LaC_2 slip casting synthesis

UC_x is the only target of the ISAC collection that is chemically synthesized in house as opposed to mixing commercial components. The conventional methodology to produce this target consisted of two steps. In the first step, the precursors UO_2 and graphite were carbothermally reduced; in the second step, the resulting UC_2 and excess carbon were slip cast on exfoliated graphite foil (details in Section 2.3).

Analogously, LaC_2 slip cast target material was developed in two steps at TRIUMF [32], but it was not irradiated due to its promptness to oxidation. For this work, a LaC_2 slip cast target has been synthesized in one step by successfully carbothermally reducing $La(OH)_3/C$ over graphite foil.

A $La(OH)_3/C$ slurry was prepared with $La(OH)_3$ and graphite as target material and reducing agent, respectively. 20 g of $La(OH)_3$ powder was mixed with with 7 g of pre-milled graphite of 35 µm (pre-milling procedure in Appendix A.2), and 18 ml of deionized (DI) water at 60 RPM for approximately 18 hours. Then plasticizers, surfactants, and other substances listed in Table 2.5 were added to the $La(OH)_3/C$ mixture and were mixed at 60 RPM for 4 hours. The $La(OH)_3/C$ slurry was cast on a graphite foil and let dry in a fume hood for two days. Next, a batch of 30 discs of 14 mm diameter was cut from the cast with a hammer-driven hole puncher; then, they were weighed and measured to calculate their bulk density and total porosity (Table 2.6).

Table 2.5: Substances in $La(OH)_3/C$ slurry; mass% and mol% in function of $La(OH)_3$.

Substance	**Function**	**Mass%**	**Mol%**
DI water	Solvent	90.0	948.6
Graphite	Reducing agent	35.0	553.5
Ammonium citrate	Emulsifier	1.8	1.5
Glycerol	Dispersant	2.8	1.3
Polyethylene glycol 400	Plasticizer	2.8	5.8
Polyvinyl alcohol (7% aq. sol.)	Plasticizer	44.8	439.1
η-Butanol	Surfactant	3.2	8.3
Methanol	Surfactant	2.4	14.1

After thermal treatment, the ISAC target materials lose their flexibility and become fragile. Thus, to facilitate their retrieval after their thermal treatment, the $La(OH)_3/C$ discs were introduced in a 2.4 cm long testing container (Fig. 2.14a). The testing container was loaded in a tantalum tube (Fig. 2.14b) to allow resistively heating the discs in the non actinide furnace (Fig. 2.3b).

The thermal treatment of the $La(OH)_3/C$ discs lasted approximately four days (Fig. 2.17a). First, the current was manually increased to 40 A; then, an automatic ramp of 0.2 A/min was set up to 250 A. Similar to the pellets thermal treatment, the current ramp was being automatically paused intermittently between 40 A and 100 A, but it was continuous above

100 A until 250 A when the ramp was paused for 3 hours to allow the pressure to decrease. After that, the current was increased manually instead of automatically such that it could be increased faster. The current was increased manually to 350 A in a rate of ≈1.6 A/min. The current ramp was reduced to 0.3 A/min until 517 A; after 1 hour at 517 A, the current was reduced to 488 A (≈1800 °C) because the temperature had unintentionally risen to 1936 °C (Fig. 2.17b). To condition them, the discs were kept at this temperature for about three days to fully carbothermally reduce the material, and get rid of impurities.

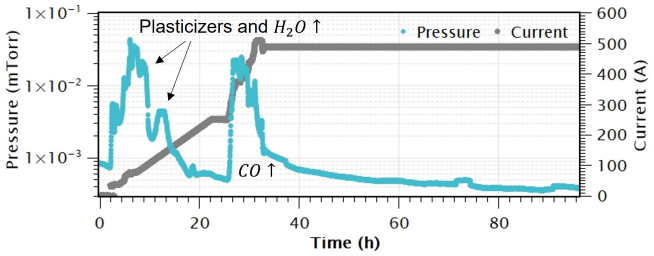

(a) Evolution of the $La(OH)_3$ discs thermal treatment.

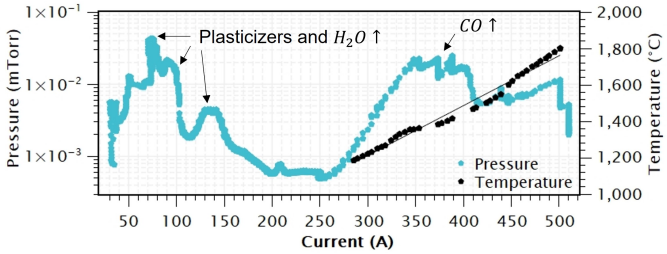

(b) Temperature and pressure corresponding to the current supplied for resistive heating the $La(OH)_3$/C discs.

Figure 2.17: Heating treatment of thirty $La(OH)_3$/C discs. The treatment lasted around four days (a). The first 20 hours encompassed the water release due to the decomposition reaction of $La(OH)_3$ into La_2O_3. At around 260 A, the pressure rose indicating the carbohtermal reduction of La_2O_3, that started around 1200 °C (b). Lastly, the current was increased to 488 A corresponding to ≈1800 °C (b). The discs were conditioned at ≈1800 °C for about three days.

During the thermal treatment of the $La(OH)_3$/C discs, two regions of pressure peaks were observed (Fig. 2.17a and 2.15b). The first region of peaks corresponds to the evaporation of water and organics from the slurry (100 °C to 650 °C [32], [39]); and analogous to the pellets gas released trend, it most likely includes the water released from the decomposition reactions of $La(OH)_3$ and LaOOH at ∼ 330 °C and ∼490 °C (Eq. 2.11a) [57]. The second region corresponds to the CO released due to the carbothermal reduction of the La_2O_3 and the consequently synthesis of LaC_2 (Eq. 2.11b) [7].

Since LaC_2 is yellow-ochre [58], the change in colour of the discs suggested that they carbothermally reduced (at least superficially). To avoid their oxidation, the LaC_2/C discs were stored in an argon glove box where they were weighed and their thickness was measured

to calculate the LaC_2/C bulk density. The total porosity of the LaC_2/C composite was calculated with its bulk density and the LaC_2 theoretical density of 5.29 g/cm^3 [59].

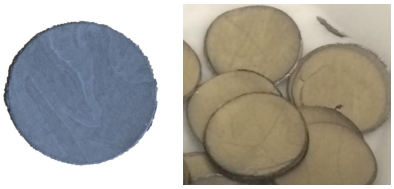

(a) $La(OH)_3/C$ **(b)** LaC_2/C

Figure 2.18: LaC_2 discs synthesized in-house (b). Before carbothermal reduction, these discs were dark grey (a).

Table 2.6: Characteristics of $La(OH)_3/C$ and LaC_2/C discs. The graphite foil were excluded from the calculations such that the values only reflect the properties of the composite. The mass of the binders in the $La(OH)_3/C$ discs is not excluded from the calculations.

Characteristic	**$La(OH)_3/C$**	**LaC_2/C**
Mass (g)	0.059±0.003	0.043±0.003
Diameter (cm)	1.40±0.01	1.40±0.01
Thickness (cm)	0.027±0.009	0.018±0.004
Bulk density (g/cm^3)	1.42±0.47	1.57±0.39
Total porosity (%)	0.59±0.20	0.65±0.16

Compared with the LaC_2/C pellets, the LaC_2/C discs have higher total porosity (Table 2.7). This is expected because unlike the pellets, the discs contained binders that when evaporating contribute to their porosity formation. Since LaC_2 oxidizes promptly when exposed to air, it was not feasible to perform pycnometry analysis to this target material, so the open porosity of the LaC_2/C composite was not determined. Assuming that the total porosity is also reflected in the open porosity, the discs would have a better isotope effusion performance than the pellets. On the other hand, the discs higher porosity could result in a lower heat conductivity in comparison to the pellets; however, the discs' graphite foil might compensate for this reduced thermal performance. The characterization of the LaC_2/C thermal attributes would be performed in the Chamber for Heating Investigations (CHI) [34] when commissioned.

Table 2.7: Comparison of the total porosity of LaC_2/C pellets and slip cast discs. The higher total porosity of the discs might have formed during the evaporation of their plasticizers during thermal treatment.

LaC_2/C	Total porosity
Pellets	0.52±0.02
Discs	0.65±0.16

SEM microscopy was attempted on a LaC_2/C disc, but its rapid oxidation modified the microstructure of the final material. The $La(OH)_3/C$ micrograph shows the small particle

size of the $La(OH)_3$ attached around the flake-like graphite (Fig 2.19a). In contrast, the LaC_2/C micrograph (Fig 2.19b) does not have graphite in sight and shows swollen particles suggesting that the LaC_2 oxidized; hence, the LaC_2/C micrograph does not show the morphology corresponding to LaC_2, but most likely the one corresponding to $La(OH)_3$ [58]. LaC_2/C samples are stored under argon for future analysis when facilities, apparatus, or techniques to analyze rapid oxidable materials are available.

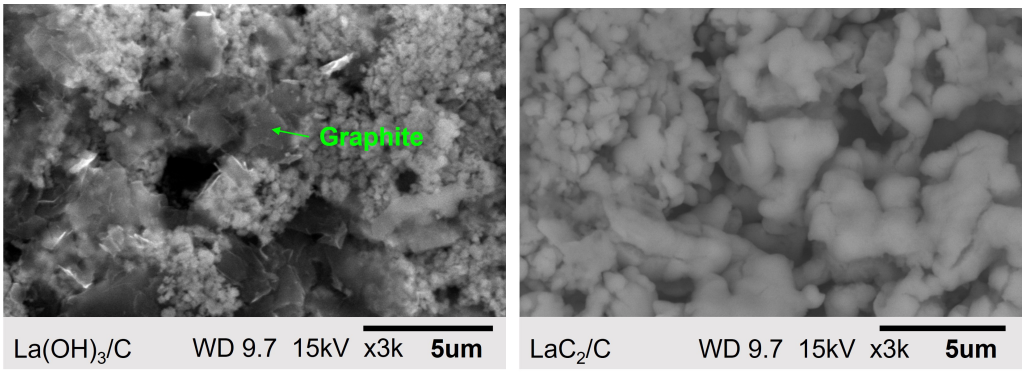

(a) $La(OH)_3/C$ disc **(b)** LaC_2/C disc exposed to air

Figure 2.19: Micrograph of $La(OH)_3/C$ (a) and LaC_2/C (b) discs. $La(OH)_3$ has small grains attached to graphite while the oxidized LaC_2 sample has swollen particles.

To submit LaC_2/C to XRD, the sample was prepared such that air exposure was minimized. A LaC_2/C sample was prepared in a glove box under argon atmosphere. LaC_2 from three discs was peeled off from the graphite backing foil and ground in an agate mortar. Then, the LaC_2/C powder was compacted and flattened on an XRD sample holder. To protect the LaC_2/C from air, the XRD holder was wrapped with cling foil (Fig. 2.8). The cling foil contributed to the background signal but did not mask LaC_2 characteristic peaks.

Tetragonal lanthanum carbide (α-LaC_2) [60, 61] was identified in the resulting XRD pattern of the LaC_2/C discs (Fig. 2.20). According to the La:C phase diagram (Fig. 2.9) [46], α-LaC_2 is obtained below 1060 °C. Most likely β-LaC_2 was synthesized during the discs thermal treatment, but it returned to the α phase when the discs were cooled down. If the target were to be operated at 1700 °C, the prevalent phase would be β. Since the composite has excess graphite, carbon was expected to be in the LaC_2/C discs' XRD-pattern as well, but the peaks matching with this element were masked by some of LaC_2.

A peak at 24° was not identified as part of the peaks constituting the LaC_2 pattern [60, 61]. However, together with other peaks it resembles the pattern corresponding to $C_{47}H_{66}La_2O_4$ [62]. This compound might indicate some oxidation during the transportation to UBC for XRD analysis and during the analysis itself. If not, the peak at 24° could also be an artifact given by the plastic wrap (polyethylene [63] $C_{2n}H_{4n+2}$ [64]) used to protect the LaC_2 from oxidation (Fig. 2.8). In contrast with the UC_x composite patterns (Section 2.3), no impurities like tungsten or cobalt were identified in the resulting LaC_2

composite's patterns, suggesting that slow mixing (60 RPM) delivers slurries with a low impurity content.

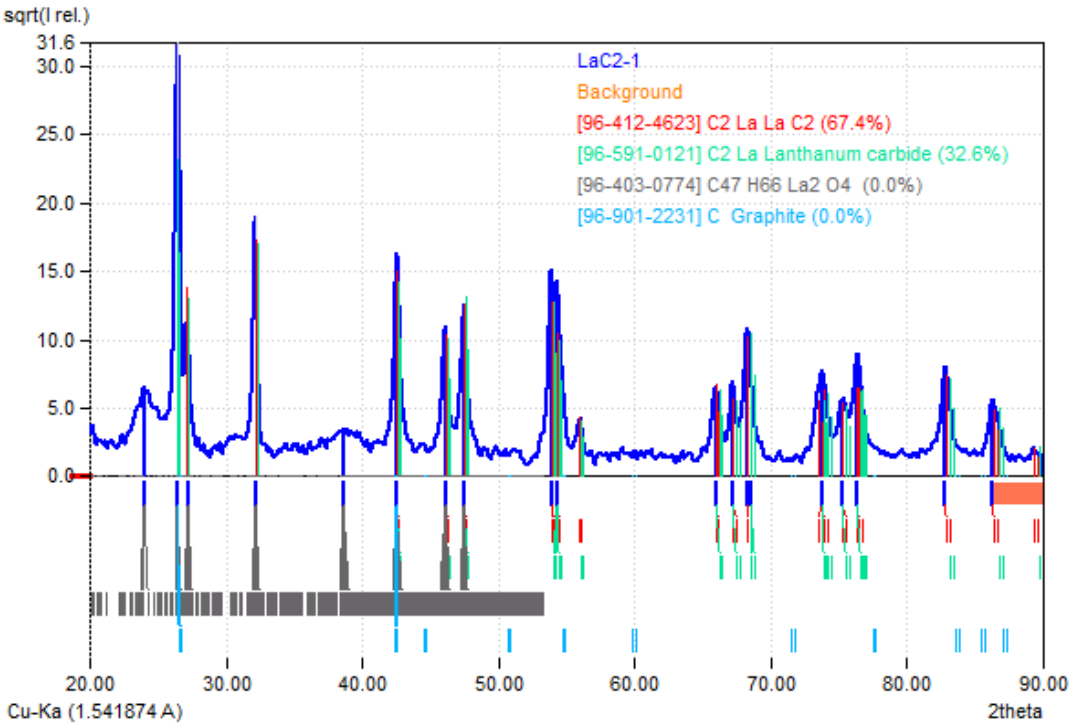

Figure 2.20: XRD patterns of LaC_2 powder sample. LaC_2 [60, 61] was identified in the pattern. Graphite [65] was expected, and the peaks corresponding to its pattern matched with those of the LaC_2 powder, but were masked with those of LaC_2. A peak at 24° in the LaC_2 pattern matched with some peaks corresponding to $C_{47}H_{66}La_2O_4$ [62]; however, this peak most likely corresponds to an artifact produced by the polyethylene [63] used to protect the sample from oxidation. The LaC_2 powder pattern was also compared to that of $La(OH)_3$, and La_2O_3 but the patterns did not match.

$La(OH)_3/C$ has been successfully carbothermally reduced over graphite foil in a single step. The synthesis process of this small batch of $La(OH)_3/C$ took less than 4 days in contrast with the 8 days it would have taken if the material would have been synthesized in two steps. To accelerate this process further, the pressure limits of the furnace have been changed from 0.4×10^{-1} mTorr to 500 mTorr allowing higher pressure and steeper current ramps. With the higher pressure limits and the lessons learned, UC_x was successfully carbothermally reduced over graphite foil faster (details in Section 2.3).

The effects in the material microstructre because of synthesizing in one step were not conclusively identified due to the unavailability of equipment with capabilities to analyze materials that oxidize quickly. However, the LaC_2/C pellets and slip-casting total porosity is within the reported porosity of LaC_2/C pellets synthesized at other facilities (Table 2.4). Moreover, even when oxidized and swollen, the LaC_2/C disc grains were below 10 µm (Fig. 2.19b), implying that the pristine LaC_2/C discs had smaller grain size. These results suggest that the 1-step casting deliver material with propensity for isotope release.

2.3 UC_x target synthesis

A new method to synthesize UC_x targets have been developed and tested for this work [8]. This new UC_x production method consists of slip casting UO_2 over graphite foil with enough graphite powder to not only synthesize UC_2, but also to have excess graphite and obtain, in one single step, the same stoichiometry of the conventional ISAC UC_x targets (U:C 1:1.76) (Fig. 2.21).

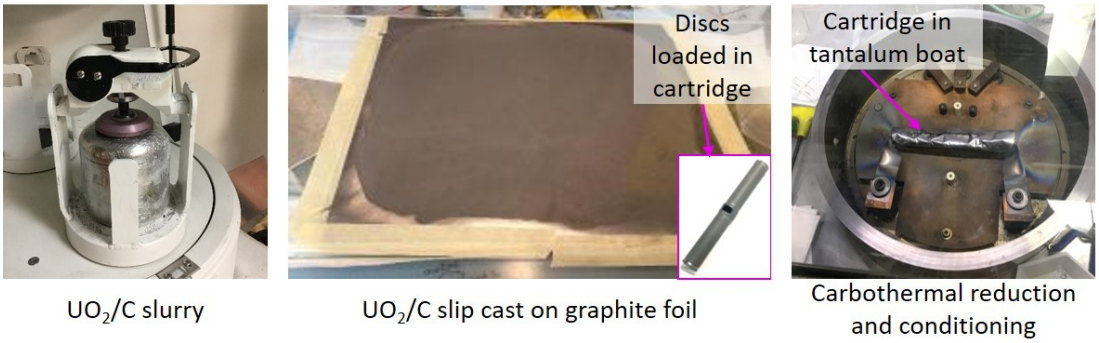

Figure 2.21: In the new method to synthesize UC_x targets, UO_2 and graphite powder are ground in a slurry that is cast over graphite foil. When the slurry is dry, discs are cut and loaded in a graphite cartridge that is set in a tantalum boat. When the carbothermal reduction and conditioning are completed, the cartridge is loaded in a tantalum container.

ISAC's UC_x targets used to be produced in two-steps (Fig. 2.22) [6]. In the first step (Fig. 2.22a), UC_2 was synthesized by carbothermal reduction of UO_2 powder

$$UO_2 + 4C \rightarrow UC_2 + 2CO \uparrow \tag{2.12}$$

with 11% molar excess carbon [6]. In the second step (Fig. 2.22b), the synthesized UC_2 was mixed in a slurry with plasticizers and extra graphite powder for a total of 31% molar excess carbon in the final material. The UC_2/C slurry was slip-cast on a flexible exfoliated graphite sheet (called *green cast*), cut into D-shaped discs (called *green discs*), and heated under vacuum to evaporate the plasticizers from the slurry. The resulting discs contained UC_2, UC, graphite excess, and WUC_2 (a contaminant from the WC jars where the slurry was prepared) [6].

The UC_x targets produced with the two-step casting method have been used for the delivery of RIBs to many experiments during the last eleven years. However, producing a UC_x target with this method is time and workforce consuming. The production of one target could take up to two months, and in the ARIEL era, we expect a demand of at least twenty UC_x targets per year which could not be fulfilled with the current resources and infrastructure. Moreover, the conventional production method prevented the development of new materials because it constrained the personnel to production.

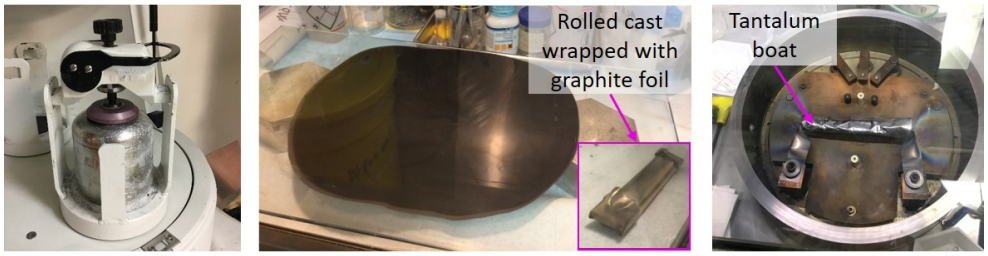

(a) First step: Carbothermal reduction

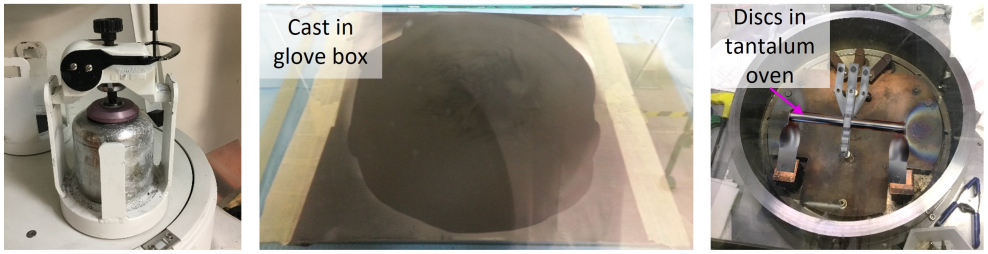

(b) Second step: Conditioning

Figure 2.22: Two step casting method to produce UC_x targets. (a) An UO_2/C slurry was cast over a glass plate; when dry, the UO_2/C cast was peeled off the plate, rolled, and wrapped with graphite foil; the roll was carbothermally reduced in a tantalum boat. (b) The resulting UC_x flakes were ground with graphite powder in a slurry, and slip cast on graphite foil. When dry, discs were cut from the cast, loaded in a tantalum oven, and conditioned. Details of the 2-step casting method are published in [6].

In contrast, the new UC_x target production method developed during this study produces one target in eight days, representing an eightfold reduction in production time. The result is an accelerated production process that provides a sustainable method to satisfy the upcoming UC_2 target demand, and allows time and equipment for further target material research and development.

Unlike the rest of the ISAC composite discs of 18.3 mm diameter, in the new method the UC_x discs are 13 mm in diameter to fit in a graphite container (Fig. 2.23). The graphite container functions as a target material vessel for carbothermal reduction, and as a target material cartridge that can be directly inserted in a tantalum oven for proton irradiation. The graphite container allows the carbothermal reduction of the material in a tantalum boat (Fig. 2.14b); thus, the tantalum oven is not submitted prematurely to a high-carbon atmosphere like in the old method (Fig. 2.22b). In this way, additional heating and premature carbon penetration, which have been found detrimental to the oven (Chapter 3), are avoided.

As with the conventional method, in the one-step casting method, the UO_2 carbothermal reduction is performed under vacuum. However, the pressure limits of the actinide

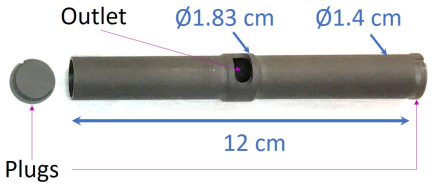

Figure 2.23: Graphite container. Target discs are loaded in this container that acts as a vessel for carbothermal reduction, and as a cartridge for loading the target material in a pristine oven (Fig. 1.7b) for target irradiation.

furnace have been changed from 0.4×10^{-1} mTorr to 500 mTorr to allow faster UC_x material processing (Fig. 2.24 and 2.25). Changing the furnace's pressure limits broadens the range of possible current rates to resistively heat the material, such that the thermal treatments can be performed slowly or quickly as required.

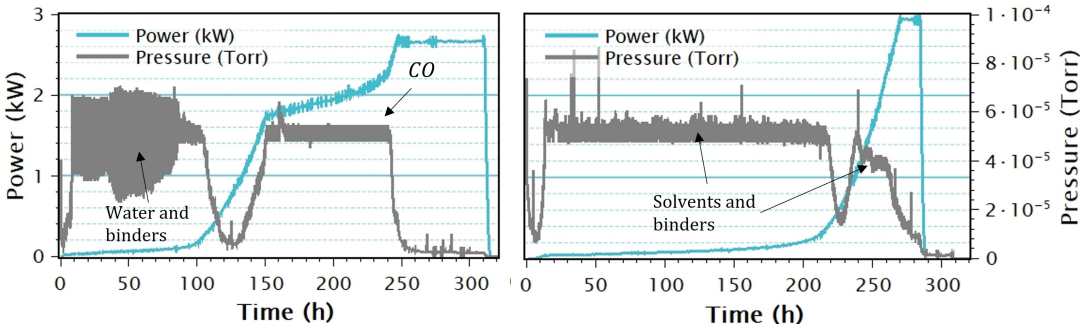

(a) Carbothermal reduction **(b)** Conditioning

Figure 2.24: Two-step casting thermal treatment. In the first step (a), UO_2 is carbothermal reduced. The UC_x produced in the first step is mixed with graphite, slip cast on graphite foil, and conditioned to evaporate the slip-cast's plasticizers and impurities (b).

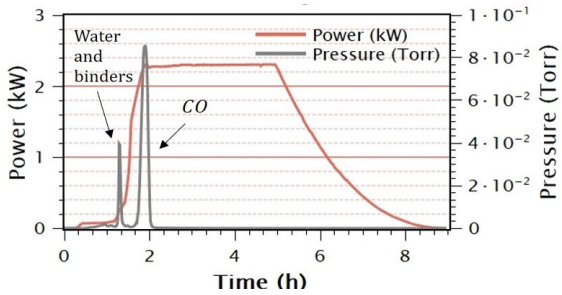

Figure 2.25: One-step casting thermal treatment. The new thermal treatment method allows higher pressure than the conventional one (Fig. 2.24) such that higher current rates can be applied resulting in a faster production process.

The new method's thermal treatment carbothermally reduces the UO_2, and evaporates the slurry's plasticizers and solvents. Also, the thermal treatment densifies the target material by joining its particles together, and reducing its porosity; this process is called sintering

and is activated by atomic diffusion [16]. Ideally, the synthesized UC_x slip-cast would be dense, but porous, and it will have small particle size such that when irradiating it, the material has high isotope yield, and enhanced isotope release (Eq. 1.12).

The sintering driving force is the reduction in surface free energy of the particles in the material [40]. A material densifies when matter migrates from inside the grains to the pores. On the other hand, it coarsens when matter rearranges among the surfaces of the pores without reducing the pore size; the coarsening process hinders densification. If coarsening dominates, porosity is favoured, but density prevails when densification dominates. In general, heating a material leads to its densification and coarsening; the rates of these processes increase with the thermal treatment's duration and temperature [16].

In the new method, the thermal treatment of the UO_2/C slurry has three stages. In the first stage solvents and binders in the slip cast are removed. On the second stage, the UO_2 is carbothermally reduced, and in the third stage, called conditioning, impurities are removed and the carbothermal reduction is completed.

Controlling the microstructure of the one-step casting material is difficult because the induced reaction adds complexity to its densification and coarsening. In addition, unlike the furnace used to carbothermal reduce the $La(OH)_3$/C discs, the furnace used to synthesize actinide targets does not have the capabilities for measuring temperature; the differences in pressure occurring through the thermal treatment indicate the approximate temperature. In the old method and in the beginning of the new method, two pressure peaks are observed during thermal treatment (Fig. 2.24a and 2.25). The first corresponds to the evaporation of water and plasticizers in the slip-cast, and the second corresponds to the CO released during the carbothermal reduction of UO_2 (Eq. 2.12).

In the one-step casting, two current ramping rates are applied during the thermal treatment. The first current ramp induces the evaporation of water and binders, and the second one induces the carbothermal reduction of UO_2; both current ramps are accelerated. The first ramp is accelerated to boil the plasticizers with the intention of promoting open porosity. The second ramp is accelerated to reach the carbothermal reduction temperature quickly, limiting the UO_2 densification such that the graphite does not have time to react with a densified and sintered UO_2 block, but with UO_2 micrometric particles; this should promote the homogeneous completion of the carbothermal reduction.

Irradiating a partially carbothermal reduced UC_x target is problematic. Conventional operation conditions during irradiation could induce the carbothermal reduction of remaining UO_2 and the consequent release of CO; this gas can reduce the ion source efficiency [66]. Alternatively, the remaining UO_2 could evaporate during irradiation since the operational temperature of the UC_x targets is 1950 °C, and the UO_2 vaporization temperature is 1504 °C [67] at 1×10^{-6} Torr [48]. UO_2 could accumulate in the extraction electrode (Fig. 2.26b), reducing or even suppressing the isotope extraction and its consequent delivery to experi-

ments (ISAC ion sources on Appendix C). To prevent having UO_2 in the UC_x targets, the material is conditioned even though this leads to particle growth and densification.

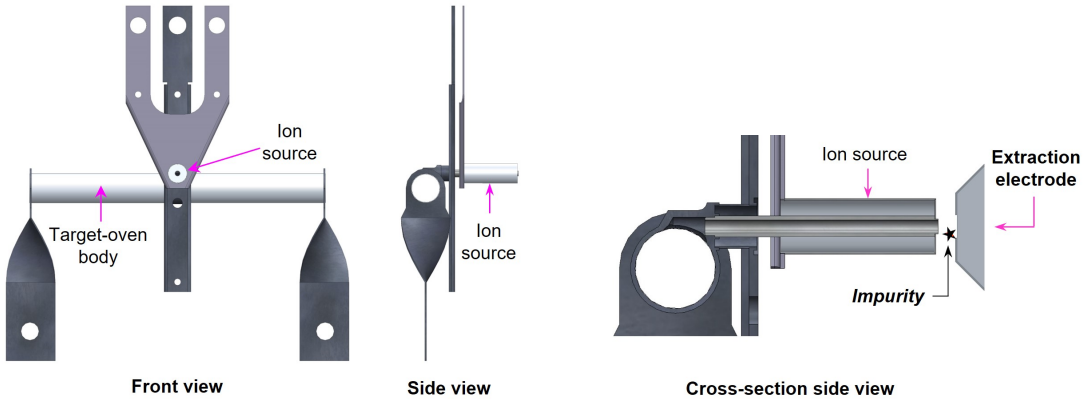

(a) Target oven **(b)** Target oven and extraction electrode

Figure 2.26: Diagram of target oven (a) showing the ion source. Impurities in the targets (e.g. UO_2, cobalt, plasticizers) can evaporate during irradiation and condense in the extraction electrode (b). A voltage difference between the extraction electrode and the oven allows extracting the isotopes from the ion source, but condensed impurities can connect both parts, causing a short circuit and preventing the isotopes' extraction. More information about ion sources can be found in Appendix C.

The CO released during carbothermal reduction forms open pores in target materials like LaC_2/C and UC_x [7]. In the old method, the open pores formed during carbothermal reduction are discarded when the synthesized UC_2 is milled and suspended in a slurry (Fig. 2.22b); thus, the porosity of the old UC_x target is formed during conditioning in the second step, and relies on the evaporation of plasticizers. Therefore, it would be expected for the 1-step casting UC_x to have a higher open porosity than the UC_x synthesized with the 2-step casting method because the porosity of the UC_x made with the new method is given by both the release of CO during carbothermal reduction, and the evaporation of the plasticizers in the slurry. On the other hand, since particle growth is expected during thermal treatment, skipping milling the synthesized UC_x, as it is done in the conventional method, carries the risk of ending with larger UC_x particle size when synthesizing with the new method.

UC_x slip-cast targets were synthesized for this work with UO_2 (depleted uranium-238) from International Bio-analytical Industries Inc., and graphite powder from Alfa Aesar. The particle size of the UO_2 was -50 mesh ($<$297 µm) and its purity $>$99% [68]. The graphite powder had a particle size of -325 mesh ($<$44 µm) and a purity of 99.9995% [55].

Two sets of UC_x slip-casts with different quantities of excess graphite were developed to deliver materials with different densities. One set of casts contained 11% molar excess graphite, like the UC_2 resulting from the first step of the 2-step casting method; the second set of casts contained 31% molar excess graphite, like the UC_x targets conventionally

synthesized with the old method. Only the UC_x targets synthesized with the 1-step casting method containing 31% molar excess graphite have been irradiated online and have delivered isotopes to experiments.

The new UC_x material have been characterized to identify the effects on its micromorphology and porosity given by the thermal treatment. Furthermore, in this work the particle morphology and size, as well as the porosity of the UC_x target material made with the two-step casting method were explored. The results are compared with those corresponding to the UC_x synthesized with the 1-step casting method (Table 2.9, 2.11, 2.10, and 2.12).

SEM micrographs of the 2-step casting surface and cross-section were observed (Fig. 2.28). To expose their cross-section, the discs were bent until fracturing; then, a fragment of the disc was adhered to a stub (Fig. 2.7). During SEM exploration, the stub was rotated 15° to observe the cross-section. In the micrographs, the clearer particles are UC_x and the darker are graphite (Fig. 2.28). In the areas scanned, UC_x seems to be uniformly distributed, suggesting that the UC_2 was properly suspended in the slurry, allowing a homogeneous distribution of UC_2 in the cast; nevertheless, many more micrographs would be required to confirm this homogeneity.

During the sintering of a material, boundaries are formed between adjacent particles due to atom diffusion. Eventually, the atoms migration forms necks (Fig. 2.27). Continuous sintering generates additional particle boundaries and consumes pores [16]. Necking was observed among UC_x particles in surface and cross-section micrographs (Fig. 2.28). Further signs of sintering were evidenced by the large blocks of sintered UC_x particles observed on the surface of the discs. On the other hand, the micrographs in Fig. 2.28 show graphite encapsulating UC_x, which might help prevent their sinterization.

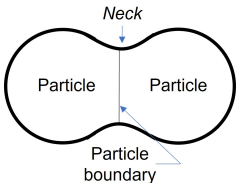

Figure 2.27: Diagram of a neck formed between two particles due to sintering.

The UC_x particle size was estimated by measuring the diameter of several particles in micrographs of the slip-cast produced with the two-step casting. The UC_x particles are not spherical, but their largest dimension was taken as their diameter, and it was reported as their size. With the Amscope software [69], the particles were circled, and the diameter of the circles was registered (Appendix A.5). For the samples made in this work with the 2-step casting method, the average UC_x particle size was 1.7 µm, the minimum was 0.5 µm, and the maximum was 5.1 µm.

The two-step casting open porosity had not been analyzed before. Samples of this material had not been stored because the 2-step casting UC_x targets were dedicated to pro-

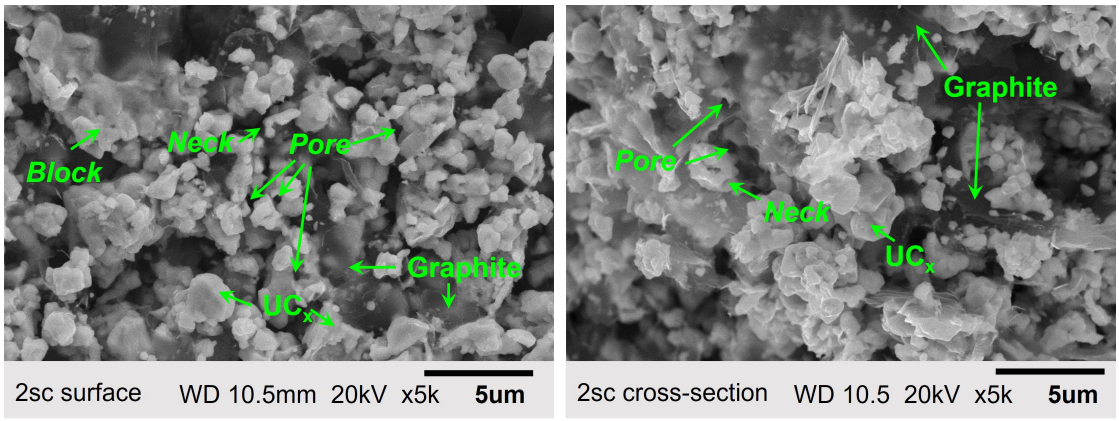

(a) Surface **(b)** Cross-section

Figure 2.28: Microstructure of UC_x discs produced with the two-step casting method. The clear particles are UC_x, and the darker are graphite.

duction; moreover, no more UC_x targets have been syntesized with the 2-step casting since the 1-step casting method, developed in this work, was established. To have enough material for pycnometry analysis, a batch of previously discarded *green*[1] UC_x discs (Fig. 2.29) were conditioned (Fig. 2.30).

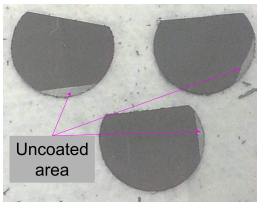

Figure 2.29: *Green*[1] UC_x discs produced in the second step of the 2-step casting method that were discarded because their UC_x slip cast does not completely cover the graphite foil.

In the second step of the 2-step casting, the UC_x synthesized in the first step is slip cast on graphite foil (Fig. 2.22). The UC_x slip cast is cut in stripes that are then feed in a rotatory die cutter (Fig. 2.2). Discs that are not fully covered with UC_x slip cast are discarded (Fig. 2.29), and reserved for disposal; the rest are loaded in a target oven for conditioning. The uncoated areas would skew the density and pycnometry measurements, so smaller discs (of $1.02\,cm^2$ area) were cut from the discarded ones.

A batch of fifteen UC_x discs were introduced in a testing graphite container, loaded in a tantalum boat, and set under vacuum in the actinide furnace. The conditioning treatment of a 2-step casting target used to take more than a week to be completed (Fig. 2.24b), but the furnace was booked for the production of another target, so the UC_x batch conditioning only took five days (Fig. 2.30). To achieve a faster conditioning, the electrical current ramp was steeper, this could lead to the boiling of the plasticizers and consequently higher porosity

[1] A disc is referred as green when it have not been thermally treated.

than the original material that was slowly heated (Fig. 2.24b). The total porosity of the conditioned UC_x discs was of 0.57±0.01, and the open porosity was 0.47±0.10; however, this porosity results might not reflect the original two-step casting UC_x porosity since the material had to be thermally treated faster than conventionally.

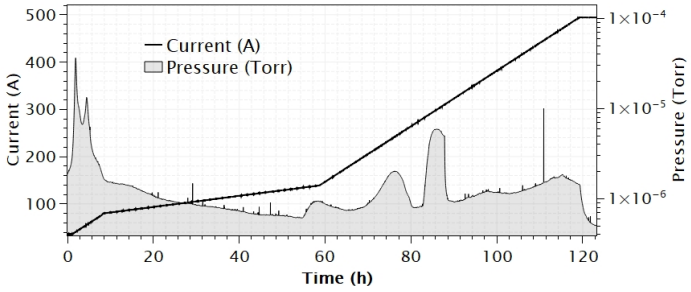

Figure 2.30: Conditioning of a batch of previously discarded UC_x discs prepared in the first step of the 2-step casting method. The pressure peaks in the first 10 hours correspond to the evaporation of binders. The next peaks corresponds to CO released due to carbothermal reduction of UO_2. In principle, the slip-cast on the discs is composed by UC_x, so no carbothermal reduction should occur; however, a fraction of the material most likely oxidizes during the milling of the UC_x (Fig. 2.22).

In the following sections, the thermal treatments of the UC_x discs made with the new method are described. Moreover, the SEM and XRD characterization of these materials is presented, discussing the implications of their respective thermal treatments. Furthermore, these results are compared to those of the two-step casting obtained in this work.

2.3.1 UC_x composites with 11% molar excess carbon

In the conventional method, UC_2 is synthesized with 11% molar excess, which represents a C/U atom ratio of 4.5. According to the U:C phase diagram by Storms [70] (Fig. 2.31), U_2C_3+C is obtained for a C/U atomic ratio larger than two at a temperature below 1400 °C; above 1514°C α-UC_2 (tetragonal phase) is synthesized, and above 1765 °C β-UC_2 (cubic) is obtained. *Green*[2] UO_2/C slip cast discs were made with 11% molar excess (i.e. 4.5 C/U atom ratio), and heated to ≈1800 °C (presumably). The resulting UC_x discs should be composed of β-UC_2.

An UO_2/C slurry was prepared following the conventional ISAC method. First, 50 g of UO_2 are milled with 10 mL of deionized water in a planetary ball mill at 400 RPM during 1 min (5 repetitions). Then, 20 mL of deionized water and 10 g of pre-milled graphite powder (Appendix A.2) are blended with the UO_2 at 60 RPM for ∼16 hours using ammonium citrate as emulsifier. Finally, the dispersants, plasticizers and surfactants listed on Table 2.8 are mixed with the UO_2/C at 60 RPM. After 4 hours of mixing, the slurry is ready and is cast on graphite foil (Table 2.1).

[2] A cast is referred as green when it has not been thermally treated.

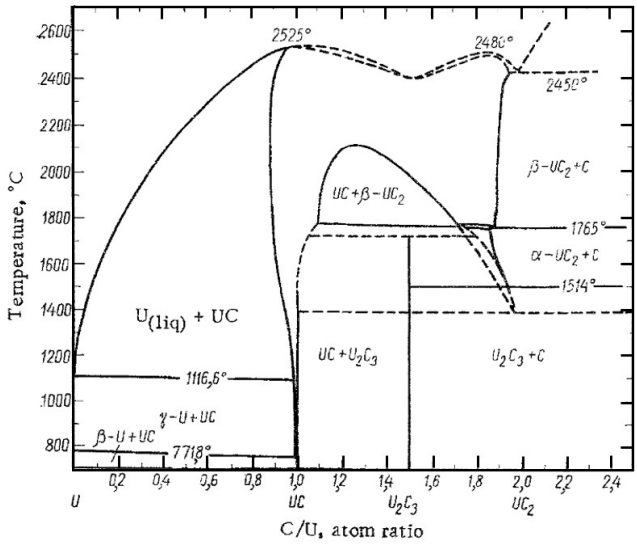

Figure 2.31: Uranium carbon phase diagram from [70].

Table 2.8: Substances mixed with UO_2 and graphite powder to prepare a slurry. All substances are in mol% with respect to UO_2.

Substance	**Function**	**Mass%**	**Mol%**
Ammonium citrate	Emulsifier	0.02	0.02
Glycerol	Dispersant	0.03	0.08
Polyethylene glycol 400	Plasticizer	0.03	0.02
Polyvinyl alcohol (5% aq. sol.)	Plasticizer	0.45	6.38
η-Butanol	Surfactant	0.03	0.12
Methanol	Surfactant	0.02	0.20

Once the green UO_2/C cast was dry, 14 mm diameter discs were cut from it with a hammer driven punch. The discs were weighed and measured to calculate their density. Also, a fragment of a discs' slip cast was observed with BSE (Fig. 2.32); in the micrographs, the brighter and clearer particles are UO_2 and the dark ones graphite. The UO_2 particles in the micrograph were measured with Amscope [69] (Appendix A.5). The average diameter of the UO_2 particles was 1.5 µm; the smallest UO_2 particle was 0.4 µm, and the largest UO_2 cluster particles when agglomerating was 6 µm (Table 2.9).

After characterization, a batch of thirty UO_2/C discs was introduced in small graphite containers (Fig. 2.14a) to proceed with its thermal treatment. The batch was carbothermally reduced by resistively heating the tantalum boat where the cartridge was set (Fig. 2.14b). Different thermal treatments were applied to different batches in order to observe their effect in the microstructure of the slip cast, and their efficacy in carbothermally reducing the UO_2.

The thermal treatments of four batches have been compared (Fig. 2.33, 2.34, 2.35). The thermal treatment of the first batch (B1) slowly reached the carbothermal reduction temperature (Fig. 2.33) similarly to how it would have been done in the old method (Fig. 2.24a);

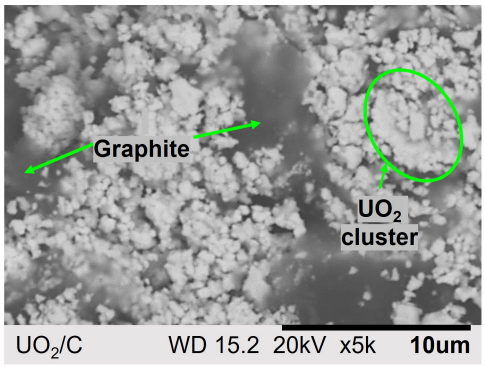

Figure 2.32: BSE image of UO_2/C green cast. The difference in contrast enables the distinction between the graphite, a low Z material that appears dark, and UO_2, a high Z compound that appears bright. The UO_2 agglomerates in clusters around the flake-like graphite particles. The smallest UO_2 particle measured in the micrograph's diagonal is 0.4 µm

.

this slow thermal treatment would give us a baseline of the microstructure obtained by reacting and conditioning in the same step without the additional milling of the second step.

The thermal treatment of the second batch (B2) was similar to the one of the batch number 3 (B3) (Fig. 2.34). Their treatments differ in their conditioning duration (Fig. 2.36), so their resulting microstructure should show the effect of long conditioning, and sintering.

The thermal treatment of the last batch (B7) was the most aggressive one (Fig. 2.35). The slope to reach its carbothermal reduction temperature was the steepest among all the batches, so B7 thermal treatment should indicate the efficacy of quickly heating on the densification of the slip cast.

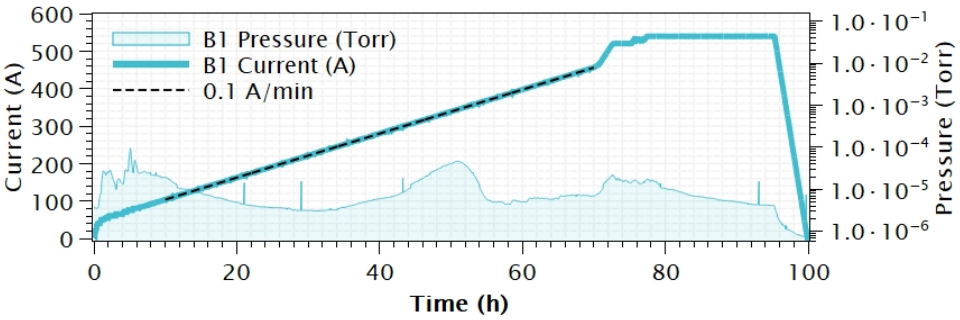

Figure 2.33: Batch 1 thermal treatment to carbothermally reduce UO_2/C slip cast discs with 11% molar excess graphite in one-step.

After the pressure reduces indicating that most of the UO_2 has carbothermal reduced, the batches were held hot to condition the discs (Fig. 2.36). Limiting the duration and temperature of this final heating stage is important to prevent the densification and coarsening of the UC_x; however, controlling it without a temperature reading is difficult because the thermal properties of the UC_x are not widely studied, so we can not rely on numerical

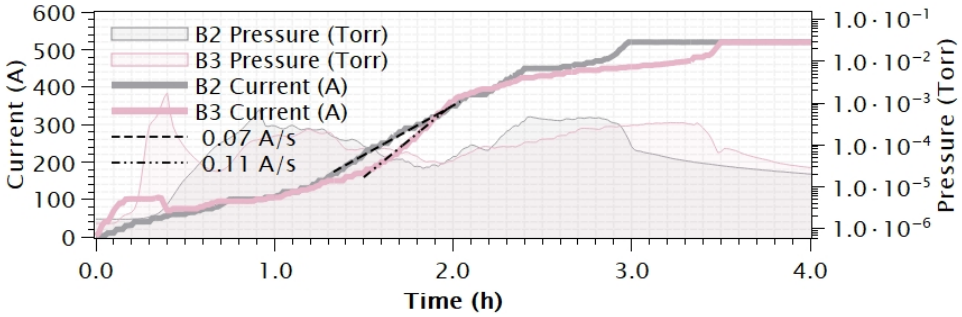

Figure 2.34: Comparison of batch 2 and 3 thermal treatments to carbothermally reduce UO_2/C slip cast discs with 11% molar excess graphite in one-step.

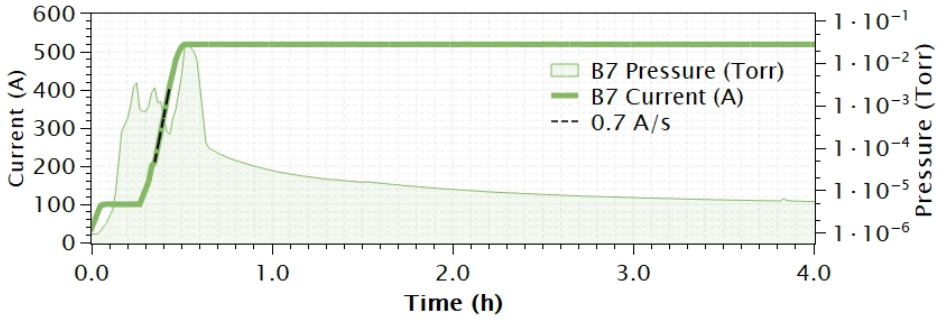

Figure 2.35: Batch 7 thermal treatment to carbothermally reduce UO_2/C slip cast discs with 11% molar excess graphite in one-step in an accelerated way.

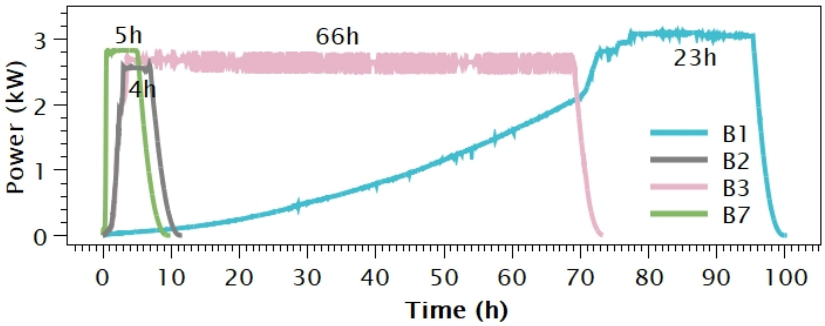

Figure 2.36: After each UO_2/C batch was carbothermally reduced, they were held at 2.84±0.16 kW for different time lapses.

models. Moreover, the chemical reaction between UO_2 and graphite add complexity to the thermal treatment.

The CO released during the carbothermal reduction of the UO_2 (Eq. 2.12) aided in determining the maximum power used to condition the batches. In contrast, the duration of the conditioning was based on the first step of the old method, and its efficacy had to be confirmed based not only on the UO_2 carbothermal reduction completion but also on the evaporation of impurities.

Among the batches presented in this work, B1 had the longest thermal treatment (four days) (Fig. 2.33), but not the longest conditioning time (≈1 day) (Fig. 2.36). The discs of B1 stayed at 3.04 kW±0.10 kW for 23 hours; taking in consideration the conditioning time, and the thermal treatment length before carbothermal reduction, it would be expected for the UC_x of B1 to be sintered. The comparison between the green UO_2/C slip cast (Fig. 2.32) and the B1 sample thermally treated (Fig. 2.37a), confirms that UC_x particles of the B1 batch have grown and are not as round as the UO_2 precursor particles, but have edges that indicate sintering [16]. B1 particles do not present much necking, and in the area scanned, only a few spaces between the particles resemble pores.

The B3 discs carbothermal-reduction was faster than that of B1 (Fig. 2.34 and 2.33). However, B3 had the longest conditioning time of all batches (Fig. 2.36) (66 hours at 2.65 kW±0.02 kW); as expected, those discs' particles were sintered. Since B3 and B2 had similar carbothermal-reduction ramping rates, the effects of a lengthy conditioning can be identified by comparing the microstructure of these batches' discs.

The UC_x particles of sample B3 sintered, resembling a monolith. Nonetheless, the B3 sample has pores indicating that the UC_x densification was not completed; however, since there is not enough graphite between particles to constrain their sintering, the B3 material could likely completely densify and lose its pores if heated for longer.

Batch B7, the one carbothermally reduced the fastest (Fig. 2.35), was conditioned for 5 hours at 2.83 kW±0.01 kW (Fig. 2.36). B7 seems to have many pores on its surface, and its particles are not sintered as B3. B7 surface morphology is similar to B2 even though their thermal treatments were different (Fig. 2.37d). In average, the particles in B7 surface are slightly smaller than the particles of B2 (1.4 µm and 1.8 µm respectively); however, considering the method to measure the particle size (Appendix A.5), this difference should be considered insignificant. The similarity in particle size of this samples suggests that both ramps, 0.07 A/s and consequently 0.70 A/s lead to about the same UO_2 densification. More importantly, the microstructure similarity of B2 and B7 indicate that their conditioning power and conditioning duration kept the composite at an adequate temperature for long enough to obtain UC_x particles in comparable size than those of the two-step casting UC_x (Table 2.9).

The smaller UC_x particles of the batches are almost double in size than the smallest UO_2 particle in the green cast. On the other hand, the largest particle spotted in the UO_2/C micrograph is not as large as the largest UO_2 cluster spotted in the UO_2/C cast (Table 2.9). However, particles even larger than 6 µm are very likely to be found in other zones of the cast surface that were not explored. Furthermore, the average size of particles for every UC_x batch (except for B3) are around the average size of the UO_2 clusters, suggesting that the UC_x particle size is linked with the initial distribution of the UO_2 particles in the green cast.

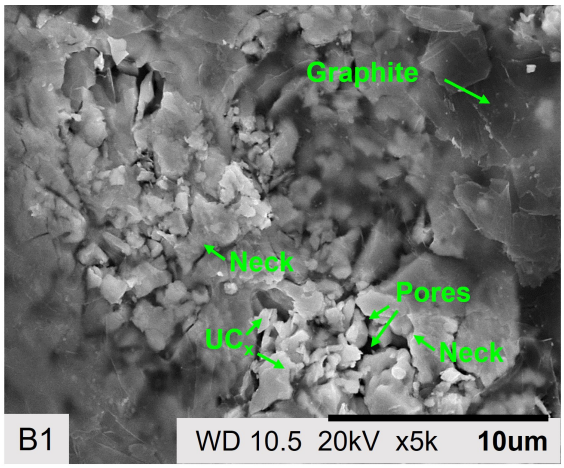

(a) UC_x B1 surface

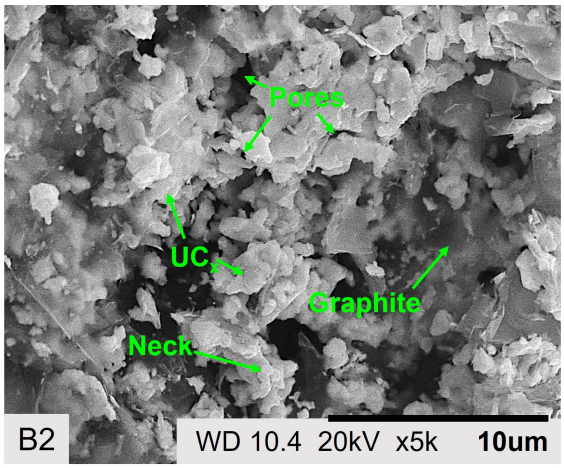

(b) UC_x B2 surface

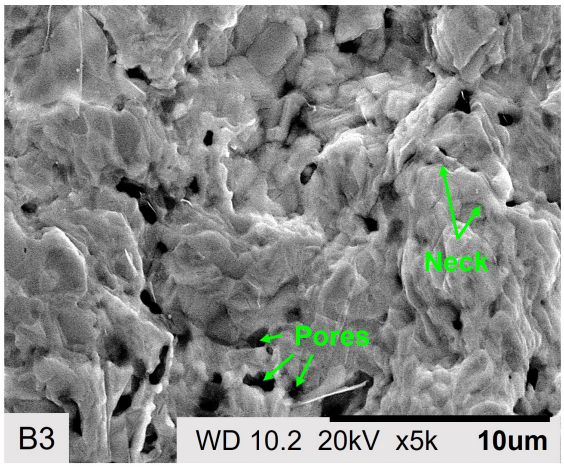

(c) UC_x B3 surface

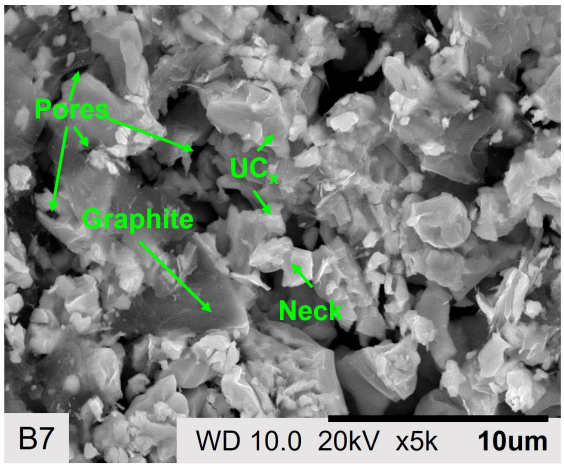

(d) UC_x B7 surface

Figure 2.37: SE micrographs of the discs surface of UC_x batches B1, B2, B3 and B7 with annotations to indicate some of their pores, their UC_x and graphite particles, as well as necking formation between UC_x particles. B3 UC_x particles are the most sintered; no graphite can be observed on the B3 sample. B1 UC_x particles seem encapsulated in graphite. B2 and B7 have similar morphology.

Table 2.9: UC_x particle size measured on SE micrographs of the surfaces of B1, B2, and B7. Average UC_x particle size is similar to 2-step casting average particle. Minimum and maximum particle size values are spread, but they are most likely to converge if more area of the samples is explored. Green cast maximum and average particle size correspond to the size of UO_2 agglomerations and not particle size.

	Particle size (µm)		
Sample	**Minimum**	**Maximum**	**Average**
Green	0.4	6.0	1.5
B1	0.7	3.8	1.7
B2	0.7	3.2	1.8
B7	0.9	2.9	1.4
2-step	0.5	5.1	1.7

The total porosity of the B1, B2, B3, and B7 samples ranged from 0.53 to 0.64. However, the total porosity variation between batches is within their error bars (Fig. 2.38). Similarly, the open porosity variation among batches is within the error bars (Fig. 2.38) even though the surface's microstructure of B1 was very different from B3 (Fig. 2.37). These results indicates that the porosity through the bulk does not match with the porosity expected from the surface microstructure, suggesting that there is more sinterization on the discs' surface than through the bulk.

Table 2.10: Bulk density, and open and total porosity fraction of UC_x batches, and 2-step casting target material conditioned unconventionally.

Batch	Total porosity	Open porosity
2-sc	0.57±0.01	0.47±0.10
B1	0.64±0.08	0.47±0.14
B2	0.58±0.05	0.37±0.10
B3	0.53±0.08	0.42±0.16
B7	0.57±0.07	0.40±0.10

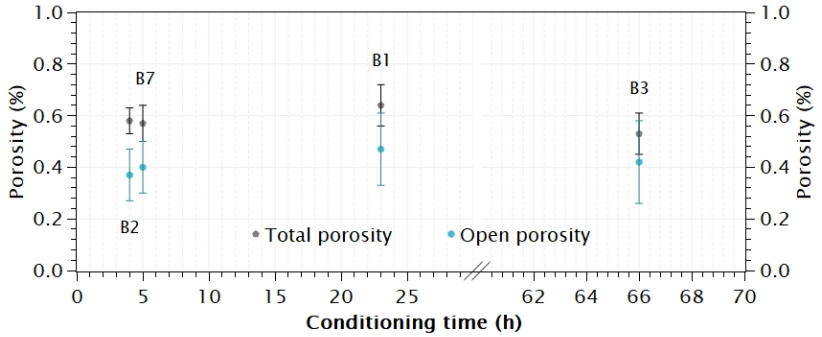

Figure 2.38: Total and open porosity fraction of the UC_x batches. The error associated wih each result is large, but the results among samples is consistent.

The XRD patterns of the UC_x samples presented (B1, B2, B3, and B7) match that of α-UC_2 (tetragonal phase) [71] (Fig. 2.39). The U:C phase diagram (Fig. 2.31) [70] predicts the synthesis of β-UC_2 (cubic), but the α (tetragonal) phase appears likely due to the cooling down the discs. Nonetheless, at the operational temperature of ≈1950 °C, the prevalent UC_2 phase would be β. Ideally, a combination of both, α-UC_2 and β-UC_2, would be present in the material to avoid sintering.

The XRD patterns of the batches also matched with WUC_2 (orthorhombic phase) [72], graphite (rhombohedral structure) [65], UC (cubic phase) [73], and UC_2 (tetragonal phase) [71] (Fig. 2.39). UC_2, UC and graphite are expected to be present in all the UC_x targets due to their precursors. However, tungsten is an impurity that comes from the WC jars where the UO_2/C slurry is mixed (Fig. 2.1b).

Another impurity introduced during milling is cobalt. This metal also comes from the jars, but unlike tungsten, cobalt is not a refractory metal. Cobalt evaporates at ≈1080 °C [47]

at 10^{-6} Torr (operational pressure during irradiation [48]). The UC_x target operational temperature of 1950 °C, is more than enough to vaporize cobalt during irradiation; if it is not removed during conditioning, this metal could evaporate during irradiation, and it can condense on the extraction electrode of the ion source (Fig. 2.26b), ultimately reducing the RIB intensity. Patterns corresponding to cobalt, as well as cobalt compounds containing oxygen, carbon, uranium, and tungsten were compared to the experimental patterns of the batches B1, B2, B3, and B7, but none matched, suggesting that the UC_x samples did not contained cobalt, or that this metal was in quantities below the XRD detection limit (Table 2.2).

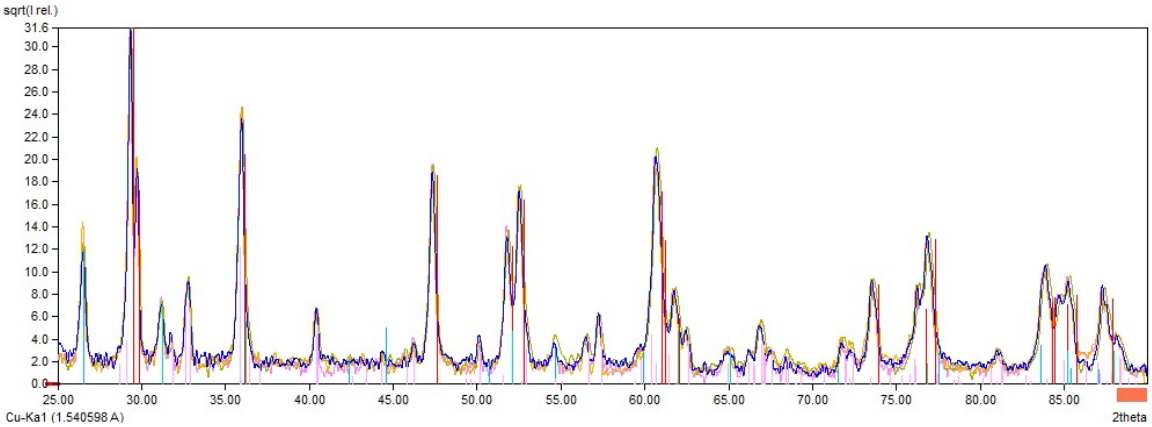

Figure 2.39: Overlapped XRD patterns of the UC_x samples B1, B2, B3, and B7. All peaks in the XRD patterns were identified and matched with UC_2 [71] (red), UC [73] (green), WUC_2 [72] (pink), and graphite [65] (blue).

Similarly, patterns corresponding to uranium oxides and oxicarbides were compared with the XRD patterns of the batches. No uranium oxides, nor oxicarbides were identified (within the limits of detection compiled in Table 2.2), confirming that the amount of graphite used in the cast was enough to fully carbothermally reduce the UO_2. The absence of uranium oxides imply that the thermal treatment was effectively carbothermally reducing UO_2 despite the process being done in one-step instead of the conventional two-step casting method. Furthermore, not having uranium oxides in the samples suggest that four hours of conditioning is long enough to complete the carbothermal reduction. Lastly, this result suggests that the samples did not oxidize during transport nor during XRD analysis.

In conclusion, UC_x target material was synthesized in one-step. The resulting material was analyzed under SEM and with XRD. The average UC_x particle size was comparable with that of the conventional ISAC UC_x made with the two-step casting. The XRD patterns of the UC_x samples matched with UC_2, UC, graphite, and WUC_2 [71, 73, 72, 65], with WUC_2 being an impurity introduced during milling. The methodology developed to synthesize this material will be applied to synthesis UC_x targets for irradiation in both ISAC and ARIEL.

2.3.2 Online targets

Five UC_x targets prepared with the one-step casting are presented in this work. In chronological order of production they are labelled UCx26, UCx27, UCx28, UCx29 and UCx30. All these targets were irradiated online, and delivered isotopes to experiments with the exception of UCx27 that failed prematurely, and UCx28 that was removed early due to an electrical short unrelated to the target material. Additional targets produced with the one-step casting method have been irradiated, but their characterization and performance is not included in this work.

The new slurries to prepare online targets have 31% molar excess carbon to provide the same stoichiometry as the conventional ISAC UC_x targets. The same methodology used to prepare the slurry with 11% molar excess carbon (Sec. 2.3.1) was used to prepare the one with 31% molar excess carbon. Except for the graphite, all the other substances in the slurry were in the same wt% with respect to UO_2 as in the 11% molar excess carbon slurry (Table 2.8).

Before carbothermal reduction, the smallest UO_2 particle has a diameter of 0.2 µm (Fig. 2.40). Nevertheless, when agglomerated, the largest cluster of particles is 5.1 µm, and the average cluster size is 1.3 µm. Considering the measurement methodology, the particle size of the green casts of 11% and 31% molar excess carbon is in agreement. This is expected because the grinding method of both slurries is identical.

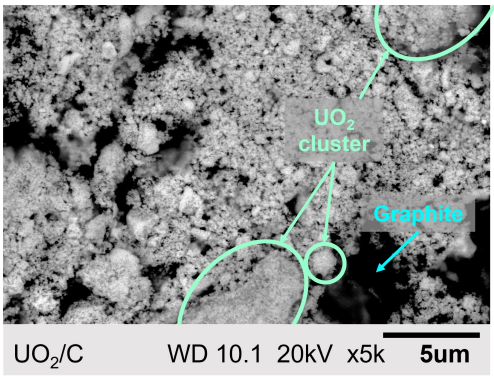

Figure 2.40: Microstructure of UO_2/C green target material. The clearer particles are UO_2 and the darker are graphite. The largest UO_2 cluster is 5.1 µm, and the average UO_2 particle size is 1.3 µm.

A 12 cm long graphite container (Fig. 2.23) was filled with an average of 242±18 UC_x discs. The D-shaped discs were 1.35 cm diameter and 1.1 cm height. Ten additional discs were loaded for characterization. Similarly to the small batches (Section 2.3.1) these loaded containers required an average of 2.62±0.23 kW to complete the discs' carbothermal reduction. Further, these target materials were also conditioned to evaporate impurities and fully carbothermal reduce the UO_2 (Fig. 2.41).

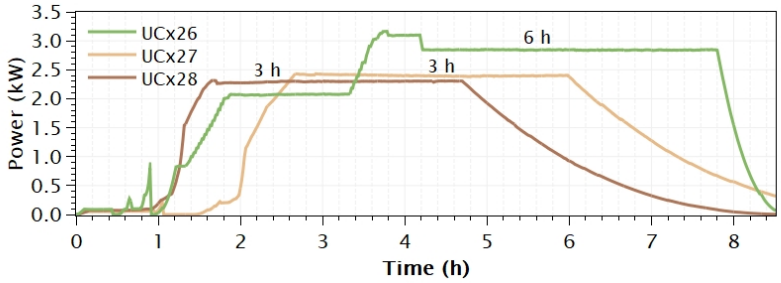

(a) UCx26, UCx27, and UCx28 thermal treatment's electrical power

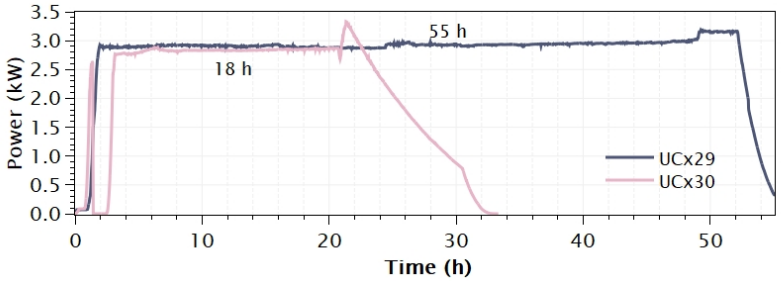

(b) UCx29 and UCx30 thermal treatment's electrical power

Figure 2.41: The UC_x targets with 31% molar excess carbon were conditioned at an average of 2.62±0.23 kW. To make sure that no more CO was released from the UC_x 29 and UC_x 30, the power was increased after conditioning.

Since the mass of these targets was larger than the mass of the batches, they release more gas during their thermal treatment. Therefore, the current ramps applied to the batches did not function for this larger amount of material, yet the thermal treatments were limited not by the amount of gas, but by the speed at which the pumps were able to extract gas released due to the thermal treatment. The vacuum limits of the actinide furnace were changed from 0.04 mTorr to 500 mTorr in order to allow versatile thermal treatments. However, during the UCx26 and UCx30 thermal treatments the furnace tripped to 0 A even though the pressure had not overpassed the new vacuum limit, interrupting the composites thermal treatment. This malfunction was tracked by TRIUMF's Controls group, but it was addressed after the targets of this study were synthesized.

The power ramps that induced the UO_2 carbothermal reduction are shown in Fig. 2.42, 2.44, 2.46, 2.48 and 2.50. The red line in the plots indicates the vacuum limit of the furnace (5×10^{-1} Torr). Among all the UC_x targets' thermal treatments, only the UCx27 target tripped the current to 0 A not because of a furnace failure, but because the pressure over passed the vacuum limit (Fig. 2.44).

UCx26 thermal treatment tripped twice, at both occurrences, the pressure was below the vacuum limit and going down (Fig. 2.42). Both UCx26 trips occurred during what must have been the evaporation of the water and binders in the slip cast. At atmospheric pressure the water boiling point is 100 °C, and the binders melting points range from 200 °C to 650 °C

[32, 39] (at 1×10^{-6} Torr their vaporization temperature would be below those values). In studies on the sintering of UO_2 [74], the relative density of a UO_2 sample would increase by 1% when heated at 650 °C, so assuming that the UCx26 temperature was ≤650 °C we should not expect a large densification during the evaporation of the binders, neither during reheating; thus, even though the porosity formation due to the water and binders evaporation was interrupted, it could continue when reheating.

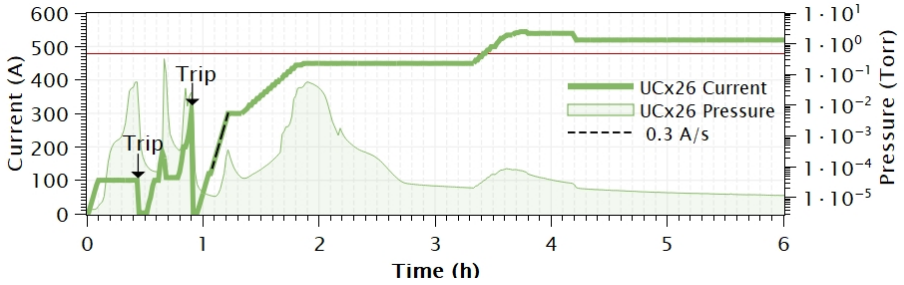

Figure 2.42: UCx26 thermal treatment to carbothermally reduce UO_2/C slip cast discs with 31% molar excess graphite in one-step. This thermal treatment had two current trips due to a failure of the actinide furnace.

The second current trip of the UCx26 thermal treatment happened at 299.8 A, 2.7 V, 0.8 kW, closer to the carbothermal reduction temperature (>1500 °C). Thus, the CO release was interrupted and with it, the pores formation. Moreover, the material had to be re-heated, increasing the chances for material densification, and potentially compromising the material's carbothermal reduction homogeneity because the carbon would be reacting with larger UO_2 particles. To address the risk of not completing the UO_2 carbothermal reduction, instead of conditioning for four hours as we found effective to fully carbothermally reduce the batches, this material was conditioned for six hours at 2.67±0.36 kW.

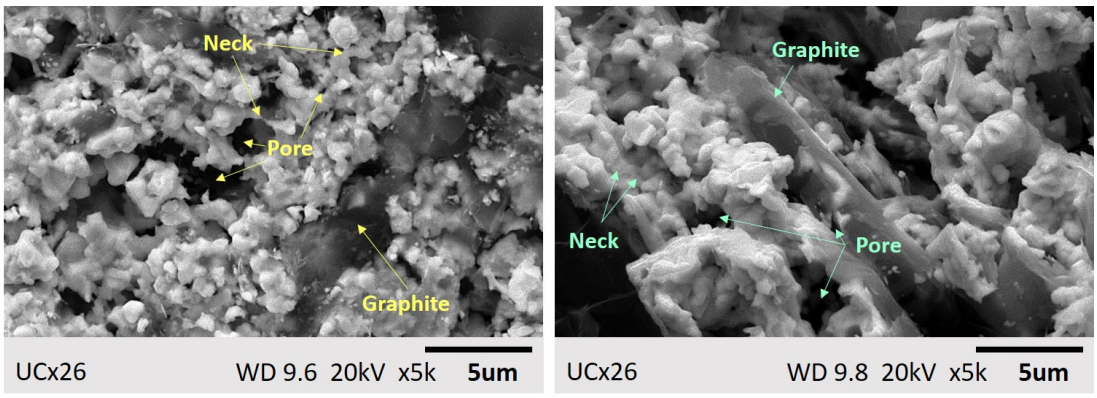

Figure 2.43: UCx26 surface (left) and cross section microstructure (right). The UC_x sintered and formed necks, but the sample still has pores.

Compared with the 11% molar excess batches B2 and B7 (Fig. 2.37), the particles in the surface of UCx26 are coarser (Fig. 2.43). These particles have more necking and show

larger pores. This is most likely due to the excess graphite acting as a sintering constrainer that prevents densification, but that it does not prevent coarsening. The particles measured in the UCx26 cross section are slightly larger and more sintered than those in its surface (Fig. 2.43) but their average diameter difference is negligible (Table 2.11).

UCx27 was set to 80 A and was left at that current for about an hour to allow the target to outgas slower than UCx26. However, the waiting was not long enough and the steep current ramp applied abruptly increased the pressure, and consequently the current tripped to 0 A. When integrating the area under the pressure-curve it was found that this target outgassed more than the rest of the targets. Since the slurry for this target was prepared in the same fashion as the others, there was no additional material that could have caused the outgassing. Probably, the slip-cast discs corresponding to this target were not completely dry before their thermal treatment, so a higher amount of water and solvents evaporated during heating.

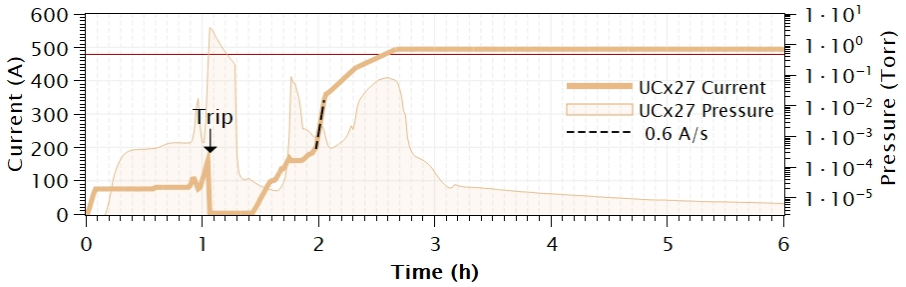

Figure 2.44: UCx27 thermal treatment to carbothermally reduce UO_2/C slip cast discs with 31% molar excess graphite in one-step. The current tripped during this themal treatment because this target outgassing overpassed the pressure limit of 5×10^{-1} Torr (red horizontal line).

UCx27 only stayed at 2.40±0.01 kW for three hours (Fig. 2.41a). This target outgassed during irradiation and had poor isotope release. Uranium dioxide and a cobalt oxide were identified with XRD in the samples of this target (Fig. 2.55), so the UC_x 27 outgassing was most likely due to its incomplete carbothermal reduction, and the evaporation of cobalt during irradiation.

Even though UCx27 was only conditioned for three hours at lower power than UCx26, its surface's microstructure looks more sintered than that of UCx26. This suggests that the waiting time for the binders outgassing might have contributed to the densification of the UO_2 particles on the discs surface or that the target might have been at a higher temperature than 650 °C. The UCx27 cross section on the other hand, is only partially sintered in comparison to the surface. The average size of the UC_x particles in the UCx27 cross section is comparable to that of UCx26 (Table 2.11). More sintering is expected on the surface of the discs because the particles and grains there have more free energy [16].

Similarly to UCx27, UCx28 was conditioned for three hours[3], but at a lower power

[3]Afterwards, UCx28 was submitted to an additional conditioning to assure its cleanliness. This target did not outgas online. It was not feasible to collect additional samples after conditioning, so the results showed here corresponds to the material previous its second conditioning.

(2.30±0.01 kW). In contrast to UCx27, UCx28 thermal treatment went through uninterrupted, so the material did not have to be heated twice; thus, we would expect less particle densification than for UCx27.

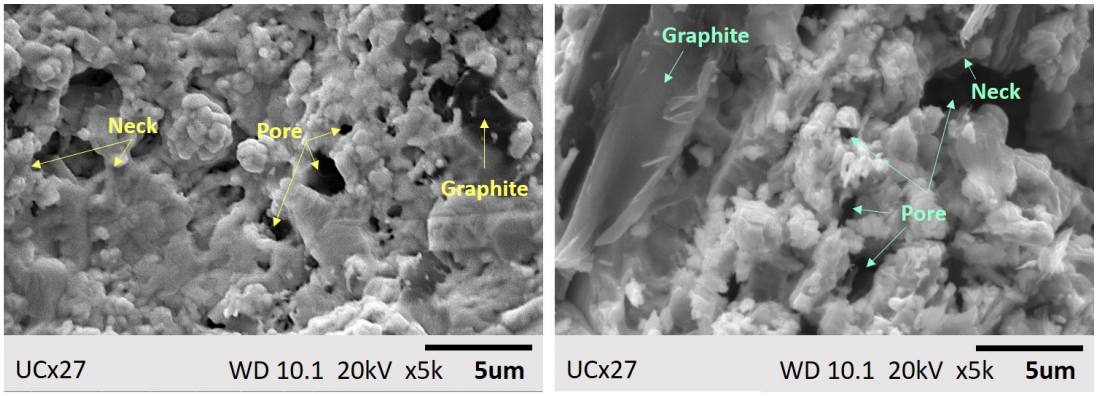

Figure 2.45: UCx27 surface (left) and cross section (right) microstructure. The particles in the cross section of UC_x 27 are sintered, but not as much as those on the surface.

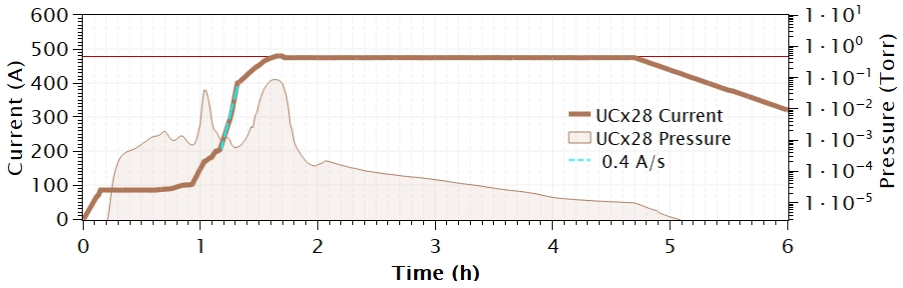

Figure 2.46: UCx28 thermal treatment to carbothermally reduce UO_2/C slip cast discs with 31% molar excess graphite in one-step. This thermal treatment was not interrupted by a current trip.

The isolated UC_x particles on the surface of UCx28 are smaller than those on UCx27 (Fig. 2.47 and 2.45). However, the UCx28 presents large zones with sintered particles identical to those on UCx27. This support the assumption that the waiting time for the water and binders evaporation contributes to the densification of the particles on the discs surface. Furthermore, UCx28 cross section resembles that of the UCx26 and UCx27 confirming that the sintering process is more prominent in the surface than in the material bulk.

UCx29 thermal treatment was not interrupted (Fig. 2.46), and it was similar to that of UCx28. However, UCx29 was conditioned longer and at higher power; it stayed at 2.89±0.01 kW for fifty five hours (Fig. 2.41b). The comparison between the microstructures of UCx29 and UCx28 indicates the effects of the conditioning in the materials. The UC_x particles on the surface of UCx29 are substantially larger than those of UCx28. Also, necks and large pores are visible on the UCx29 surface, but graphite particles are not.

Comparing the surface of UCx29 (Fig. 2.49) with the disc's surface of the batch B3 (Fig. 2.37c) that was conditioned for 66 hours (Fig. 2.36), UCx29 UC_x particles are coarser,

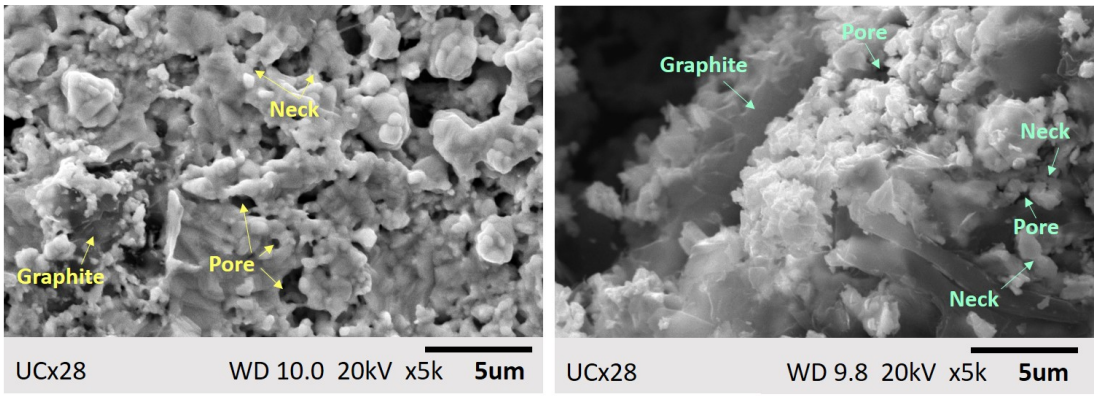

Figure 2.47: UCx28 surface (left) and cross section (right) microstructure. The cross section of this sample is sintered, but not as much as the surface. The surface microstructure of this sample is similar to that of the UCx27 (Fig. 2.45).

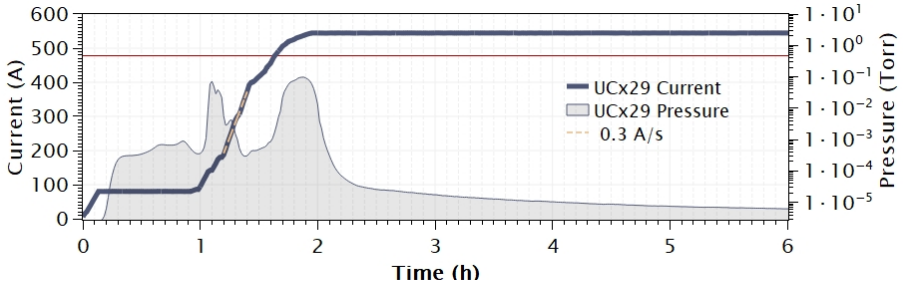

Figure 2.48: UCx29 thermal treatment to carbothermally reduce UO_2/C slip cast discs with 31% molar excess graphite in one-step. This thermal treatment was not interrupted by a current trip.

so less packed with larger pores than B3. This is most likely because of the graphite excess in UCx29 acting as a sintering constrainer. On the other hand, the difference in microstructure between UCx29 and B3 can also be attributed to the UCx29 shorter conditioning time of 55 h. Nevertheless, the UCx29 large pores give the impression that, even if the target was conditioned for a longer time, the particles in the surfaces of these discs would not densify as those of B3; however, the UCx29 discs would have to be conditioned for the same time length as the B3 batch to confirm or refute this assumption.

The UC_x particles in the cross section of UCx29 are not as large as in its surface, but are larger than those in the cross section of UCx26, UCx27, and UCx28 (Table 2.11). In general, the UC_x particles of the UCx29 present more necking, particle growth, and coarsening than all the rest of target samples. Particle growth is not convenient for isotope release, because diffusion through the grain and particles is less efficient than between their boundaries. Therefore, conditioning for 55 hours is not recommended for the UC_x targets.

The thermal treatment of UCx30 only tripped once during the release of CO. By then, the pressure was reducing suggesting that most of the UO_2 in the target had been carbothermal reduced, but the discs were returned to high power to assure their homogeneous carbothermal reduction (Fig. 2.50); however, determining that the carbothermally reduction is complete

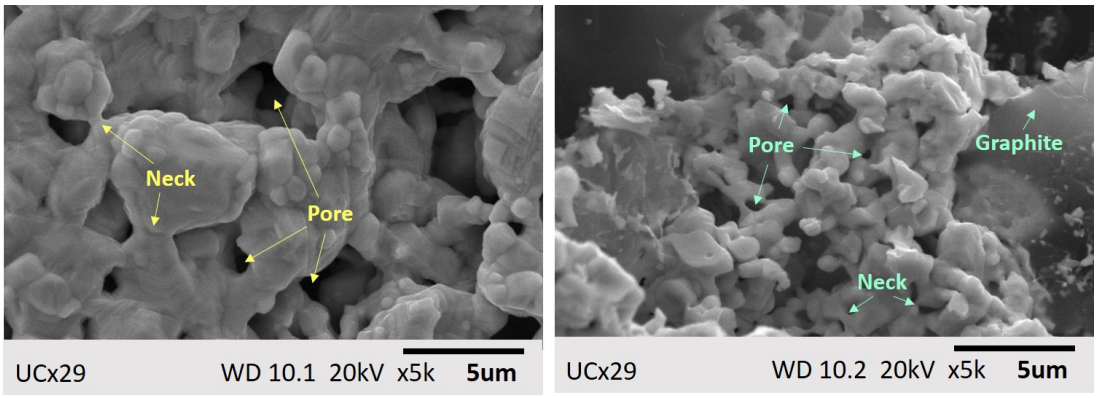

Figure 2.49: UCx29 surface (left) and cross section (right) microstructure. This target has the largest particle size in both, its surface and its cross section; nevertheless, this material has pores.

after a trip like this is difficult because most CO had already been released; thus, the pressure difference at high temperature is not perceptible while ramping the current up. To address this situation, after the material was conditioned for eighteen hours at 2.84±0.06 kW the power was increased to 3.3 kW at 0.15 A/min to make sure no more CO was left to be released (Fig. 2.50).

The shape of the UC_x particles in the UCx30 surface was similar to those of UCx29, but UCx30 particles were smaller (Fig. 2.49 and 2.51). Many particles of the UCx30 surface present necking, inherent of particle growth and sintering. The surface also has pores due to coarsening. Like the other targets, UCx30 cross section particles were smaller than those in the surface (Fig. 2.51).

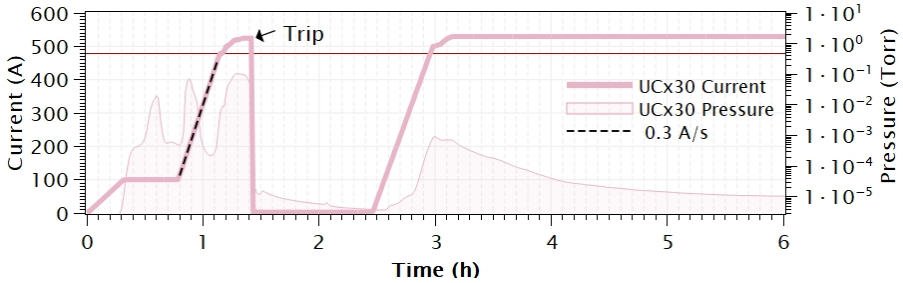

Figure 2.50: UCx30 thermal treatment to carbothermally reduce UO_2/C slip cast discs with 31% molar excess graphite in one-step. This thermal treatment was interrupted by a current trip when the material was already in the carbothermal reduction stage. The current was returned to 530 A to complete the reduction.

The smaller particles measured in all the samples surface and cross section varied from 0.5 and 0.8 µm. The larger particles had a wider range of sizes going from 2.8 to 6.2 µm. Not surprisingly, the sample with the largest particle was measured in the surface of the UCx29 micrograph corresponding to the target with the longest conditioning. Among the cross section micrographs, the sample with largest particle was the UCx27 (5.04 µm). In average, the particles in the samples cross section are 1.7±0.4 µm (Table 2.11).

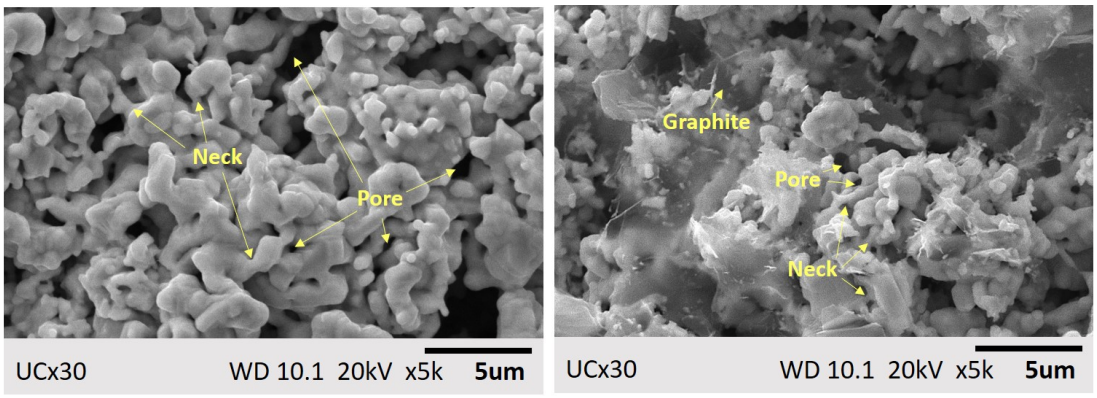

Figure 2.51: UCx30 surface (left) and cross section (right) microstructure. The morphology of this target material is similar to that of the target UCx29 (Fig. 2.49), but its particle size is smaller.

No cross section presented sinterization as the surface of UCx29 (Fig. 2.37) that had the largest particle growth, and coarsening. This confirms that the differences due to the accelerated thermal treatments and conditioning time have more impact in the surface morphology of the disc than through their bulk. The particles in the bulk also grow and sinter as it can be seen in UCx29 cross section (Fig. 2.49), but not as much as in the surface. Both, the sintering in the bulk and in the surface of the discs should be avoided because even if the discs have high porosity and small particle size though the bulk, a sintered surface will likely hinder isotope release.

In agreement with the batches particle-size growth, the particles of the targets analyzed in this section also were correlated with the original size of the UO_2 clusters. The smallest particles measured in the UC_x samples correspond to the surface of UCx28 (0.4 µm), being twice as large as the smallest UO_2 particle; also, the average particle size corresponds to the average size of a UO_2 cluster in the UO_2/C green cast (Table 2.11).

Compared with the targets produced with the old method, the new targets have similar UC_x particle size in the cross section, but the morphology of the UC_x particles on their surface differs (Table 2.11). Reducing the time to evaporate the binders most likely would contribute to the reduction of the UC_x sintering on the surface. To attain this, a slower initial ramp is recommended such that the outgassing is constant, but it does not trip the system, preventing reheating. To further avoid sintering, the conditioning time should not be longer than six hours.

The similar morphology of the target materials cross sections is evident at low magnification (Fig. 2.52). A fractured unpolished disc, facing almost parallel to the view plane, show the UCx26 and UCx27 samples cross section (Fig. 2.52a and 2.52b). The graphite is layered and elongated; between the graphite layers there is UC_x and pores. The cross section sampled of UCx28, UCx29, and UCx30 are not facing completely parallel to the view plane, they are fractured angularly to the cross section (Fig. 2.52c, 2.52d and 2.52e).

Table 2.11: Minimum, maximum, and average particle size of UC_x online targets and green (UO_2/C) cast. The UO_2 particle size was only measured on the surface, but it is most likely the same in the cross section since the green slip cast is not thermally treated. In contrast, the particles on the surface and cross section of the UC_x slip cast were measured and it was found that, in average, they are larger on the surface. Micrographs measured are available in Appendix A.5.

	Particle size (µm)					
	Surface			Cross section		
Target	Min	Max	Ave	Min	Max	Ave
Green	0.2	5.1	1.3	NS	NS	NS
2-sc	0.5	5.1	1.7	0.5	3.2	1.5
UCx26	0.7	2.9	1.3	0.6	5.0	1.9
UCx27	0.7	3.2	1.6	0.6	5.2	2.2
UCx28	0.4	3.2	1.4	0.6	3.6	1.2
UCx29	0.8	6.2	1.8	0.8	3.0	1.7
UCx30	0.5	4.8	1.8	0.7	2.8	1.3

Nevertheless, in agreement with the layered structure of UCx26 and UCx27 cross-sections, UCx28, UCx29 and UCx30 (but specially UCx28) also look stepped.

Except for the target UCx27, the samples reserved for characterization were enough for SEM, XRD, and porosity measurements. The UC_x samples were stored in a glove box where their thickness and mass were measured. With the results, the bulk density of the target composite was calculated. The apparent volume of the UC_x samples was also estimated to obtain their open porosity.

The average total porosity of the targets was 0.64 (Fig. 2.53). Compared with the total porosity, the open porosity ranges from 55.25 % to 39.88 % for UCx26 and UCx30 correspondingly. In between are UCx28 and UCx29 that have a similar open porosity of 47.62 % and 48.77 % respectively. The highest porosity of UCx26 most likely is due to its shortest time of binder evaporation.

The low open porosity of the target UCx30, was likely related to the way its samples were analyzed. These composites were fragile, and their slip cast unattached from their graphite foil, so only the slip cast of the UCx30 samples was submitted to pycnometry; since only its open porosity is low and not its total porosity, it seems like the interface graphite foil - slip cast plays a role in the porosity measured. It is possible that a region of open pores is formed between the graphite foil and the slip cast, and that it was accounted in the results of the other targets that were analyzed over their graphite foil. Nonetheless, more UC_x dedicated to characterization should be reserved to obtain more reliable pycnometry measurements. Synthesizing a full UC_x target for characterization is advised; this will allow collecting samples from different sections of the container to assess the material's microstructure and porosity homogeneity throughout, discarding or validating a correlation with possible temperature gradients in the container during the target material thermal treatment.

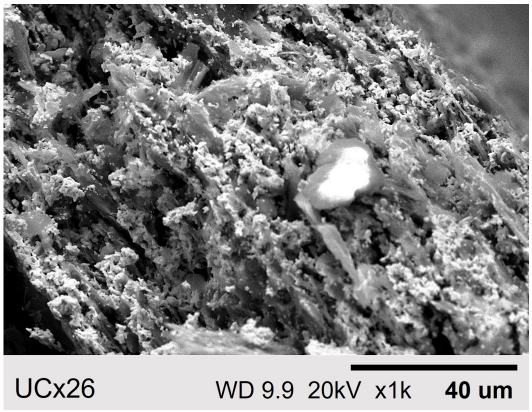

(a) UC_x 26

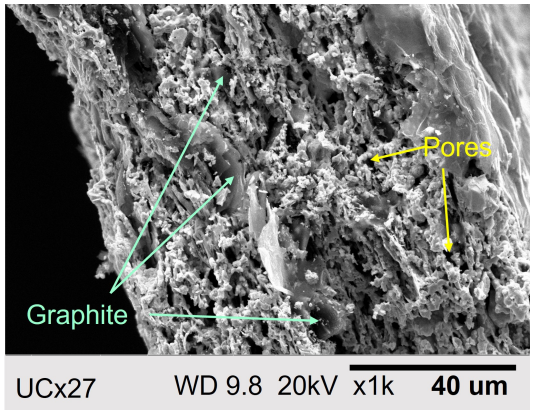

(b) UC_x 27

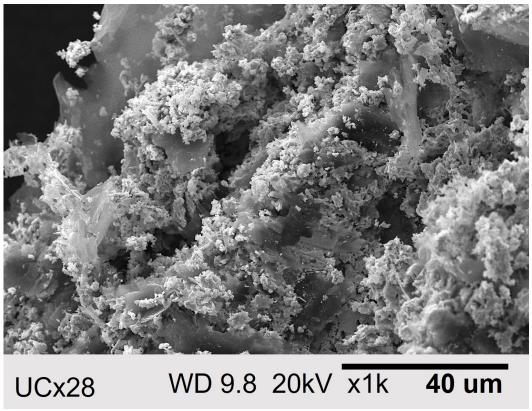

(c) UC_x 28

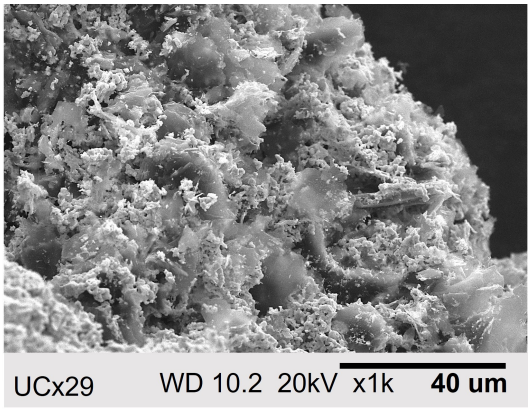

(d) UC_x 29

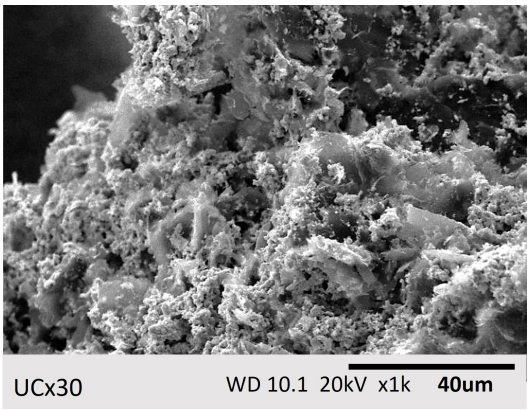

(e) UC_x 30

Figure 2.52: UCx26 (a) and UCx27 (b) cross sections are almost facing completely parallel to the viewer, so they show the layer distribution on the graphite with the UC_x distributed between the layers resembling the Greek dessert *Baklava*. UCx28, UCx29, and UCx30 cross sections are partially facing the viewer, these cross section show the layers of the material resembling steps in a stair.

Table 2.12: Total and open porosity of UC_x targets irradiated online and 2-step casting discs prepared unconventionally (p. 45).

Target	Total porosity	Open porosity
2-sc	0.57±0.01	0.47±0.10
UCx26	0.64±0.01	0.54±0.04
UCx28	0.63±0.01	0.48±0.02
UCx29	0.66±0.01	0.49±0.02
UCx30	0.64±0.02	0.40±0.02

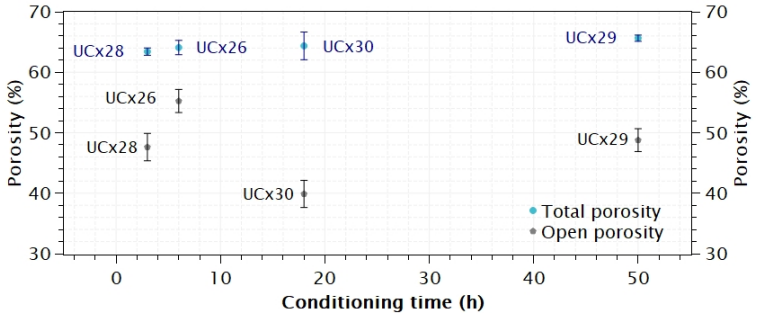

Figure 2.53: Open porosity of the UC_x targets made with the 1-step casting method that were irradiated. UCx27 porosity was not included because not enough sample was reserved for analysis, so the results had a large error associated.

As with the batches, the UC_x targets made with the new method were analyzed under XRD. These targets were conformed by α-UC_2 (tetragonal phase) [71], UC (cubic phase) [73], graphite (hexagonal structure) [65], and also WUC_2 (orthorhombic phase) [72] (Fig. 2.54).

Patterns corresponding to uranium oxides and oxycarbides were compared with the XRD patterns of the targets made with the new method. Only UCx27 and UCx28 XRD patterns have peaks that were identified as UO_2 [75] (Fig.2.54 and 2.55). Having a short conditioning time was most likely the reason for these two targets to not fully carbothermally reduce. Moreover, a peak at 38.4°was identified in the UCx27 pattern (Fig. 2.54) and matched with a cobalt oxide [76]; however, the principal peaks of this cobalt oxide also coincide with those corresponding to WUC_2. Since WUC_2 has been found in all the UC_x targets including those made with the old method [6], it is difficult to confirm that the peak corresponds to $Co_{0.885}O_2$ [76] since the pattern is masked by that of the WUC_2.

The UCx27 cross-section was mapped with EDS (Fig. 2.56) to find its elemental composition. As expected, the sample showed uranium, carbon, and tungsten, but no cobalt (Fig. 2.56); this impurity might had been in quantities that could not be detected with EDS, or not present in the areas explored. Furthermore, mapping the slip cast cross section informed about the distribution of the elements and pores in the sample. The uncoloured zones in the EDS map correspond to areas mapped where no element was identified, so they were interpreted as pores (Fig. 2.56b); their distribution among the layers is consistent with

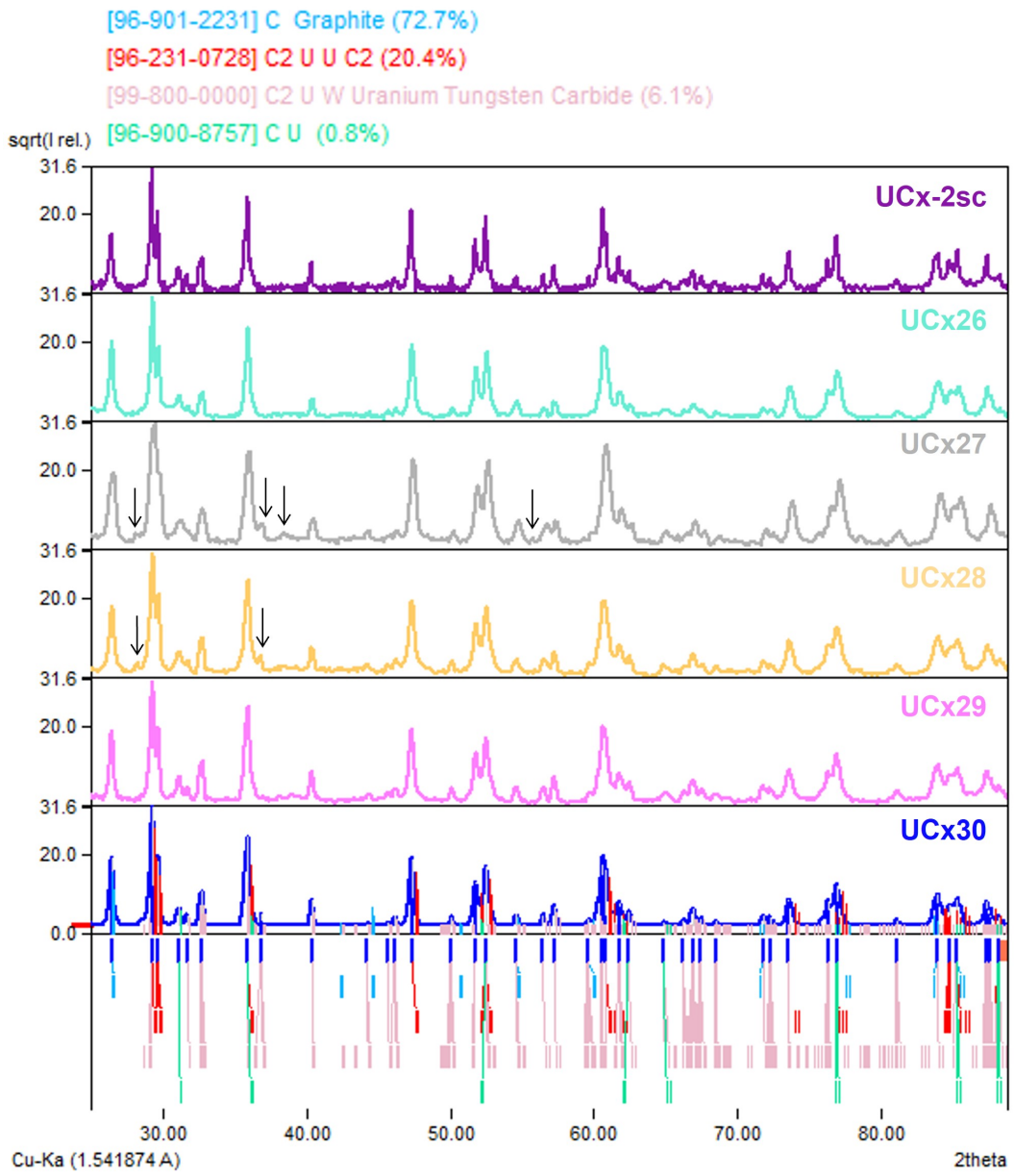

Figure 2.54: XRD phase identification of the targets UC_x 26, UC_x 27, UC_x 28, UC_x 29, and UC_x 30. With exception of the peaks indicated with arrows, all the peaks in the XRD patterns were identified and matched with UC_2 [71], UC [73], WUC_2 [72], and graphite [65].

the one observed in the SEM micrographs of the samples cross sections (Fig. 2.52). The carbon layered-like distribution (Fig. 2.56e) also agrees with the observations in the SEM micrographs (Fig. 2.52); moreover, the elongated zones in blue that are not over uranium indicate the graphite in excess, and the dimmer blue zones represent the carbon bonded to uranium that forms the UC_x.

As expected, uranium dominates and it is present on all the map except for some zones with graphite excess, and in the areas identified as pores (Fig. 2.56b and 2.56c). Since

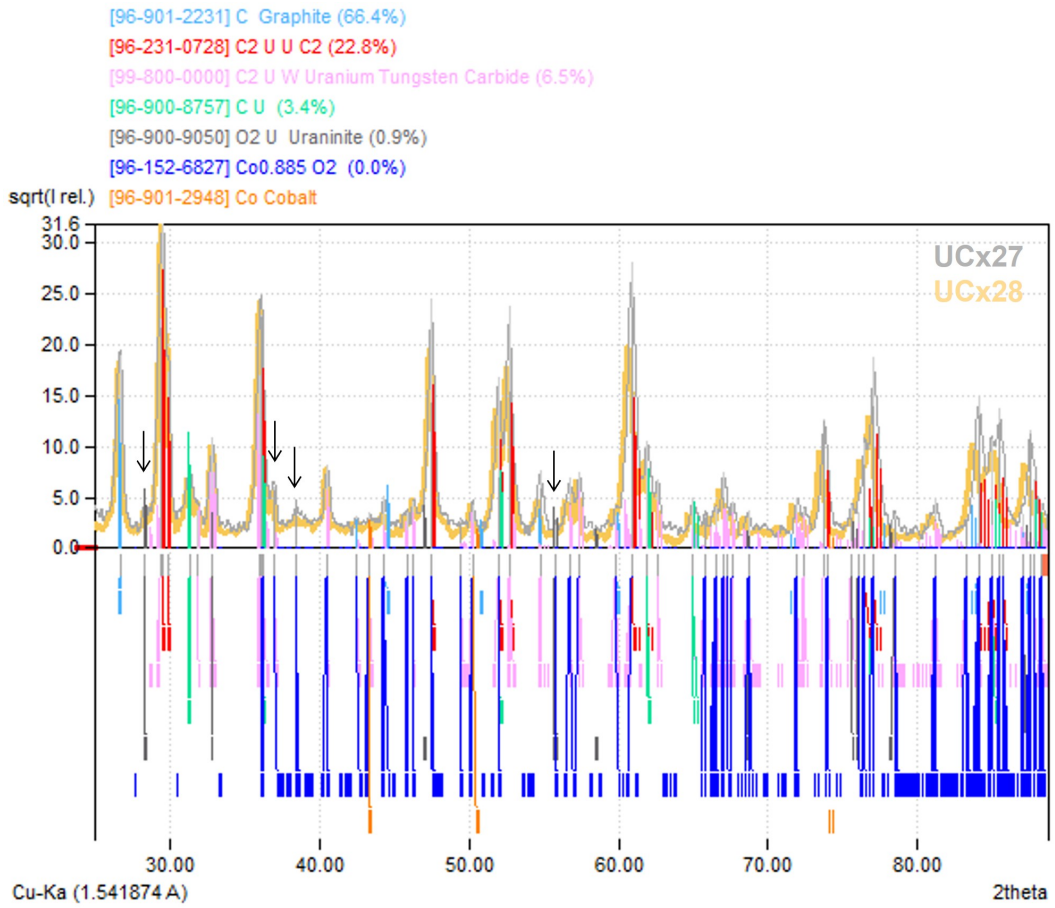

Figure 2.55: UC_x 27 (grey) and UC_x 28 (yellow) XRD patterns. Unlike the rest of the targets, the UC_x 27 and UC_x 28 have peaks that indicate remaining UO_2. Furthermore, the previously unidentified peak at 38.4° on the UC_x 27 XRD pattern was matched with $Co_{0.885}O_2$ [76].

tungsten (W) is a high Z material, it can not be distinguished from the UC_x with SEM like graphite is distinguished; however, EDS reveals the tungsten's location in the slip cast (Fig. 2.56d). Tungsten is largely distributed all over the cross section and it forms agglomerates like the one indicated on Fig. 2.56a and 2.56d.

Agate jars and balls could be used instead of WC to reduce the target's tungsten contamination. However, UO_2 and agate have similar hardness; the UO_2 hardness goes from 6 to 7 Mohs and the agate goes from 6.5 to 7 Mohs, so instead of tungsten contamination the targets would have silicon oxide with a melting point of 1600 °C. Another solution to deliver UC_x targets with less tungsten could be to use smaller milling balls. Currently, the balls used are 19 mm diameter, and the volume of UO_2 and water during the UO_2 milling is below the recommended to avoid abrasion; therefore, the milling periods are detrimental for both the jars and the balls, and the worn WC ends up in the UC_x material. With smaller balls the milling volume will match with the recommended to prevent abrasion; moreover, milling with smaller balls is more efficient; thus, the milling time could be reduced and so

the tungsten content in the target material. On the other hand, purchasing smaller grain size UO_2 would allow skip the milling step of the process; hence, the introduction of WC in the slurry. However, UO_2 providers are scant, so there is not a wide offer to choose from.

To further analyze the failed target UCx27, UCx28, the target that had a similar thermal treatment as UCx27, was reconditioned and its released vapour was analyzed. The UCx28 was conditioned in the actinide furnace; since it was loaded in a target oven, it could only outgas through the ion source (Fig. 2.26a). A tantalum cap was set at the exit of the ion source, but not in contact with it, such that the cap could stay colder than the ion source, and the gas could condensate on the cap. Then, the deposits were analyzed with EDS. The impurity found was cobalt (Fig. 2.57), a metal that also comes from the WC grinding jars. Its vaporization temperature is only 1077 °C [47] at the operational pressure of 1×10^{-6} Torr [47], so if it is not removed during conditioning it is very likely to vaporize during irradiation.

Target UCx27 is not the first one outgassing during irradiation. Targets before have outgassed, but the reason behind it is not always pinpointed. A methodology to retrieve irradiated samples was developed in this work. The targets are opened after irradiation in a hot cell and material is collected and stored for analysis. When the samples' dose rate is below 1 mSv/h a sample can be retrieved from the hot cell and decontaminated. Currently, TRIUMF has capabilities for the analysis of irradiated samples under SEM (just SE and BSE, but not EDS), but authorizations are being sought for the analysis of irradiated materials at SFU, where additional characterization equipment is available.

For this work, non irradiated and irradiated samples of UCx27 were analyzed at SEK CEN Belgian Nuclear Research Centre. The samples were ion beam milled to remove the oxidized surface layer that the targets had accumulated during storage. The UCx27 EDS map of the milled sample show uranium, carbon, tungsten, and cobalt (Fig. 2.58). In comparison with tungsten that its distributed in clusters, stripes of cobalt are pinpointed in the sample surface. Furthermore, oxygen has been detected only in the regions that were not milled, suggesting that there are no uranium oxides in the bulk.

In conclusion, the UC_x targets made with the one-step casting, have a similar particle size to the targets made with the old method in their cross section, but their surface tends to sinter and have larger particle size compared to the old UC_x material. Given their similarities, the UCx targets made with the new method should have a comparable isotope release with respect to the old targets. Comparing all the targets made with the new method, the one expected to have the higher release is UCx26 since it has the smallest particle size and the highest open porosity.

Since the new-method slurries are prepared in the same way as the old ones, the 1-step casting exhibits tungsten contamination. Cobalt has also been identified as a contaminant; this metal has the potential of outgassing during irradiation, but it can be removed during conditioning. Nevertheless, conditioning for more than six hours compromises the

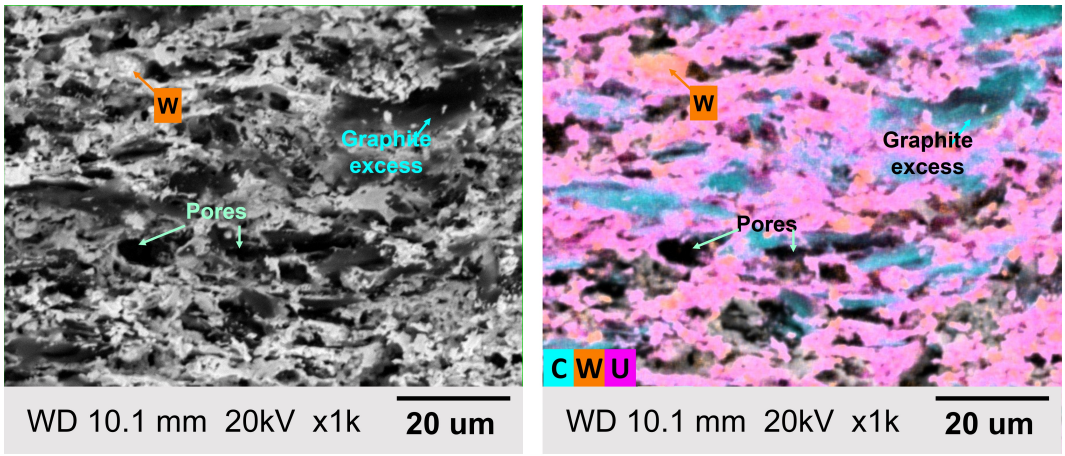

(a) BSE cross section

(b) EDX map

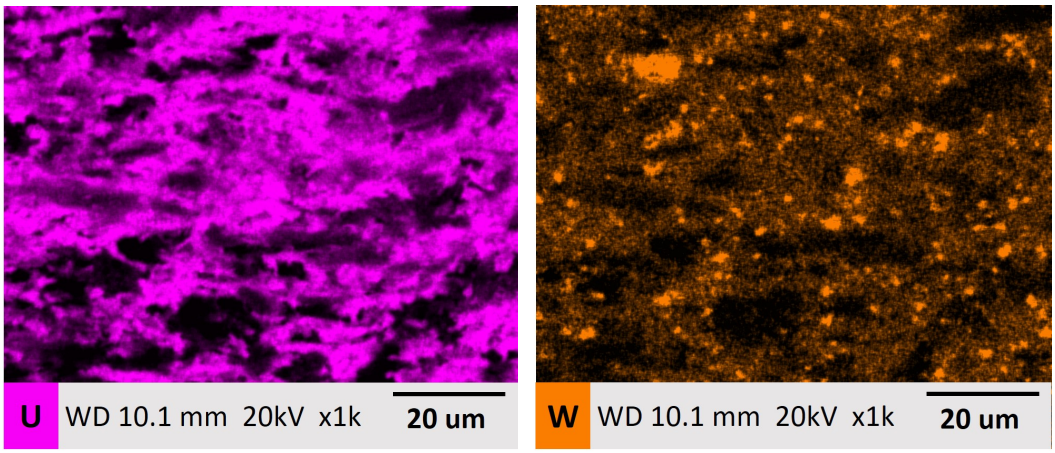

(c) Uranium

(d) Tungsten

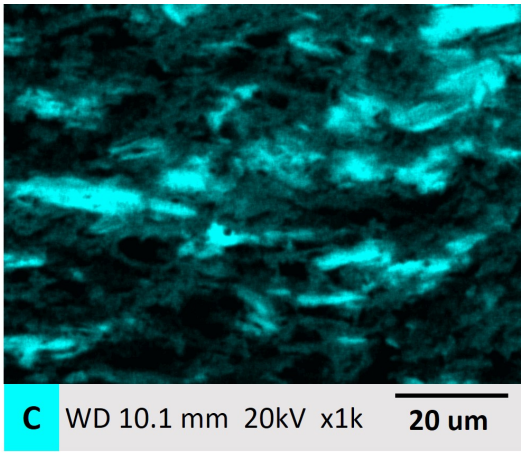

(e) Carbon

Figure 2.56: Cross section of UCx27 observed with BSE (a), EDS mapping of cross section (b), and individual maps of uranium, carbon, and tungsten.

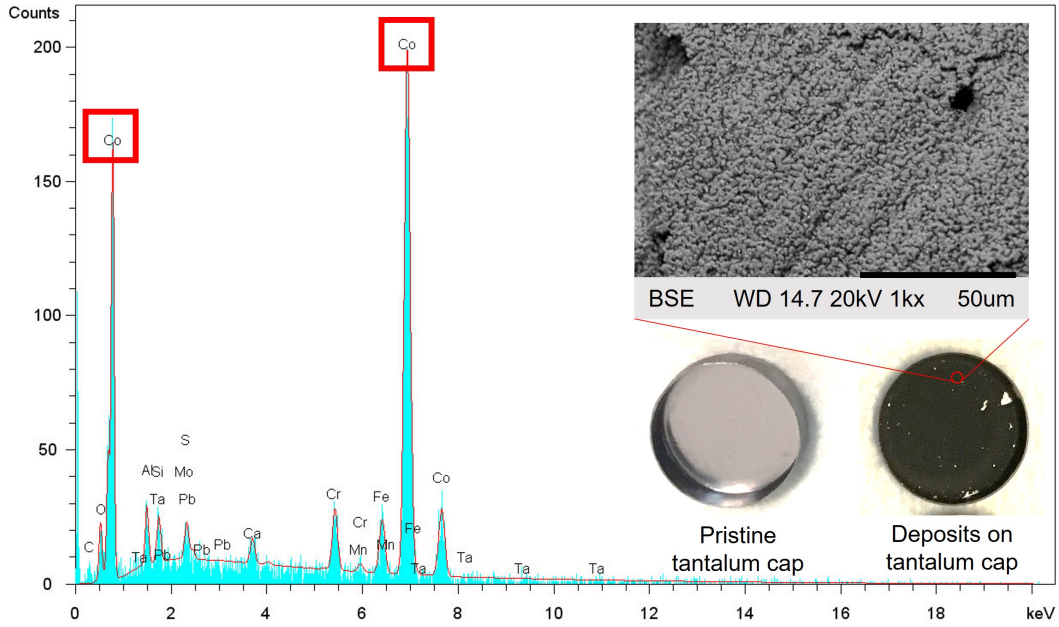

Figure 2.57: EDS area scan of deposited material from conditioning the target UCx28. Before conditioning the target, the pristine tantalum cap had a silvery color and it was shinning. The cobalt deposited on the cap looks black.

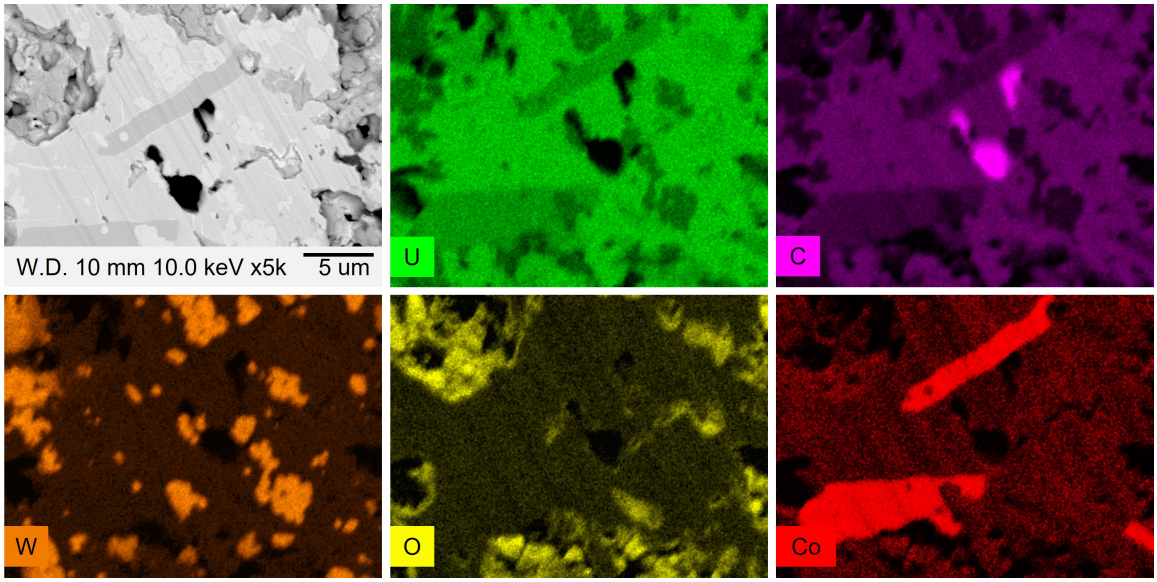

Figure 2.58: EDS mapping of non irradiated UCx27 ion beam milled surface sample. Uranium and carbon are distributed all over the sample as expected; tungsten is localized as found in previous sample (Fig. 2.56). Cobalt is localized in stripes, and oxygen is localized on unpolished areas. Micrographs obtained at SCK CEN.

microstructure of UC_x. Therefore, we propose to modify the methodology for milling the slurry. Milling with smaller WC balls could decrease the wear of the WC jars, and consequently reduce the tungsten and cobalt contamination, allowing a briefer conditioning time

to deliver fully carbothermally reduced targets, with small particle size, and lower impurity content. Shorter milling times would further reduce the production time of the UC_x targets, allowing the R&D on other target materials.

The reduction in production time attained with the one-step casting so far, released equipment and resources for the production of a new target material. The new graphite target has been synthesized and characterized (Section 2.4). Also, it has been irradiated and has delivered lithium and beryllium RIB to experiments (Chapter 4).

2.4 Graphite-composite target synthesis

The graphite-composite target developed for this work consists of graphite powder slip cast on top of graphite foil. To prepare a graphite slurry, 20 g of graphite powder of particle size $\leq$44 µm and 99.9995% pure from Alfa Aesar [55] was mixed with deionized water and ammonium citrate as dispersant at 60 RPM in the planetary mill for one hour. After that, dispersants, plastizicers, and surfactants were incorporated to the slurry (Table 2.13) and mixed for an additional hour at 60 RPM.

Table 2.13: Substances mixed to prepare a graphite slurry; mass% and mol% are in function of graphite powder.

Substance	**Function**	**Mass%**	**Mol%**
Ammonium citrate	Emulsifier	7	0.03
Deionized water	Solvent	140	93
Glycerol	Dispersant	5	0.02
Polyethylene glycol 400	Plasticizer	5	1
Polyvinyl alcohol (7% aq. sol.)	Plasticizer	61	0.38
η-Butanol	Surfactant	5	1
Methanol	Surfactant	4	1

The graphite slurry was poured and spread on a thin layer over a graphite foil (Fig. 2.1c). Then discs were cut from the slip cast when it was dry. In contrast to the ISAC targets, the graphite discs were thermally treated in a tantalum tube (Fig. 2.59c) and not in a target oven (Fig. 2.59d). Avoiding thermally treating the graphite-composite target in an oven prevents prematurely exposing the oven to carbon, which was found in this work (Chapter 3), to induce the formation of tantalum carbides that modify the properties of the target oven. Ideally, this target would be loaded in a graphite container (Fig. 2.23) to ease its transfer from a tantalum boat (Fig. 2.14b) to a target oven (Fig. 2.59d), reducing the contact between the discs and the oven. However, the graphite-composite targets presented in this work were developed in 2020, during the lockdowns enforced due to COVID-19. Therefore, material suppliers and personnel were unavailable or scarce, such that procuring adequate graphite containers for the graphite-composite target was unfeasible.

Instead of cutting the cast with the rotatory die cutter (Fig. 2.2) like the ISAC slip casts, the graphite cast was cut with a laser cutter (Fig. 2.59a). The discs cut with the rotatory die have an interference-fit [77] with the tantalum oven, so cutting the graphite discs with it would hamper their transfer from the tantalum tube to an oven after their thermal treatment. Thus, the graphite discs were laser cut with a smaller diameter to have a transition-fit [77] with the tantalum tube (Fig. 2.59).

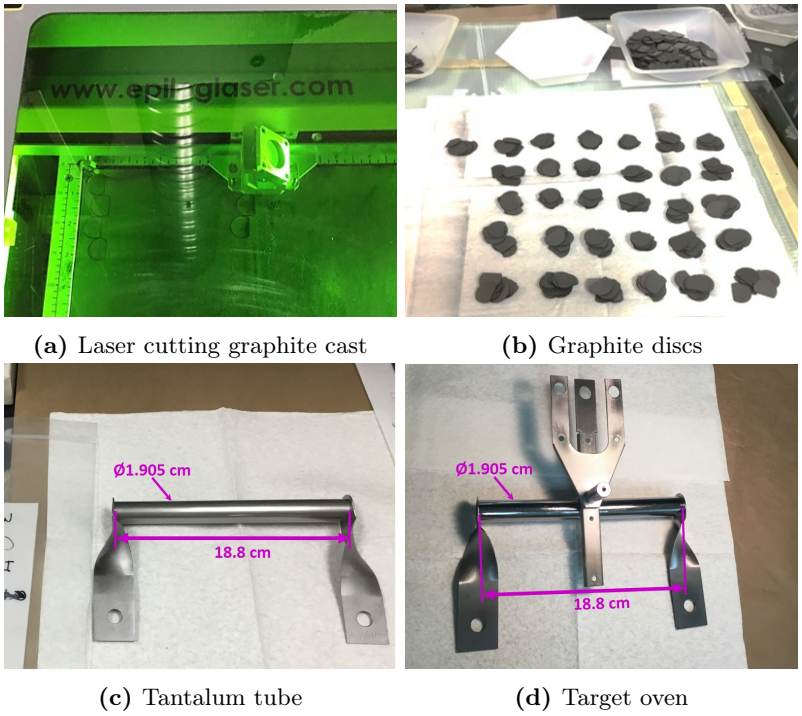

(a) Laser cutting graphite cast **(b)** Graphite discs

(c) Tantalum tube **(d)** Target oven

Figure 2.59: Process for cutting and loading graphite composites for thermal treatment, and irradiation. Once the slip cast is dry, D-shaped discs (b) are laser cut (a) and loaded in a tantalum tube (c) for thermal treatment; then, the discs are transferred to a tantalum oven (d) for online use at ISAC.

A total of 450 graphite-composite discs (fig. 2.59b) were thermally treated. The D-shaped discs of 1.828 cm diameter were loaded in a tantalum tube (Fig. 2.59c) and set in the non-actinide furnace (Fig. 2.3b). The material was resistively heated at 2000 °C under vacuum (Fig. 2.60). The objective of their thermal treatment was to evaporate the water and plasticizers in the slip-cast, and to remove impurities like cobalt; a metal that is introduced to the slurries due to the wear of the milling jars (Fig. 2.1) where the slurries are mixed.

The thermal treatment of the graphite target lasted around six hours (Fig. 2.60). During the first two hours, the electrical current was set to automatically increase 1 A each 10 s, then the ramp was increased to 2 A each 10 s. The automatic ramping was set to pause the electrical current input if the pressure reached 3×10^{-2} Torr, and to reduce it if the pressure reached 5×10^{-2} Torr. The final current corresponding to 2000 °C was 515 A (Fig. 2.60b). The target was kept at that current for approximately three hours to outgas the material

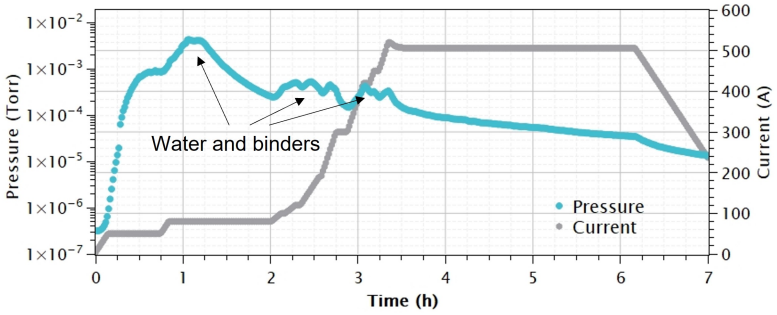

(a) Pressure during the current ramping of the graphite target's thermal treatment.

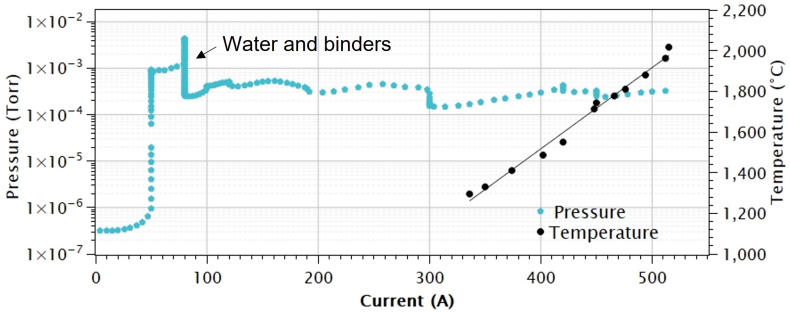

(b) Temperature and pressure corresponding to the current supplied to heat treat the graphite target.

Figure 2.60: Heat treatment of the graphite composite target. The treatment lasted around 6 hours (a). The first 3 hours encompass the power ramping to resistively heat the target. To fully outgas the target, it is held for 3 hours at 500 A corresponding to 2000 °C (b). The pressure peaks correspond to the evaporation of water and binders.

(Fig. 2.60a). Thermally treated graphite foils were later transferred to a tantalum oven that was previously coated with TaC (Section A.4); additionally, a number of target discs was reserved for characterization.

In contrast with the LaC_2/C and UC_x targets, the graphite-composite target does not undergo carbothermal reduction. Therefore, the pressure increases to 4×10^{-4} Torr only at low temperature (<1000 °C) at the beginning of the thermal treatment (Fig. 2.60b). Even though several pressure peaks are distributed within the first three hours of the thermal treatment, all are due to the evaporation of binders and water in the slip cast; these substances were released intermittently because the automatic ramping would pause at the established vacuum limit (3×10^{-2} Torr).

The pressure before cooling down was 3.5×10^{-5} Torr. Since this target material was going to be irradiated online, it was thermally treated again once the discs were loaded in the tantalum oven. All ISAC non-actinide targets are routinely submitted to this thermal treatment in preparation for online irradiation (Fig. 2.61); its purpose is to ensure the cleanness of the target-assembly, to evaluate their electrical and thermal performance, and to spot leaks in the assemblies' water-cooling tubes.

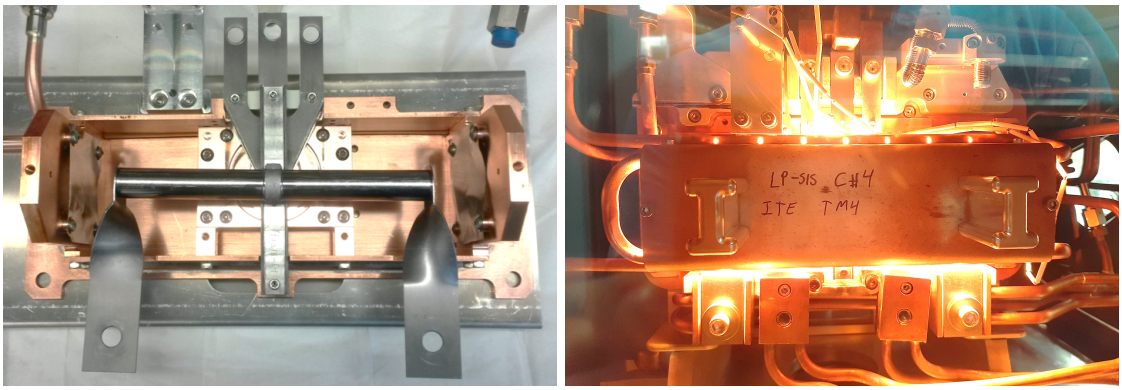

(a) Open assembly showing target oven **(b)** Resistively heating target in assembly

Figure 2.61: Before submitting the ISAC targets online for irradiation, they are installed in an assembly (a). The target-assemblies routinely undergo a quality-control process where they are thermally treated (b) to guarantee their cleanness, assess their electrical and thermal performance, and test the assembly for water leaks.

The ISAC's target quality-control consists of resistively heating the target-oven body with an electrical current of 580 A, and its ion source with a current of 230 A (Fig. 2.26a). The electrical current is automatically increased at 2 A/min, and the target is left at maximum electrical current for two days. Afterwards, the target is cooled down at 1 A/min [78]. Although the target ovens are exposed to graphite during this quality-control process, it is an established step that diagnoses the performance of the target-assemblies, and identifies flaws that can be fixed before submitting the targets online.

The clean target-assemblies are submitted online and irradiated. After the quality-control, it is not possible to retrieve target-material samples, so the effects of this process in the target-material microstructure is not assessed. Nevertheless, pristine and thermally treated graphite-composite discs are reserved for characterization; the attributes of these graphite-composite discs are presented in the section below.

2.4.1 Graphite target material characteristics

A batch of fifteen heat-treated foils and twenty-four unheated discs were reserved to weigh them and to measure their thickness and apparent volume. Also, their bulk density and porosity were estimated and compared.

Since the thermal treatment evaporates binders and other substances of the slip cast, the graphite composite discs lost mass. On the other hand, their geometrical volume did not change much, so the discs' bulk density was lower after thermal treatment. From pycnometry analysis it was found that the apparent volume was higher after conditioning, meaning that the evaporation of the plasticizers left open-pores through the slip cast. Consequently, the total and open porosity of the slip-cast was higher after the thermal treatment (Table 2.14). Note that the graphite-composite target has a higher total and open porosity than the

graphite foil (Table 2.14); this trait is beneficial for the isotope effusion and makes the graphite composites a better choice for target material over graphite foils.

Table 2.14: Characteristics of graphite foil and graphite-composite slip cast; the latter before and after thermal treatment.

		Graphite slip-cast	
Characteristic	Graphite foil	Green	Conditioned
Bulk density (g/cm^3)	1.15±0.04	0.95±0.01	0.77±0.03
Apparent density (g/cm^3)	2.03±0.01	1.72±0.18	2.02±0.39
Total porosity	0.49±0.02	0.57±0.01	0.66±0.03
Open porosity	0.44±0.01	0.52±0.02	0.62±0.05
Closed porosity	0.05±0.02	0.05±0.02	0.04±0.03

The improvements in the open porosity gained with the thermal treatment of the graphite composite translated into fragility. After heating, the graphite slip cast could be easily removed when friction was applied; nevertheless, the material had enough structural stability to be transferred to a tantalum oven. Nonetheless, transferring the discs from the tube to a target oven would be effortless if they were loaded in a graphite container, so the development of an adequate container for this target material should be pursued.

Under SEM, the unheated graphite cast looks like an agglomeration of flakes. Similarly, the thermally treated graphite casting looks like layered graphite flakes, but laid flatter than in the green cast (Fig. 2.62) because the plastiziers are not holding the graphite flakes of the conditioned material. The flakes are most likely rearranged into their native van der Waals bonds, or holding by electrostatic charge-up. Besides slight re-arrangement of the flakes due to the evaporation of the binder, no large changes in the graphite target microstructure were expected because its thermal treatment at the applied temperatures does not induce any chemical reaction nor particle sintering in graphite.

The amorphous plasticizers in the green-cast's can not be observed under SEM. However, their presence is evidenced by the specimen-current that makes the graphite flakes look overexposed (Fig. 2.62a), even when using 10 kV instead of 20 kV electron beam as a mitigation measure for specimen-current. On the other hand, the white particles in the conditioned graphite micrograph are organic contamination (most likely paper lint) caught by the material during its preparation for SEM analysis (Fig. 2.62b).

The conditioned graphite slip cast was mapped to identify impurities in the material. The area mapped showed only carbon, and the scan spectrum estimated an atomic percent of 99.975 carbon, and 0.025 tungsten, but no localized tungsten was found on the are mapped, so the result might be within the detector error range.

The XRD patterns of the green and conditioned graphite casts show predominantly hexagonal graphite (a= 2.461 Å, c= 6.708 Å) [65]. In contrast with the LaC_2/C and the UC_x, the graphite-composite samples were analyzed under XRD without any plastic wrapping, so

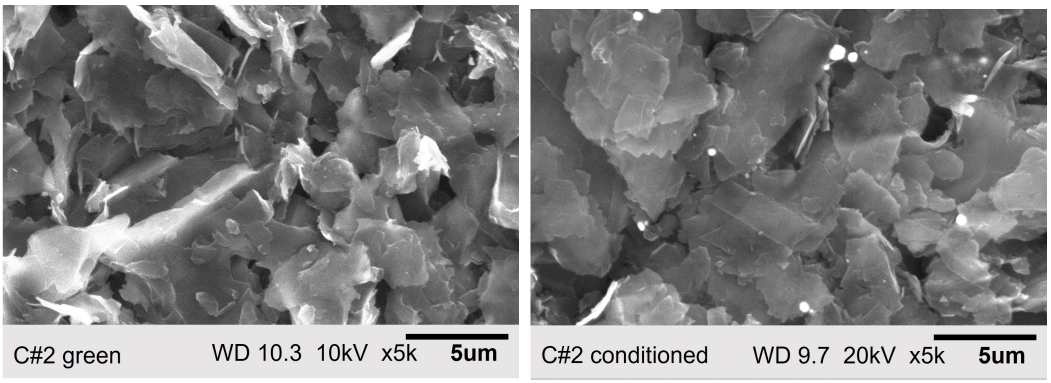

(a) Green **(b)** Conditioned

Figure 2.62: Micrograph of graphite-composite slip-casting before (a) and after (b) heat treatment. The green slip-cast was observed at lower beam energy because it was charging due to its plasticizers. The similarity in the slip-casts' morphology indicates that beside evaporating the solvents and plasticizers, the thermal treatment did not modify the graphite particles.

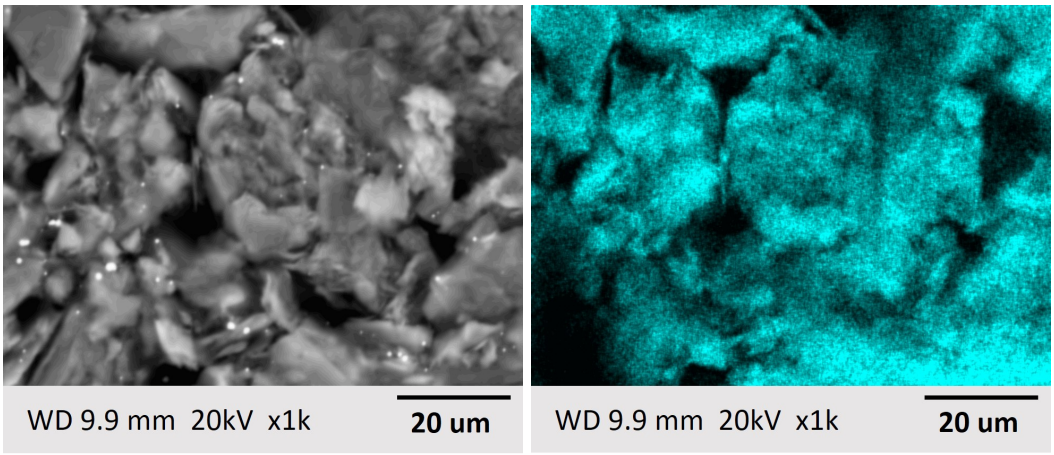

(a) BSE micrograph **(b)** EDS map

Figure 2.63: BSE image of graphite composite sample after thermal treatment (a), and EDX map of same area showing carbon in cyan, and pores in black. No other elements were found during the scanning of the area.

no background signal was expected to mask their XRD patterns. Nevertheless, the first peak in the XRD pattern corresponding to the green graphite-composite cast (orange pattern in Fig. 2.64), is most likely an aberration due to its amorphous plasticizers. Additionally, low intensity peaks become visible only when the patterns are scaled with the relative square root of the intensity; these peaks were identified as the tungsten carbides WC and W_2C (Fig. 2.64) [79, 80]. These carbides are impurities introduced to our target materials during their mixing process in WC milling jars (Fig. 2.1).

Another impurity expected from the milling process is cobalt (Co). Co is troublesome during target irradiation because it vaporizes at ≈1080 °C at 10^{-6} Torr [47] (the operational pressure during irradiation [48]), and it can clog the target ion source reducing the

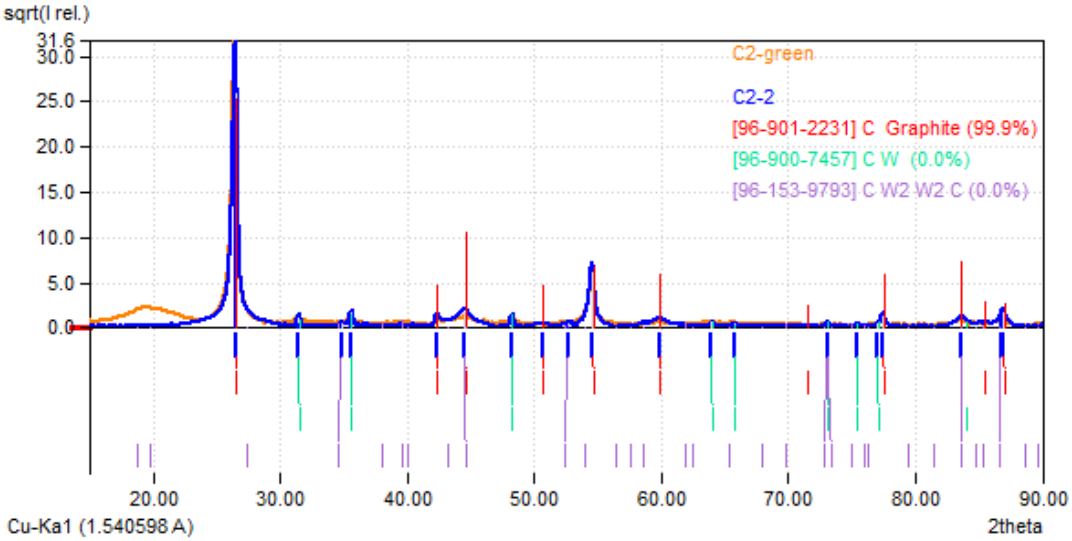

Figure 2.64: X-ray phase identification of graphite cast before (orange pattern) and after thermal treatment (blue pattern). Graphite predominates [65], but WC [79] and W_2C [80] are also identified.

RIB intensity (Fig. 2.26b) if the target is operated above 1080 °C. No peaks corresponding to cobalt or any compound containing it were identified in the graphite target pattern (Fig. 2.64). This result was expected because during the graphite-composite thermal treatment, the maximum pressure at 2000 °C was 3×10^{-5} Torr (Fig. 2.60), and at this pressure, cobalt starts vaporizing at ≈1080 °C [47]; thus, if there was cobalt in the green graphite discs, it most likely would have evaporated since the target material was heated above its corresponding vaporization temperature during conditioning.

The graphite target has an open porosity of 0.62, and micrometric particle size. Both qualities are essential for the isotope diffusion and effusion. The graphite target has ≈41% higher open porosity than commercially available graphite foil (Table 2.14), so it was expected to have a better isotope release performance. Compared with the graphite foils, the graphite-composite discs had a tenfold fraction release of ^{7}Be (Section 4.1). Therefore, even though the graphite-composite material was fragile, this target was selected for online irradiation. The graphite-composite target was used for the production of ^{8}Li, ^{9}Li and ^{7}Be, and its yields are reported in Section 4.6.

The graphite target developed in this work, now forms part of the ISAC target repertoire, and it will also be part of the ARIEL targets. Nevertheless, to achieve the best performance of the ARIEL targets, their tantalum ovens must withstand elevated temperatures. However, when tantalum is heated in presence of carbon it form carbides, becomes fragile, and its electrical resistance changes. Thus, the investigations carried out with the ISAC tantalum ovens will be crucial for their optimum operation. Coatings for the ISAC ovens have been investigated with the objective of increasing the oven longevity at high temperatures under high carbon concentration conditions like those during the irradiation of the graphite target.

Chapter 3

Implications of using high-carbon content targets

Target materials are irradiated online in target ovens made out of tantalum. This is the established metal for ISOL-target ovens because its ductility allows manufacturing the ovens in any desired shape; furthermore, the tantalum's high melting point and electrical conductivity allow resistively heating the target-ovens, consequently increasing the target material temperature, and promoting isotope release (Table 3.1). Moreover, tantalum does not chemically interact with several elements [81], so many of the target materials and produced isotopes do not affect the tantalum oven.

Table 3.1: Comparison of some physical properties of Ta, Ta_2C, and TaC [9]. Tantalum has a lower melting point than Ta_2C and TaC, but it is more ductile, and it is a better electric and heat conductor.

Property	**Ta**	**Ta_2C**	**TaC**
Melting point [°C]	3000	3335	3990
Hardness [GPa] at 20°C	0.4	9.5	13.0
Tensile strength [MPa] at 20°C	200-1000	230-275	80-240
Resistivity [$\mu\Omega - m$] at 1730-2230 °C	0.79-0.95	-	1.2-1.5
Thermal conductivity [W/m-K] at 1730-2230 °C	80-84	-	37-39

Tantalum, in the presence of carbon, an element present on most ISAC composite targets (Section 1.2), starts forming tantalum carbides at 1300 °C under vacuum [81]. The formation of tantalum carbides embrittles the tantalum oven and impairs its performance as a crucible, diminishing the temperature dependant isotope release; moreover, it increases the risk of premature target failure. ISAC composite targets consist of a high-porosity target-material layer, often a carbide, deposited on exfoliated graphite foil (Fig. 2.4). In this work, graphite and UC_x targets, both with a high carbon content, have been synthesized, characterized (Chapter 2) and irradiated (Chapter 4).

This chapter presents the physical mechanisms dominating the embrittlement of tantalum. Moreover, this chapter describes the target's carbon sources and strategies to extend the longevity of the target ovens, starting with the one currently used at ISAC, consisting of coating the interior of the target ovens with tantalum carbide (TaC). The chapter also presents a new strategy proposed in this work, consisting of coating the interior of the ovens with metallic rhenium (Re), the Re-coating methodology developed, and the characterization of Re-coated samples.

3.1 Sources of carbon in ISAC targets

The interior of tantalum ovens that are used for irradiating ISAC composite targets is coated beforehand with tantalum carbide (Appendix A.4). This coating is applied to prevent the carbon penetration through the tantalum-oven bulk. Nevertheless, tantalum embrittlement is often observed during inspection after irradiation (Fig. 3.1).

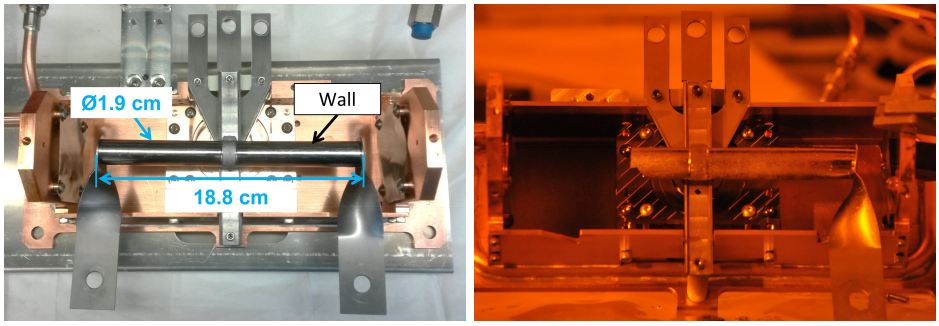

(a) Pristine target oven. **(b)** Fractured target oven.

Figure 3.1: Appearance of targets before and after irradiation. Before irradiation (a), the target ovens welds and electrical resistivity state are checked. After irradiation, the targets are transferred to a hot cell where the ovens are inspected remotely. Some target ovens fracture during operation or inspection (b).

If a tantalum oven is turning into TaC and Ta_2C, changes in the oven's electrical resistance are expected because TaC and Ta_2C have different thermal, electrical and mechanical properties with respect to tantalum (Table 3.1). The formation of tantalum carbides is not imperative to observe changes in the ovens' properties, carbon accumulation in the grain boundaries of the tantalum could lead to embrittlement. Also, Hörz et al. reported that increasing the carbon concentration dissolved in tantalum reduces linearly the electrical resistivity of the metal [82]; this is because impurities in a crystal structure like tantalum, scatter the conduction electrons [83]. Thus, even if tantalum carbides are not formed in the oven bulk, dissolved carbon would change the resistivity and consequently the temperature of the ovens during irradiation.

Signs of embrittlement are observed in post-irradiation inspections of tantalum ovens used for targets routinely operated below 2000 °C like SiC and ZrC (1650 °C and 1850 °C

respectively) (Fig. 3.1). Since tantalum carbides are formed directly when tantalum and carbon are heated together under vacuum around 1300°C and 1500°C [81], the ovens' embrittlement is most likely because of tantalum carbide (TaC and Ta_2C) formation through the bulk of the tantalum walls. The carbon sources of these targets are their backing graphite-foils, and the carbon stoichiometry contribution in SiC and ZrC. The target ovens used with the SiC and ZrC targets are TaC coated but present signs of embrittlement after irradiation, suggesting carbon diffusion through the oven's TaC coating.

The graphite target developed in this work consists of ≈450 D-shaped composite discs (Section 2.4). As with all the ISAC targets, the graphite composite discs are loaded in a tantalum oven with its interior wall previously coated with TaC (Appendix A.4), and they are enclosed in the oven by sealing the sides with tantalum caps to limit the isotopes leakage anywhere but into the ion source (Fig. 2.26a). The tantalum caps are also coated with TaC (Fig. 3.2b).

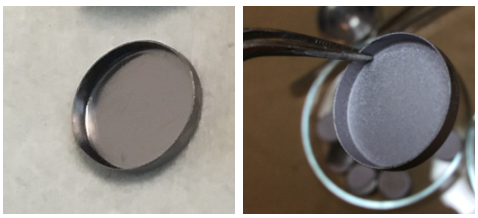

(a) Pristine cap. **(b)** TaC coated cap.

Figure 3.2: Tantalum caps (a) are TaC coated (b) to be used for sealing target material in an oven for use online. The coating on the cap looks identical to the one in the target ovens. Instead of a coated tantalum tube, a coated cap is presented because the cap displays the coating clearer than the inside of a tube.

Except for their chord, the D-shaped graphite-composite discs are in contact with the coated tantalum tube through the area that encompasses their perimeter (Fig. 3.3). Altogether the 450 discs occupy a ≈15 cm length (Fig. 3.3). The graphite composite target is operated at ≈2000 °C to enhance isotope release; therefore, due to sourced carbon from the target material diffusing through the TaC coating, the tantalum oven containing this target is expected to become brittle during operation.

The carbon content of the UC_x targets developed in this work comes from its graphite excess, graphite foil, the stoichiometry contribution in UC_x, and its graphite container (Section 2.3.2). In contrast to the graphite-composite target, the UC_x discs are inserted beforehand in a graphite container, so the UC_x discs are not in direct contact with the TaC-coated oven.

Even though the graphite containers are only in contact with the centre of the oven (Fig. 3.4), indications of the carbon penetration through the rest of the oven wall are observed after operating at ≈2000 °C (Fig. 3.10). Carbon reaches the rest of the oven because its sublimating temperature is around 2000 °C at the ISAC operational pressure of 1×10^{-6} Torr

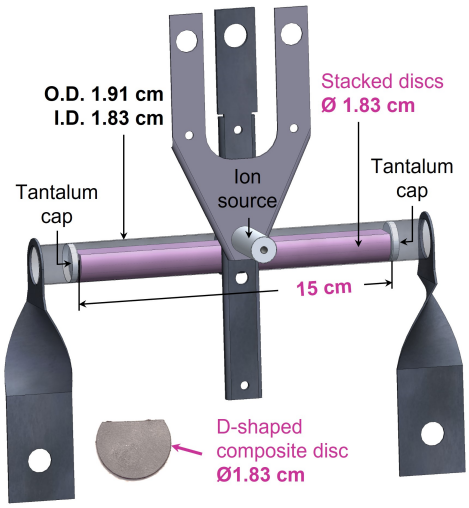

Figure 3.3: CAD model of composite discs in oven. The D-shaped composite discs are stacked and centred in the oven. The pink face represents the area of the target composite that is in contact with the oven.

(1×10^{-3} Pa) (Fig. 3.5) [48, 47]. According to isotope release experiments (Section 4.1), pellets made with the same graphite grade as the graphite containers have poor isotope release performance. Therefore, no isotopes are expected to diffuse through the graphite container, so the pressure in the space between the graphite container and the tantalum oven is most likely around 1×10^{-6} Torr.

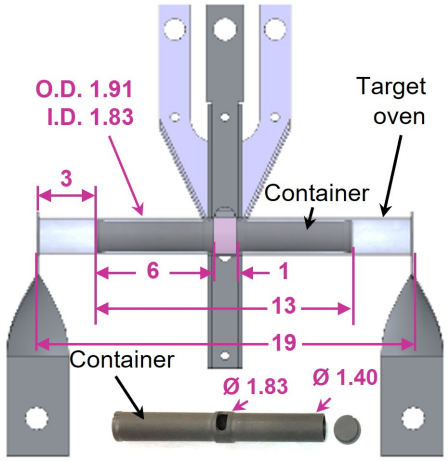

Figure 3.4: CAD model of target oven used in ISAC (all units are in cm). The cartridge is only in contact with the oven through its central belt highlighted in pink.

Two strategies could be followed when irradiating the ISAC targets. The first strategy is to operate them below 1300°C, with the consequence of limited isotope release. The second strategy is to operate the targets at high temperature despite carbon penetration in the tantalum oven, but abiding by the eventual changes in the electrical conductivity of

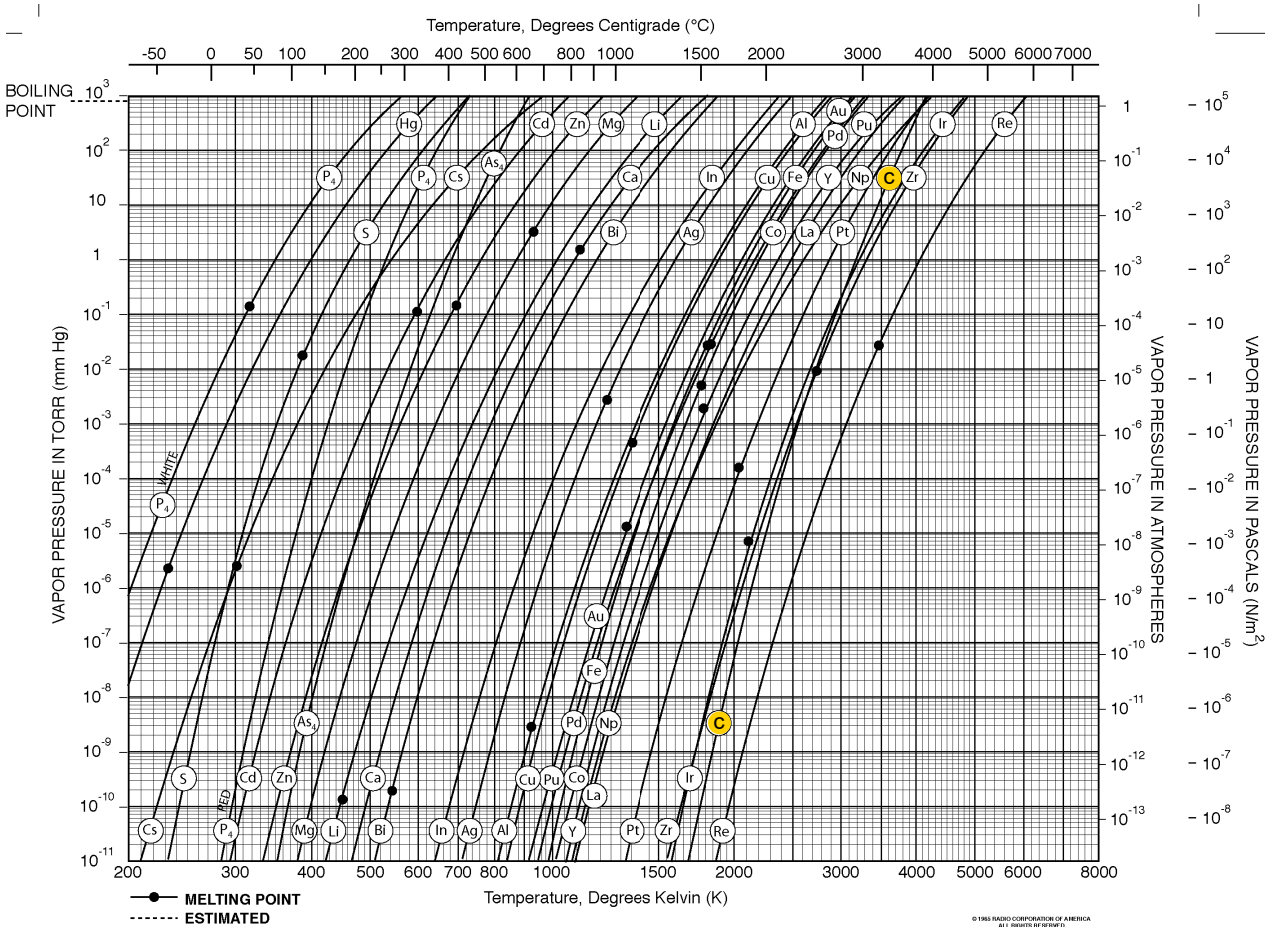

Figure 3.5: Vapour pressure of various elements at different temperature [47]. The curve corresponding to carbon is tagged in yellow. According to the diagram, carbon starts sublimating when heated at 2000° C under vacuum at the ISAC operational pressure of 10^{-6} Torr ($\sim 10^{-3}$ Pa) [48].

the oven that impairs the control over the target temperature, and consequently the RIB decline. At ISAC, the targets are operated at high temperature with the consequence of limiting the offered RIB to three weeks per composite-target. To operate the target with a more stable temperature, and ultimately offer high-intensity RIBs for longer periods, the physical mechanisms responsible for the embrittlement of the target oven are investigated, and a rhenium coating is considered as a diffusing barrier against carbon penetration in this work.

The carbon attack by the graphite container and the graphite foils was proved experimentally to embrittle the tantalum oven. The section below describes two destructive tests performed in full-length simplified ovens (Fig. 3.6a). The interior wall of two ovens was coated with TaC following the procedure in Appendix A.4. A graphite container was loaded in one of the ovens, and graphite foils to the other. Then, the ovens were resistively heated at 2000 °C for one week. The electrical current and voltage were monitored during the test to spot the changes in electrical resistivity due to carbon penetration.

3.1.1 TaC coating investigations on full-length ovens

Two full-length TaC-coated tantalum ovens of simplified geometry (Fig. 3.6a) were submitted to a destructive test. The objective was to assess the changes in electrical resistivity of the ovens during their thermal treatment, and to compare the damage resulting from two different sources of carbon. One oven was loaded with graphite foils, and the other with a graphite container (Fig. 3.6c and 3.6d). Both were resistively heated under vacuum for seven days at 2000 °C. It was expected for the graphite foils to cause greater tantalum embrittlement than the graphite container because, as all the ISAC composites, the graphite foils were pressed against the tube, hence the carbon did not need to sublimate to reach the oven; however, the results were similar even though the graphite container only touched the oven in two points, and it had to sublimate to attack the rest of the oven. Since these containers were filled only with carbon and not with target composites, these tests do not consider chemical reactions that the target material or the nuclear reaction products might have with the tantalum oven during online irradiation.

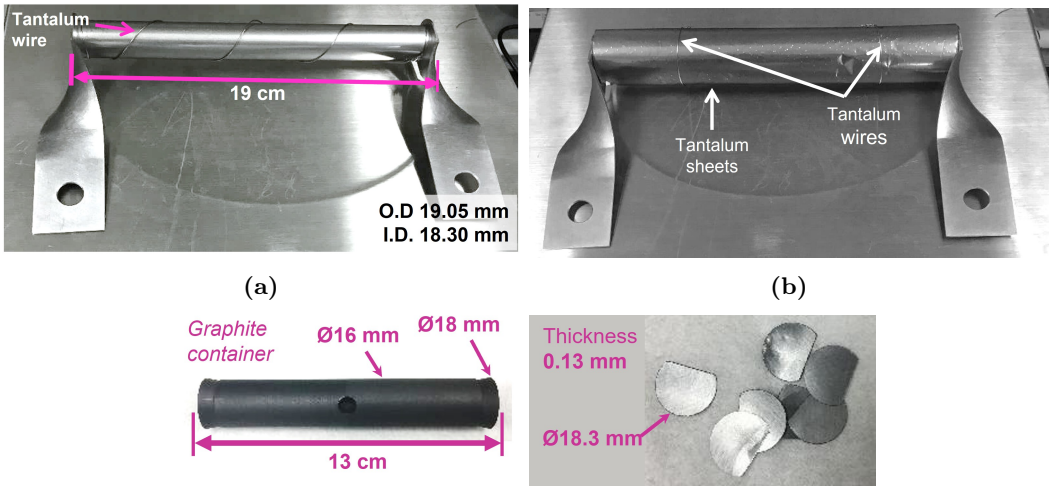

Figure 3.6: Simplified tantalum oven loaded with a graphite container or ≈600 graphite foils and heated for a week at ≈2000 °C. As the target ovens, the testing tubes were TaC coated, and were thermally treated with heat shields on.

Simplified ovens were assembled in TRIUMF's machine shop with extruded tantalum tubes. The tubes were vacuum melted extruded unalloyed tantalum of 99.98% purity from Grandview Material Inc. (ASTM B 521 R05200). Their linear dimensions were identical to the target ovens, their outside diameter was 19.05 mm, and their thickness was 0.381 mm. In contrast with the online target ovens that have a centre block with two 9 cm long tubes welded (Fig. 3.4), the simplified ovens were continuous, and had a length of 19 cm (Fig. 3.6); this difference in geometry eased their manufacturing, and reduced their cost.

The electrical power (P) applied to the testing tube was calculated with Eq. 3.1:

$$P = VI - P_{loss}, \tag{3.1}$$

where V and I are the voltage and electrical current registered with EPICS [37] during the test. P_{loss} is the power loss in the actinide, or in the non-actinide furnace supply lines (Fig. 2.3) [84]:

$$P_{loss} = \begin{cases} 6.91 \times 10^{-4} I^2 + 5.61 \times 10^{-3} I & \text{Actinide furnace,} \\ 8.04 \times 10^{-3} I^2 - 3.01 \times 10^{-1} I & \text{Non actinide furnace.} \end{cases} \tag{3.2}$$

The electrical power (Eq. 3.1) was used to calculate the electrical resistance R (Eq. 3.3):

$$R = \frac{P}{I^2}, \tag{3.3}$$

and in turn, the electric resistivity ρ_e of the tantalum tube (Eq. 3.4):

$$\rho_e = R\frac{A}{l}, \tag{3.4}$$

with l and A being the length and the cross-sectional area of the testing tube (0.188 m and 2.63×10^{-4} m^2 respectively). Neither the legs nor the shielding are affected by the carbon, so they are not taken in consideration in the resistivity calculations.

The loaded simplified ovens were resistively heated by increasing the current passing through their legs. The voltage on the other hand was not controlled, but it changed in accordance to the changes in the resistivity of the tantalum caused by carbon penetration during thermal treatment. These variations in voltage caused increments or decrements on the electrical power, and consequently changes in the temperature.

One TaC coated simplified oven was loaded with graphite foils cut from the same exfoliated graphite foil [85] used in all the casting targets (Chapter 2). To recreate the conditions of a tantalum oven loaded with a regular ISAC target, the graphite foil geometry was identical to the one corresponding to the ISAC target composites (Fig. 1.8 and 3.6). The discs were D-shaped and 18.3 mm in diameter; their total mass was 20 g and their occupied length in the testing tube was 8 cm. The heating test was performed in the actinide furnace (Fig. 2.3a). However, this furnace does not have the capabilities to measure temperature, so the testing tube was first heated in the non-actinide furnace (Fig. 2.3b) to determine the current and voltage required to heat it at 2000 °C. The heating process was not completed in the non-actinide furnace because this piece of equipment was booked for target production.

In the actinide furnace, the testing tube was brought to 478 A at 1 A/min, corresponding to a power of 2.46 kW. To reduce the increasing power, after five hours the current was

reduced to 477 A, and consequently the power readjusted from 2.48 kW to 2.46 kW. Five hours later, the power increased to 2.57 kW due to a change in resistance most likely due to absorption of carbon in the tantalum [82]; the current was reduced to 475 A attempting to reduce the temperature rise expected from the power increment. After these two adjustments, the current was not changed anymore; the testing tube was left at 475 A to observe further changes in the power during heating (Fig. 3.7). Seven days later, the current was reduced to 0 A at a rate of 1 A/min.

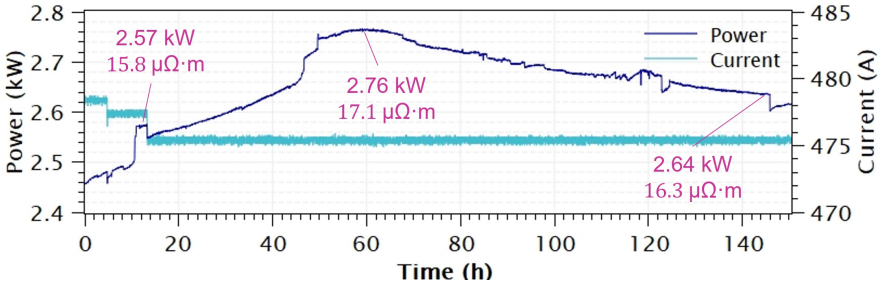

Figure 3.7: Heating test of graphite foils loaded in tantalum testing tube. The system was resistively heated (aiming at 2000 °C) under vacuum. The power reduced accordingly to current reduction, but it also adjusted independently of the current because of the changes in the testing tube resistivity caused by the formation of tantalum carbides.

Table 3.2: Principal changes in the electrical power during the heating test of a tantalum tube loaded with graphite foils. While the current remained constant, the power adjusted according to changes in the resistivity of the tantalum testing tube.

Time (h)	Power (kW)	Resistivity (µΩ ·m)	Current (A)
0	2.46	15.0	478
4.7	2.48	15.2	477
11.0	2.57	15.8	477
13.5	2.55	15.8	475
59.7	2.76	17.1	475
144.5	2.64	16.3	475
149.4	2.62	16.2	475

The resistivity of the tantalum went from 15.0 µΩ·m to a maximum of 17.1 µΩ·m through the thermal treatment. Ultimately, the resistivity reduced to 16.2 µΩ·m (Fig. 3.7). According to Hörz et. al., the dissolution of carbon in tantalum causes a linear increase in the electrical resistivity [82]; on the other hand, carbides precipitating in tantalum decrease its electrical resistivity [86]. Thus, the carbon diffusing in the tantalum bulk most likely caused an increase in the oven's electrical resistivity at the beginning of the thermal treatment, but the formation of TaC and Ta_2C, and their precipitation most likely caused the reduction on the ovens electrical resistivity at the middle of the thermal treatment.

The absolute values of the resistivity estimated with these tests do not match with the literature values corresponding to the TaC and tantalum resistivity. The discrepancy is due

to systematic errors (e.g. resistivity of contacts, and electrical conduction through the foils) (Table 3.1 and 3.2); nevertheless, the relative changes in resistivity of the system give us an indication of the heating effects on the properties of the tantalum tube.

The difference between the initial resistivity and the maximum resistivity after 60 hours at 475 A is 2.1 μΩ·m which represents a 14% increment in resistivity. According to the literature (Table 3.1) [81], depending on the temperature, the TaC electrical resistivity is 52%-58% higher than the corresponding to Ta. Therefore, the 14% increment in resistivity observed in the test suggests that the testing tube did not become TaC in its entirety. This was confirmed by observing the centre of the testing tube where the graphite foils were resting which changed from a silver colour to golden, became brittle, and fractured when removing its heat shields (Fig. 3.8). The ends of the tantalum tube on the other hand, were recrystallized indicating grain growth (but heating at ≤1800 °C induces tantalum grain growth [87]), so the recrystallization of this regions might be partially due to the thermal treatment itself and not only due to carbon penetration.

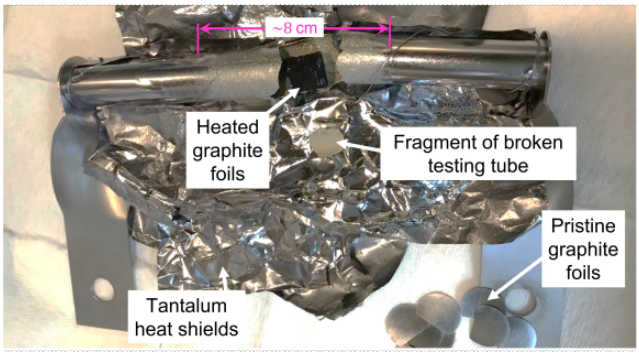

Figure 3.8: TaC precoated testing tube loaded with graphite foils after heating test. The system was heated at ≈2000 °C under vacuum for a week. Tantalum carbide formed over the area where the graphite foils rested. The affected zone was brittle and fractured while removing the heat shields; also, its appearance changed from shiny and silvery to dull and golden.

Another simplified oven, also TaC coated, was loaded with an empty graphite container (Fig. 3.6c). As the graphite containers used for the UC_x targets, the one used in these experiments had an average particle size of 10 μm, a density of 1.83 g/cm^3, and a thermal conductivity of 105 W/m-K (Sigrafine R7510 [88]). To make the sublimated graphite the main source of carbon for this test, the geometry of the graphite container used in this experiment differed from the one corresponding to the online graphite containers; the one used for this experiment had two small points of contact with the tantalum oven instead of a large one in the centre (Fig. 2.23). The graphite container consisted of a cylindrical body and two identical conical plugs (Fig. 3.6c). The hollow cylindrical body was 12 cm long, and its outside and interior diameters were 16 mm and 14 mm respectively. The larger diameter of the conical plugs was 1.8 cm. Assembled, the graphite container was 13 cm long and weighed ≈18 g.

The simplified oven loaded with a graphite container was heated in the non-actinide furnace, so it was feasible to monitor the temperature. In contrast with the graphite foils' test, the electrical current of this test was reduced during the thermal treatment to keep the temperature at 2000 °C.

The cartridge heating started by increasing the current at 1 A/min to reach 2000 °C. The corresponding current and power were 500 A and 2.4 kW respectively. After 18 min at those conditions, the power and temperature reduced to 2.2 kW and 1959 °C respectively, so the current was increased to 510 A. After two hours at 510 A, the temperature had increased to 2010 °C; thus, the current was reduced to return the temperature to 2000 °C. Nevertheless, ten hours later the temperature had increased to 2012 °C, so the current was reduced again. The power stayed stable at 2.34 kW for around 14 hours, but then increased to 2.58 kW. After that increment, the power stayed stable at 2.40 kW for ten hours until it rose to 2.58 kW corresponding to 2055 °C. The current was reduced and the power decreased to 2.30 kW, but after 14 hours the power had increased to 2.55 kW corresponding to 2030 °C, so the current was reduced, and the power and temperature stabilized to 2.32 kW and 2030 °C respectively.

After that last current reduction, the testing tube was kept at 466 A for the rest of the heating test. Approximately two hours after reducing the current, the power reduced to 2.2 kW, but it increased to 2.3 kW three hours later. The power kept oscillating around 2.3 kW and 2.4 kW for 8 hours; during that period, the temperature stayed around 2012±5 °C. Again, these changes in resistivity are most likely caused by the carbon penetration, forming TaC and Ta_2C in the tantalum.

The power and resistivity of the testing tube loaded with the cartridge were calculated taking in consideration the power loss in the non-actinide furnace (Eq. 3.2). The resistivity at the beginning of the heating test was 13.4 μΩ·m, and the maximum resistivity was 15.4 μΩ·m. This represents a change of 15%, close to the graphite foils test result of 14%.

Table 3.3: Principal changes in the electrical power during the heating test of graphite container. The power adjusted according to changes in the resistivity of the tantalum testing tube, and due to changes in the current that we implemented to keep the tube temperature at ≈2000 °C.

Time (h)	**Power** (kW)	**Resistivity** (μΩ·m)	**Current** (A)	**Temperature** (°C)
0.6	2.40	13.4	500	2000
4.3	2.50	13.5	507	2010
46.2	2.58	14.2	503	2055
59.7	2.55	15.3	484	2030
109.4	2.40	15.4	466	2012

Even when the temperature and electrical power were continuously adjusted, the tantalum tube loaded with a cartridge cracked while removing its heat shields (Fig. 3.10). Identical to the tantalum tube loaded with graphite foils, the tantalum tube was golden in

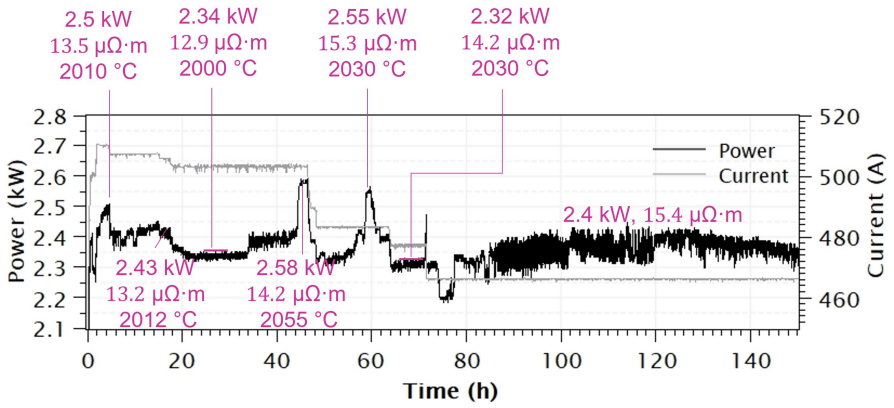

Figure 3.9: Heating test of graphite container loaded in tantalum testing tube. The system was resistively heated under vacuum at ≈2000 °C. The power adjusted in accordance to the changes in the testing tube resistivity caused by the formation of tantalum carbides. We adjusted the current during the test to keep the temperature of the tube around 2000 °C.

the area occupied by the graphite cartridge despite that there was no mechanical contact between the graphite container body and the tantalum tube. This suggests that for both, the graphite container and the graphite foils, sublimated carbon dominates the TaC formation.

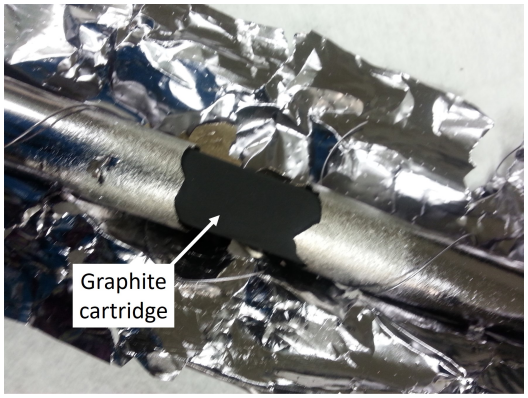

Figure 3.10: TaC-coated testing tube loaded with graphite container after heating test. The system was heated under vacuum at around 2000 °C for a week. Tantalum carbide formed on the centre of the testing tube even though the graphite container body was not in contact with the affected zone; this suggests that sublimated carbon reacted with the tantalum. The affected zone fractured while removing the heat shields.

These bench top experiments demonstrate that sublimated carbon from an empty graphite container or graphite foils attacks the TaC-coated tantalum oven and changes its resistivity when heated at ∼2000 °C. Furthermore, these experiments demonstrate that the temperature of the targets will change during irradiation as the carbon from the targets, whether graphite foils or graphite container, will penetrate the tantalum, and it will happen even if the ovens are TaC coated.

The maximum change on resistivity of 15% would be very challenging to detect and control during target irradiation given all the other conditions that affect the target oven

during irradiation (e.g. proton beam, chemical reactions between target material and oven, constant changes in current to regulate target temperature and promote isotope release). Moreover, from the tests, it was observed that the tantalum embrittles even when the electrical power is adjusted to keep the target around 2000 °C. Rather than attempting to keep the target temperature below this range, investigating the mechanisms of embrittlement, and improving the diffusion barrier against carbon is the required approach to extended the longevity of the target ovens at temperatures above or equal to 2000 °C.

3.2 Physical mechanisms of embrittlement

The atoms in metals are periodically positioned in lattices that are arranged in crystal structures (Fig. 3.11a) [89]. Generally, metals are polycrystalline, such that they are conformed by many crystals with different orientations also called grains (Fig. 3.11b); the transition regions between them are grain boundaries (Fig. 3.11c) [90].

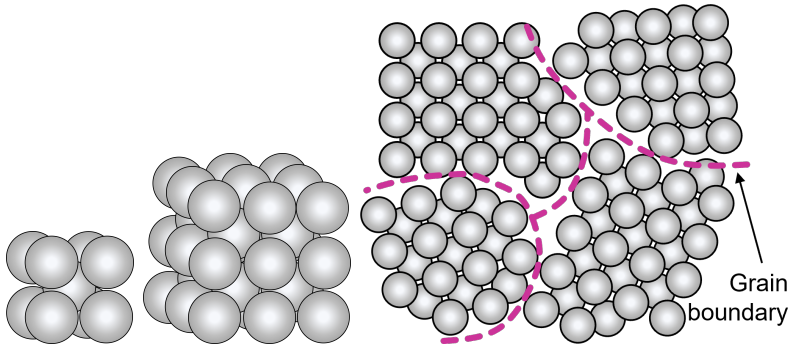

(a) Lattice. **(b)** Grain. **(c)** Grain boundaries.

Figure 3.11: Atoms in a metal are positioned in lattices (a) that are arranged in an orderly manner forming grains (b). Often, solid metals are conformed by many grains in different orientations; the transition regions among grains are grain boundaries (c).

Grain boundaries are high diffusivity paths [91]. They have higher free energy in comparison to the crystal bulk; to reduce this energy, the grain boundary interact with crystal defects that can lead to the accumulation of foreigner atoms in this region [90]. A possible mechanism for the embrittlement of tantalum is the reduction of cohesion along grain boundaries that leads to intergranular fracture. This mechanism can be caused by segregation of foreigner atoms like carbon, or by the distribution of second-phase particles like TaC (cubic) or Ta_2C (trigonal or hexagonal) [9] at grain boundaries [92] in tantalum (body centred cubic) [81].

Grain boundary failure is promoted in metals with large grains because the given impurities distribute over a small boundary area per unit volume. Thus, small-grain tantalum is preferable for the ISAC ovens. The size and shape of the grains conforming a pristine metal depend on its forming. On this work, extrusion and cold rolling were investigated.

During extrusion, metals are heated above their recrystallization temperature to promote their ductility, allowing their compression through a die. When heating a metal at its recrystallization temperature, grains with new phases are produced due to the elimination of dislocations in the metal's crystal structure [93]. The tantalum's recrystallization temperature goes from 800 °C to 1200 °C depending on its purity and deformation [94]. Metals are usually formed below recrystallization temperature to increase their hardness by plastically deforming and reducing the metal's grain shape and size. However, since extrusion is conventionally performed above the metal's recrystallization temperature, some grains return to the state they had before forming [40, 95]. Conventionally, the ISAC target ovens are made of vacuum-annealed extruded tantalum because of the manufacturing reliability and competitive cost.

Cold rolling consists of squeezing a metal between opposing rolls [40]. This forming technique is performed below recrystallization temperature so it delivers smaller grains; their final shape depends on the initial form of the metal (e.g. powder, ingot) and the annealing process that is performed after rolling. The cold-rolled tubes used in this work were manufactured with tantalum powder in order to obtain small grains, such that the tubes had a larger grain boundary network to reduce the proneness of the oven to grain-boundary failure.

Beside moving between grain boundaries, foreigner atoms can also diffuse through the grains by two main mechanisms that are self-diffusion and interstitial-diffusion. Mediated by the movement of vacancies in the lattice, self-diffusion is the fundamental diffusion process of metal atoms in metals. However, small atoms like carbon diffuse much faster than the diffusion of lattice atoms [96]. Interstitial atoms only need their thermal energy to match the activation energy for jumping freely between interstitial sites in the lattice [97].

A coating can act as a diffusion barrier to avoid carbon penetration, or to retard the carbon reaching the tantalum of the target ovens. As of 2002, the interior of the target ovens have been coated with TaC. The objective back then was to avoid gallium isotopes to form tantalum gallide with the oven, and to prevent the ZrC (target material) reacting with the tantalum oven [98]. Even though no studies were done to confirm the effectiveness of the TaC coating as a barrier between the target material and the oven, its performance proved to be useful anecdotally, so coating the interior of the target ovens with TaC (Section A.4) was established as part of the preparation for all target materials [99].

Currently, the purpose of the TaC layer that covers the interior wall of the ISAC ovens is to prevent the carbon from the targets to penetrate the oven's tantalum bulk. However, instead of acting as a diffusion barrier, the TaC coating could act as a carbon source. According to Cotton's experiments [100], during the annealing of a TaC-coated tantalum crucible at 1600 °C, the carbon in the TaC diffuses by vacancies' movement, forming a Ta_2C layer underneath the TaC coating; the Ta_2C layer keeps feeding on carbon until the TaC layer depletes.

The Ta_2C layer growth coefficient (k_{Ta_2C}) reported in [100] is 63.25×10^3 µm^2·h^{-1}. The Ta_2C layer thickness (w_{Ta_2C}) is predicted with Eq. 3.5 [101]

$$w_{Ta_2C} = \sqrt{k_{Ta_2C}}\sqrt{t_a}, \tag{3.5}$$

where t_a is the annealing duration. Assuming a TaC-coated tantalum sample is annealed at 1600 °C, a 2 mm-thick Ta_2C layer would form in the sample within three days given that the carbon in the TaC layer does not deplete first. Under these circumstances, the whole cross section of an ISAC oven (0.38 mm-thick) would turn into Ta_2C, lose its ductility and the oven would become fragile. The TaC coating of the ISAC ovens might not be thick enough to have sufficient carbon to form a Ta_2C layer thicker than 0.38 mm; however, the target materials are carbon sources that could feed the tantalum surface, avoiding the TaC layer depletion, and consequently enlarging a Ta_2C layer in the tantalum bulk.

In this work, rhenium was considered and tested as a diffusion barrier. Rhenium is a good candidate to act as a diffusion barrier because it has high melting point (3180±25°C), and as tantalum, it does not react with most elements [81]. Moreover, it only forms carbides at ultra-high pressures (6-18 GPa) [81, 102], and the carbon diffusion coefficient in rhenium is very small (Table. 3.4). Furthermore, even though it has been found that rhenium forms an interdiffusion layer with tantalum when heating a Re-coated tantalum sample (1900 °C) [103], an interdiffusion region of only 18 µm thickness is expected after seven days of annealing a Re-coated sample at 1900 °C. The growth coefficient of the interdiffusion layer is 1.2×10^2 µm·h^{-1} [103], and the Re-Ta interdiffusion layer forms in Re-coated tantalum samples when heated at 1900 °C in agreement with Eq. 3.6 [103]

$$w_{Re} = \sqrt[3.4]{k_{Re}t_a}, \tag{3.6}$$

where w_{Re} is the interdiffusion-layer thickness, k_{Re} is the interdiffusion-layer growth coefficient (1.2×10^2 µm·h^{-1}) and t_a is the annealing time.

The efficiency of the TaC and rhenium coating was analytically evaluated. The barriers were considered as regions of pure TaC or Re with no grain boundaries. The assumption is that the carbon diffuses through the barriers in a steady state regimen. For simplicity, instead of analyzing the coated target oven as a hollow thin cylinder, a small section of it was considered (Fig. 3.12). By analyzing a small piece, the coating can be described as a flat volume. Assuming that the diffusion flux J of carbon through the coating is unidirectional and constant over time, the carbon diffusion is described with Fick's first law:

$$J = -D\frac{\partial C}{\partial x}, \tag{3.7}$$

where D is the diffusion coefficient, and C is the concentration through x; the minus sign indicates that the diffusion flux goes from high to low concentration.

The diffusion coefficient D is given by

$$D = D_0 \exp\left(-\frac{Q_d}{RT}\right). \tag{3.8}$$

In Eq. 3.8, D_0 is a temperature independent preexponential, Q_d is the activation energy for diffusion, R is the gas constant (8.31 J/mol-K), and T is the temperature. The diffusion coefficient of carbon diffusing at 2000 °C (2273 K) in tantalum, TaC, and rhenium, was obtained by considering the D_0 and Q_d values of carbon diffusing in tantalum, TaC, and rhenium found in the literature (Table 3.4).

Assuming a linear concentration in a thin sheet, Eq. 3.7 can be expressed as:

$$J = -D\frac{C_1 - C_2}{x_1 - x_2}, \tag{3.9}$$

where C_1 is the initial carbon concentration, C_2 is the concentration at the border between the coating and the tantalum, and $x_2 - x_1$ is the coating thickness.

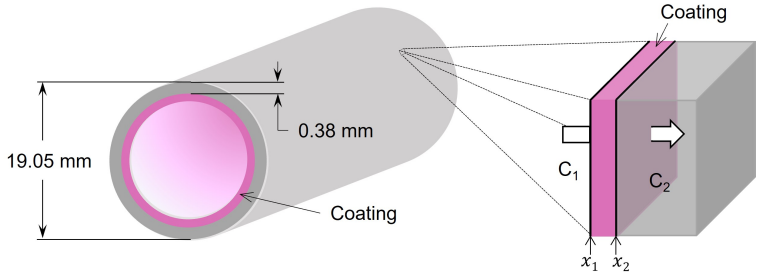

Figure 3.12: Small section of a tantalum coated tube, depicting coating in pink. Carbon diffuses uniformly and radially from the axial centre of the tube, of an initial concentration C_1, towards C_2, where C_2 is zero at $t = 0$; the carbon flux goes from left to right as the white arrow indicates.

In comparison with tantalum and TaC, rhenium would be the best option for inhibiting carbon penetration. Eq. 3.9 was evaluated to estimate a carbon diffusion flux through each coating option. The carbon concentration in the tantalum bulk (C_2) was assumed 0 g/cm^3. The initial carbon concentration, $C_1 = 1.3$ g/cm^3, was calculated dividing the mass of the graphite container (≈17 g), that was assumed as the total carbon mass available to sublimate and diffuse through the tantalum tube, over the volume between the graphite container and the oven (≈13 cm^3).

Comparing a tantalum, TaC, and rhenium coating of the same thickness (1 µm), for the same carbon concentration difference of 1.3 g/cm^3, and evaluating Eq. 3.9 with the respective diffusion coefficient (D) for each coating (Table 3.4), tantalum would allow the largest rate of carbon transfer. Following tantalum would be TaC and finally rhenium, the latter being the material with the lowest diffusion coefficient for carbon (Table 3.4) [101, 104]. Based on these diffusion fluxes, a TaC coating delays the carbon penetration through the tantalum

Table 3.4: Diffusion coefficient D and diffusion flux J of carbon in Ta, TaC, and Re at 2000 °C. The diffusion coefficients were estimated for 2000 °C, using the respective D_0 and Q_d. The diffusion flux corresponds to a coating 1 µm-thick, and a carbon concentration difference of 1.3 g/cm^3.

Material	D_o **(m²/s)**	Q_d **(m²/s)**	D **(m²/s)**	J **(mg/cm²·s)**
Ta	1.94×10^{-6} [101]	0.32×10^{6} [101]	5.6×10^{-11}	7.3
TaC	1.94×10^{-6} [101]	0.20×10^{6} [101]	6.6×10^{-14}	8.6×10^{-3}
Re	6.50×10^{-17} [104]	0.18×10^{6} [104]	5.8×10^{-21}	7.5×10^{-10}

bulk and it should act as a diffusion barrier, but this approach does not take in consideration the potential contribution of carbon from the TaC coating layer nor imperfections on it.

Currently the target ovens are made of commercially available extruded-tantalum of competitive cost and reliable purity. In this work, extruded tantalum has been compared with cold-rolled tantalum since cold-rolling is expected to grant a higher resistance against carbon penetration due to its small grain size and larger grain-boundary density. Section 3.4 shows the micromorphology characterization of extruded and cold-rolled tantalum in pristine state, as well as after annealing for three days at 2000 °C with and without carbon. In addition, cold-rolled and extruded tantalum samples were TaC-coated and thermally treated with and without carbon; the characterization of the samples is presented in Section 3.5. Furthermore, in this work rhenium is proposed as a new coating material, and the developed coating methodology is described in Section 3.6. Samples of both, extruded and cold-rolled tantalum were Re-coated, and heated with and without carbon. The characterization of the Re-coated samples is compiled in Sections 3.6.1 and 3.6.2

3.3 Strategies for inhibiting carbon diffusion

Samples of ≈1 cm×2 cm were cut from extruded and cold-rolled tantalum tubes that were either uncoated, TaC coated, or rhenium coated. A ring 1 cm tall was cut from the centre of each tube (Fig. 3.13). Three samples were cut from each ring, one was kept pristine, another was heated at 2000 °C for three days, and the last sample was also heated at 2000 °C for three days, but in presence of carbon. The microstructure of the samples and their respective coatings were analyzed with Secondary Electron Microscopy (SEM), and their composition was investigated with Energy Dispersive X-ray Spectroscopy (EDS).

The samples of the coated tubes were heated under vacuum at 2000 °C for three days to assess the durability of the coatings when operating at high temperature. The batch of tantalum samples that were either uncoated, TaC coated, or rhenium coated received the same thermal treatment, but in presence of carbon. They were bundled in pairs with a graphite wedge of 4.6 g±0.1 g (Fig. 3.14b). Afterwards, their carbon content was investigated with EDS; furthermore, the microstructure of the coatings as well as the tantalum cross section were observed with SEM. The micrographs of the coatings were compared with

those of pristine samples and with the ones corresponding to samples that were not heated in presence of carbon.

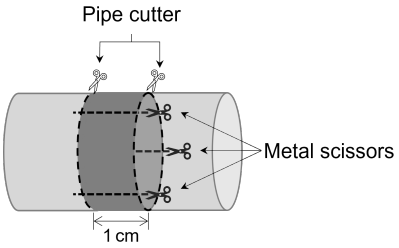

Figure 3.13: Three samples were cut from the centre of a tantalum tube. Each of them was ≈1 cm×2 cm. The circumference of the sample was cut with a pipe cutter and the resulting ring was sectioned in three parts with metal scissors.

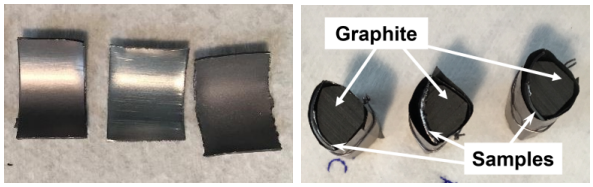

(a) **(b)**

Figure 3.14: Samples designated for thermal treatment. (a) Samples reserved for heating, from left to right: uncoated rolled tantalum, rhenium-coated extruded tantalum, and TaC-coated rolled tantalum. (b) Tantalum sample bundles, each bundle consists of two samples and a graphite wedge wrapped with Ta foil.

The tantalum samples were resistively heated simultaneously at ≈2012 °C. The current was increased from 0 A to 502 A at a rate of 5 A/min. After three days of heating, the current was reduce to 0 A at the same rate. During their thermal treatment, all the samples were contained in an uncoated tantalum tube to avoid introducing additional carbon; they were separated and sealed in three groups within the tube with tantalum caps. Those bundled with graphite were grouped together. With the intention of preventing the unlikely introduction of carbon from the TaC to the carbon-free samples, the TaC coated samples that were heated without graphite were grouped separately from the uncoated and rhenium coated tantalum samples.

The bundled samples were weighed before and after thermal treatment (Table 3.5). All the samples had a larger mass after thermal treatment, suggesting carbon penetration. In agreement with the larger carbon penetration expected, the samples without a coating had a larger mass difference in comparison to the rhenium and TaC coated ones. The mass increment of the extruded samples was larger in comparison to that of their analogous rolled samples, suggesting that the extruded samples retained more carbon. For both, the extruded and rolled samples, the before and after thermal treatment mass-difference was larger for Re-coated samples than for TaC-coated ones, implying that the TaC coating

was more effective preventing the carbon penetration which is unexpected since the carbon diffusion flux in rhenium is slower than in TaC (Table 3.4). Thus, the rhenium coating might have been too thin, or might have only partially covered the surface, allowing carbon penetration. Note however, that the mass difference is small and that the results in Table 3.5 do not discern between possible mass changes due to the samples' outgassing, the coatings' outgassing, or tantalum diffused from the wrapping foil to the samples. The samples were characterized with SEM and EDS to assess the changes in micromorphology caused by the thermal treatment (Sections 3.4, 3.5.1, 3.6.2 and 3.6.1).

Table 3.5: Mass of samples before and after heating under vacuum in contact with graphite. A 0.5×10^{-3} g error is associated to all the mass values.

	Mass (g)		
Tantalum sample	Before heating	After heating	Difference (1×10^{-3})
Extruded uncoated	1.5492	1.5543	5.1
Extruded TaC coated	1.6350	1.6376	2.6
Extruded Re coated	1.6819	1.6848	2.9
Rolled uncoated	1.5944	1.5989	4.5
Rolled TaC coated	1.6276	1.6288	1.2
Rolled Re coated	1.4648	1.4669	2.1

Two specimens of ≈5 mm×7 mm were cut with metal scissors from the centre of each sample. One of the specimens of each pair was meant for the analysis of its surface, and the other specimen was intended for the analysis of the samples' cross section. The samples were examined with SEM to observe their micromorphology, and Re-coated specimens were analyzed with EDS to characterize the composition of their coating.

Since all the samples were cut with metal scissors, their cross sections were sheared. The samples designated for surface analysis did not require further preparations, but the ones assigned to cross-section analyses were polished at the cut to expose a representative cross-section area. Conventionally, specimens are held in resin to obtain a uniform polishing; however, resin contributes to the specimens' carbon signal when investigating with EDS. Thus, instead of resin, our specimens were mounted and polished on stainless steel holders that were designed and machined at TRIUMF (Fig. 3.15). To avoid detecting the carbon signal expected from the stainless steel, the cross-section samples were taller than the depth of the slots, such that they stick out from the holder. The cross section samples were held with set screws in the slots of the holder. All the cross section samples were polished at the same time and under the same conditions seeking for identical height and polishing finish (polishing procedure in Appendix A.3).

The specimens were inserted and analyzed in the SEM using the designed holders. The sets of unpolished surface samples were adhered with carbon tape to the centre of the holder; these samples were laying flat exposing their coated or un-coated surface. On the other hand,

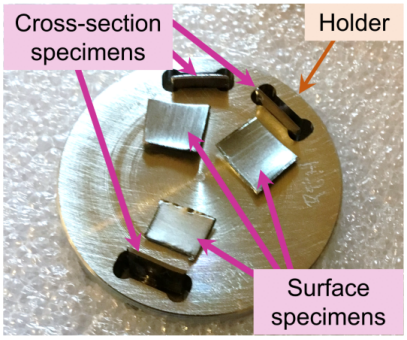

Figure 3.15: Set of tantalum specimens mounted on holder. Closer to the perimeter of the holder are the cross-section specimens; they were polished simultaneously while mounted in the holder to obtain an identical height and polishing finish. These cross-sections were analyzed with SEM to identify their coatings thickness, and with EDS to investigate their coating composition and to assess their carbon concentration when applicable. In the centre are the surface specimens, they were attached with carbon tape to display their coating when applicable; the micro morphology of the surface specimens was observed with SEM, and their chemical composition with EDS.

no carbon tape was required to fix the cross section samples; those were held upwards with a set screw.

The following section presents the characterization of cold-rolled and extruded tantalum samples' micromorphology before and after heating them with and without carbon. All the samples were characterized at the University of Victoria (UVic) with the help of Daniel Hedji from the Physics and Astronomy department. The time available to use the characterization equipment was limited, so it was not possible to analyze all the samples with EDS. Thus, the EDS analyses of cross-section samples heated in presence of carbon were prioritized, as well as the EDS mapping of the Re-coating. Neither the surface of the TaC-coated samples nor the surface of uncoated samples were mapped or scanned; nonetheless, their morphology was analyzed with SEM.

3.4 Pristine tantalum characterization

Seamless tubes of 18.3 mm internal diameter, like the ones used to manufacture ISAC target ovens (Fig. 3.4), are formed by extrusion through a die. In contrast, forming the same tubes by cold rolling is very expensive because relatively small rolls have to be manufactured and set up. Instead, to comply with the requested specifications of the tubes, Eagle Alloys [105] manufactured cold rolled tantalum sheets; then, formed the tubes by curling the sheet to desired radius and welding them. Welding a 0.38 mm thick sheet became, yet another complication for the provider; nevertheless, Eagle Alloys delivered tubes within the specifications of our target ovens, but the welding presented micrometric cracks (Fig. 3.16). This imperfections are undesirable because they could promote crack propagation when heating the tubes, and they could be a path for carbon penetration, as well as isotope losses.

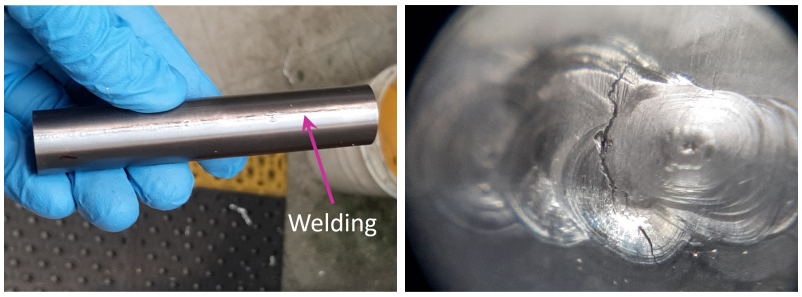

(a) Welded rolled Ta sheet **(b)** Crack in Ta tube welding

Figure 3.16: Cold-rolled tantalum tubes for testing. Cold-rolled tantalum sheets of 0.38 mm thickness were curled to tubes (19.1 mm O.D., 10 cm length) and welded (a); the welding presented microfractures (Mag. 30x) (b).

Samples of extruded and cold-rolled tantalum were thermally treated under vacuum at 2000 °C. The objective of this test was to observe the difference in sintering between the two types of tantalum. Moreover, extruded and cold-rolled samples were also heated to 2000 °C, but in contact with carbon in order to compare the changes in the samples' microstructure due to carbon penetration.

3.4.1 Micromorphology of cold-rolled tantalum

Under SEM at x500 magnification, the pristine sample surface of the rolled tantalum seems to have a rough surface with string like formations in different directions (Fig. 3.17a). These strings are most likely grain boundaries. At high magnification (Fig. 3.17b), junctions and ridges indicate polygonized subgrain structures.

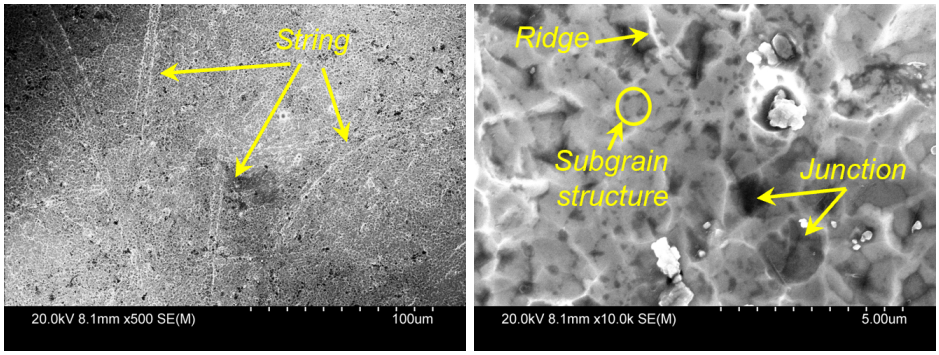

(a) Magnification: x500 **(b)** Magnification: x10k

Figure 3.17: SEM micrographs of pristine cold-rolled tantalum sample. At low magnification, the sample's surface seems rough and shows strings (a); at higher magnification, we observe the sample's subgrain structures forming ridges and junctions.

After heating, the cold-rolled tantalum surface becomes smoother (Fig. 3.18). Since the thermal treatment removes the residual stress of the subgrain-structures, they become grains through a process called recrystallization [93]. If a metal is heated above its recrystallization

temperature, that was most likely the case for the tantalum samples, the metal undergoes grain growth. Since the samples analyzed were not polished nor etched, grains boundaries can not be ascertained in the micrographs of the tantalum samples, so the grain growth can not be quantified. Nevertheless, sinterization is indicated by the reduced number of junctions observed in the tantalum samples heated at 2000 °C, and the development of pores. While the largest junction measured in the pristine specimen has a diameter of 3.7 µm, after heating, the largest pore on the cold-rolled specimen has a diameter of 7.4 µm; this change in morphology occurs because when a metal sinters, some grains grow at the expense of others shrinking [106].

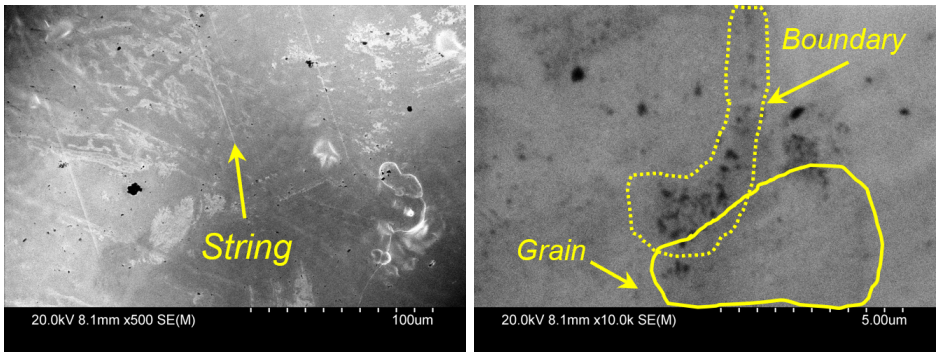

(a) Magnification: x500 **(b)** Magnification: x10k

Figure 3.18: SEM micrographs of cold-rolled tantalum after heating for three days at 2000 °C. String formations are still present, and pores have formed due to grain growth and coarsening.

The surface of the tantalum sample heated in presence of carbon is smoother than the pristine one (Fig. 3.19 and 3.17). As expected, the thermal treatment removed residual stress from the tantalum subgrain structures, increasing the grain size, and smoothing the surface; additionally, the carbon most likely formed a TaC layer on the tantalum's surface. Furthermore, two new patterns are observed, the first one resembles a dendritic structure (Fig. 3.19a), and the second has the shape of the letter Y (Fig. 3.18b), resembling the junctions observed in Fig. 3.17b. The dendritic structures are most likely TaC, Ta_2C, or carbon accumulations through the grain boundaries of the tantalum, causing defects on its lattice. Similarly, the Y formations are most likely grain-boundary junctions that appear bright due to edge charging effect because they are either swollen due to TaC or Ta_2C formation, or cracked because of the accumulation of C within grain boundaries that led to grain-boundary cohesion loss and embrittlement. In comparison with the samples that were heated without graphite, less pores are observed on the specimens' surface corresponding to the sample heated with carbon (unexplored areas might have higher porosity).

The cross-sections of the cold-rolled samples were explored with SEM. The samples' bulk-morphology differs depending on whether the sample is pristine, heated, or heated with carbon (Fig. 3.20). The pristine sample presents more pores than the thermally treated ones;

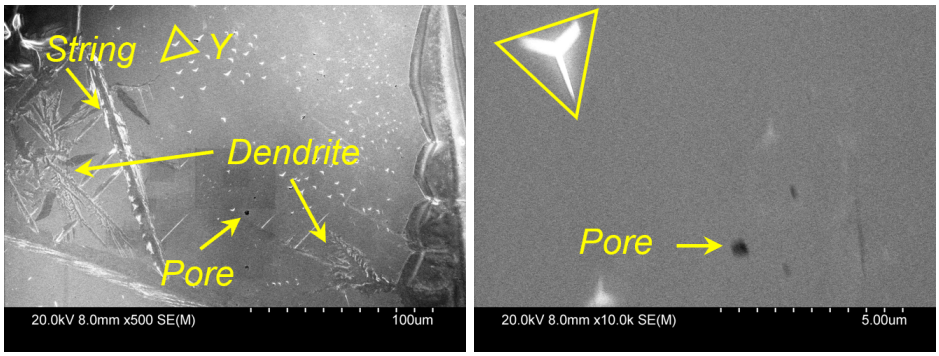

(a) Magnification: x500 **(b)** Magnification: x10k

Figure 3.19: SEM micrographs of cold-rolled tantalum sample after heating for three days at 2000 °C in presence of carbon. Carbon accumulation leads to the *Y* formations, and the swelling and ramification of the original string formations observed in the pristine specimen.

this indicates that the thermal treatment not only promotes superficial sinterization but also bulk sinterization. To determine the depth of carbon penetration, the cross section of the sample heated with carbon was scanned with EDS; however, no carbon was found. Thus, the formation of a TaC coating on the sample surface can not be confirmed; however, the edge corresponding to the surface in contact with the carbon wedge looks swollen (Fig. 3.20c), suggesting changes in morphology due to carbon penetration.

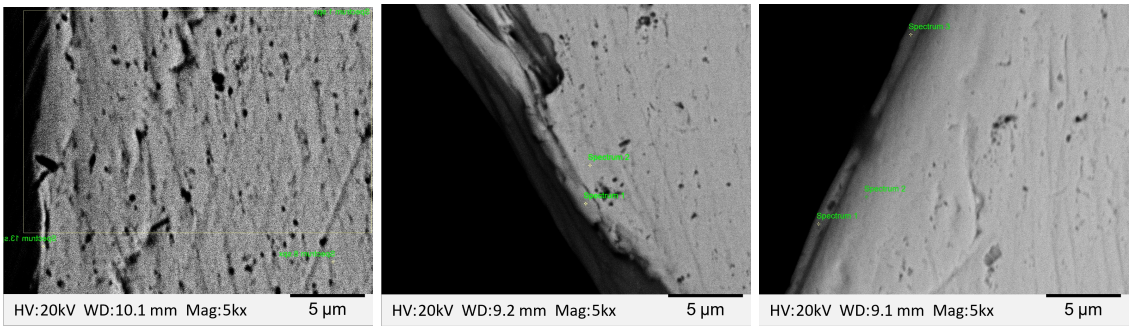

(a) Pristine **(b)** Heated **(c)** Heated with carbon

Figure 3.20: Cross section samples of uncoated cold-rolled tantalum: pristine (a), heated (b), and heated in contact with graphite (c). The thermally treated samples (b) and (c) present less pores than the pristine sample. The left edge of the sample heated in contact with carbon (c) seems more sintered in comparison to the sample heated by itself, suggesting carbon penetration.

3.4.2 Micromorphology of extruded tantalum

As expected, the pristine sample corresponding to extruded tantalum has a preferred orientation (Fig. 3.21a). Even though the grains are not exposed by etching, long boundaries and ridges indicate that the tantalum grains are oriented in elongated formations (Fig. 3.21). Some other boundaries are round, and others are shaped like the letter *L* (Fig. 3.21b).

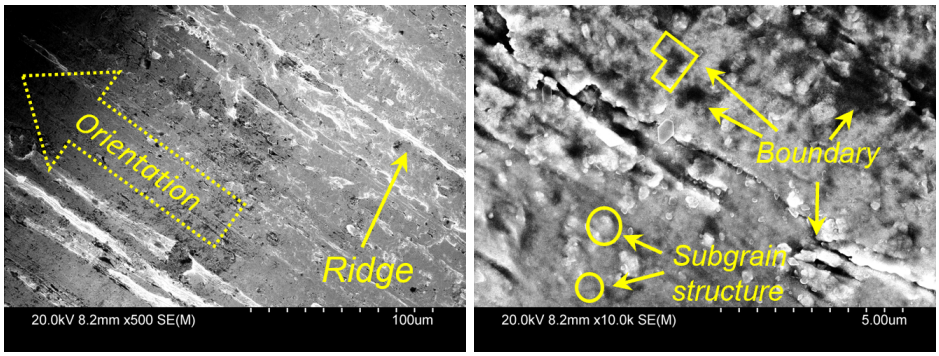

(a) Magnification: x500 **(b)** Magnification: x10k

Figure 3.21: SEM micrograph of pristine extruded tantalum sample. A clear extrusion orientation is observed at both magnifications. At high magnification (b), subgrain structures can be pinpointed, and L shaped boundaries are present.

The orientation of the extruded tantalum remains after heating it at 2000 °C for three days (Fig. 3.22). Compared with the analogous cold-rolled specimens, the extruded ones seem less smooth, suggesting less sinterization (Fig. 3.22a). On the other hand, some pores of the extruded specimen (Fig. 3.22b) appear larger than those of the cold-rolled one, but smaller pores are found on other areas of the sample; By measuring the specimens' pores diameter with Amscope [69], it was found that the pores of the cold-rolled are larger than those of the extruded samples heated at 2000 °C, suggesting that the extruded tantalum might have more densification.

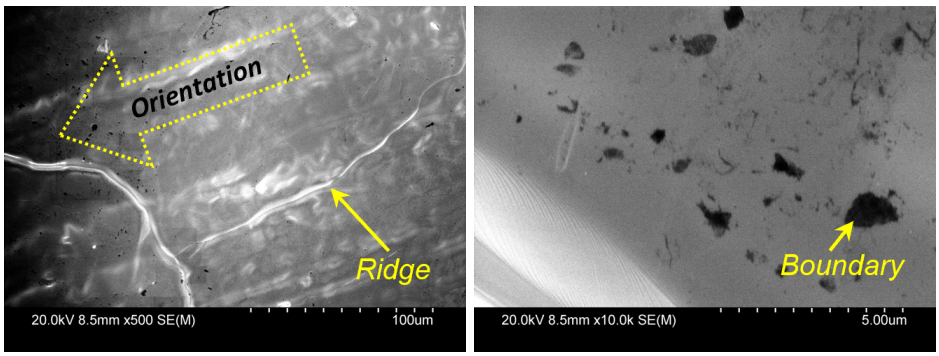

(a) Magnification: x500 **(b)** Magnification: x10k

Figure 3.22: SEM micrograph of extruded tantalum sample heated at 2000 °C. After thermally treating, the extrusion orientation of the tantalum is faded but still visible (a). At high magnification (b), pores can be pinpointed; they are most likely formed due to coarsening.

Although faded, the specimens corresponding to the sample that was heated in presence of carbon still presents orientation (Fig. 3.23). Similarly to the sample heated by itself, the one heated in contact with carbon also has pores. The thermally treated samples differ in that the sample heated in contact with carbon might have a TaC layer on its surface, justifying their morphology differences. The charged formations of the sample heated with

carbon are in the shape of a capital L or needles l (Fig. 3.23), resembling the grain boundaries observed in the pristine extruded samples (Fig. 3.21). The charged formations are most likely accumulation of TaC in the grain boundaries, twin deformations caused by TaC or Ta_2C accumulation, or cracks caused by grain-boundary cohesion loss due to carbon accumulation.

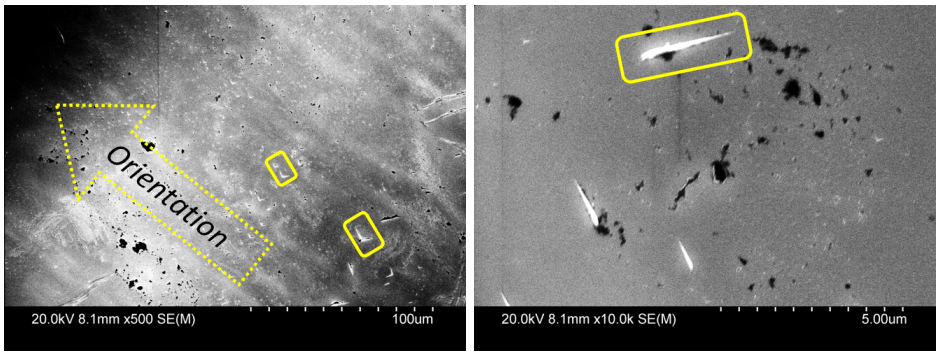

(a) Magnification: x500 **(b)** Magnification: x10k

Figure 3.23: SEM micrographs of extruded tantalum after heating it at 2000 °C in contact with carbon for three days. Although grains are indistinguishable, the extrusion orientation of the tantalum is still visible (a). Charged line formations (b), resembling grain boundaries, suggest loss of grain-boundary cohesion. Pores are also visible at both low (a) and high (b) magnification.

The cross-sections of the extruded samples also have different morphology depending on the sample being pristine, or heated with or without carbon. The heated extruded tantalum samples have less pores than the pristine one, indicating that the tantalum sample sinters not only in the surface but also through the bulk. In comparison with the cold-rolled pristine sample (Fig. 3.20a), the pristine extruded sample has less pores (Fig. 3.24a). In contrast, the amount of pores visible in the thermal treated extruded and cold-rolled samples is similar, suggesting that annealing recrystallizes, sinters, and densifies the tantalum, removing the micromorphology characteristics obtained with the different forming methods.

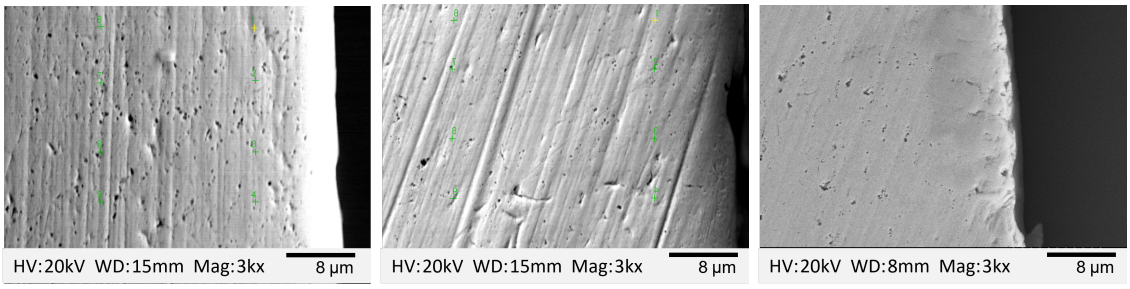

(a) Pristine **(b)** Heated **(c)** Heated with carbon

Figure 3.24: Cross-section samples of uncoated extruded tantalum: pristine, heated, and heated in presence of carbon. The porosity of the samples diminish after heating. The sample heated in presence of carbon shows swelling in the zone that was in contact with carbon (right edge); changes in morphology suggests carbon penetration even though no carbon signal was detected from EDS scanning.

As with the analogous cold-rolled sample, the cross section of the extruded-sample heated with carbon was analyzed with EDS to determine the depth of carbon penetration. No carbon was detected in the scans, so it was not possible to confirm that a TaC coating formed on the sample's surface, but the edge corresponding to the surface in contact with the carbon wedge looks swollen (Fig. 3.24), suggesting changes in morphology due to carbon penetration.

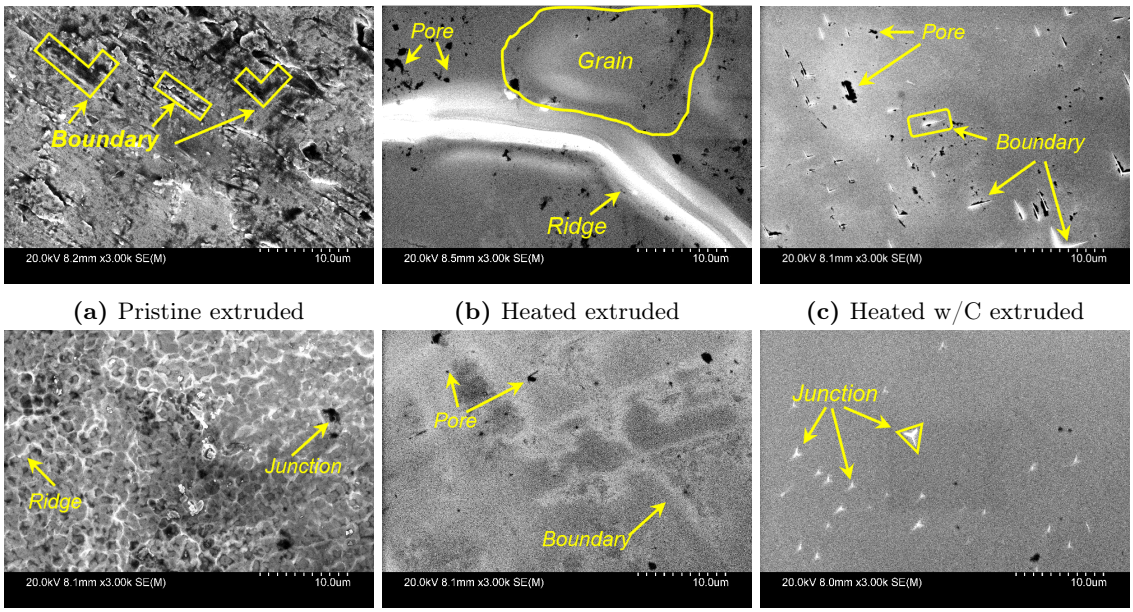

(a) Pristine extruded **(b)** Heated extruded **(c)** Heated w/C extruded

(d) Pristine cold-rolled **(e)** Heated cold-rolled **(f)** Heated w/C cold-rolled

Figure 3.25: Sintering and grain growth alter the microstructure of both cold-rolled and extruded tantalum after heating at 2000 °C. Charged formations in both samples, suggest carbon penetration after heating in presence of this element. The rectangular zone in the heated with carbon samples is contamination, this phenomena is attributed to the deposit of foreign material on the analyzed sample due to the SEM electron bombardment [41].

During heating, the grains of the cold-rolled and extruded tantalum recrystallized and grew. The thermal treatment caused the surface micromorphology of both cold-rolled and extruded samples to fade (Fig. 3.25b and 3.25e), and pores in the cross section to vanish (Fig. 3.20b and 3.24b). The extruded and cold-rolled samples changed their morphology during heating due to residual stress removal from subgrain structures. Grain growth reduces the grain boundary density, making the material harder, and potentially brittle. The extruded-sample retained its orientation (Fig. 3.22a), suggesting that the sample did not sinter completely after annealing. When heating with graphite, extruded and cold-rolled tantalum seem to accumulate carbon in their grain boundaries (Fig. 3.25c and 3.25f); this presumably leads to the formation of TaC and Ta_2C, grain-boundary cohesion loss, and embrittlement. Based on the samples' mass difference before and after heating in presence of carbon, the extruded tantalum allowed more carbon penetration, but this was not pos-

sible to confirm because carbon was not detected in the samples when analyzed with EDS. Based on that most of the differences in microstructure are lost after heating, and that the speculated difference in carbon penetration is marginal, it is inadvisable to substitute the extruded tubes with cold-rolled ones that are more expensive and difficult to manufacture.

3.5 TaC coated tantalum characterization

Routinely, a TaC coating is applied to the internal face of the target ovens to protect them against carbon during operation online. The target containers are coated in house; the procedure consists of suspending TaC powder in a slurry that is flushed in the interior of a container, and then the TaC coating is sintered by resistively heating the coated container (Appendix A.4).

Since the TaC coating is done manually, it varies among tubes. The TaC coating had only been characterized before sintering to assess its coverage uniformity over the tantalum surface. For this work, the internal face of a cold-rolled tantalum tube was TaC coated and sintered, and a pristine sample of the TaC-coated tube was analyzed under SEM; two additional samples were heated under vacuum at 2000 °C, one of them was heated in the presence of carbon and the other was heated by itself. After their thermal treatment, both samples were analyzed under SEM. On the other hand, since extruded tantalum is reserved for operation, a pristine sample of TaC-coated extruded tantalum was not available, but samples heated with and without carbon were available and were analyzed (Section 3.5.2). The two following sections present the analysis of the micromorpholgy of TaC-coated extruded and cold-rolled samples in their pristine state, as well as after heating them with, and without carbon.

3.5.1 Micromorphology of TaC coated cold-rolled tantalum

A cold-rolled tantalum tube was coated with TaC and sintered as described in Appendix A.4. The coating completely masks the morphology of the cold-rolled pristine sample (Fig. 3.26a); the pristine TaC-coating is sintered and only exhibits a few well defined particles of TaC (average diameter of 11.3 µm±4.4 µm), so the coating appears smooth, but it has pockets and pores most likely formed during the coating sintering (Fig. 3.27a). The pockets represent areas with a thinner TaC-coating, while the pores might be passages leading to bare tantalum, with the potential to be diffusion paths for carbon.

Heating the TaC-coated cold-rolled tantalum sample for three days at 2000 °C further sintered the coating (Fig. 3.26b). The number of pockets and pores on the coating is reduced in comparison to the pristine sample, but with an increased diameter (Table 3.6). The diameter of the pores in several micrographs was measured with Amscope [69] to compare their size before and after thermal treatments.

Table 3.6: Average pore diameter of TaC cold-rolled tantalum. The pores were measured in the micrographs of Fig. 3.26; when the sample is heated with and without carbon, the number of pores increases, but their diameter decreases.

State	Average pore diameter (µm)
Pristine	1.44±0.61
Heated	2.04±0.98
Heated with carbon	2.76±1.28

The sample heated in presence of carbon (Fig. 3.26c) has a reduced number of pockets and pores than the sample heated by itself (Fig. 3.26b). With respect to the pristine sample, the diameter of the pores on the TaC-coating of the sample heated with carbon is ≈35% larger, suggesting that the carbon penetration promotes the sinterization of the TaC coating. Also, in comparison to the predominantly smooth surfaces observed in the other two samples (Fig. 3.27a, 3.27b), the sample heated with carbon have wrinkles and some cracks (Fig. 3.27c). This is most likely due to carbon penetration in the coating itself; the carbon might be causing dislocations in the TaC lattice that consequently modify the TaC grains shape; on the other hand, the cracks could be loss of cohesion between TaC grain-boundaries.

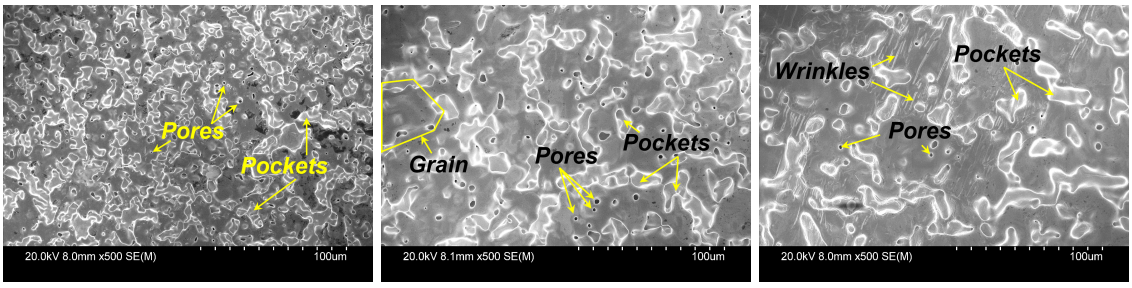

(a) Pristine **(b)** Heated **(c)** Heated with carbon

Figure 3.26: Low magnification micrographs of TaC coated cold-rolled tantalum tube. Pockets and pores are distributed over the pristine TaC coating, these features formed most likely during the TaC firing due to the evaporation of binders in the green coating. When heating the TaC coated sample for three days at 2000 °C, the coating sinters, and its pockets and pores increase in size, but reduce in number (b); this effect is more drastic on the sample that is heated in presence of carbon (c).

Ideally, a diffusion barrier completely covers the surface of the material it is meant to protect. The pristine TaC-coated sample seems sintered, but it has pores that could represent paths for the carbon to penetrate the tantalum; also, even if the pockets or the pores in the coating do not expose bare tantalum they are most likely thinner than the rest of the coating, reducing the efficacy of the coating to prevent carbon penetration. Heating the TaC coating at 2000 °C seems to sinter the TaC coating, but it might also sinter the tantalum below, contributing to its hardening and embrittlement due to carbon diffusion from the coating to the bulk. Moreover, heating the TaC-coated sample in presence of carbon seems to further sinter the TaC-coating.

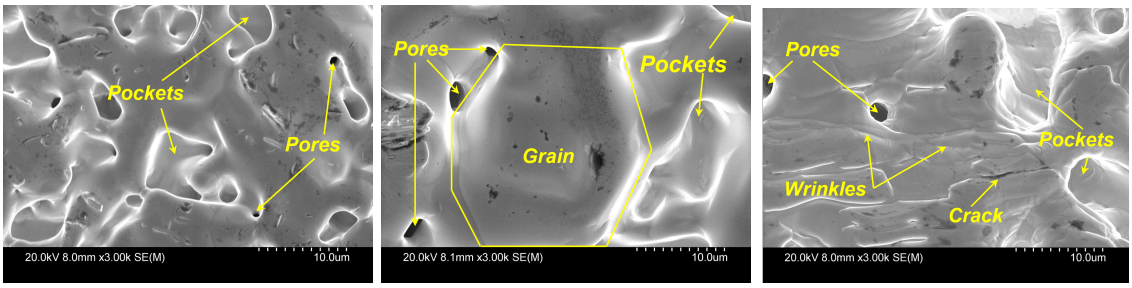

(a) Pristine **(b)** Heated **(c)** Heated with carbon

Figure 3.27: High magnification micrographs of TaC coated cold-rolled tantalum tube in pristine, heated, and heated with carbon state. The pristine sample (a) has a higher amount of pores, followed by the heated sample (b), and the one that was heated with carbon (c), this indicates that the thermal treatment further sinters the samples. The wrinkles on the samples heated with carbon are most likely caused by carbon penetration in the coating.

3.5.2 Micromorphology of TaC coated extruded tantalum

The extruded-tantalum tubes (Fig. 3.6a) available for destructive experiments are limited because they are reserved for production. A 19 cm long extruded-tantalum tube was coated with TaC as described in Appendix A.4; then, this tube was loaded with a graphite container, sealed with tantalum caps, and heated under vacuum for three days at 2000 °C. Two samples were retrieved from this tube, they were cut after the cap with the intention of having samples that were not exposed to sublimated carbon from the graphite container. One of the samples was reserved for representing a TaC-coated extruded sample heated without carbon. The other sample was heated in contact with carbon in a bundle (Fig. 3.14b). Since these samples were taken from a 19 cm long tantalum tube loaded with a graphite container, they are more representative of the phenomena of carbon penetration in the online target ovens; however, preparing all the samples in this way would have taken longer and it would have been more expensive.

The morphology of the TaC coating heated with and without carbon is similar between both extruded samples (Fig. 3.28). In contrast with the TaC-coated rolled samples, there is not a pronounced difference in the degree of sinterization between the coating of the extruded-sample that was heated apart from carbon, and the one heated in contact with carbon, suggesting that not much further sinterization was achieved with the later thermal treatment. Both coatings sintered and do not exhibit grain boundaries; also, both samples have narrow islands and round plateaus.

At first glance, the TaC-coating morphology of the extruded and cold-rolled samples is very different. However, the difference might originate from the difference in degree of sinterization between the TaC coating on the extruded and cold-rolled samples; the narrow islands observed in Fig. 3.28 might be analogous to the pockets of the TaC-coated cold-rolled samples, and the plateaus observed in Fig. 3.28 are most likely analogous to the grains in

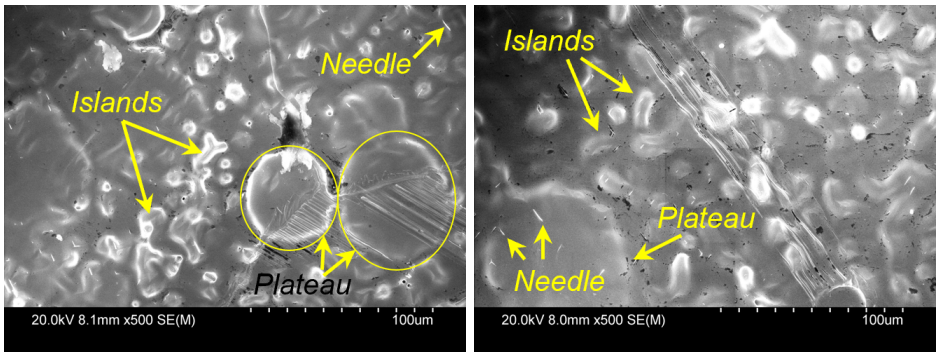

(a) Heated **(b)** Heated with carbon

Figure 3.28: Micrographs of extruded tantalum coated with TaC and heated with and without carbon for three days at 2000 °C. Their microstructure is similar, but the formations on the sample heated with carbon are somewhat larger and fewer.

Fig. 3.27b, but enclosed by depleted pockets. In contrast with the rest of the samples that were first cut and then heated in a tube (Section 3.3), the TaC-coated extruded samples were cut from a tube that was directly resistively heated, so these samples were probably thermally treated at a higher temperature.

In contrast with the cold-rolled TaC coated samples, the corresponding extruded samples present charged formations (Fig. 3.29). These needle-like formations have been observed only in samples that had been heated in the presence of carbon; however, the extruded sample that was heated apart from the carbon also presents them (Fig. 3.29a). These charged formations suggest carbon penetration beyond the separating caps, indicating longitudinal carbon diffusion through the tantalum-tube wall.

As with the TaC coating on the cold-rolled heated samples, the TaC coating on both extruded samples hides the tantalum's extrusion orientation (Fig. 3.29). Compared with the coated cold-rolled tantalum, the extruded sample has fewer and smaller pores (Fig. 3.29a); while the average pore diameter of the analogous cold rolled specimen is 2.04 µm±0.98 µm, the few pores in the extruded sample are in average 1.55 µm±0.31 µm, which represents a ≈24% smaller diameter. If this coating is the same thickness or thicker than the cold-rolled TaC coating, fewer pores with a smaller diameter would make the TaC coating of the extruded tantalum a more efficient barrier against carbon penetration.

As with the cold-rolled tantalum, the TaC coating of the extruded sample that was heated in presence of carbon have wrinkles (Fig. 3.29b). A couple of cracks are visible around the wrinkle area of the coating, but their direction is perpendicular to the wrinkles while the fissures on the analogous cold-rolled sample are aligned with the wrinkle direction (Fig. 3.29). These wrinkles could be defects in the TaC crystals induced by carbon penetration in the coating.

The cross-section of the TaC-coated samples that were heated with carbon was explored with SEM and analyzed with EDS. No carbon was detected with EDS neither in the bulk nor in the edges where the TaC-coating was expected to be observed. Moreover, besides a larger

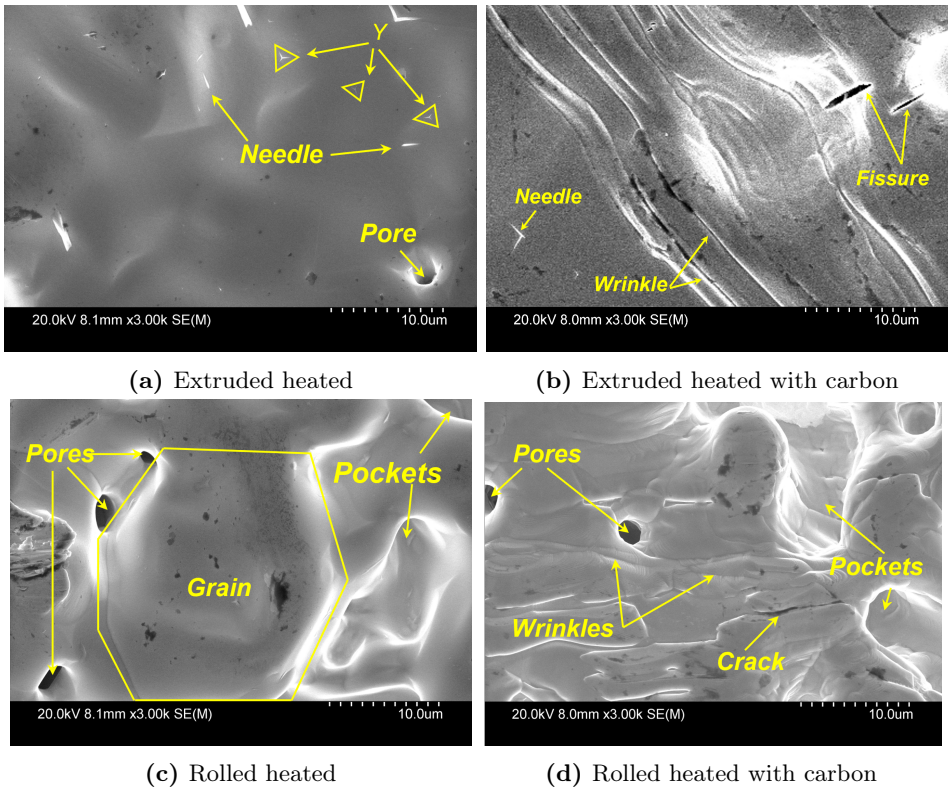

(a) Extruded heated **(b)** Extruded heated with carbon

(c) Rolled heated **(d)** Rolled heated with carbon

Figure 3.29: Micrographs of extruded tantalum coated with TaC and heated with and without carbon for three days at 2000 °C.

number of pores, the edge where the TaC coating was expected to be is not different from the rest of the tantalum bulk in either the extruded or the cold-rolled sample (Fig. 3.30). By dismounting the cross-section samples from the holder, and laying them flat, their surfaces were observed with SEM; in this way, it was verified that the samples were TaC-coated and correctly positioned in the holder, so the possibility of the sample not being coated was discarded. Thus, the reason for the cross-section sample for not exhibiting a coating must be either that the TaC-coating is too thin, or that the sample polishing methodology was not effective in exhibiting the coating. Nonetheless, micromorphology differences are observed between the TaC-coated extruded and cold-rolled samples. The TaC-coated extruded sample shows less pores than the cold-rolled one, which is expected since the TaC-coating on the surface of the extruded sample presents more signs of sinterization than the cold-rolled one. Furthermore, the extruded TaC-coated sample presents precipitation-like formations (Fig. 3.30a). These formations might be Ta_2C or carbon, but since no carbon was detected with EDS, their composition is not determined. The precipitation-like formations were not spotted in cross-section areas of the cold-rolled sample.

Both, the extruded and the cold-rolled TaC-coated samples have signs of carbon penetration. The difference in morphology between the TaC-coated extruded and rolled sample's

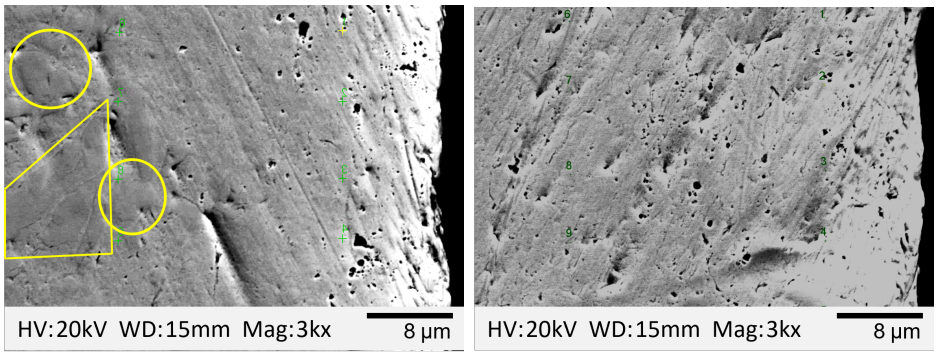

(a) Extruded **(b)** Cold-rolled

Figure 3.30: Micrographs of the cross section of extruded and cold-rolled TaC-coated tantalum heated with carbon for three days at 2000 °C. The right edge of the samples is suppoused to show a different morphology since it corresponds to the TaC-coating and to the side where the sample was in contact with graphite during heating; however, besides a larger number of pores, the edges do not show an important micromorphology difference with respect to the bulk. Precipitation-like formations are enclosed in yellow (a); they are most likely Ta_2C or carbon accumulation. These formations were not observed in cold-rolled samples.

coatings, most likely originates from their heating method. Since the extruded samples were heated in the conventional way, these samples were probably treated at higher temperature than the cold rolled samples, so their TaC coating and bulk were more sintered. On the other hand, the cross-section of the pristine cold-rolled sample shows more pores (Fig. 3.20a) than the analogous extruded sample (Fig. 3.24a), so the sintering difference in the bulk of the samples, might also be predisposed by the forming methods of the material. Another important observation is that the morphology of the TaC-coated extruded sample that was heated apart from graphite, also present indications of carbon penetration, suggesting longitudinal carbon diffusion through the tantalum wall.

According to the difference in mass before and after heating the TaC-coated samples with carbon, the extruded-tantalum sample had more carbon penetration (Table 3.5). The mass difference supports the assumption that the precipitation-like formation on the TaC-coated extruded sample are Ta_2C. If this is the case, TaC-coated cold-rolled tantalum would be better than extruded-tantalum in preventing carbon penetration; however, it should be emphasized that since the TaC coating is applied manually, it might be different between tubes; thus, the TaC coating of the extruded samples might have been thinner than that of the cold-rolled sample, allowing more carbon penetration. Determining the thickness of the TaC coating is imperative for predicting its efficacy in preventing carbon penetration. To find out the coating thickness it is proposed to analyze samples with a Focused Ion Beam (FIB). With this technique a section of the coating could be removed from the surface of a coated sample by ablation and then the height (or thickness) of the coating could be measured. Also pores and imperfections through the coating could be spotted with this technique.

Rhenium has been considered as an alternative to TaC for coating the interior of the target ovens. The following section outlines the methodology developed in this work to apply a rhenium coating in the interior of a tantalum tube. Also, the characterization of the coating's micromorphology is presented and compared before and after heating at 2000 °C with and without carbon.

3.6 Rhenium coating setup and procedure

In this work, a setup was developed to apply a metallic rhenium (Re) coating on the internal surface of an extruded and cold-rolled tantalum tube. The tubes were 4 cm long and had an internal diameter of 1.83 cm. The coating's procedure was carried out in the non-actinide furnace (Fig. 2.3b). A rhenium wire (1 mm diameter, 10 cm length, 99.97% pure from Sigma Aldrich) was held between two copper legs such that the wire passed through a tantalum tube (Fig. 3.31). To match with the rhenium vaporization temperature at $\sim 4 \times 10^{-7}$ Torr, the wire was resistively heated to 2120 °C [47].

To estimate the required power to reach the rhenium wire vaporization temperature, a numerical simulation was performed with COMSOL Multiphysics® [107]. This software uses Finite Element Analysis (FEA) to solve diverse physics and engineering problems. The joule heating and structural modules were used to estimate the voltage drop in the system, the temperature of the parts at different currents, and the deformation expected in the rhenium wire during heating.

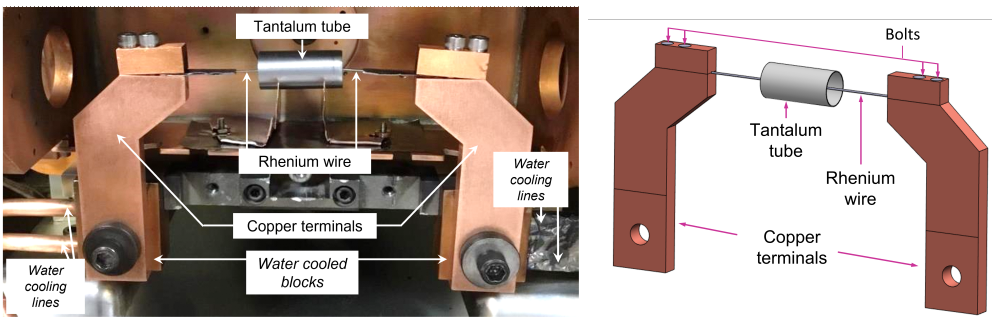

(a) Re coating setup. **(b)** Re coating setup CAD.

Figure 3.31: System for coating the internal surface of a tantalum tube with rhenium. The 1 mm diameter rhenium wire was held between two copper terminals to resistively heat it. The tantalum tube was only heated by the radiation heat from the wire. The difference in temperature between the tube and the wire allows the condensation of rhenium on the interior of the tube.

A CAD model of the rhenium coating system was imported to COMSOL. The model was drawn in Solidworks® [108]; it included two copper terminals, four stainless steel bolts, one rhenium wire, and one tantalum tube (Fig. 3.31b). The CAD model did not include any part of the non-actinide furnace, and it did not include the bolts fixing the copper legs to

water cooling blocks in the furnace either (Fig. 3.31a). The electrical and thermal contact between the clamping system, the wire, and the bolts was considered ideal. The current flow was constant and direct through the copper legs, the rhenium wire, and the stainless steel bolts. The copper legs were water cooled on the area enclosed up to the line indicated in the CAD model (Fig. 3.31b). All the parts of the system dissipated heat to the ambient. Additionally, the rhenium wire dissipated heat to the tantalum tube surrounding it; the radiative heating of the rhenium wire was the only heat source of the tantalum tube.

A ramp consisting of increments of 10 A was implemented in the copper terminals to obtain the voltage drop and temperature of the rhenium wire. According to the simulation, the Re-wire reaches 2120 °C at a current of 38.7 A (Fig. 3.32), with a corresponding voltage drop of 6.3 V; taking in consideration the power loss of the non-actinide furnace (Eq. 3.2), we aimed at a power of 220 W.

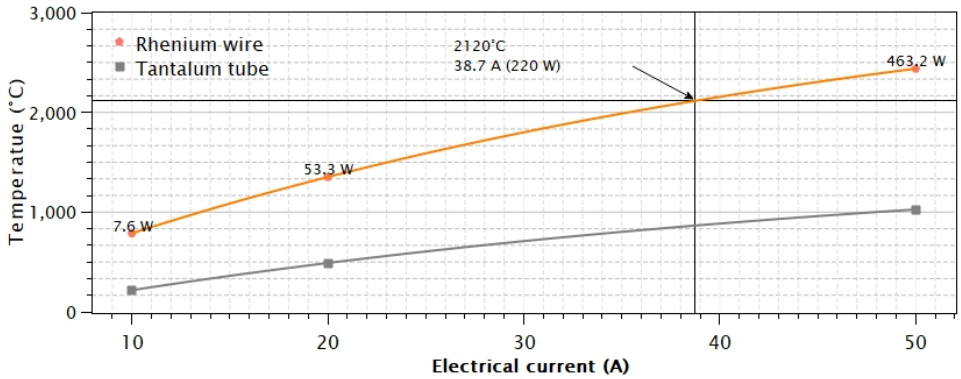

Figure 3.32: Rhenium wire temperature obtained from COMSOL simulations. The rhenium vaporization temperature of 2120 °C is supposed to be reached inputting 220 W in the non-actinide furnace.

The current to heat the wire was increased manually in 0.5 A steps. During heating, the wire expanded and arched more than expected (Fig. 3.33b). However, the wire arching allowed temperature measurements; a filament pyrometer was aimed at the wire during the coating experiment, and the temperature was measured every two steps (i.e. at every increment of 1 A).

During the first attempt to rhenium coat a tube, the Re-wire arched until touching the tube. When the system cooled down, the wire remained attached to the tube wall, and it was not possible to recover it intact. To reduce the wire's arching, its length was shortened, and was clamped with two tantalum plates of 0.5 mm thickness, ∼4 cm length and 0.7 cm width. The plates were folded longitudinally and the wire was placed in the fold, then the plate was fully folded clamping the wire (Fig. 3.34).

During another coating attempt, the Re wire snapped. Thus, less power and hence lower temperature was used in further trials. These changes in heating conditions, combined with the COVID-19 restrictions that forbade access to characterization equipment (i.e. Energy

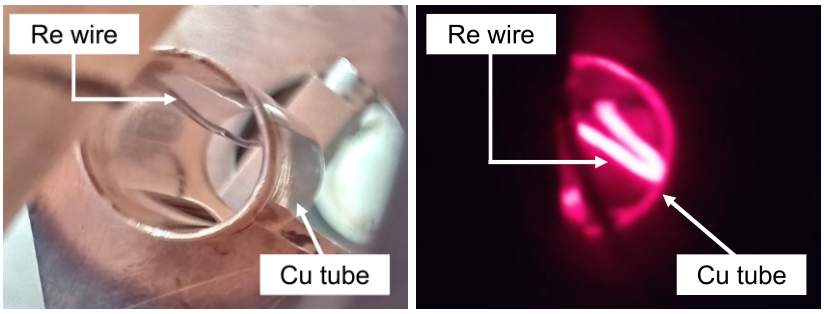

(a) Re wire at ambient temperature. **(b)** Re wire at ≈2000 °C.

Figure 3.33: Rhenium wire arching during experiment to coat the interior surface of a copper tube. When the non-actinide furnace was turned off, it was possible to capture a close-up from the side of the coating system (a); the wire was held off-centre to compensate its imminent arching during heating (b). Although the wire bending was troublesome, it allowed aiming at the wire with a filament pyrometer such that temperature measurements were viable.

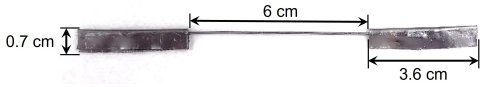

Figure 3.34: Clamping system to shorten rhenium wire length and avoid arching. The clamps are tantalum plates of 0.5 mm thickness folded.

Dispersive X-ray Spectrometer, X-ray Powder Diffraction) at UBC, made it difficult to confirm if a coating was deposited on the tubes. To identify if the coating system was working, a copper (Cu) tube was rhenium coated instead of a tantalum one. The difference in colour between the Re (grey-silver) and the Cu (orange-copper) allowed us to distinguish with the naked eye that a coating was on the internal surface of the tube (Fig. 3.35). The heating conditions for coating the copper tube were replicated to coat an extruded and a cold-rolled tantalum tube (Fig. 3.36).

(a) **(b)**

Figure 3.35: The internal surface of a copper tube that was originally orange (a) became greyish (b) after rhenium coating the tube.

The same rhenium wire was used for coating all the tubes. The cold rolled tantalum tube was coated last, and at that trial, the Re wire seemed to be slightly hotter at the same power than on the two previous coating trials (i.e. Cu tube, and tantalum extruded tube) (Fig. 3.36); this was most likely because the same rhenium wire was used for coating all the tubes, so it was losing material at each experiment. To coat the tantalum tubes, the wire was held at 2120 °C for ninety minutes at ≈90 W (Fig. 3.36).

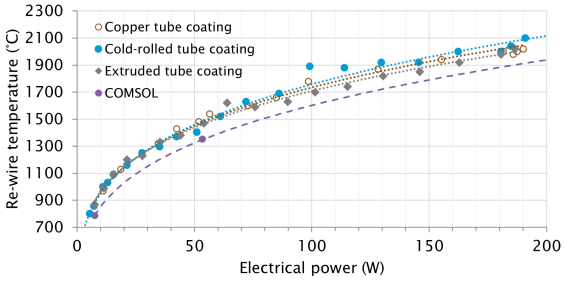

Figure 3.36: Measured temperature of rhenium wire at given electrical power. All the tubes were rhenium coated with the same wire. The chronological order of coating was: copper tube, cold rolled tantalum tube, and extruded tantalum tube. The measurements were taken with a filament pyrometer and have an error associated of ±50 °C. Also COMSOL temperature prediction in violet dashed line.

The mass m of a layer of material coating a surface is given by Eq. 3.10 [109]:

$$m = P\alpha a_p t \left(\frac{2\pi RT}{M}\right)^{-1/2}, \tag{3.10}$$

where P is the vapour pressure of the coating material, α is its vaporization coefficient, a_p is the projected surface area of the coated sample, t is the experiment duration, R is the gas constant (8.31 J/K·mol), T is the temperature, and M corresponds to the atomic weight of the coating material which is 186.2 for rhenium.

According to Eq. 3.10, heating the Re wire at 2120 °C (≈2393 K) for 90 min sublimates 0.26 g of rhenium. The expected thickness of the rhenium coating (t_{Re}) can be estimated based on the mass of the evaporated rhenium (m_{Re}), the projected surface area expected to be coated (a_p), and the density of the rhenium:

$$t_{Re} = \frac{m_{Re}}{a_p \cdot \rho}. \tag{3.11}$$

Assuming the ideal case where the vaporization coefficient is one, and the sublimated rhenium creates an even layer on the internal surface of the tube, a 5.6 µm thick coating would be obtained when heating at the conditions on Table 3.7. Using the difference in mass of the cold-rolled tantalum tube before and after heating (≈8 mg), the estimated coating thickness is ≈0.2 µm which is 28 times thinner than predicted; plausible, since the coating system is not ideal. Factors that could influence the coating thickness are the temperature and micromorphology of the tantalum wall, and the temperature uniformity of the Re-wire.

The thicker the coating, the lower the diffusion flux of the carbon (Eq. 3.9). Besides having a thick coating, it is imperative to fully cover the surface intended to be protected. Cracks and pores in a diffusion barrier are paths for impurities to access the bulk of the material it is intended to protect. During annealing, grains grow at the expense of others shrinking, leading to coarsening, and promoting porosity formation; nonetheless, the thicker

Table 3.7: Parameters and corresponding values used to find the Re evaporated mass (Eq. 3.10) and thickness (Eq. 3.11) during the experiment to rhenium coat the inner surface of tantalum tubes.

	Parameter	**Value**
P	Pressure (Pa)	4×10^{-5}
t	Duration of the experiment (s)	5400
α	Vaporization coefficient	1
a_p	Projected surface area (cm^2)	23
T	Temperature (K)	2393
M	Atomic weight of Re (g/mol)	186.2
R	Gas constant (J/K·mol)	8.314
ρ_{Re}	Rhenium density (g/cm^3)	21.04

the diffusion-barrier coating the more chances it has to avoid depletion, heal, densify and fully cover the coated surface when heated.

Samples of extruded and cold rolled tubes coated with rhenium were analyzed under the SEM and EDS to observe their state before and after heating them at 2000 °C. Also, another couple of samples was heated in the presence of carbon and examined with SEM and EDS.

3.6.1 Characterization of Re-coated extruded tantalum

To examine the uniformity of the rhenium coatings, two specimens were cut from a pristine Re-coated tube. One specimen was cut from the centre of the tube, and the other from its outskirts. The surface of two specimens was scanned with EDS.

In contrast with the specimens from the centre that had an average of wt. 99.81% rhenium, the area scanned of the outskirt specimen had wt. 48.35 % rhenium. According to the COMSOL simulations, the rhenium wire is hotter in the centre and colder at its extremes (Fig. 3.37a), but the temperature difference is only relevant on the area where the wire is clamped with the copper legs; for the most part, the wire temperature is uniform, so its temperate gradient should be negligible for the coating thickness.

During the coating experiments, the wire arched more than expected, so it was off-centred in the tantalum tube (Fig. 3.33b). The wire deformation was not taken into consideration in the temperature FE simulations. The COMSOL simulation assumed that the only heat source of the tube was the Re-wire, that dissipated heat by radiation. A difference of 117 °C between the maximum and minimum temperature of the Ta-tube (Fig. 3.38) was obtained when simulating a Re-wire resistively heated at 50 A. However, in the experimental setup a small area of the tantalum wall was most likely hotter than 1026 °C due to its proximity to the hot Re-wire; furthermore, the tube's temperature gradient was probably larger than 117 °C. An uneven rhenium coating is expected as a consequence of the tube's temperature, favouring the hotter area of the tube. Thus, the Ta- tube centre, that was hotter and closer to the Re-wire, was expected to have a more uniform and thicker coating than the outskirts.

Both the outskirt and the centre sample's EDS-maps show tantalum and rhenium. The EDS-maps' indicate tantalum in red and rhenium in blue (Fig. 3.39a and 3.39b). The

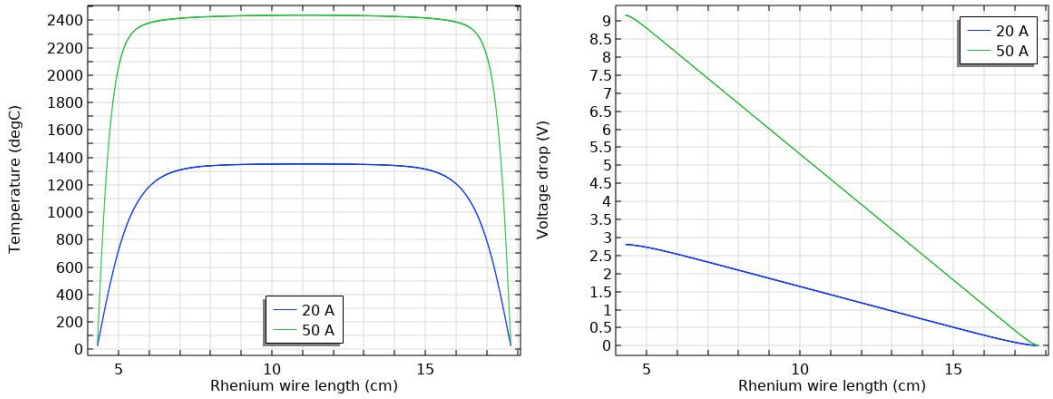

(a) Temperature gradient **(b)** Voltage drop

Figure 3.37: Temperature gradient (a) and voltage drop (b) of rhenium wire at 20 A and 50 A. During coating, a 4 cm long tantalum tube was situated in the centre of the wire, where the temperature was expected to be uniform.

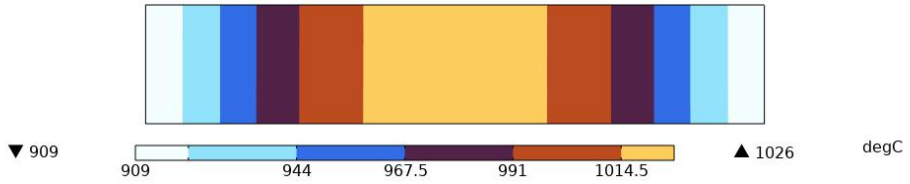

Figure 3.38: The centre of the tube closer to the wire is expected to have the thickest rhenium coating; the opposite side is expected to have a thinner coating.

outskirt map is more pink indicating a higher Ta signal (Fig. 3.39a), while the centre map is more purple indicating a higher Re signal (Fig. 3.39b). On the outskirt map, blue and red grooves suggest that the Re-coating is not uniform (Fig. 3.39a). The spectra corresponding to the outskirt's map confirms that tantalum was exposed; on average, the outskirt specimen scans indicate that the surface is composed by ≈50% rhenium and ≈50% tantalum. Further, the composition of a small zone on the map remained unidentified; the zone was probably a defect (e.g. micro-notch, micro-dent) in the tube, and its depth probably prevented its corresponding signal to reach the detector.

Even though the magenta map of the specimen from the tube's centre suggests that its surface has both, rhenium and tantalum (Fig. 3.39a), only rhenium was identified on the spectrum's map (Fig. 3.39c). Three additional areas scanned on the same specimen confirmed that the specimen was rhenium coated; on average, the scanned areas have wt. 99.81% rhenium.

The centre EDS-map (Fig. 3.39a) is magenta and not just blue most likely because the software interprets the hump of the 1.8 keV Re-peak (fig:plot-Re-extrud-map) as Ta signal. However, no peaks corresponding to Ta were obtained at 8.1 keV, 9.34 keV, or 9.65 keV (Fig. 3.39c). Nonetheless, the hump of the 1.8 keV-peak could correspond to tantalum. According to CASINO (monte CArlo SImulation of electroN trajectory in sOlids) [111] sim-

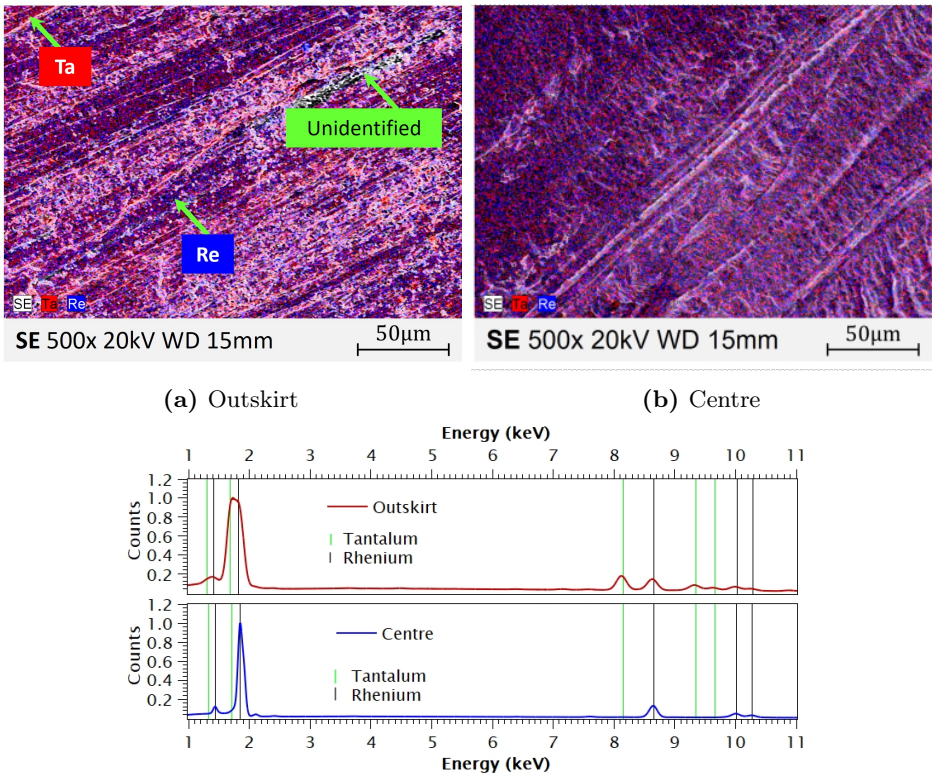

(a) Outskirt **(b)** Centre

(c) Maps' EDS spectra

Figure 3.39: EDS maps of SEM micrograph of pristine rhenium coating on extruded tantalum. Tantalum is indicated with red, and rhenium with blue. The map of the outskirt sample (a) is more pink in comparison to the map corresponding to the centre that is more purple (b). Both maps indicate a combination of tantalum and rhenium. However, the spectrum of the central map (c) does not have Ta characteristic peaks (M 0.833 keV and Lα 8.145 keV [110]), suggesting that, in contrast with the outskirts sample, its rhenium coating was fully covering the scanned area.

ulations, an electron beam of 20 kV would penetrate up to ≈0.3 µm in rhenium. Therefore, if the rhenium coating is thinner than 0.3 µm (and it most likely is) signal from the tantalum underneath could have been detected as well.

The centre Re-coated specimens were further explored under SEM at high (x10k) and low (x3k) magnification (Fig. 3.40). The Re-coating was confirmed by rhenium grains closely packed (Fig. 3.40c); nevertheless, dents are present (Fig. 3.40d). Also, grooves on the rhenium coating are evidenced (Fig. 3.40b); these imperfections seem to match with the extrusion orientation and boundaries of the pristine extruded tantalum (Fig. 3.40a). The rhenium grains conforming the coating have well defined boundaries, and they have different shapes and sizes but overall they are flat. By considering them circular, the diameter of several was measured with Amscope [69]; in average, they are 0.97 µm±0.36 µm.

In the hypothetical case that the rhenium grains were symmetric, the coating thickness would also be 1 µm, almost six times thinner than expected (see section 3.6). However, the rhenium coating could be thicker if more than one layer was deposited on the surface of the

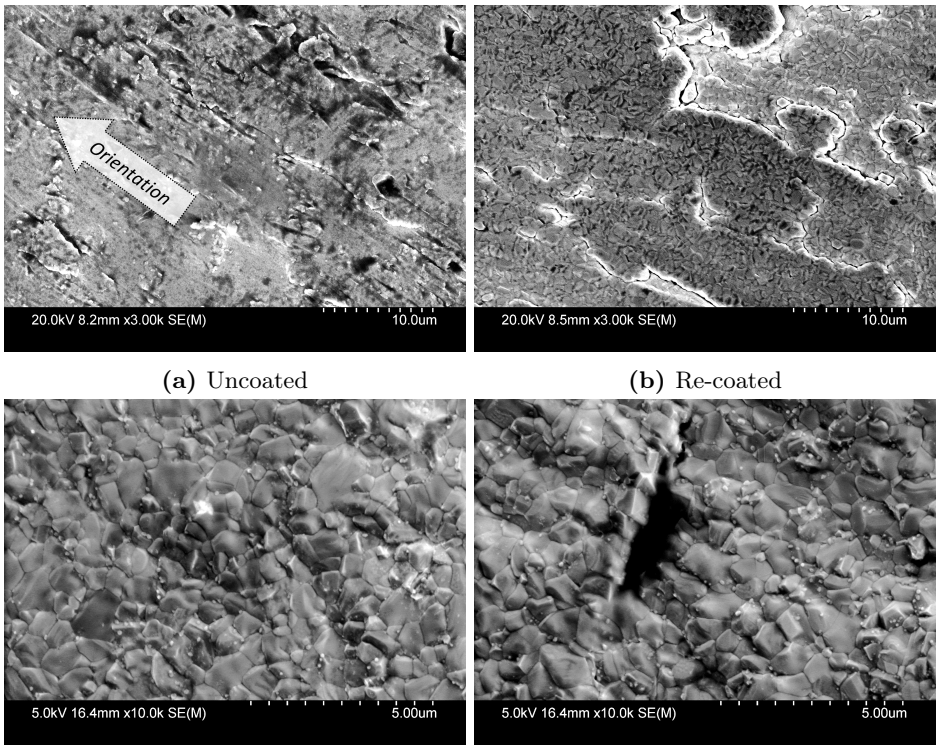

(a) Uncoated **(b)** Re-coated

(c) Re-coated **(d)** Re-coated

Figure 3.40: Comparison of SEM micrographs of uncoated (a) and rhenium-coated extruded tantalum (b, c, d). The grooves on the Re-coating shown at low magnification (b) seem to match with the boundaries of the pristine extruded Ta (a). Closely packed Re grains conform the coating (c), but some areas present dents (d).

tube. The Re-coating could also be thinner if the rhenium grains are not symmetric. To investigate the coating thickness, cross-sections of the coated samples were observed under the SEM, and analyzed with EDS; however, rhenium was not detected when scanning the cross-sections, and no important difference in micromorphology allowed the identification of the coating.

Rhenium was not detected with EDS scans in any of the cross section specimens. To verify that the cross section samples were Re-coated, they were dismounted from the holder and lay flat; even though rhenium was detected on their surfaces, no Re-signal was identified on the cross sections. This is most likely because of the sample preparation methodology (Sec. 3.3). The thin rhenium coating was probably sheared when cutting the samples, and their polishing might had not been enough to remove the sheared part. In fact, the polishing might have contributed to further shearing the specimens edges because the samples were not mounted in epoxy, so they might have lacked support to withstand mechanically-polishing shearing (Fig. 3.41). The specimens were going to be polished mounted in removable epoxy, but due to delays associated with the COVID-19 pandemic, the epoxy arrived when the analysis of these specimens was already culminated. Nevertheless, polishing the samples

in removable epoxy is strongly recommended for further investigations in coatings against carbon.

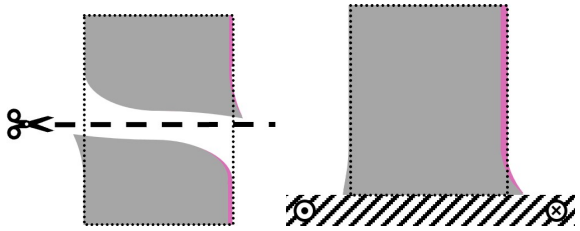

(a) Scissor cut **(b)** Polishing

Figure 3.41: Depiction of sample preparation. When cutting with metal-scissors, the tantalum (grey) and the coating (pink) shears; consequently, the coating smears or thins in the sheared zone (a). Since the samples were polished without epoxy, they did not have support to prevent further smearing (b). All sides of the cross-section samples were subject to smearing during polishing. Sample deformation due to polishing is most likely the reason why the coating was not exposed and then observed under SEM.

To assess the changes in morphology of the rhenium coating due to heat, a rhenium-coated tantalum sample was heated under vacuum for three days at 2000 °C. The rhenium grains of the heated specimen were 8.8 µm ± 3.5 µm in diameter (Fig. 3.42), almost nine times larger than those of the pristine sample (≈1 µm). This increment in size is due to the sintering of the rhenium grains, and it would be beneficial if the grains grow and cover more area even if the coating gets thinner; however, this effect is limited by the thickness of the Re-coating before annealing; since sintering induces material migration away from dents and fissures to feed other Re grains, it leaves pores and cracks behind if the coating is thin. In contrast, a thick coating has more material available to heal imperfections during sintering, leading to densification instead of coarsening. The heated specimen exhibits cracks and pores over its rhenium coating (Fig. 3.42b), which represent potential diffusion paths for carbon to reach the tantalum. The cracks on the Re-coating also suggest that the Re-coating was thin since it was not able to heal itself during sintering.

The heated specimen was mapped with EDS to observe the distribution of rhenium on the tantalum surface (Fig. 3.43). A hue of red is concentrated around a fissure (Fig. 3.43b), indicating a higher signal from tantalum; this suggests that the rhenium coating in that zone is thinner than the rest, confirming that the coating sintering resulted in material migration away from some fissures. Longer coating times followed by annealing would promote further coverage. In this way a thicker Re-coating will be achieved and it will uniformly cover the tantalum when sintered due to annealing.

Another rhenium coated sample was heated under the same conditions but in the presence of carbon. The corresponding specimen was sintered, and it does not show rhenium grains like the pristine one. The coating of this specimen shows small dark zones that were not identified as tantalum, rhenium, or carbon (Fig. 3.44 and 3.45); they are most likely

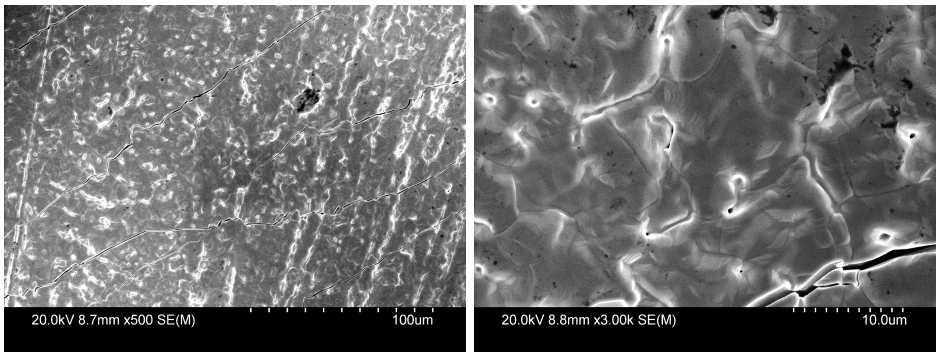

(a) **(b)**

Figure 3.42: Rhenium coated extruded tantalum heated to 2000 °C. The coating has pores and cracks that are high diffusivity paths for carbon to reach the tantalum beneath. The average grain size considering them as circles is $8.8\,\mu m \pm 3.5\,\mu m$, almost nine times larger than the rhenium grains on the pristine sample, this indicates that the coating sintered.

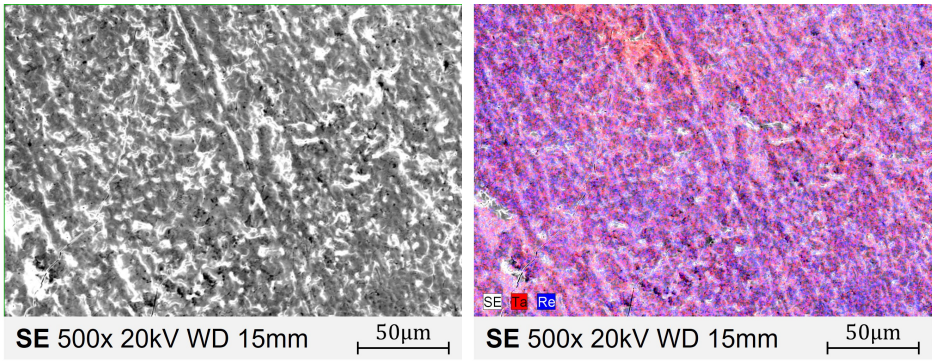

(a) SE micrograph **(b)** EDS map

Figure 3.43: SEM micrograph of rhenium coated extruded tantalum heated at 2000 °C. The corresponding EDS map (b) shows a reddish area around a fissure indicating a higher tantalum signal, implying a lower rhenium one.

pores formed within remaining grain boundaries. Similar dark zones have been spotted in specimens of uncoated extruded-tantalum that have been heated for three days at 2000 °C (Fig. 3.22); since those specimens were not in contact with carbon, it is inferred that their dark zones are pores, supporting the assumption that the dark zones in the Re-coated samples heated with carbon are also pores. Moreover, the Re-coating of the sample heated with carbon seems more sintered than the sample that was heated without carbon. A reason for this could be that carbon penetrated in tantalum through cracks and pores, and formed TaC and Ta_2C, causing defects on the tantalum lattice; the deformation of the tantalum surface could modify the morphology of its Re-coating.

The sample heated with carbon was mapped and scanned with EDS. No carbon was spotted in the EDS-map of the Re-coated extruded sample heated in contact with carbon, but it was detected with area scans. This element was probably in the tantalum bulk

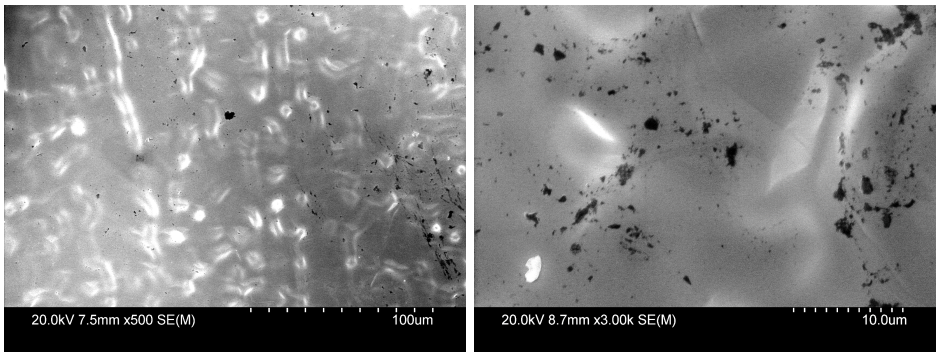

(a) **(b)**

Figure 3.44: Micrographs of a Re-coated extruded-tantalum sample that was heated at 2000 °C in contact with carbon. Protrusions are remaining from sintered grains.

beneath the Re-coating. The average concentration of rhenium, tantalum and carbon in three areas scanned was 19.96%, 71.06% and 8.98% respectively. In contrast with the EDS-map of the sample that was heated by itself (Fig. 3.43b), the map of the sample heated with carbon does not show intenser red or blue localized areas; instead, its magenta hue is mostly uniform (Fig. 3.45). The average rhenium concentration of this sample is lower than the Re-concentration of the other two samples (Table 3.8); suggesting that the rhenium coating is thinner than the other two specimens, such that the signal from the tantalum beneath is detected. Given the expected asymmetry of the Re-coating along the tube's diameter, there is a possibility for the sample that was heated in contact with carbon to have the thinnest Re-coating among the three samples. Another reason for this Re-coated sample to have the lowest rhenium concentration is that the greater sintering of the tantalum beneath contributed to the thinning of the Re-coating.

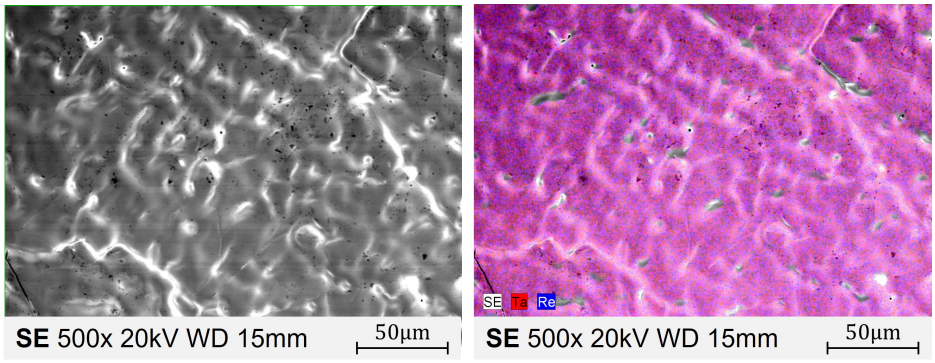

(a) SE micrograph **(b)** EDS map

Figure 3.45: SEM micrograph of rhenium coated extruded tantalum heated at 2000 °C with carbon. (a) The corrugated area seems like a swollen version of the sample that was heated without carbon (Fig. 3.42). (b) A uniform hue of magenta indicating a thin layer of rhenium covers most of the area scanned; grey islands represent fissures that were too deep for the map to be resolved, these islands are exposed tantalum.

The rhenium weight percent detected in the specimens surface was lower in the following order: pristine, heated and heated with carbon (Table 3.8). The pristine specimen had an average of 99.81%, indicating that a rhenium coating was covering the areas scanned. On the other hand, the specimens corresponding to the samples heated with and without carbon had 42.02 wt.% and 19.96 wt.% rhenium concentration respectively, suggesting that these coatings were not fully covering the tantalum or that they were thinner (Fig. 3.46).

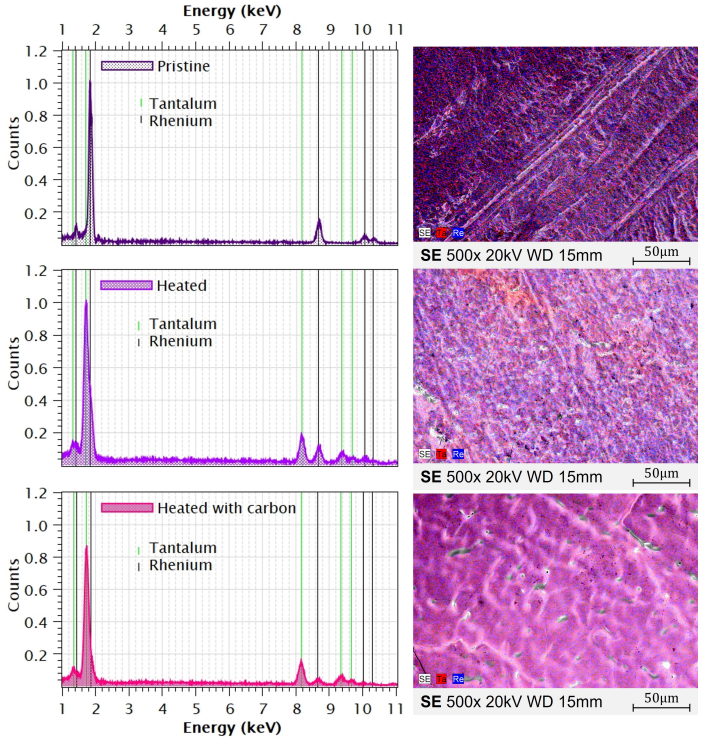

Figure 3.46: EDS spectra (left), and EDS maps (right) of Re-coated extruded samples in pristine state, heated and heated with carbon. In the spectra Re-peaks are indicated with black vertical lines, and Ta with green vertical lines. In the maps Re is indicated in blue, and Ta in red. The pristine sample has a strong signal of Re and no Ta peaks, suggesting that the Re-coating masked the Ta and was covering most of the scanned area; the corresponding map is violet indicating that Re prevails on the surface of the sample. The rhenium signal is weaker for the heated specimen, and is the weakest for the specimen that was heated in presence of carbon, meaning that imperfections in the coating exacerbate due to the thermal treatment, exposing tantalum areas. The maps of the specimens go from purple to pink as less rhenium and more tantalum is detected. The spectra of both heated samples have Re and Ta characteristic lines.

The morphology of the bare extruded tantalum has been compared with that of the rhenium coated (Fig. 3.47). Clear extrusion orientation is observed in the pristine uncoated specimen (Fig. 3.47a) but not so much on the rhenium coated one (Fig. 3.47d); some fissures, and boundaries are present, but according to the EDS scans, those features are covered with rhenium. When the tantalum extruded sample is heated, its extrusion orientation is less evident (Fig. 3.47b), but due to sintering, some boundaries disappear and others become

Table 3.8: Normalized wt% of rhenium, tantalum , and carbon in specimens that were pristine, heated, and heated with carbon. The specimen with the lowest rhenium signal was the one heated with carbon, followed by the one heated by itself, and the pristine one. The lower tantalum signal is due to the sintering of the Re-coating during heating that lead to the migration of Re and the consequent exposure of tantalum.

	Element		
Specimen	**Re**	**Ta**	**C**
Pristine	99.81	0.19	-
Heated	42.02	57.98	-
Heated with carbon	19.96	71.06	8.98

deeper and wider. Similarly, the rhenium-coated sample sinters, and the grainy rhenium coating develops fissures and pores due to the sintering of its grains and the ones of the tantalum underneath (Fig. 3.47e). In contrast with the bare extruded tantalum that was heated in presence of carbon (Fig. 3.47c), the Re-coated specimen that was submitted to the same thermal treatment does not present charged formations (Fig. 3.47f), suggesting that, in the observed area, the carbon did not cause cohesion loss in the tantalum's grain-boundaries underneath the rhenium coating. Also, the coating do not show grain boundaries anymore indicating its sintering.

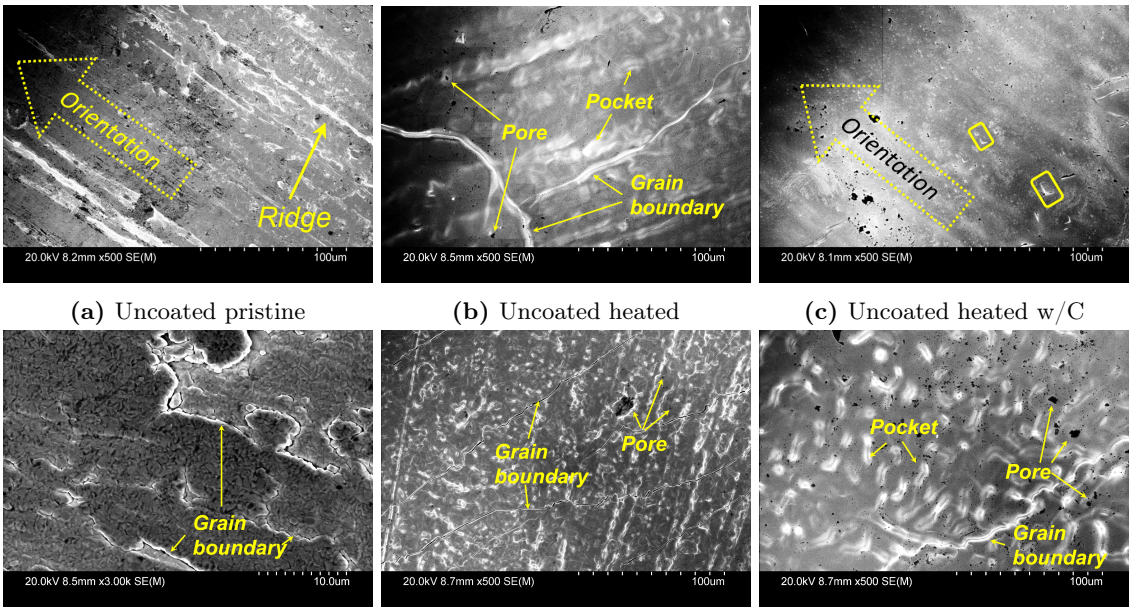

(a) Uncoated pristine **(b)** Uncoated heated **(c)** Uncoated heated w/C

(d) Re-coated pristine **(e)** Re-coated heated **(f)** Re-coated heated w/C

Figure 3.47: Micrographs of extruded tantalum without (a, b, c) and with a rhenium-coating (d, e, f) in a pristine state and heated at 2000 °C in contact with and without carbon.

In conclusion, a Re-coating was deposited on an extruded sample. The scanned areas of pristine Re-coated samples were fully covered. Cross-sections of the pristine Re-coated samples were prepared to determine the coating's thickness, but no characteristic Re-peaks were detected when scanning the cross-sections, neither distinctive micromorphology dif-

ferences allowed the identification of the Re-coating, suggesting that the coating was thin. Heating a Re-coating for three days at 2000 °C induced the sintering of the tantalum and the Re-coating. The Re and Ta grain growth seem to reduced the thickness of the Re-coating. Furthermore, the changes in morphology and the lower rhenium concentration of a Re-coated sample heated in contact with carbon for three days at 2000 °C, indicated that the sample's Ta and Re grains sintered, forming pores and cracks. Also, the extended sintering of the Re-coating, suggests that the carbon penetrated the Ta underneath, formed TaC or Ta_2C, and modified the Ta morphology, consequently affecting the Re-coating morphology.

It seems like the Re-coating was too thin, so pores and cracks formed during sintering, allowing tantalum exposure and carbon penetration. A thicker coating should be deposited on tantalum, and samples heated with and without carbon should be analyzed before and after annealing to quantify the effectiveness of the coating in each sample. Moreover, the setup for heating samples in contact with carbon should be modified such that the carbon is enclosed in a Re-coated tantalum tube; in this way, sublimated carbon won't be able to penetrate through uncoated tantalum areas like it could in the current samples (Fig. 3.14b). However, before proceeding to attempt coating another tube, more trials should be done with the coating-setup to assure that it delivers samples completely coated with a uniform coating-thickness, such that the coating can heal during annealing.

3.6.2 Characterization of Re-coated cold-rolled tantalum

The rhenium coating of pristine cold-rolled specimens were examined under the SEM. The morphology of the rhenium coating differs among different areas of the same pristine specimen. Some areas barely hide the morphology of the cold-rolled tantalum (Fig. 3.48b) while others even have rhenium accumulations (Fig. 3.48c).

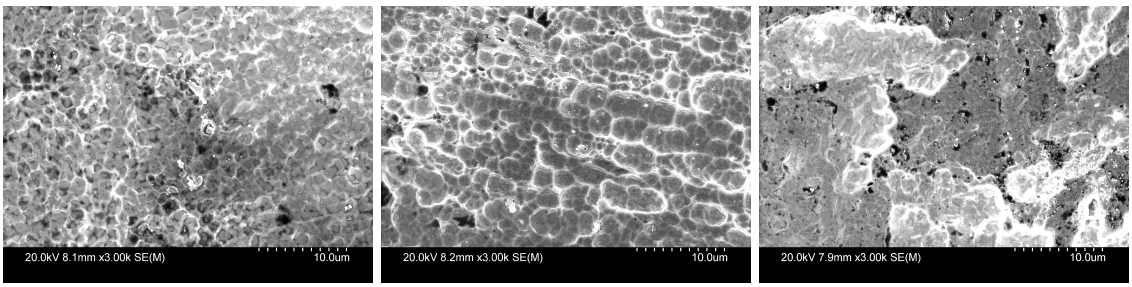

(a) Uncoated **(b)** Re coated **(c)** Re coated

Figure 3.48: Comparison of SEM micrographs of bare cold-rolled tantalum with rhenium-coated specimen. The coating was not uniform across the same specimen. Some areas like (b) hardly hid the cold-rolled surface morphology (a), and others like (c) masked better the tantalum morphology, but are uneven.

The surface of the pristine cold-rolled specimen was examined with EDS to assess the uniformity of its rhenium coating in the centre of the tube. In average, the coating's rhenium

concentration was 83.55 wt.%, which is 16% lower than the concentration of the analogous extruded sample. The average Re and Ta concentrations in the pristine Re-coating of the cold-rolled sample suggest that the fissures and pores observed on the micrographs (Fig. 3.48) are exposing the tantalum surface. Point-scans revealed that some of the pore-like zones (Spectrum 3 on Fig. 3.49) have a higher rhenium concentration than relatively smooth zones (Spectrum 2 on Fig. 3.49), meaning that the Re-coating is not only patchy, but it is also thin, such that the signal from the tantalum beneath the Re-coating is detected.

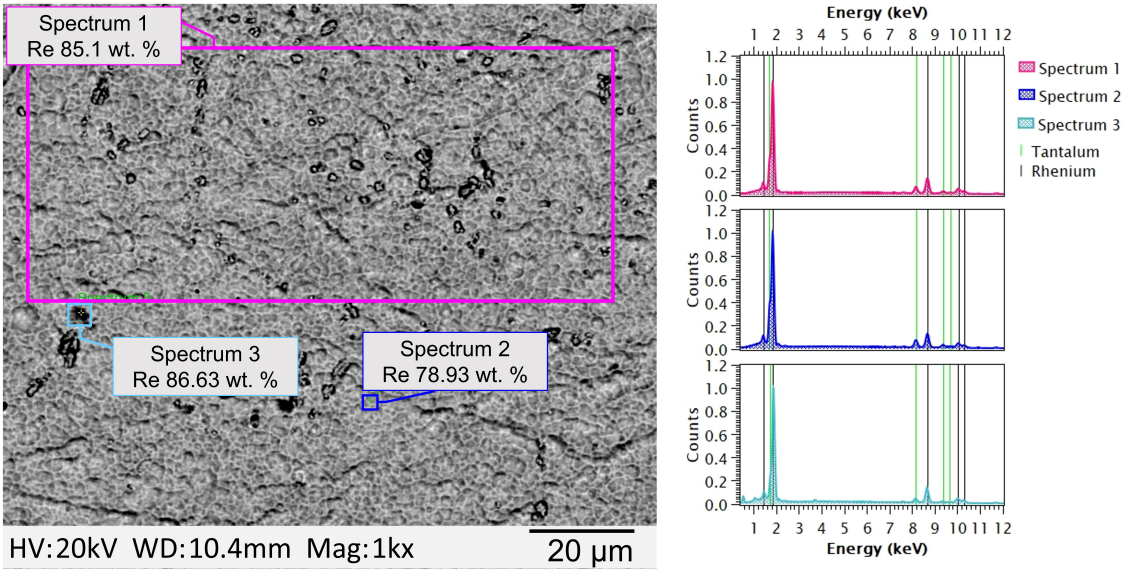

Figure 3.49: EDS scan of rhenium-coated surface of cold-rolled tantalum pristine specimen. Three areas were scanned. 85.1 wt.% rhenium and 14.9 wt% tantalum was detected on the large area delimited by a pink rectangle; the spectrum 2 corresponding to a point scan on a relative smooth area indicated a lower rhenium concentration with respect to the spectrum 3 corresponding to a point scan on a pore-like feature.

A zone of the Re-coated pristine cold-rolled tantalum was explored at high magnification (x10k) to inquire into the composition of imperfections on the coating. A Re-coated area was scanned aiming at a fissure and a pore (Fig. 3.50a); the EDS mapping of the zone indicates in red that the fissure is deep enough to expose tantalum (Fig. 3.50d), while the pore is not (Fig. 3.50c). The average concentration of rhenium on the mapped area is 80.27 wt.%, and the tantalum concentration is 19.73 wt.%.

A rhenium-coated pristine cold-rolled sample was cut from the tube's outskirt. As with the analogous extruded tube, the rhenium coating of the cold-rolled tube varied across the length of the tube. The coating on the outskirt did not hide the micromorphology of the tantalum, and it did not seem to have fissures or pores. A large zone was scanned with EDS to obtain the overall rhenium concentration (Fig. 3.51a). While the specimen cut from the centre of the tube had an average rhenium concentration of 83.55 wt.%, the specimen from the outskirt had an average of 50.58% wt rhenium. Additionally, a small area where

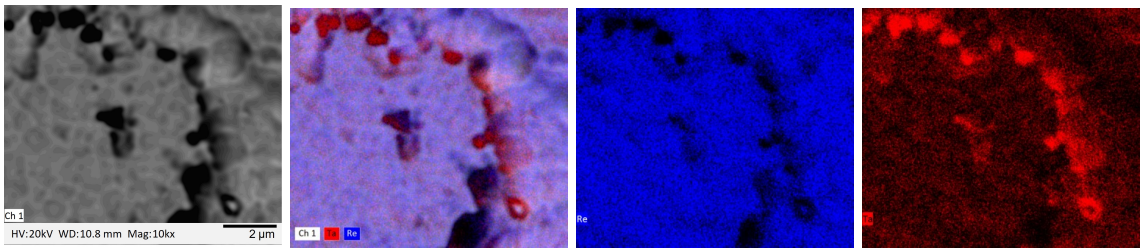

(a) Micrograph **(b)** EDS map **(c)** Rhenium **(d)** Tantalum

Figure 3.50: EDS map of pristine rhenium-coated cold-rolled tantalum. A fissure on the coating was explored and map to identify if it was deep enough to expose tantalum; the red shade confirms that tantalum was detected.

no fissures were pinpointed was scanned and had similar rhenium content (47.80 wt.%) (Fig. 3.51b), suggesting that the coating is not only partially covering the area, but it is also thin.

The rhenium coating of the centre of the cold-rolled tube was examined at higher magnification (Fig. 3.52). Both scanned areas seem to be fully covered with small rhenium grains (Fig. 3.52c and 3.52d). One of the Re-coated scanned areas (Fig. 3.52c) does not hide the sub-grain structures of the cold-rolled tantalum (Fig. 3.52a). Another Re-coated scanned area (Fig. 3.52d) masks the morphology of the cold-rolled tantalum, suggesting more accumulation of rhenium, and most likely a thicker Re-coating. Comparing different micrographs shown so far, it is concluded that the Re-coating morphology and coverage varied widely through the cold-rolled sample.

On average, the rhenium particles forming the coating on the cold-rolled tantalum were 0.11 µm±0.02 µm. In comparison with the particle size of the rhenium coating on the extruded tantalum (≈1 µm), this one is ten times smaller (Fig. 3.53). This sample's Re-coating grains may be smaller because of the substrate morphology. Besides washing them, the tantalum tubes were not prepared in any other way, so the tantalum morphology due to its manufacturing process could have discriminated the Re-grains to be deposited, favouring the accumulation of small ones. Furthermore, the rhenium coating grains of this sample might be thinner since all coatings were done with the same rhenium wire, and the cold-rolled tube was the last one to be coated; given that the wire had lost material with the previous coating trials, the overall amount of Re evaporated during the coating of the cold-rolled sample might have been marginal.

In the hypothetical case where the rhenium grains are symmetric, the cold rolled tantalum would have a 0.11 µm thick Re-coating. With such thickness, the Re-coating cross section would be hard to observe under the SEM given the specimen preparation circumstances. Even if we assume that as the extruded tantalum, this coating is composed of two layers, the 0.2 µm-thick rhenium coating would still be easy to get lost on the smeared tantalum. Rhenium was detected on the surface of this cross-section-sample when dismounting

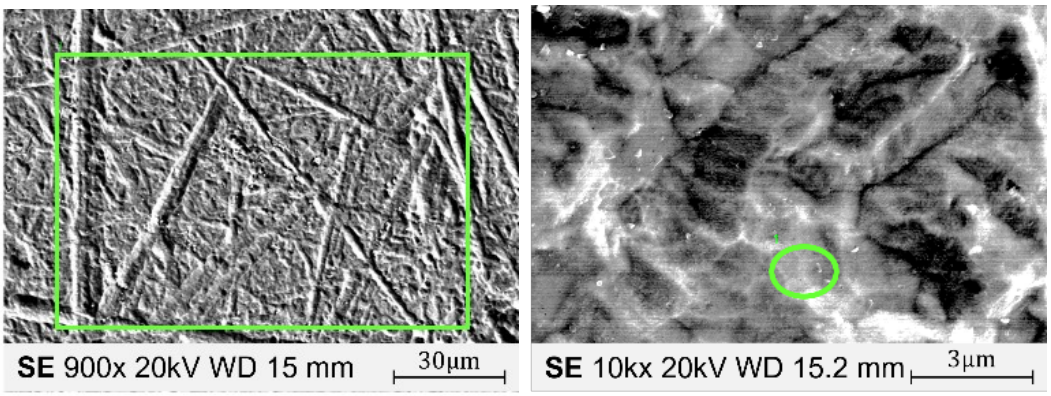

(a) Zoom-out **(b)** Close-up

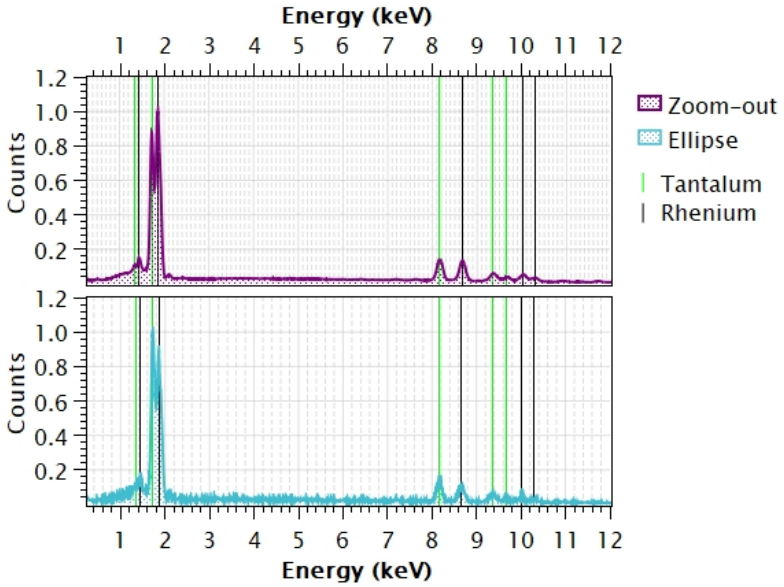

(c) Spectra corresponding to areas (a) and (b.). In contrast with the analogous rhenium coating on extruded tantalum, the spectra corresponding to cold-rolled tantalum not only have rhenium but they also have tantalum characteristic lines (indicated with green vertical lines).

Figure 3.51: Micrographs and spectra corresponding to a rhenium-coated cold-rolled tantalum specimen. Both areas had an average of 50.58% wt rhenium; such a low result is expected for the large area scanned in (a) because at low magnification cracks and holes might not be evident and the exposed tantalum might be more than what can be seen; however, at high magnification (b), the low rhenium content is only explained by having a thin layer of rhenium.

it and laying it flat, supporting the assumption that rhenium was not detected in the cross section because of the samples preparation.

To assess the changes in the coating when operating at high temperature, a cold-rolled sample was heated under vacuum at 2000 °C for three days. The specimen shows swollen veins (grain boundaries) and pores (Fig. 3.54b). It also presents similar protrusions to those observed in the extruded rhenium-coated sample that was heated with carbon (Fig. 3.44a),

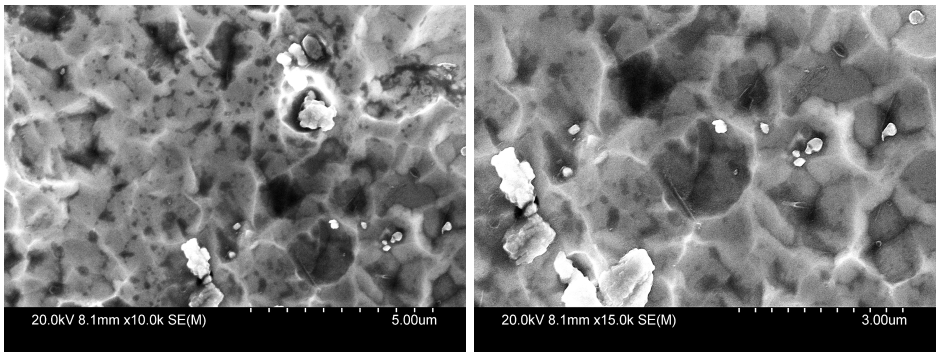

(a) Uncoated x10k **(b)** Uncoated x15k

(c) Re-coated x10k **(d)** Re-coated x15k

Figure 3.52: Comparison of SEM micrographs of naked (a and b), and rhenium-coated (c and d) cold-rolled samples. The Re-coating in (c) does not mask the tantalum morphology as the Re-coating in (d) does, this difference suggest that the Re-coating on the second area is thicker.

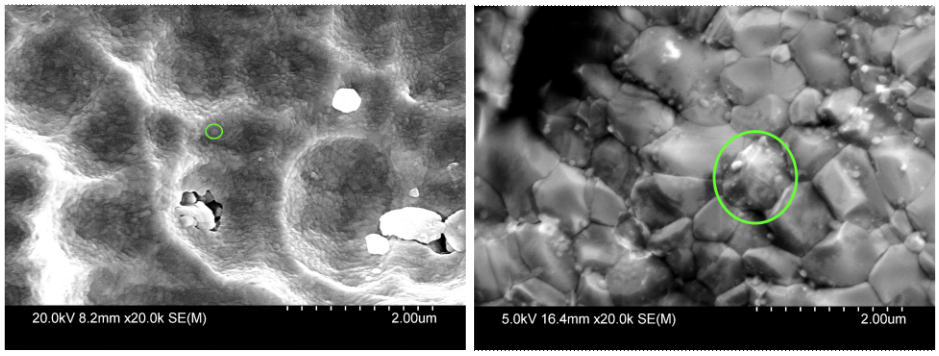

(a) Cold-rolled tantalum **(b)** Extruded tantalum

Figure 3.53: Comparison of SEM micrographs of Re-coated cold-rolled (a) and extruded tantalum (b). The Re particles (indicated with a green circle) of the cold-rolled specimen are 10 times smaller than those of the extruded one.

but the ones in this sample are more subtle. Also, this sample surface was analyzed with EDS; its spectrum does not present the characteristic X-rays of rhenium (Fig. 3.56). This Re-coated sample was not analyzed under SEM before heating, and it could have been the case that its Re-coating was patched, leaving large tantalum areas exposed. In this case, the tantalum sintering underneath as well as the Re-sintering could enlarge the areas of bare Ta.

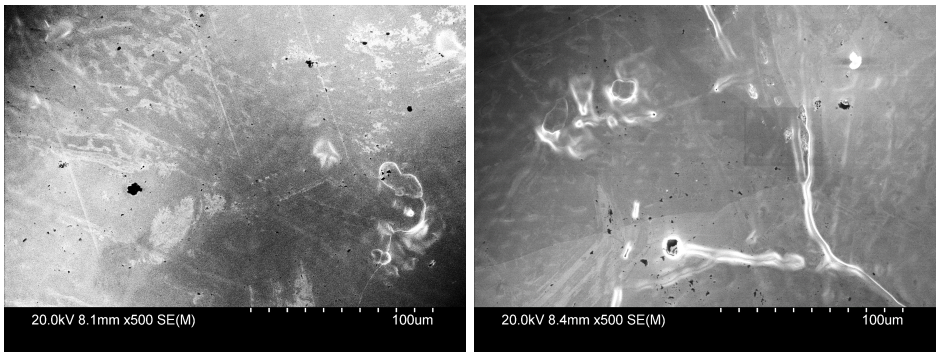

(a) Uncoated **(b)** Rhenium coated

Figure 3.54: Comparison of SEM micrographs of uncoated and rhenium-coated specimens that were heated at 2000 °C for three days. Both samples are relatively smooth with respect to pristine cold-rolled tantalum. (b) The coated specimen has veins formations that are most likely tantalum ridges covered with rhenium; it also has pores similarly to the uncoated specimen (a).

An additional sample that was previously coated with rhenium was heated for three days at 2000 °C in presence of carbon. The micromorphology of this specimen is similar to the uncoated one, but charged formations are smaller. Also, the area analyzed has several dark areas (pores) (Fig. 3.55b). No rhenium nor carbon characteristic X-ray peaks were obtained in the spectrum corresponding to this sample, only tantalum was detected (Fig. 3.56). Given the variation in Re-coating uniformity among samples, it is possible that this sample's Re-coating was very thin and patchy, so carbon penetrated the tantalum, forming carbides, and consequently modifying the tantalum's morphology. The severity of the morphology change suggest that the rhenium coating coverage prior to heating was poor.

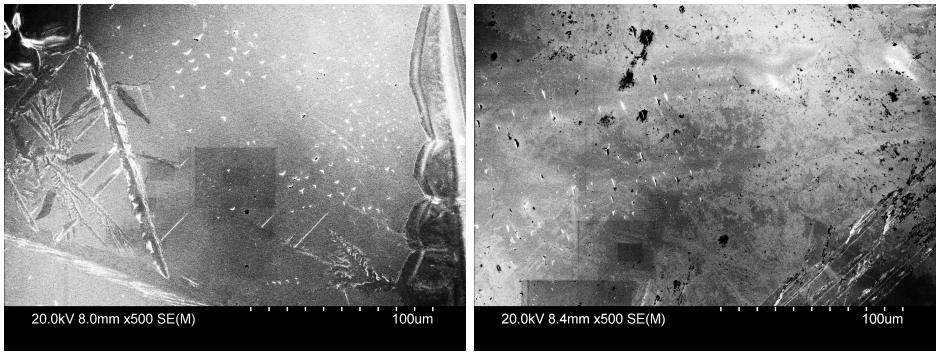

(a) Uncoated **(b)** Rhenium coated

Figure 3.55: Comparison of SEM micrographs of bare and rhenium-coated cold-rolled tantalum that were heated at 2000 °C in contact with carbon. Both samples have charge formations that are most likely carbon or TaC accumulation. The rhenium-coated sample has less charge formations, and it has more pores.

Since it was not possible to analyze the samples while performing the experiment, the Re-coating of the samples was not analyzed before heating. Thus, the homogeneity of the Re-coating was not confirmed, so there is a chance that the samples heated with and without

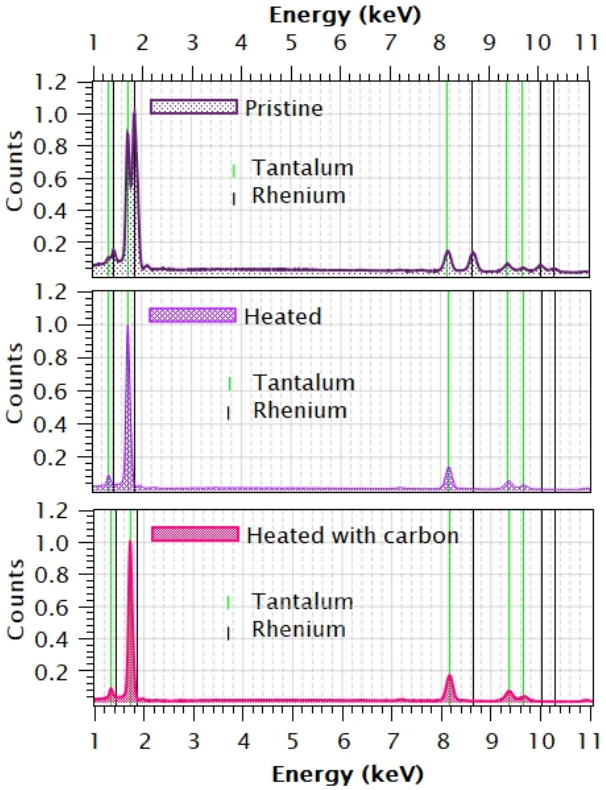

Figure 3.56: EDS spectra of cold-rolled specimens coated with rhenium. Only the pristine specimen presents Re. The samples that were heated with and without carbon were only analyzed after their thermal treatments, their coating might have been originally patchy, so during heating sinterization of the tantalum and rhenium could promote the expansion of uncoated areas. Furthermore, carbon most likely penetrated into the sample heated in contact with graphite, formed TaC and Ta_2C, modified the tantalum lattice, and promoted the Re-coating thinning.

carbon had a non-homogeneous rhenium coating layer even before heating. Assuming that the Re coating covered the tantalum tube surface evenly, there is a chance that the coating broke into islands during heating and uncovered the tantalum surface due to the particle growth of the tantalum beneath. An improvement to our rhenium coating methodology would be to analyze the same coated sample before and after heating it; in this way, the Re concentrations of the samples could be compared confidently.

The Re coating relative concentration is higher on the extruded than on the rolled tantalum even though the samples where coated under the same conditions and for the same time. Since the samples were analyzed under the same conditions, the difference in concentration between samples suggests that a more uniform rhenium coating was deposited on the extruded sample than on the rolled one. Additional trials are suggested, complimented with EDS and SEM analysis of the samples to assess the Re-coating coverage.

The samples heated with carbon are the ones that have the lowest rhenium concentration of all. These samples sintered morphology indicate carbon penetration. The carbides

expected to be formed with tantalum seem to modify the tantalum morphology as well as the rhenium coating on top. Allowing longer time for Re-coating tantalum samples could deliver thicker coatings with the ability to heal during heating. In fact, before heating the Re-coated samples in contact with carbon, they should be annealed and characterized. Additional coating trials are suggested, complimented with step by step EDS and SEM analysis of the samples to assess their Re-coating coverage before and after thermal treatments, and unequivocally evaluate the influence of the carbon on the Re-coating morphology.

No rhenium was detected in the bulk of any rhenium coated sample. This suggest that Re from the coating did not diffuse through the bulk; or if it did, it did not conglomerate or precipitate in the tantalum bulk, preventing spotting it when scanning. Moreover, the rhenium coating of the given samples was not evident across the cross-section edge; this might be due to sample preparation methodology. The tantalum was most likely sheared when cutting the sample. During polishing the sheared edge probably smeared, further hiding the coating. Similarly, the TaC coating was not observe in the cross-section samples; furthermore, the expected Ta_2C layer was not found in the TaC-coated samples. Moreover, no carbon was evident when exploring the samples' cross section.

Instead of analyzing the samples' cross-section with EDS, another method should be used to determine the effectiveness of the coatings. An option is to analyze the coated samples with a Focused Ion Beam (FIB). With this technique, the surface of the sample can be explored to confirm the existence of a coating, then the coating can be ablated in situ to measure its thickness. Alternatively, Re-coated tantalum tubes could be submitted to destructive tests like the ones made in section 3.1.1 to identify the changes in the resistivity of the tantalum; however, this experiment will be lengthy, and the uniform coverage of the tantalum surface must be assured for the results to be valid.

Not enough evidence was found to determine the superiority of any coating over the other. However, destructive tests demonstrate that carbon penetrates the tantalum tubes even if they are TaC coated, leading to tantalum embrittlement and resistivity variations that change the oven temperature, which reduces the isotope release efficiency of the target materials when it happens during irradiation. Rhenium could be a better option to coat the interior of the tantalum tubes because carbon diffuses slower in Re than in TaC. However, a thick and sintered rhenium coating should be deposited and tested to quantify its efficiency preventing carbon penetration.

An alternative to a diffusion barrier would be to prevent the vaporization of the carbon. This strategy would only work for targets, that like the UC_x, are loaded in a graphite container because the graphite container is only in contact with the oven in an small area. The vaporization temperature of the carbon increases with the pressure (Fig. 3.5), so if the pressure in the gap between the tantalum oven and the graphite container is increased to 1×10^{-3} Torr the vaporization temperature would be ≈2200 °C; around 300 °C above the

operational temperature of the UC_x target. Argon could be injected in the oven to increase the pressure in the gap between the graphite container and the tantalum oven.

In the meantime while a solution for tantalum embrittlement is developed, the targets should be irradiated keeping in mind that their temperature will vary during irradiation as carbon penetrates the oven. Even though the small changes in resistivity are extremely difficult to spot during irradiation, the knowledge that the oven deterioration modifies the target's temperature gives an insight on the possible justifications for changes in the isotope release of targets irradiated online.

The following chapter presents the isotope yields of a graphite-composite and UC_x targets irradiated online. The yields are plotted against target temperature. The chapter also presents the comparison of isotope yields measured at the beginning and at the end of the irradiation campaign, showing a decline in isotope release due to the embrittlement of the target oven.

Chapter 4

Radiotracer release and online isotope production studies

Since the isotopes can be separated by mass in the ISOL method, yields of different isotopes from the same element can be measured to investigate each species' release efficiency. However, ionization, Radioactive Isotope Beam (RIB) formation, and delivery efficiencies form part of the overall efficiency; exacerbated by inherent instabilities of the very complex ISOL RIB production and delivery, untangling the ISOL method contributions to isolate the one corresponding to the release of a given specie is often impractical. Also, online systematic experiments are scarce and many times the isotopes investigated are limited to those that are of interest for the experimenters requesting RIB. Under these circumstances, collecting enough information to systematically characterize the release properties of a target material becomes challenging, and correlating release properties to systematically varied material characteristics, such as density, grain size, or porosity is virtually impossible.

Radiotracer release studies are an option for the systematic target material characterization. These studies consist of irradiating target material samples to activate them and generate a representative isotope distribution inside of them. Comparing a specific isotope activity before and after heating the samples provides a figure for the material release efficiency at a given temperature [27, 112, 113, 18].

The radiotracer, or offline, release studies estimate the efficiency given solely by the release of the isotopes from the target material. In contrast with the ISOL method, the offline release studies exclude the ionization, and transport contributions, and allow systematic measurements on larger sets of samples. However, unlike the ISOL method, on the radiotracer release studies, studying short-lived species is not feasible because handling is required before starting the study, typically requiring several hours. In addition to this waiting time, in many cases including ours, samples have to be transported between heating treatments and γ-spectra acquisitions.

Radiotracer release studies permit systematic and extensive measurements, allowing the development and comparison of new target materials before using valuable and scarce online experimental time. Nevertheless, there are phenomena that can only be studied online, like short-lived isotopes release, target material aging, and Radiation Enhanced Diffusion (RED). Using both, the ISOL and the radiotracer studies, a complete characterization of a target becomes attainable. In this work, graphite samples were submitted to radiotracer release studies to study ^{7}Be release (Section 4.1); also, besides delivering RIB to experiments, during the irradiation online of a graphite-composite target, lithium and beryllium isotopes were collected at different temperatures and proton beam intensities (Section 4.6).

4.1 Offline ^{7}Be release of graphite target materials

Offline release experiments were performed in individual target discs. Ionization and transport delays, do not influence the release of the species in these experiments. The diffusion-effusion process necessary to escape the target material pack is also excluded; in this way, the release study focuses entirely on individual discs and hence on the target material properties, comparing the characteristics that potentially promote release like porosity and grain size.

The release time from the target has to be shorter than the isotopes' half-life for an isotope to escape from a target. Moreover, the half-life of the isotope has to be long enough for it to survive through the offline experiment procedure in order to be able to characterize its release with this technique. The ∼53 days half-life of ^{7}Be, an isotope produced in the graphite target (Fig. 1.2c), allows its investigation with offline experiments. The ^{7}Be release fraction of three target material candidates of graphite were investigated by comparing the intensity of their emitted γ transitions before and after heating them. The three types of graphite target materials consisted of pellets, foils, and composites (Fig. 4.1).

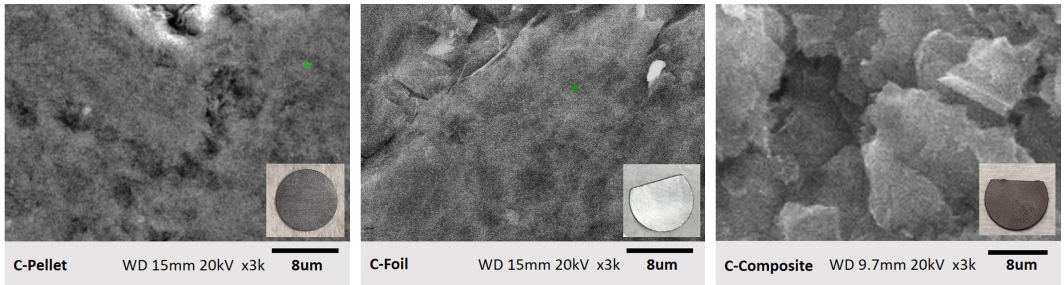

(a) Pellet **(b)** Foil **(c)** Composite

Figure 4.1: Graphite samples used to investigate ^{7}Be release from different graphite materials. The samples' diameter is 1.8 cm; the pellet thickness is 0.054 cm, the foil is 0.013 cm, and the composite is 0.035 cm. The surface of the samples was examined under SEM. The pellet has large areas with few or no pores, the foil show no pores but some wrinkles that might be fissures to the bulk. The composite is flaky, resembling its graphite powder precursor.

The graphite pellets were manufactured out of the graphite used to fabricate containers (Fig. 2.23). The pellets were cut and polished in TRIUMF's scintillator shop from graphite rods purchased from SGL; the rods were Sigrafine R7510, isostatistically pressed, with average grain size of 10 µm [88]. The graphite pellets diameter was 1.8 cm and their thickness 0.054 cm. The porosity of the pellets was assessed with pycnometry, and the results were in agreement with the porosity reported by the vendor (12.44% and 10% respectively). The pellets were polished as part of their manufacturing; they had a smooth surface with few pores (Fig. 4.1a) as expected given the low open porosity estimated with pycnometry. Furthermore, the pellets grain size was not evident in its micrographs (Fig. 4.1a), but according to the provider, the graphite rods, and thus the pellets, should have a grain size of 10 µm.

The graphite foils were made out of the same material used as backing in all ISAC target composites. They were cut from exfoliated graphite sheets of 0.013 cm thickness from CeraMaterials [85]. The geometry of the graphite foils was identical to the ISAC composites, they were D-shape, and held an area of 2.12 cm^2. Graphite foils were also submitted to pycnometry, the results suggested a high open porosity of 43.54% (Section 2.4.1); however, no pores were observed on the graphite foil surface (Fig. 4.1b). In contrast with the pellets, the foils porosity could not be corroborated since the vendor does not provide this information. With such high open porosity many pores would be expected on the graphite foil surface, but that is not the case (Fig. 4.1b). One could suspect that the open porosity result was inaccurate, but at least the total porosity (Eq. 4.1) should be high given that the theoretical graphite density is 2.3 g/cm^2 [40, 114, 115] and that the foil's bulk density measured (1.15 g/cm^3) is in agreement with that reported by the vendor (1.10 g/cm^3).

$$P_{tot} = \left(1 - \frac{\rho_{bulk}}{\rho_{th}}\right). \tag{4.1}$$

Layers of graphite are observed in the graphite foil's cross section (Fig. 4.2). The graphite sheets consist of pressed exfoliated graphite particles that resemble worms or garlands [116, 117]. The graphite worms interlock between each other forming flexible layers [118]. The resulting material is anisotropic and it is possible that most of the graphite foils void volume is distributed transversely through the sheet connecting the edges of the foil, but not forming pores through the foil thickness (Fig. 4.2). The interlocked elongated-graphite particles resemble hair at high magnification (Fig. 4.2b) with a thickness of ≈1 µm. The length of the particles is unknown, and the vendor does not provide this information.

The graphite composites consist of graphite powder slip cast over a graphite sheet. The graphite powder was purchased from Alfa Aesar [55] and the sheet from CeraMaterial [35]. The composite's synthesis methodology, as well as their characteristics, are detailed in Sections 2.4 and 2.4.1 respectively. The average thickness of a composite disc was 0.035 cm where 0.013 cm corresponds to the thickness of its backing graphite foil. Since the backing

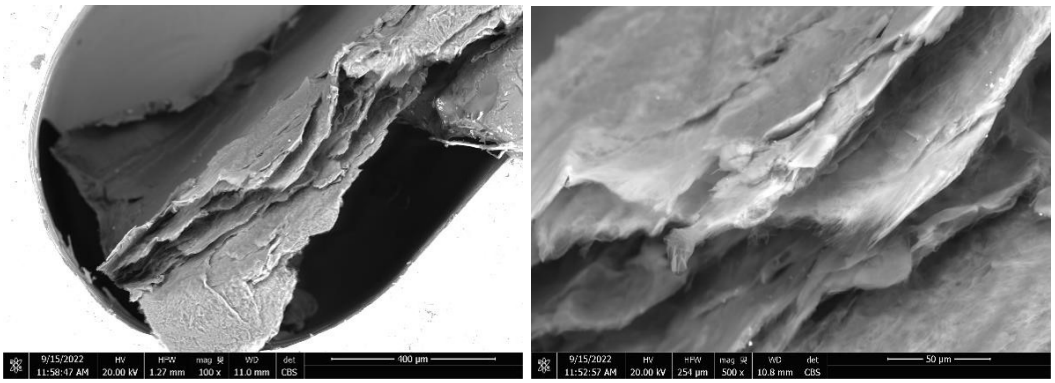

(a) 100x **(b)** 500x

Figure 4.2: Micrographs of the graphite foils' cross-section. At 100x magnification (a) the layers of the graphite sheet are visible. At 500x magnification (b) hair-like graphite particles are visible.

foil is the same as the one mentioned above it has the same characteristics. On the other hand, the slip cast consists of graphite flakes of ≈12 µm diameter in average, and its open porosity ≈ 62% (Table 4.1).

Table 4.1: Characteristics of the graphite samples used in release studies. The procedure to obtain the open porosity and thickness are described in Chapter 2.

Target material	**Thickness (mm)**	**Open porosity**
Graphite pellet	0.538±0.011	0.12±0.01
Graphite foil	0.129±0.004	0.44±0.01
Graphite composite	0.345±0.064	0.62±0.05

All the studied target samples were irradiated for 300 s with a proton beam with an energy of ∼450 MeV and a current of 5 µA at the Isotope Production Facility (IPF) (Fig. 4.3). To irradiate the target samples they were packed in IPF flasks of 12 cm diameter and 0.8 cm thickness. These IPF flasks have a volume capacity of 28.1 cm^3 (6.4 cm diameter by 0.9 cm height) which allows the allocation of either two pellets, three composites, or six foils. The target samples were vacuum sealed in the IPF flask, and remotely loaded in the IPF cassettes that are enclosed in a hot cell (Fig. 4.4).

After irradiation, the IPF flasks stay in the hot cell until their dose rate at 50 cm is below 50 mSv/h, so they are safe to handle. The graphite samples were retrieved from the hot cell via a dedicated remote-handling process; then, they were decontaminated and opened. One of the retrieved samples was then carried over to the ARIEL yield station (AYS) to acquire its radioisotope inventory via its γ energy spectrum. Two consecutive acquisitions of 1 hour each were taken per sample (longer acquisition times were tried, but the standard deviation did not reduce from 2%). A γ spectra ranging from 0 to 5000 keV was obtained from each

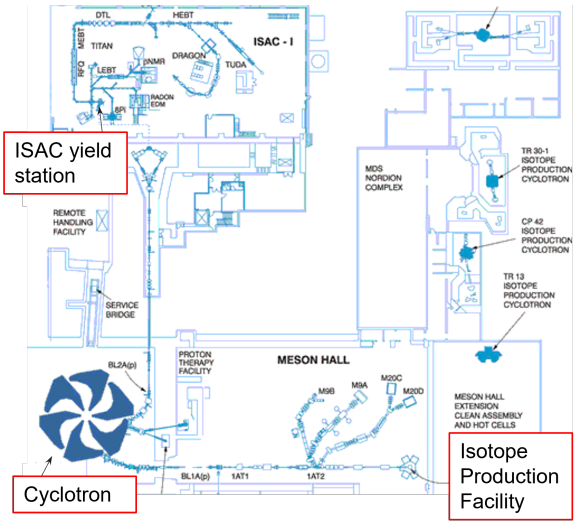

Figure 4.3: The Isotope Production Facility (IPF) receives protons from the cyclotron.

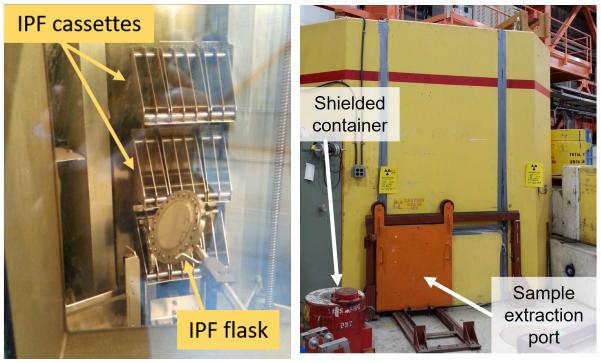

(a) IPF flask and cassettes **(b)** Back of IPF hot cell

Figure 4.4: Samples loaded in IPF flasks are allocated in cassettes and remotely positioned for proton irradiation.

measurement (Fig. 4.5a). Given that the ^{7}Be γ transition is 477.6 keV, the region of interest (ROI) selected in each spectra for all samples was $RL = 473.32$ keV and $RR = 478.75$ keV (Fig. 4.5b). The summation of the counts within this region (C_T) minus the corresponding background counts (C_B) are the net counts (C_N) of ^{7}Be γ transitions in the sample (Eq. 4.2 to 4.4) [78].

$$C_T = \sum_{i=RL}^{RR} C_i \tag{4.2}$$

$$C_B = (C_{BL} + C_{BR}) \left[\frac{RR - RL + 1}{2} \right] \tag{4.3}$$

$$C_N = C_T - C_B \tag{4.4}$$

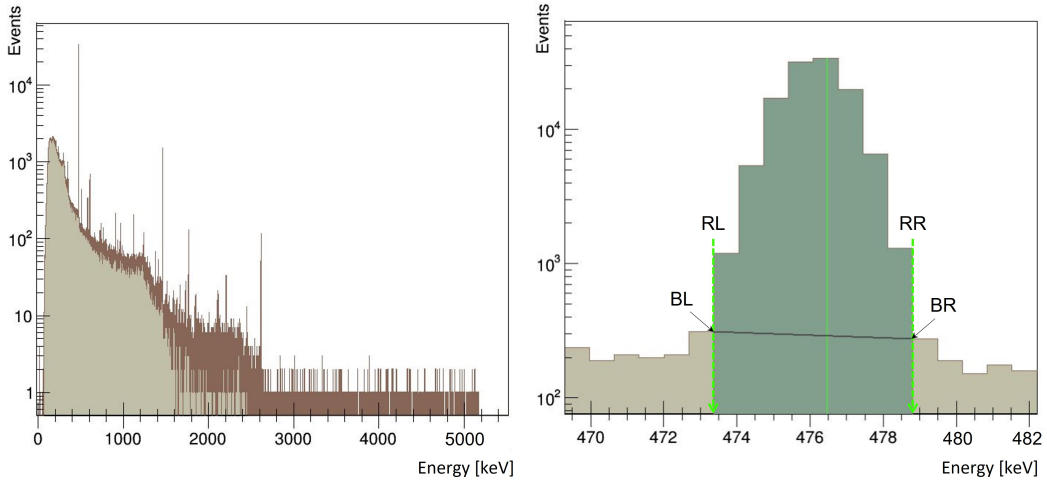

(a) γ spectra **(b)** ^{7}Be γ transition ROI

Figure 4.5: (a) Complete γ spectra from irradiated graphite pellet, and (b) ^{7}Be γ region of interest (ROI).

After determining its initial γ transitions intensity, the sample was heated at 1668° C for one minute; then its γ transitions were measured again. Later on, the sample was heated at 1910° C also for a minute, and its γ transitions intensity was re-assessed in the same measurement geometry. Ideally, a different sample should be used for each temperature, but in order to minimize the inventory of irradiated samples (and hence the dose rate of stored target material) each sample was heated at two different temperatures.

All the heat treatments were performed in the Chamber for Heating Investigations (CHI) [34] (Fig. 4.6). CHI has a resistor consisting of two parallel 0.0254 mm thick tantalum foils that are 2 cm wide and 5 cm long; the bottom foil has two lips 1 mm tall where the sample is placed (Fig. 4.7). The sample is heated when the pressure is under 10^{-4} Pa.

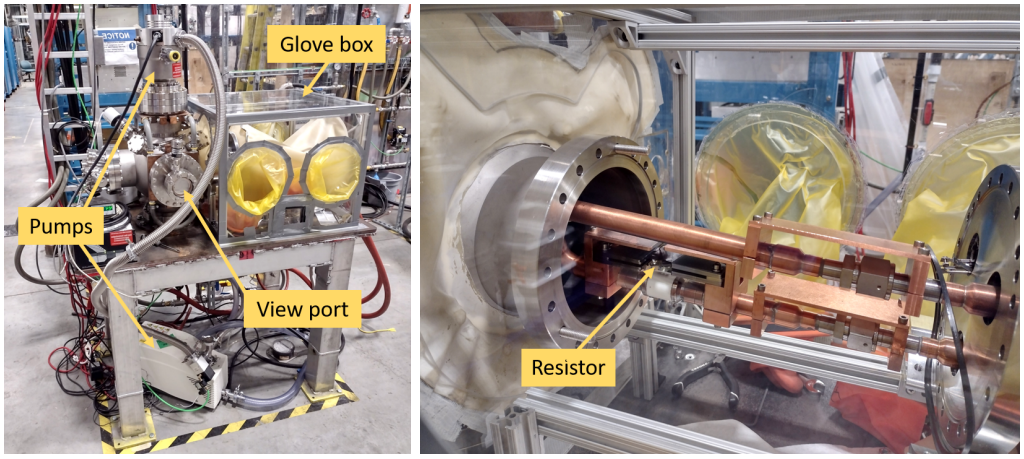

(a) CHI test stand **(b)** CHI resistor

Figure 4.6: The CHI tests stand heats samples under vacuum.

To estimate the temperature in CHI at different electrical powers, a titanium and a vanadium wire were placed on a non-irradiated graphite foil of the same dimensions and characteristics as the ones irradiated (Fig. 4.7). The wires were monitored with a two colour pyrometer while the electrical power was gradually increased to pinpoint the power at which they melt. The reference temperatures of 1668° C and 1910° C corresponding to the titanium and vanadium melting points respectively were matched to 987±135 W and 1355±152 W (Table 4.2). The heating treatments relied on this calibration since it was not feasible to measure the temperature of the sample due to its orientation with respect to the view port (i.e. pyrometer could only aim at the sample's rim).

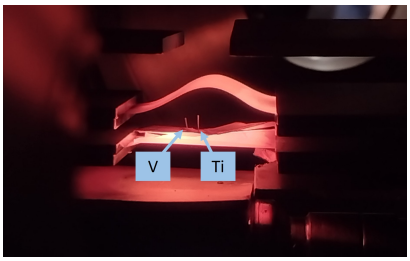

Figure 4.7: Vanadium and titanium wires on a graphite foil sample. The wires and the temperature of the resistor were monitored during heating to identify the voltage, current, and power required to melt the wires.

Table 4.2: CHI voltage, current, and power corresponding to the melting points of vanadium and titanium.

Temperature	**1668±167 °C**	**1910±145 °C**
Voltage $[V]$	4.34±0.32	5.14±0.23
Current $[A]$	228±26	264±27
Power $[W]$	987±135	1355±152

The γ transition of each sample was measured before and after heating. Since the isotope of interest, ^{7}Be has a half-life of 53 days, losses due to decays were not a concern, and the measurement time was set in a range of 300 s to one hour depending on the initial counts. The measurement time was not varied for the same sample (i.e. if a graphite pellet was initially measured for half an hour, all subsequent measurements would take half an hour). Each sample was measured twice before and after heating.

Among the three types of graphite target samples, the composite showed the highest release (Fig. 4.8). The low release of the pellet is expected due to its low porosity; however, since the graphite foil has high porosity, a higher release was expected from it. The low release of the graphite foil might as well be related to its anisotropy. The release of the long lived ^{7}Be isotope might be governed by effusion and not diffusion through particles, and assuming that the foil's empty space between layers only connect the edges of the foil,

then ^{7}Be only escapes the material through the rim of the foil instead of through pores distributed on the entire surface.

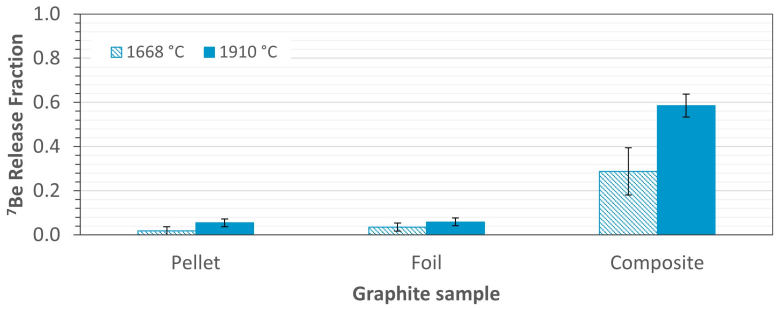

Figure 4.8: Comparison of the ^{7}Be release fraction among graphite samples irradiated under the same conditions (480 MeV and 5 µA for 300 s), and heated at two different temperatures.

The backing graphite foil gives structural stability to the ISAC composite targets; without it, the thin and highly porous slip casts would easily crumble. The release fraction reported for the composite considers the sample as a whole (Fig. 4.8), so the ^{7}Be that is not released from the composite's graphite foil results in an overall lower release fraction. By subtracting the ^{7}Be counts expected from the graphite foil, the composite's slip cast release fraction is 0.6 for 1668 °C and 1 for 1910 °C, which is an excellent result that promises a great online performance.

Offline release studies allow the comparison of several target materials in a fraction of the time that comparing them online takes. Excluding the waiting time for the irradiated samples to reduce their dose rate, studying the isotope release of three target materials with the offline methodology takes about a week, while the same comparison online would take months. Furthermore, given the offline studies results (Fig. 4.8), the beryllium provided to experiments would have been poor for two out of the three runs; thus, during those online campaigns, valuable experimental time would have been wasted as well as reliability and trust, necessary when trying to introduce a new target material to the established collection. The easy availability of the graphite foil and pellets make them attractive options to incorporate as online target material; however, the offline release experiments allow the comparison of their release and demonstrate that the ^{7}Be release fraction of the graphite composite is superior, suggesting that implementing a graphite-composite target would give a better yield performance online.

4.2 Online isotope release of target materials

During online irradiation, protons impinging the ISAC targets, induce fission, fragmentation and spallation in the target material. These processes produce isotopes that, after releasing from the material, are ionized and collected in experimental stations. As any other empirical

process, the ISOL method is not 100% efficient; some isotopes are lost during transport, others are not ionized, and many more isotopes decay before being released from the target material.

The isotope production rate is linearly proportional to the intensity of the proton beam current (Eq. 1.1), and the target material is heated to promote the isotopes' diffusion and increase the release efficiency (Eq. 4.6). At ISAC, the targets are irradiated with a proton beam energy of 480 MeV and currents up to 100 µA. Since the deposited power depends on the energy and intensity of the proton beam, the higher the proton-beam energy and current, the hotter the target material (Fig. 4.12). This is because as the proton beam passes through the target material it losses energy due to collisions with electrons and nuclei; in turn, the target gains energy and increases its temperature [119]. Ultimately, the intensity of the proton-beam current is limited by the capacity of the target material to dissipate the deposited proton-beam power.

At low proton currents, the target temperature is often not high enough to promote isotope release. To increase the temperature of the targets in a controlled manner, besides the heat due to proton-power deposition the targets are also resistively heated. Joule heating is a release efficiency booster because it increases the temperature of the oven, contributing to the increase and homogenization of the target material temperature. During online irradiation, the ISAC targets are heated via a dynamic combination of joule heating and beam power heating to increase and homogenize the target material temperature to deliver more intense Radioactive Isotope Beams. To estimate the target's operational temperature, that cannot be measured during online mode, the temperature is estimated with an analytical model [120] (Section 4.4).

The following sections present the RIB-release results for one graphite composite target and five UC_x targets that were submitted online. At the onset of the COVID-19 pandemic in-house development was prioritized over international research campaigns, which enabled this study and two weeks online development irradiation became available for the graphite composite target. In contrast, the time allowed to take yield measurements from UC_x targets varied from one to three days since these targets were irradiated on regular schedules when the isotope demand for experiments was high and competitive.

The isotopes measured from the graphite composite target were ^{8}Li, ^{9}Li, ^{11}Be, and ^{7}Be. To investigate the release efficiency of the graphite composite target, its yields were measured at a fixed temperature and at varied proton beam current, as well as at a fixed driver beam current and increasing temperature. The lowest proton driver beam current used was 10 µA, and the maximum was 80 µA; with increments of 10 µA.

Diverse isotopes were extracted from the UC_x targets made with the 1-step casting method. The isotopes measured in common among UC_x targets were ^{29}Mg, ^{31}Mg and ^{33}Mg, and ^{25}Na, ^{26}Na, ^{27}Na and ^{28}Na, as well as several francium and radium isotopes.

All the yields corresponding to each target, either graphite composite or UC_x, were analyzed. To characterize the global efficiency of their isotopes' release process ε (Eq 4.5)

$$\varepsilon = \frac{I_{obs}}{I_{in}}, \tag{4.5}$$

the targets' measured isotope yield rate I_{obs} was compared with the in-target production I_{in} which is the expected yield for the case of no isotope losses of any type. The I_{in} corresponding to UC_x and graphite-composite targets was calculated with Monte Carlo simulations (Section 4.3); the I_{in} of additional targets was obtained from ISAC's simulation database [15].

To assess the enhancement in isotope release due to temperature, some isotopes were extracted at the same conditions, but at increasing temperature. The corresponding release curves plotted against temperature were fitted with Eq. 4.6 [23] (described in Section 1.1.1):

$$\varepsilon = \frac{6}{\pi^2} \cdot \left(1 + \frac{\lambda}{\mu_0 e^{-Q/RT}}\right)^{-1}, \tag{4.6}$$

where λ is the decay constant of the given isotope, Q is the activation energy, R is the gas constant, T is the temperature, and μ_0 is

$$\mu_0 = \pi^2 \frac{D_0}{r^2} \tag{4.7}$$

with D_0 as a diffusion pre-exponential factor and r^2 the particle size of the target material.

Another approach to investigate the release efficiency of the target material is by comparing the yields of isotopes of the same element against their respective half-life. Isotopes of the same element have the same chemical properties, so their release should vary solely due to the target material characteristics and the isotope's half life, providing information on the time structure of the diffusion and effusion processes. In order to apply this approach, several isotopes from the same element are required, so it could only be applied for certain elements extracted from UC_x targets, and it was not used at all for analyzing yields from the graphite composite because the sets of isotopes per element obtained with this target were not enough. The ε curves plotted against half-life were fitted with the Lukic et. al. function [121] (Section 4.8.3)

$$\varepsilon = \frac{\varepsilon_s}{1 + (t_{1/2}/t_0)^{-\alpha}}, \tag{4.8}$$

where ε_s is the efficiency value for infinite half-lives $t_{1/2}$ (stable isotopes), α is the power function behaviour corresponding to the short half-lives, and t_0 indicates the transition from the power function behaviour to the constant behaviour as the isotopes half-lives get longer.

4.3 In-target production and power deposition

The in-target (I_{in}) production has been calculated with FLUKA, a Monte Carlo simulation package used for the calculation of particle transport and interactions of particles with matter [122]. FLUKA uses the EVAPORAT model to account for the fission, fragmentation and γ de-excitation on the nucleus of the target in order to estimate the corresponding isotope inventory for the given combination of target, and driver beam type and energy (e.g. UC_x, protons, 480 MeV). FLUKA numerically solves for the relevant nuclear reactions using the corresponding cross sections within a Monte Carlo framework. A FLUKA input was written for each target such that the I_{in} was obtained for a 1-step casting target, a 2-step casting target, a LaC_2 target, and a graphite composite target; each FLUKA input included the geometry of the given target, and its corresponding material composition.

The nominal geometry of the 2-step and 1-step casting targets was implemented in FLUKA (Fig 4.9). The 2-step casting and the graphite composite targets' geometry consist of D-shaped units with an area of 2.12 cm^2; while the 2-step casting has eight units, the graphite composite has fifteen. For the 1-step casting and LaC_2 targets, the geometry consist of 10 units with a D-shaped base of 1.2 cm^2 area and 1 cm length inside a graphite insert 12 cm long.

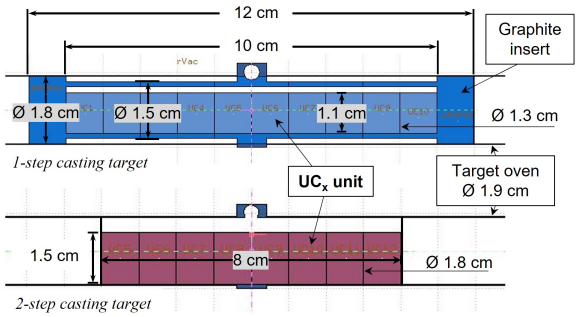

Figure 4.9: Cross section views of the online ISAC target geometries implemented for the FLUKA simulations of UC_x 1-step casting (top) and 2-step casting (bottom) targets. The graphite composite target geometry is identical to the 2-step casting target one, but instead of eight units, it has fifteen; therefore, it is 15 cm long.

The target material was implemented in FLUKA by mass fraction. The UC_x material description included the mass in a disc of carbon and uranium. The carbon mass included the carbon in the UC_2, as well as the excess graphite. The mass of the backing foil was also included in the UC_x material description (Table. 4.3). The graphite composite material, that was also described by mass fraction, included the mass of the graphite powder and the mass of the graphite foil per disc.

FLUKA uses the density of the materials declared in the code to attribute mass to each volume in the geometry. The density used in FLUKA to represent the target materials was their composed density (Eq. 2.8). For the UC_x target material, the composed density

combines the UC_2 bulk density and the graphite powder density, with the graphite foil density. Analogously, the graphite target composed density combined the density of its graphite powder composite with the density of its graphite backing foil (Table. 4.3).

Table 4.3: Densities used in FLUKA simulations for the graphite composite target, the 1-step casting and 2-step casting targets.

Material	**Density (g/cm^2)**
UC_2	3.28
Graphite powder	2.25
Graphite foil	1.15
UC_x + C on foil (1-step casting)	2.25
UC_x + C on foil (2-step casting)	2.13
Graphite composite on foil	0.97

To match with the irradiating conditions, the simulation parameters included a 480 MeV proton beam with a Gaussian profile with a full width at half maximum of 7 mm in the X and Y directions, both transverse directions of the beam.

The resulting residual nuclei were given in number of isotopes per proton for each of the units (Fig. 4.9). The number of total isotopes (I_{in}) produced in the target was obtained by adding the isotopes of each unit and normalizing to [$\mu A \cdot s^{-1}$]. To compare the isotope yields measured (I_{obs}) with I_{in}, the I_{obs} was normalized with its respective proton beam current.

The energy deposited by the proton beam was also estimated with FLUKA. Using the scoring command USRBIN, FLUKA scores the spatial distribution of energy deposited in a region. For the graphite composite target the scored region consists of the target units, and for the UC_x target the scored region included the target units and the graphite container (Fig. 4.9).

4.4 ISAC analytical model for target temperature

Measuring the target temperature accurately during irradiation is challenging. Most thermocouples drift due to transmutation and when operated above 1100 °C [123]. Advances have been done in the development of thermocouples with the capacity to measure temperatures above 1290 °C, and to withstand a fluence up to 1×10^{21} n/cm^2 [124]. However, ISAC's fluence is not neutral and the targets are high in carbon, so the thermocouples for this application not only would have to withstand the fluence but also corrosion. Additionally, the thermocouples would need to be electrically insulated to properly measure the temperature of joule-heated targets; therefore, they will be inevitably required to be (partially) thermally insulated [125].

A pyrometer is an alternative to monitor the temperature of the target. However, the area to measure the temperature is limited to the ion source (Fig. 2.59d), where optical

access is possible, so the results might not be reliable mainly because the ion source is heated independently from the target oven body. Currently, measuring the temperature of the ISAC targets online is not feasible; instead, the target temperature is estimated with the ISAC model [120], a semi-empirical analytical model that accounts for the electrical and proton-beam current contributions. This section presents the analytical model that has been used at ISAC to estimate the target temperature during its irradiation [99, 120, 126, 127] and its comparison to a Finite Element (FE) model developed in COMSOL for this work.

The objective of the ISAC model is to predict the necessary electrical and proton-beam current combination to keep the target material at high temperature for supporting isotope release, but without reaching its vaporization temperature at the operational pressure of 1×10^{-6} Torr [48]. The model assumes that the main heat exchange mechanism between the target material and the oven is conduction, so it ignores the radiative heat transfer in the void space between the flat face of the composite-discs stack and the oven. Furthermore, the ISAC model ignores the ion source and legs of the oven, as well as the ends of the oven's body; instead, it considers a tube of the length of the composite discs stack l_t (Fig. 4.10).

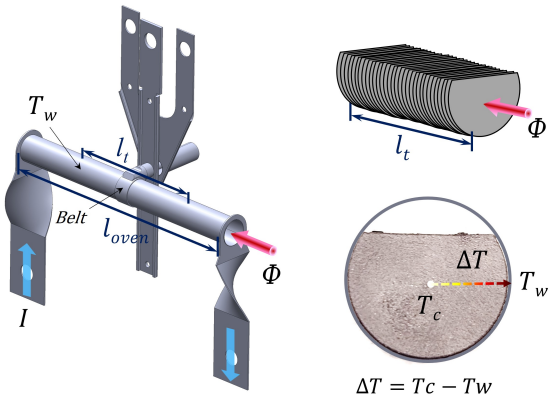

Figure 4.10: Depiction of the proton beam impinging the target, the stack of slip cast discs, and a disc indicating the location of the centre and wall temperature.

In the ISAC model, the target temperature is given by the total power deposited P_{tot}. P_{tot} includes the power deposited by the proton beam Q_{tot}, and the electric power P_e applied when the beam heating alone is insufficient to get the target to temperature. Furthermore, the ISAC model assumes that the power is dissipated by radiation from the target oven wall T_w (Fig. 4.10) to its surrounding water cooled vessel (considered a black surface), following Stefan Boltzmann's law [128]:

$$P_{tot} = \sigma \varepsilon_{eff} A_t (T_w^4 - T_a^4), \tag{4.9}$$

where σ is the Stefan Boltzmann constant (5.67×10^{-12} W·cm^{-2}·K^{-4}), T_a is the ambient temperature (i.e. 300 K), A_t is the oven area facing normally towards the vacuum vessel,

and ε_{eff} is the tantalum-oven effective emissivity that is estimated experimentally [126] (Appendix B).

In the ISAC model it is assumed that the power deposited by the beam heats the axial centre of the target material uniformly. According to this model, the central temperature T_c is the maximum temperature in the target. The temperature difference between the oven wall and the central axis of the target is given by:

$$\Delta T = T_c - T_w. \tag{4.10}$$

It follows that the temperature in the axial centre of the target T_c is

$$T_c = T_w + \Delta T; \tag{4.11}$$

the wall temperature (T_w) is obtained by solving Eq. 4.9

$$T_w = \left(\frac{P_{tot}}{\sigma \varepsilon_{eff} A_t} + T_a^4 \right)^{1/4}. \tag{4.12}$$

Substituting Eq. 4.12 in Eq. 4.11, gives an expression of the axial temperature of the target (Eq. 4.13)

$$T_c = \left(\frac{P_{tot}}{\sigma \varepsilon_{eff} A_t} + T_a^4 \right)^{1/4} + \Delta T, \tag{4.13}$$

where $P_{tot} = Q_{tot} + P_e$.

The proton beam power is deposited in an orthogonal Gaussian distribution in the axial centre of the target (Fig. 4.10). Thus, the discs would transfer heat from the centre to the target wall as in Eq. 4.14 [126]

$$\Delta T = \frac{\phi Q_{comp}}{2\pi k_c} \left(1.204 + \ln \frac{r}{3r_0} \right) \tag{4.14}$$

where k_c is the thermal conductivity of the target material, r is the radius of the target disc, and r_0 is the half width at half maximum of the Gaussian proton beam spot. The thermal conductivity k_c corresponding to the composite is calculated with the thermal conductivity of the individual components of the slip cast and their corresponding volume fraction [120]

$$k_c = \lambda_{slip-cast} k_{slip-cast} + \lambda_{foil} k_{foil}. \tag{4.15}$$

When estimating k_c with Eq. 4.15, only the composite and foil thermal conductivities are considered, while the potentially different thermal conductivity of the contact zone between them is left out. Moreover, Eq. 4.15 is evaluated with theoretical values, so it is likely that the calculated thermal conductivity differs from that of the in-house developed com-

posites. A test stand Chamber for Heating Investigations has been developed [34], and when commissioned it will allow the study of the ISAC and ARIEL target materials thermal properties.

The power deposited by the proton beam is estimated with SRIM (The Stopping and Range of Ions in Matter) [129]. The energy of the proton beam, and the density of each part of a composite disc (Fig. 2.4) are used in SRIM to obtain the power deposited of the slip-cast ($Q_{slip-cast}$) and the backing foil (Q_{foil}). The power deposition in a composite (Q_{comp}) is estimated with [120]

$$Q_{comp} = f_{slip-cast} Q_{slip-cast} + f_{foil} Q_{foil}, \tag{4.16}$$

where $f_{slip-cast}$ and f_{foil} are the fractional thickness of the slip cast and foil respectively.

The total power deposited in the target material Q_{tot} is calculated multiplying the power deposited per composite with the proton beam current ϕ, and the length that all the composites occupy to form a target (l_t) [120]

$$Q_{tot} = Q_{comp} \cdot \phi \cdot l_t. \tag{4.17}$$

The electrical power (P_e) deposited by the resistive heating used in the ISAC model is determined experimentally. The electrical power recorded when resistively heating the target in the non-actinide furnace is plotted against the corresponding electrical current; then, the curve is fitted to obtain the equation that describes the electrical power as a function of the current [126]. For the graphite-composite target, the electrical power is given by Eq. 4.18 [78]

$$P_e = (7 \times 10^{-6} I^3 + 6.73 \times 10^{-3} I^2 - 233.2 \times 10^{-3} I + 2.1275), \tag{4.18}$$

where I is the current that passes through the target-oven.

The ISAC analytical model has been also used to predict the temperature of the UC_x targets made with the new method (Section 2.3). However, unlike the rest of the ISAC targets, the new UC_x target is irradiated in a graphite container that is only in contact with the tantalum oven through a narrow belt (1 cm wide) in the centre (Fig. 3.4). To account for this difference in geometry, the ISAC model uses an electrical power function that depends on the temperature of the oven that is over the graphite container's belt (T_{belt}) (Fig. 4.10); assuming that the electrical power is dissipated to the ambient by radiation, but that the temperature of the oven belt T_{belt} dominates over the oven wall's temperature T_w, the electrical power for a target in a graphite container is given by

$$P_e = \sigma \varepsilon_{eff} A_t (T_{belt}^4 - T_a^4); \tag{4.19}$$

as before, σ is the Stefan Boltzmann constant, T_a is the ambient temperature (i.e. 300 K), A_t is the target oven area emitting heat, and ε_{eff} is the tantalum oven effective emissivity.

The temperature of the oven belt was obtained experimentally and expressed in terms of the electrical current I [78]:

$$T_{belt} = 26.3 \times 10^3 e^{I/2.5\times10^3} + 26.4 \times 10^3 + 15.6 \cdot I. \tag{4.20}$$

The established ISAC model was used to predict the online temperature of all the targets presented in this work. It was after analyzing their isotope release data that the need of new models became apparent. The temperature predictions obtained with the ISAC model for a graphite composite were compared with the results obtained with an FE model developed for this work (Section 4.5). Furthermore, the ISAC model temperature predictions for a UC_x target were compared with a FE and a new analytical model that was also developed for this work (Section 4.7.2 and 4.7.1). Similar to the ISAC model, the FE and the new analytical model consider a simplified tantalum oven, consisting of a tube without legs nor an ion source. Also, for their temperature results to be comparable, all the models were evaluated with the same values for emissivity, area, thermal conductivity, electrical power, and total power deposited by the corresponding proton beam current.

4.5 Graphite target thermal FE analysis

A Finite Element (FE) analysis simulation campaign has been carried out with COMSOL [107] to estimate the temperature gradient within the graphite-composite target. The simulations include electrical power and proton-beam power deposition by themselves and combined. The temperature results obtained with these simulations were compared with those from the ISAC analytical model [120] (Section 4.4).

A simplified geometrical CAD model of the graphite-composite target was drawn in SolidWorks [108], and imported to COMSOL. The tantalum oven drawing consisted of a tube with the same dimensions as the target oven (Fig. 4.11), but with no legs or ion source to ease the computational load. The target material geometry consisted of a D-shaped cylinder, 15 cm long and centred in the oven (Fig. 4.11).

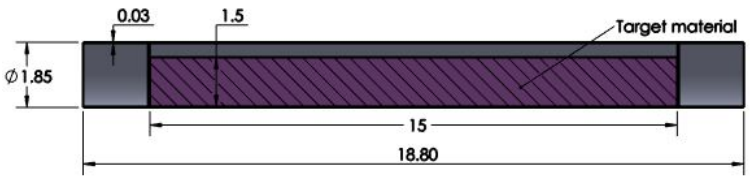

Figure 4.11: Section view of simplified oven loaded with target material with measurements in cm. In contrast with a target oven, this simplified oven does not have legs nor an ion source to ease the computation time for thermal FE simulations.

The heat sources for the FE COMSOL model are the electric power, and the driver beam power deposition. For the electric power, the simulation includes joule heating; the terminal

and ground are set on the circular edges of the oven. The used current values were 100 A, 200 A, 400 A, and 600 A. In contrast to the ISAC analytical model, that uses the power deposition estimated by SRIM, the COMSOL simulations use the power deposited by the proton beam obtained from FLUKA (Section 4.3). The volumetric power deposited per µA is scaled to 10 µA, 40 µA, 70 µA and 100 µA, and it is assigned to the volume corresponding to the target material in the COMSOL model (Fig. 4.11).

The contact between target material and oven is considered ideal. Since the target-material is D-shaped, it exchanges heat by conduction and radiation; in the simulations, the area of the target volume in contact with the oven was set for conduction, while the area that is not in contact was set to exchange heat through radiation.

The emissivity values assigned to the geometry's faces were obtained from COMSOL's library [130, 131, 132, 133] or from the values typically used in the ISAC model for online targets [134]. Since the interior of the oven was TaC coated, in the simulation its internal emissivity was set to the one corresponding to TaC [130]:

$$\begin{aligned} \varepsilon_{TaC} &= 1.04521975 - 8.37163834 \times 10^{-4} T \\ &+4.80496757 \times 10^{-7} T^2 - 2.18448349 \times 10^{-11} T^3 - 2.42182384 \times 10^{-14} T^4. \end{aligned} \tag{4.21}$$

The emissivity corresponding to the external wall of the oven was fixed to 0.34 as reported in [126] for ISAC tantalum ovens without heat shields. Furthermore, the emissivity assigned to the target material was given by Eq. 4.22, corresponding to Graphite 3474 D (solid, parallel to extrusion axis) [131]

$$\varepsilon_c = 0.6852302 + 2.856198 \times 10^{-4} T. \tag{4.22}$$

Even though this emissivity corresponds to graphite, it most likely differs from that of the graphite composite target because the emissivity depends on the material surface's condition [128]. The emissivity values for the graphite-composite target and the interior of the tantalum oven were obtained from the literature because they are not used in the ISAC model. Since 72% of the target material total area is in contact with the oven, the ISAC model assumes that conduction, and not radiation, is the dominant mechanism for heat exchange between those volumes; which, according to the FE simulation results (Fig 4.18a) seems to be the case.

The thermal conductivity values used in the simulation were also taken directly from COMSOL's library or from the values typically used in the ISAC model for online targets. The thermal conductivity (k) assigned to the tantalum oven of 60 W/m·K corresponds to the k of solid annealed tantalum available in COMSOL's library [132]. On the other hand, the thermal conductivity of the graphite composite is set to 32 W/m·K [78], corresponding to the value typically used in the ISAC model for online targets. This thermal conductivity

was estimated using Eq. 4.15 with a thickness fraction of 0.42 and 0.58 for the graphite foil and slip-cast correspondingly, and 55 W/m·K [35] and 15 W/m·K [78] for their respective thermal conductivity. Moreover, the contact between the oven and the target material was considered ideal in both, the ISAC model and the FE simulation.

To examine the temperature gradient of the graphite-composite target (Fig. 4.11) due to the proton beam current, an FE simulation was run with the proton beam power deposition as the only heat source. The simulation was evaluated at proton-beam currents between 10 µA and 100 µA to include those used during the graphite-composite target irradiation. The maximum temperature in the target material obtained with COMSOL was compared to the axial temperature estimated by the ISAC model (Fig. 4.12). Both models were evaluated under the same conditions, and with the same material properties. The difference between the compared values is negligible, being the largest difference 36 °C (Fig. 4.12).

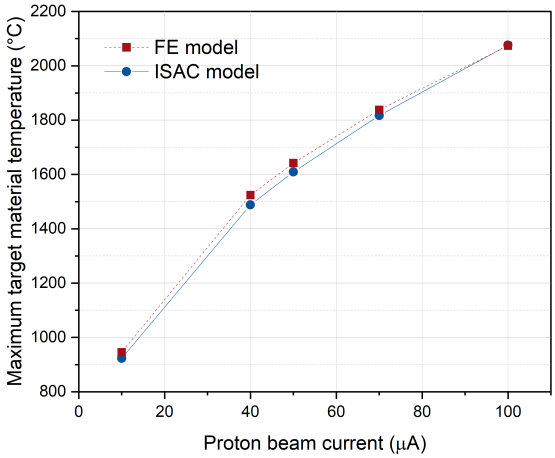

Figure 4.12: Maximum temperature of graphite composite target calculated with the ISAC model and with COMSOL simulations. The heat source in both cases is the power deposited by the proton beam current, and no joule heating is applied. (Connecting lines are for guiding the eye only).

A non-uniform temperature was obtained from the simulation of a graphite-composite target heated with the power deposited by a proton beam (Fig. 4.13). The density and geometry of the target material are taken into consideration in the FLUKA simulation (Sec. 4.3), so the power deposited by the proton beam imported in COMSOL is not uniform through the axial centre as assumed in the ISAC analytical model. The simulation results shows that when the power deposited by the proton beam is the only heat source, the zone with maximum temperature is close to the centre of the target material (Fig. 4.13); further, up to 100 µA, the hottest zone does not encompass the entire target material, and it is shifted towards the left (Fig. 4.13d) in agreement with the entrance of the proton beam, where a higher power deposition occurs according to the FLUKA simulations.

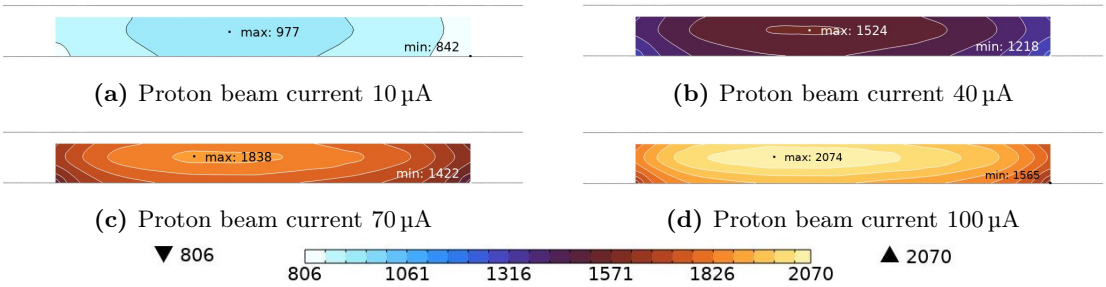

(a) Proton beam current 10 µA **(b)** Proton beam current 40 µA

(c) Proton beam current 70 µA **(d)** Proton beam current 100 µA

Figure 4.13: Temperature distributions (in °C) for a graphite target irradiated with a proton beam of 480 MeV and a beam current of 10 µA (a), 40 µA (b), 70 µA (c), and 100 µA (d).

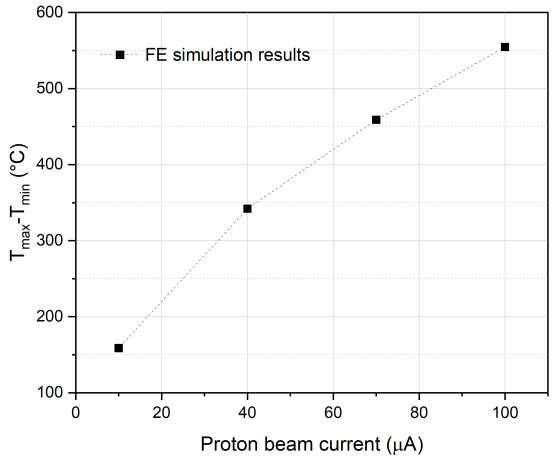

Figure 4.14: Difference between maximum and minimum target-material temperature. A graphite target was simulated with COMSOL using only proton beam power deposition as heating source. The maximum-minimum temperature difference increases as the proton beam current (line for guiding the eye only).

The COMSOL simulation results show that as the irradiating proton-beam current increases, so does the temperature gradient of the graphite-composite target. When irradiated with a proton beam current of 10 µA the difference between the maximum and minimum temperature in the target material volume is 159 °C, while it is 555 °C for the same target at 100 µA (Fig. 4.14). Large temperature gradients are troublesome; ideally, the entire target material would be at a uniform temperature to promote isotope release (Eq. 1.14). During irradiation online, it is almost never the case that the target is only heated with the power deposited by the proton beam; in an attempt to increase or homogenize the temperature, the targets are joule heated.

To investigate the graphite target material's (Fig. 4.11) temperature gradient due to electrical power, a simulation with only joule heating was performed. The simulation was evaluated at 100 A, 200 A, 400 A, and 600 A. This range encompasses the lower and upper operational limits used during target irradiation (100 A to 580 A). In contrast with the results for power deposited by protons as heat source, the longitudinal temperature gradients due

to joule heating are negligible; the largest difference of 61 °C corresponds to the case where the oven is resistively heated with an electrical current of 600 A (Fig. 4.15).

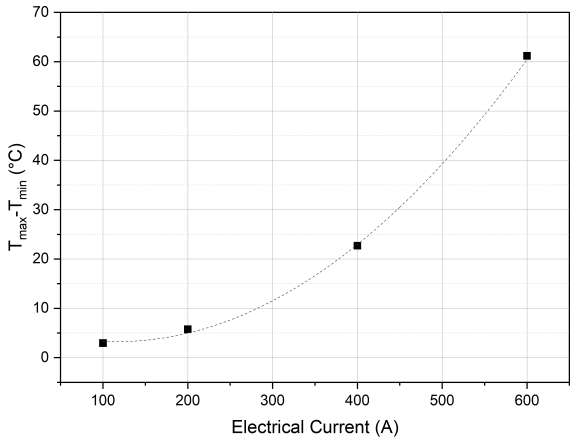

Figure 4.15: Graphite composite maximum heat gradient due to oven joule heating (line for guiding the eye only).

According to the simulations, the target material's temperature distribution due to joule heating (Fig. 4.16) is remarkably uniform in comparison to the temperature distribution given by proton-beam power deposition (Fig. 4.13). For 100 A and 200 A the difference between the maximum and minimum temperature in the axial cross section is only 2 °C and 4 °C, respectively (Fig. 4.16a and 4.16b). At higher electrical currents, the difference between maximum and minimum temperature in the axial cross section is also small, being 13 °C at 400 A and 41 °C at 600 A (Fig. 4.16c and 4.16d). The temperature distribution obtained with the simulation target is uniform because the tantalum oven (Fig. 4.11) resistance is isotropic; furthermore, the contact between the target material and the oven is considered ideal, so the target material heats uniformly by conduction.

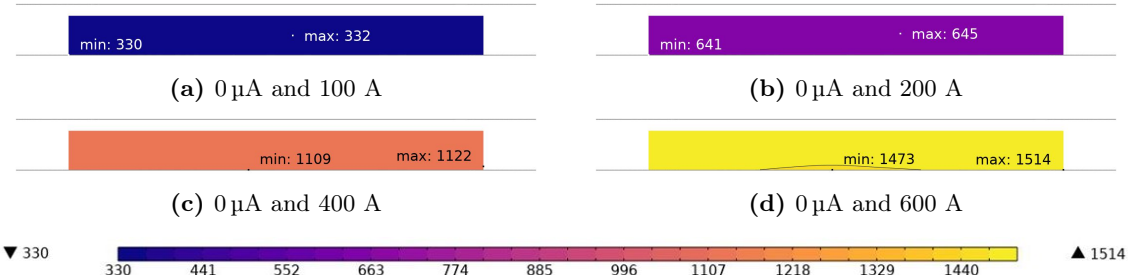

(a) 0 µA and 100 A **(b)** 0 µA and 200 A **(c)** 0 µA and 400 A **(d)** 0 µA and 600 A

Figure 4.16: Target temperature (in °C) distribution in the cross section of a graphite target resistively heated with 100 A (a), 200 A (b), 400 A (c) and 600 A (d).

The electrical power resulting from the COMSOL simulation differs from the experimental one used in the ISAC model (Fig. 4.17). The disagreement between the electrical power values predicted by the COMSOL simulations and the empirical function reflects the difference between the complete geometry of the target-oven, and the simplified geometry used in

the FE model. While the empirical electrical power corresponds to a graphite-composite target resistively heated in a tantalum oven (Fig. 1.7b), COMSOL uses a simplified geometry of the oven, that excludes the target-oven legs and ion source. However, the legs and ion source are water-cooled and might not contribute to increasing the target material temperature, but contribute to the voltage drop of the whole electric circuit (Fig. 4.11). Furthermore, the FE simulation considers the contact between the material and oven ideal.

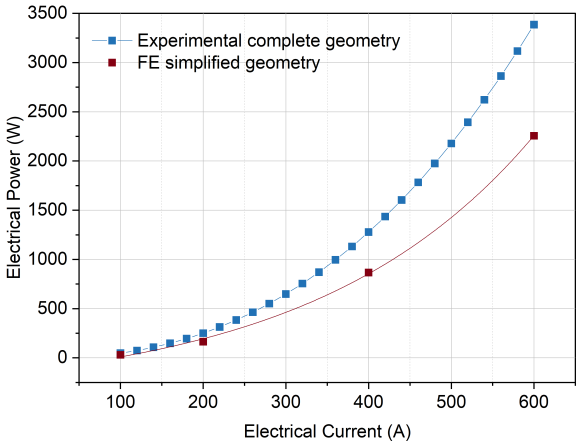

Figure 4.17: Electric power corresponding to resistively heated graphite-composite target. The electrical power obtained with COMSOL simulations is lower than that of the ISAC model that is obtained experimentally. This discrepancy is most likely due to differences between the real geometry of the target oven and the simplified geometry used in the FE simulation.

The graphite composite target's temperatures given by electrical and proton-beam current as heat sources were estimated with the FE and ISAC models, and were compared. The temperatures corresponding to a graphite target irradiated with 10 µA, 20 µA, 40 µA, 50 µA, 70 µA and 100 µA were plotted against electrical current (100 A to 600 A) (Fig. 4.18); these proton-beam and electrical currents were chosen because the graphite targets developed in this work are typically irradiated within these ranges.

The ISAC model (Eq. 4.13) was evaluated with the empirical electrical power, and with the electrical power obtained with COMSOL (Fig. 4.17). When using the FE's electrical power, the ISAC model matches well with the simulation results (Fig. 4.18a). The largest temperature difference of 57 °C occurs for a proton beam of 10 µA at an electrical current of 600 A. On the other hand, the temperatures obtained with the ISAC model when evaluated with the empirical electrical power differ from the FE simulation results up to 237 °C (Fig. 4.18b); these temperature results correspond to those used as reference during the online irradiation of the graphite-composite target.

The temperature curves corresponding to the ISAC model evaluated with the empirical electrical power have a better match for lower than for higher electrical currents (Fig. 4.18b). Since the empirical and FE electrical powers are similar below 200 A (Fig. 4.17), it is expected for the temperatures estimated with ISAC model evaluated with the empirical electrical

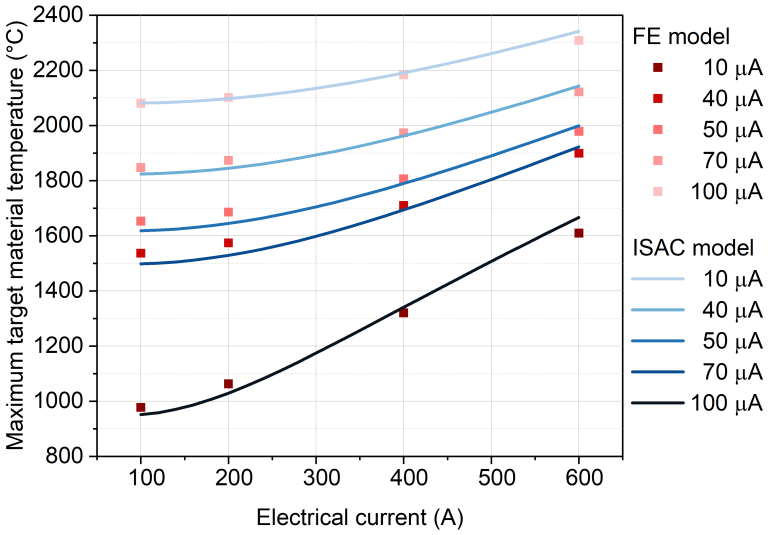

(a) ISAC model evaluated with FE resulting derived power.

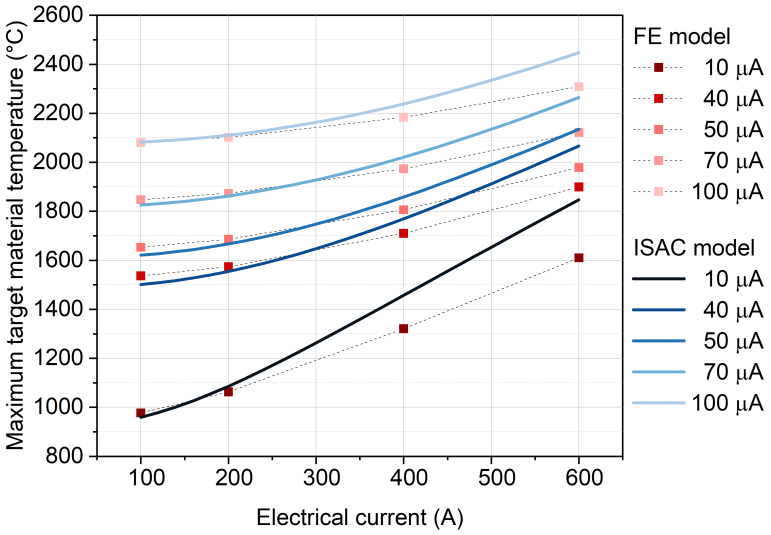

(b) ISAC model evaluated with empirically derived electrical power.

Figure 4.18: Comparison of the maximum temperature obtained with an FE model and the ISAC model for a graphite-composite target. The results correspond to the maximum temperature of the target material at different proton beam currents, and increasing electrical currents. The ISAC model (Eq. 4.13) was evaluated with the electrical power obtained with COMSOL (a), and with electrical power obtained experimentally (b).

current to match with the FE simulations below 200 A. As the proton-beam current is higher, the temperature difference reduces; this is because at high proton-beam current the power deposited dominates over the electrical contribution.

In conclusion, the maximum temperature of the target material estimated with the ISAC model agrees with FE simulations when evaluated at the same electrical power. This suggests that the analytical model is in agreement with the physical process accounted with COMSOL simulations. However, the electrical power obtained with FE simulations differs

from the one obtained experimentally, and evaluating the ISAC model with this electrical power results in temperatures that can be up to 237 °C hotter than the ones obtained with FE simulations in the range evaluated, going from 10 µA to 100 µA and from 100 A to 600 A. This discrepancy likely suggests, that the power measured empirically is not totally used to heat the system and that revisiting the methodology could help identify where the potential losses are located.

In contrast with the ISAC analytical model, temperature distributions can be extracted from the COMSOL simulations (Fig. 4.19). While the ISAC analytical model provides the highest temperature in the target, it does not estimate its temperature gradient such that it can not identify the extent of the hot and cold zones which can compromise diffusion and effusion patterns greatly. On the other hand, FE simulations allow the observation of these temperature gradients, as well as the identification of minimum, maximum, and average temperature at specific points.

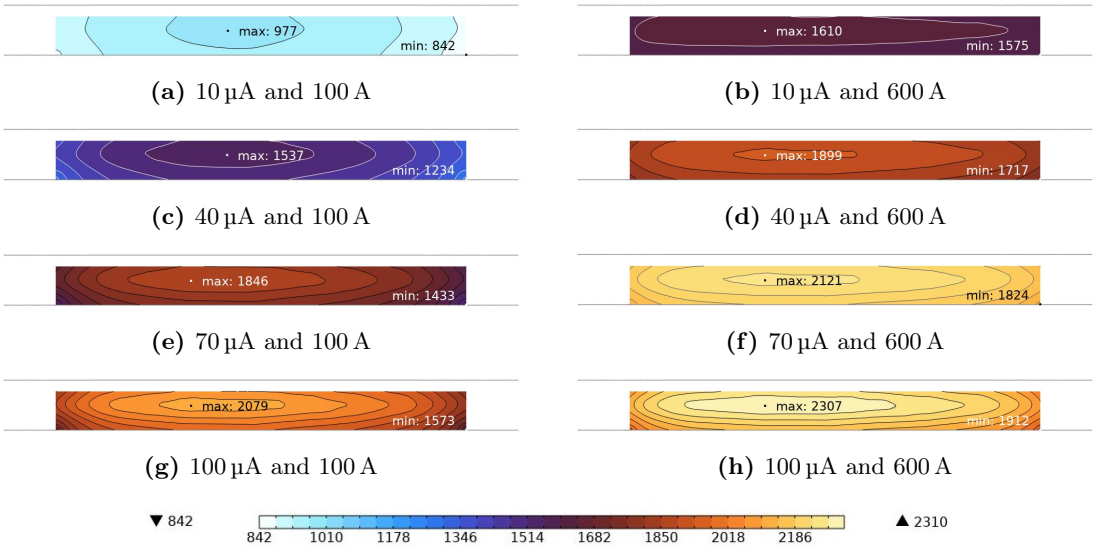

(a) 10 µA and 100 A **(b)** 10 µA and 600 A

(c) 40 µA and 100 A **(d)** 40 µA and 600 A

(e) 70 µA and 100 A **(f)** 70 µA and 600 A

(g) 100 µA and 100 A **(h)** 100 µA and 600 A

Figure 4.19: Target temperature distributions for a graphite target heated with increasing proton-beam current at 100 A and 600 A.

According to the simulations, a uniform target material temperature is not achievable within the ISAC operational range. The target material temperature gradient implies different isotope diffusion rates, favouring the hot zones. For all the combinations of electrical power and proton beam intensity, the highest temperature is close to the centre of the target, but shifted towards the left, matching the entrance side of the proton beam (Fig. 4.19). The minimum difference between maximum and minimum temperature in the axial cross section of the target corresponds to the case where the beam current is 10 µA and the electrical current is 600 A; at this combination, there is only 35 °C difference between the maximum and minimum temperature in the axial cross section of the target (Fig. 4.19b).

The joule heating reduces the overall temperature gradient of the graphite target. The difference between maximum and minimum temperature increases as the proton beam intensity increases (Fig. 4.14), but it reduces as the electrical current increases (Fig. 4.20); this tendency suggests that a larger electrical current eventually would homogenize the target temperature. However, the target material is kept below 2000 °C during operation to avoid material vaporization; since the heating electrical current can only be increased to 600 A, the maximum irradiation proton-beam current allowed is 70 µA, such that the target temperature stay below 2000 °C (Fig. 4.22).

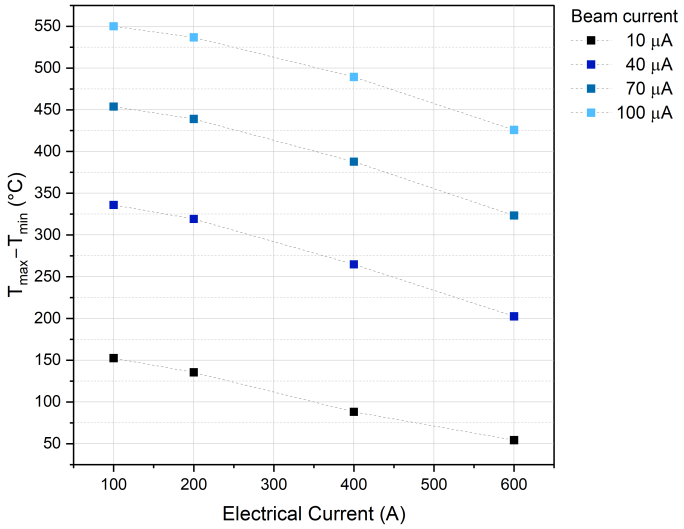

Figure 4.20: FE results for a graphite target maximum and minimum temperature difference when evaluated at increasing electrical and proton-beam currents (lines to guide the eye).

Having a large hot zone throughout the target material promotes efficient isotope release. An approach to quantify the extend of the hot zones in the target material is to compare its maximum (T_{max}) and average (T_{ave}) temperature:

$$\frac{T_{max} - T_{ave}}{T_{max}}. \tag{4.23}$$

The closer the average temperature is to the maximum temperature, the larger is the hot zone; the larger the hot zone the closer Eq. 4.23 is to zero. Among the combinations presented in Fig. 4.19, the one with the largest hot zone corresponds to the case where the graphite target is irradiated with 10 µA and resistively heated with 600 A (Fig. 4.21). This outcome is expected because this combination of proton and electric currents has the lowest temperature gradient (35 °C) through its axial centre (Fig. 4.19b). Overall, the lower the electrical current the smaller the hot zone tends to be, and the opposite effect results for higher electrical currents (Fig. 4.21).

The graphite-composite target was irradiated at increasing proton beam intensity. During proton beam ramp up, the electrical current was regulated to keep the temperature stable

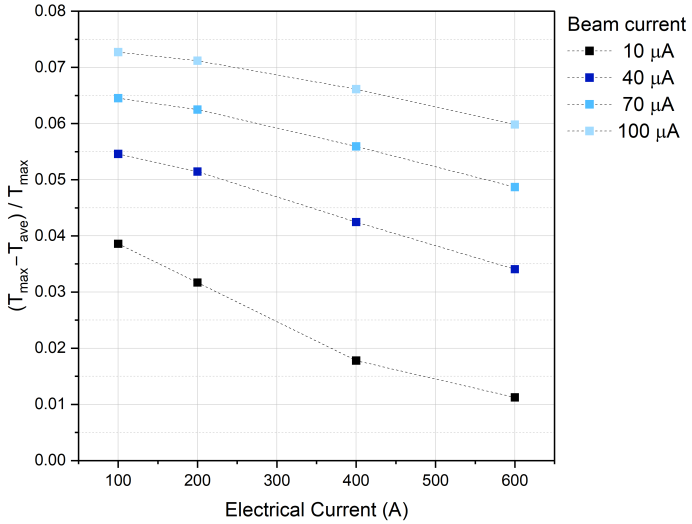

Figure 4.21: Comparison of maximum and average temperatures obtained with COMSOL for a graphite target at increasing proton-beam and electrical currents.

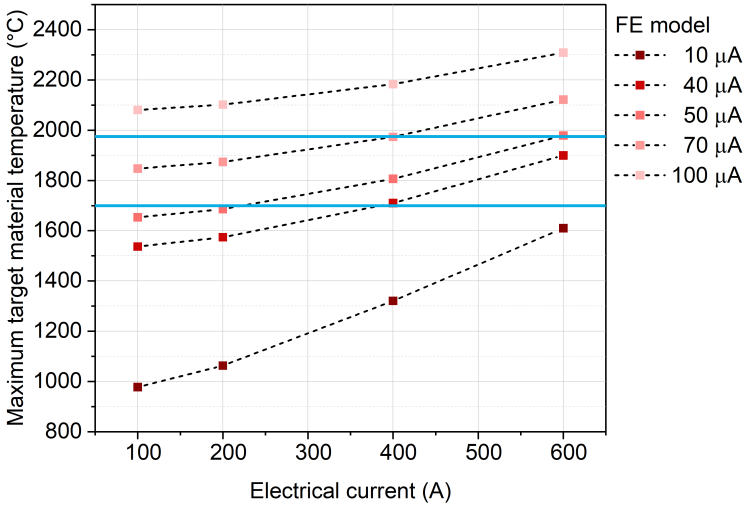

Figure 4.22: Graphite-composite isotherms of 1700 °C and 1970 °C crossing the curves for maximum temperature at different curves for several proton beam currents.

in accordance to the predictions of the ISAC model evaluated with the empirical electrical power. In first order, if the target is at a uniform temperature, the isotope release would increase linearly with the intensity of the proton beam (Eq. 1.1); however, the FE simulations indicate a temperature gradient in the target. To assess the extent of the maximum temperature in the target-material volume, two additional sets of COMSOL simulations at different proton currents were run. One set aimed at proton electrical current combinations resulting in a maximum temperature of ≈1700 °C, comprising low proton beam currents. The second set comprised high proton electrical current combinations resulting in a maximum temperature of ≈1970 °C (Fig. 4.22).

The temperature maps resulting from the simulations, show that the isotherms encompassing the maximum temperature decreases as the proton beam intensity increases (Fig. 4.23 and Fig. 4.24). Also, the temperature gradient increases with higher proton beam intensity. From the maps with maximum temperature of ≈1700 °C, the case with the smallest temperature gradient and consequently larger hot zone corresponds to the proton beam and electrical current combination of 10 µA 665 A (Fig. 4.23). Similarly, the maps with a maximum temperature of 1970 °C also show that with higher proton beam intensity the hot zone shrinks and the temperature gradient exacerbates (Fig. 4.24).

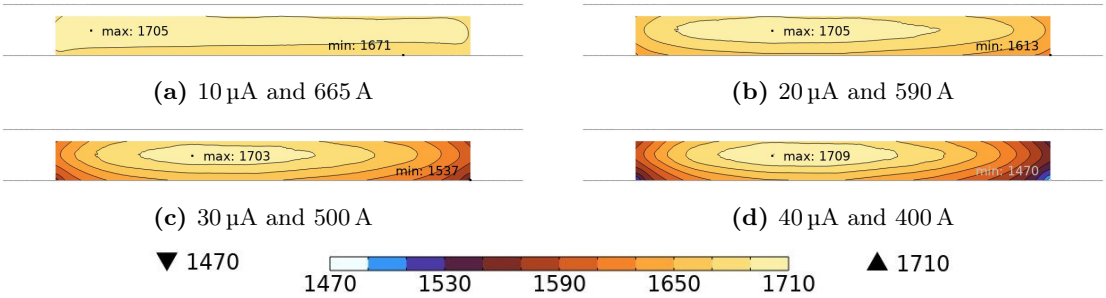

(a) 10 µA and 665 A **(b)** 20 µA and 590 A

(c) 30 µA and 500 A **(d)** 40 µA and 400 A

Figure 4.23: Temperature maps of graphite-composite target irradiated at increasing proton beam current and decreasing electrical current to stay at same nominal maximum temperature of ≈1700 °C.

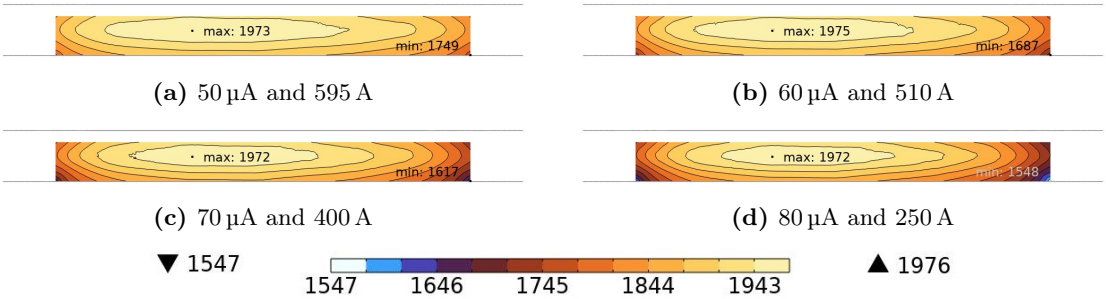

(a) 50 µA and 595 A **(b)** 60 µA and 510 A

(c) 70 µA and 400 A **(d)** 80 µA and 250 A

Figure 4.24: Temperature maps of graphite-composite target irradiated at increasing proton beam current, and decreasing electrical current to stay at same nominal maximum temperature of ≈1970 °C.

The hot zone of the target material for the cases were the maximum-temperature was 1700 °C or 1970 °C was quantified. For the simulations set to a maximum temperature of 1700 °C, the effective volume (V_{eff}) of target material at a temperature higher than 1630 °C was integrated. Similarly, for the simulation set to a maximum temperature of 1970 °C, the integrated volume had a temperature higher than 1900 °C. The effective volume fraction for a target of V_{tot} =31.854 cm^3 was calculated with:

$$V_{frac} = \frac{V_{eff}}{V_{tot}}. \tag{4.24}$$

Confirming the observations of the temperature maps, the hot zone's volume fraction decreases with increasing proton beam current (Fig. 4.25). The graphite-composite target irradiated with a proton current of 10 µA and resistively heated at 665 A is close to the ideal configuration where the target has a uniform temperature.

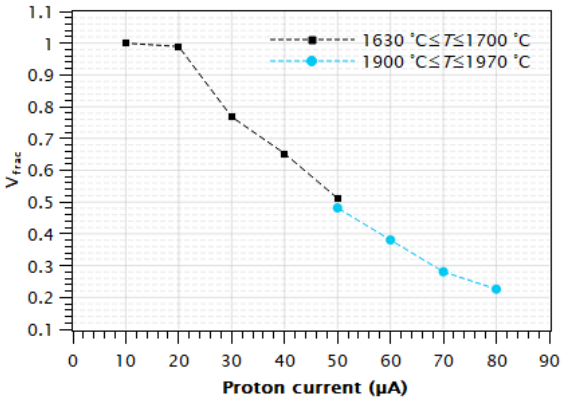

Figure 4.25: Volume fraction of target material at 1630 °C$<T<$1700 °C in black and 1900 °C$<T<$1970 °C in blue.

The isotope production (I_{RIB}) is linearly proportional to the proton beam intensity (ϕ) [10]

$$I_{RIB} \propto \phi. \tag{4.25}$$

However, as the proton-beam current increases, the target material volume that would be releasing isotopes at maximum temperature shrinks (Fig. 4.25). Although it is not the case, let's assume for a moment that the isotope production is limited to the hottest zone of the target material, and explore if the shrinking of the volume of maximum release (V_{frac}) is compensated by the higher isotope production expected from increasing proton-beam current (ϕ). For the cases where the maximum temperature is 1700 °C the hot zone shrinking is compensated up to 40 µA (Fig. 4.26). On the other hand, for the cases where the maximum temperature is 1970 °C, increasing the proton beam intensity does not compensate the shrinking of the hot zone (Fig. 4.26). This exercise demonstrates the importance of the graphite target temperature gradient; efforts in the improvement of the target's temperature homogeneity should be carried out to increase the target's overall release efficiency.

The maximum temperature of the graphite-composite target was estimated with temperature dependent emissivity. The results obtained were compared with those for fixed emissivity (Fig. 4.27). The simulation conditions were identical in both cases, except for the emissivity of the external surface of the oven, corresponding to the temperature-dependant emissivity of annealed tantalum [133] listed in COMSOL:

$$\varepsilon_{Ta} = -0.04725696 + 1.627855 \times 10^{-4} T - 1.352556 \times 10^{-8} T^2. \tag{4.26}$$

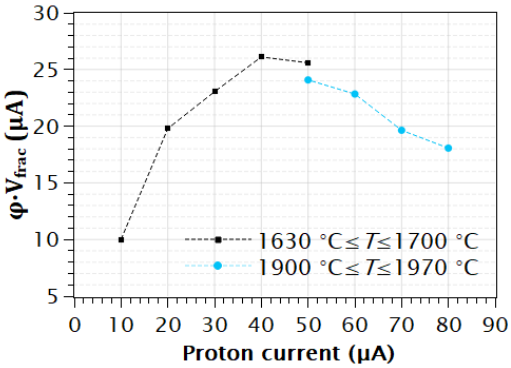

Figure 4.26: Product of the fraction of target material at maximum temperature (V_{frac}) and its corresponding proton-beam current (φ), indicating the fraction of isotopes that would be released at maximum temperature.

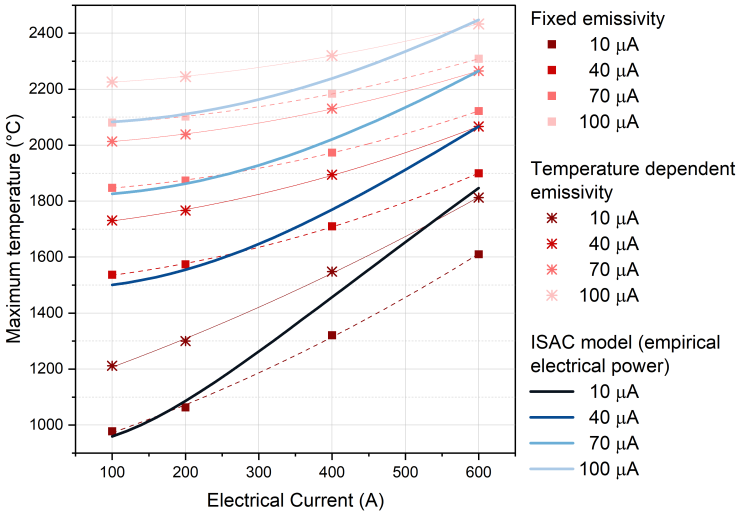

Figure 4.27: Comparison of maximum temperature results for graphite composite target when evaluated in COMSOL with fixed emissivity versus temperature-dependent emissivity.

The maximum temperature results for the graphite target are higher for COMSOL simulation using temperature-dependent emissivity instead of a fixed effective emissivity (Fig. 4.27). Fortuitously, the maximum temperatures of the ISAC model at 600 A matches those obtained with simulations using temperature dependent emissivity.

The ISAC analytical model does not estimate the target's temperature gradient such that it cannot identify the extent of the hot and cold zones which can compromise diffusion and effusion patterns greatly. On the other hand, FE simulations allow the observation of temperature gradients, minimum, maximum, and average temperatures at specific points.

Investigations into the thermal properties of the target material and tantalum oven should be carried out. Experimentally obtained values of the target's emissivity, and thermal and electrical conductivity grant more accurate simulation results that, in contrast with an analytical model, would showcase the temperature gradient distribution through the target

material and oven, allowing the optimization of the target-oven's geometry towards uniform target-material temperature. The evolution of the p2n oven design (Fig. 4.28), an ARIEL target developed by Luca Egoriti [135], is an example of the FE simulation capabilities; the temperature gradient in the p2n target (Fig. 4.28), was reduced considerably by modifying the oven's legs geometry (Fig. 4.28b). Furthermore, more accurate simulation results will allow the research and development of more efficient target materials with enhanced thermal conductivity to promote homogeneous isotope release.

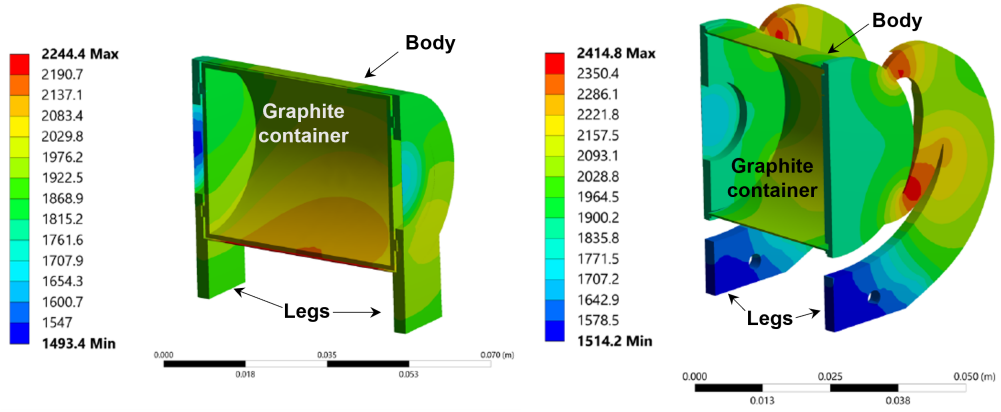

(a) Heating electrical current 1.0 kA **(b)** Heating electrical current 1.5 kA

Figure 4.28: Evolution of the legs of a target oven, aiming at reducing the graphite container temperature gradient [135].

The ISAC model evaluated with the experimental electrical power is used to estimate the temperature of the targets online. To keep the target material below 2000°C during irradiation, the current that resistively heats the oven is increased or decreased based on the ISAC model predictions for the given proton current and electrical current combination. In the case of the graphite-composite target, the temperature was not only used to stabilize the material temperature below 2000°C, but the electrical current was also regulated to ramp up the target temperature while irradiating at a fixed proton beam current. Furthermore, with the ISAC model estimations for the maximum temperature, the graphite-composite target was joule heated such that at increasing proton currents the target temperature remains the same; the objective of this operational mode was to assess the linear dependence of the isotope production to the proton beam intensity. The next section presents the yield results obtained from the online irradiation of a graphite-composite target.

4.6 Competitive graphite target isotope intensity

Until 2019, TRIUMF's demand of light isotopes was supplied mostly through tantalum, SiC, or UC_x targets. However, it was foreseen that a graphite-composite target would allow the supply of light isotopes at competitive rates (Fig. 4.29). Also, since a graphite

target is composed of carbon, a low Z material ($Z = 6$), it cannot produce heavy long-lived isotopes (i.e. ^{227}Ac, ^{209}Po) that emit alphas and complicate the manipulation and disposal of targets after operation. Additionally, being a low Z material allows operating the graphite target at higher proton-beam power since it has less power deposition, promoting higher RIB intensity (Eq. 1.1). Further, unlike UC_x targets, synthesizing graphite targets does not require special precautions because carbon is not a radioactive material, so varying the production methodology of graphite targets is more attainable.

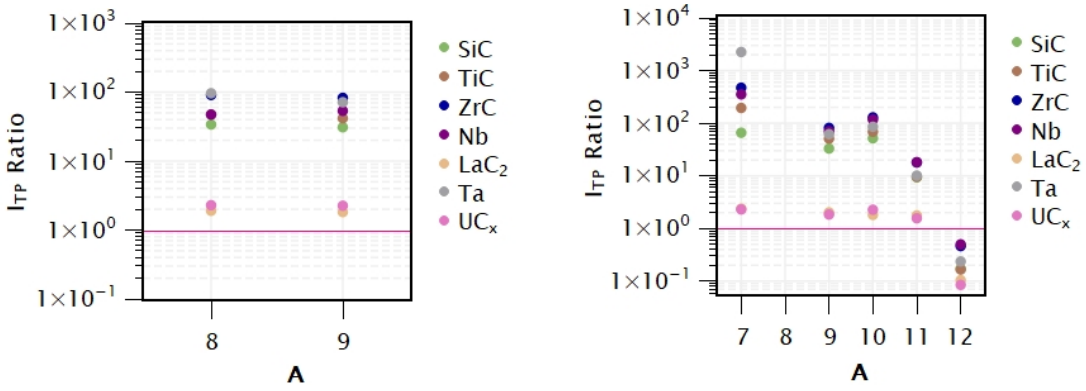

(a) Li isotopes **(b)** Be isotopes

Figure 4.29: Ratio of the In-Target Production intensity (I_{ITP}) of a graphite-composite target over other targets in the ISAC inventory. With exception to ^{12}Be, the graphite-composite target has superior I_{ITP} of lithium and beryllium isotopes as compared to UC_x, LaC_2, TiC, Ta, Nb, SiC, and ZrC.

Two graphite-composite targets were developed for this work (synthesis methodology in Section 2.4). The first graphite-composite target was set up online in August 2020, but due to a technical issue (independent of the target), this target was not irradiated. Nevertheless, since this target was going to be operated while COVID-19 restrictions were still imposing social distancing, the yield measurement campaign was organized and carried out remotely for the first time. Now, yield measurements do not have to be done in person, but can be carried out remotely, opening the possibility to expand TRIUMF's personnel and collaborators available to take yield measurements, promoting the collection of systematic data for the characterization and consequently improvement of the target materials.

The second graphite target was successfully irradiated in October 2020. Lasting three weeks, this irradiation campaign has been the longest dedicated to the systematic study of a target in ISAC records. The isotopes measured were ^{8}Li, ^{9}Li, ^{11}Be, and ^{7}Be. To assess their linear increase (Eq. 4.25), the lithium yields were measured at a fixed temperature and increasing proton beam (Section 4.6.2). Moreover, to estimate the overall release of lithium (Eq. 4.5), yields of ^{8}Li and ^{9}Li were measured at a fixed driver beam current and increasing temperature (Section 4.6.3). The irradiating conditions of this target were determined with the ISAC model evaluated with the empirical electrical power (Eq. 4.13).

The graphite target irradiation campaign started at low temperature of 1520 °C and most tests were performed below 1965 °C. This range was established because the tantalum target containers become fragile due to the formation of TaC and Ta_2C when they are heated in presence of carbon (see Chapter 3). Only at the last stage of the irradiation campaign was the temperature increased to 2200 °C and yields of ^{8}Li and ^{9}Li were re-measured to assess the effects of target-material aging (Section 4.6.4).

4.6.1 Competitive graphite target performance

The performance of the graphite target was compared with those ISAC targets that produce lithium and beryllium isotopes, being the niobium, tantalum, ZrC, UC_x, and SiC targets (Fig. 4.30 and 4.31). The ISAC targets' average lithium and beryllium yields were obtained from TRIUMF's yield database [136]. To compare the targets' overall efficiency (Eq. 1.2), their yields were normalized to the corresponding proton-beam current used during irradiation and divided by their production obtained from FLUKA for the case of the graphite target (Section 4.3), or from the ISAC's simulation database [15] for the rest of the targets.

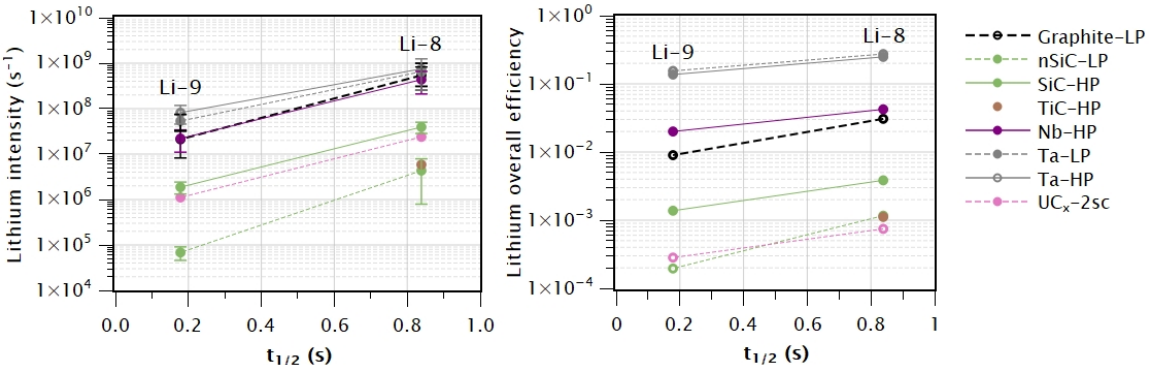

Figure 4.30: Lithium yield and overall efficiency comparison among different ISAC target materials.

The graphite-composite target ^{8}Li and ^{9}Li yields are higher than other ISAC targets except for the tantalum and niobium targets (Fig. 4.30). Nevertheless, the graphite release of lithium is within the tantalum targets standard variation. The graphite performance is competitive even though its overall efficiency during its irradiation campaign did not surpass the overall efficiency of the metallic targets (Fig. 4.30). According to the ISAC yield data base, the graphite-composite target production for ^{8}Li and ^{9}Li are higher than the rest of the ISAC targets (Fig. 4.29a), so it is unexpected for the metallic targets to have a better overall efficiency (Fig. 4.30-right). The low lithium overall release of the graphite target is most likely due to a discrepancy between the estimated and the operational temperature, with the latter being colder than the former (Fig. 4.18b).

The ^{7}Be and ^{11}Be yields of the graphite-composite target are higher when compared to the rest of the ISAC targets. In contrast, the graphite-composite target ^{12}Be production

is lower than the corresponding to tantalum targets (Fig. 4.31). These yields are in agreement with the graphite-composite target production of beryllium isotopes (Fig. 4.29b) that predicts higher ^{7}Be and ^{11}Be yields, but lower ^{12}Be.

Even though the beryllium production of the graphite-composite target is competitive, it is expected for this target to have a better ^{7}Be overall release. In offline experiments (Section 4.1), the graphite-composite target material had a ^{7}Be release fraction of 0.59±0.05 at ≈1910 °C, so it would be expected for its online ^{7}Be overall release to be one order of magnitude higher (Fig. 4.31); although, ionization, RIB formation, and delivery losses are included in the result, so they could have contributed to the lower release result.

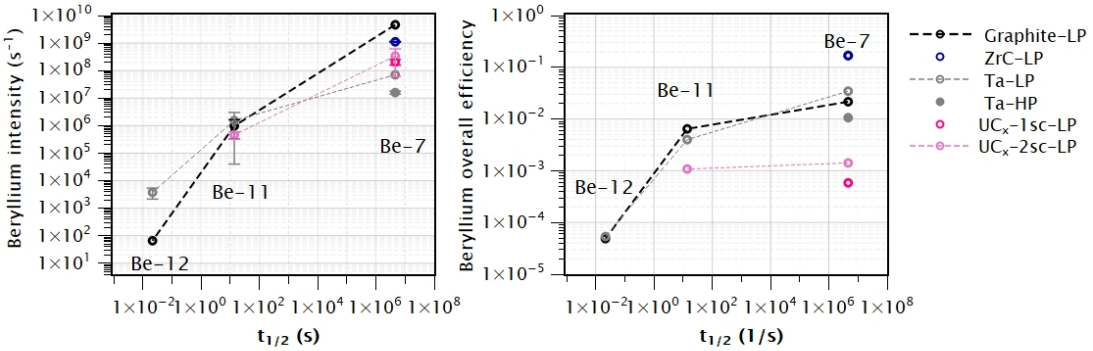

Figure 4.31: Beryllium isotopes yields and overall efficiencies comparison among different ISAC target materials.

The lithium and beryllium overall efficiency of the graphite-composite target was low most likely because the target was operated at a lower temperature than predicted. The analysis of the graphite-composite target's temperature-dependent isotope release is presented in the two following sections.

4.6.2 Non linear lithium yield increment

The graphite-composite target was irradiated at increasing proton beam current while keeping it at a fixed temperature. According to the FE simulations for the graphite-composite target (Section 4.5), increasing the irradiating proton current while aiming at a fixed maximum temperature promotes the enlargement of a thermal gradient in the target material (Fig. 4.23 and 4.24), reducing the volume of the target that is at maximum temperature (Fig. 4.25) such that if the isotope release from the hot zone dominated, the increment in isotope production due to proton current would not be enough to have an increasing yield at increasing proton current (Fig. 4.26). Thus, even though the RIB production intensity has a linear dependence with the irradiation beam current (ϕ) (Eq. 4.25), ^{8}Li and ^{9}Li yields might not have a major increment when irradiating the graphite-composite target at a fixed temperature and increasing proton beam current. Nonetheless, the yield of these isotopes

increases non-linearly (Fig. 4.32). A similar trend was observed at TRIUMF when a target was irradiated with a proton beam current higher than 10 µA; back then, the phenomenon was suspected to be Radiation Enhancement Diffusion (RED) [126].

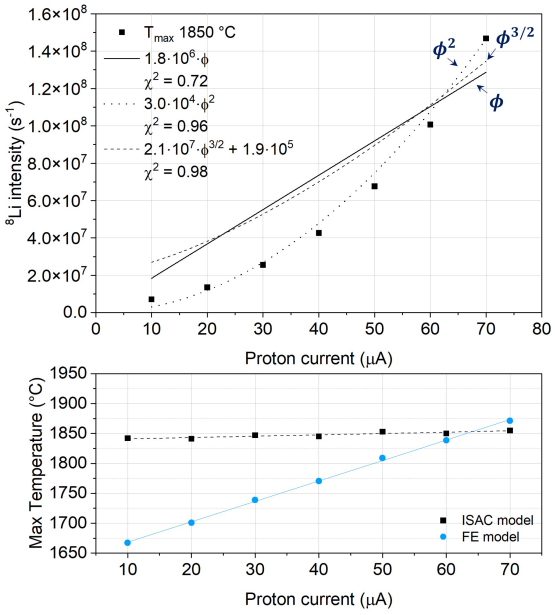

(a) ^{8}Li yield taken at ≈1850 °C

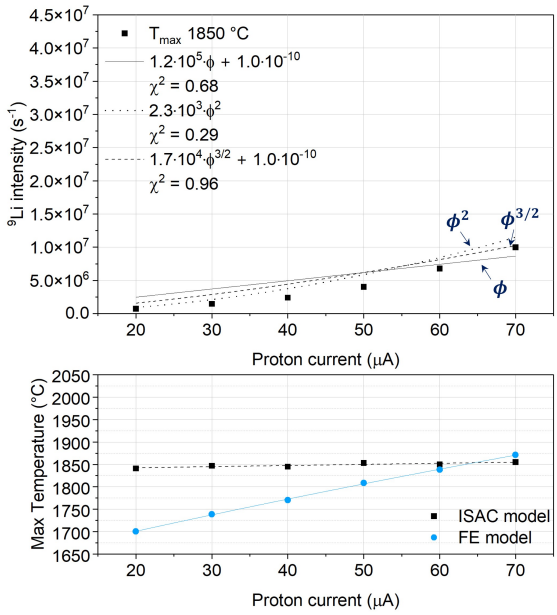

(b) ^{9}Li yield taken at ≈1850 °C

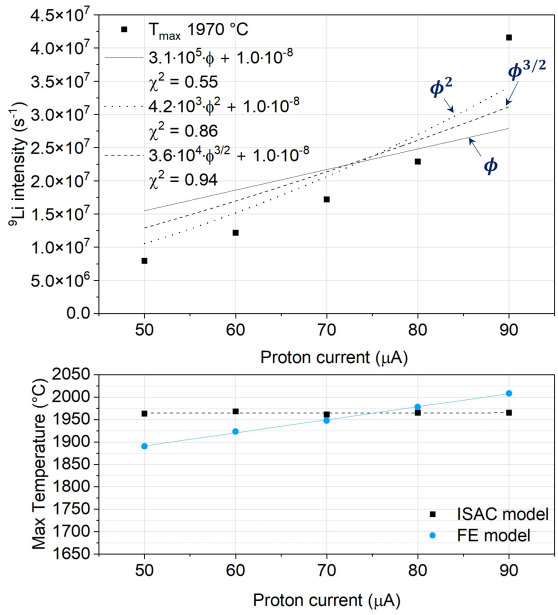

(c) ^{9}Li yield taken at ≈1970 °C

Figure 4.32: ^{8}Li and ^{9}Li yields from graphite-composite target irradiated at increasing proton current and at 1850 °C (a,b), and 1970 °C (c); the temperatures were estimated with the ISAC model evaluated with the empirical power. The operational temperature is compared with the temperature estimated with ISAC model evaluated with FE-model electrical power. All yields are fitted with a linear φ, φ^2, and $\varphi^{3/2}$ proton current dependence, the last two accounting for RED [99].

The diffusion of the isotopes is enhanced by the formation of vacancies and interstitial pairs in the lattice of a target material during irradiation [99]. Irradiating a target material induces the formation of vacancies and interstitials in its lattice. These defects are annihilated when recombining among themselves or by annealing with other defects in the lattice. When recombining, the isotope yield has a beam current (ϕ) dependence of [99]

$$I_{RIB} \propto \phi^{1/2} \tag{4.27}$$

that when considering the intrinsic linear dependence of I_{RIB} with the beam intensity (Eq. 4.25) the dependence becomes [99]

$$I_{RIB} \propto \phi^{3/2}. \tag{4.28}$$

On the other hand, the mechanism where the defects are annealed within the lattice has a linear dependence with the proton beam current, so when considering Eq. 4.25 [99]:

$$I_{RIB} \propto \phi^{2}. \tag{4.29}$$

The ^{8}Li and ^{9}Li yields (Fig. 4.32) fitted better for radiation enhancement (Eq. 4.28 and Eq. 4.29) than for a linear increment (Eq. 4.25). However, the possibility of not having the same target-material temperature in each measurement needs careful consideration. Electrical and proton-beam current combinations used during target irradiation were selected to keep a fixed temperature at increasing proton current; these combinations were obtained by evaluating the ISAC model with the empirical electrical power (Fig. 4.18). However, when evaluating the ISAC model with the electrical power obtained with COMSOL, the same electrical and proton-beam current combinations used online predict increasing temperatures. Thus, if the operational target temperature is closer to the one obtained with FE simulations, a non-linear increment in the lithium yield is expected.

The possibility of the graphite target operational temperature not being fixed at increasing proton-beam current was investigated by recalculating the target temperature using the ISAC model evaluated with the electrical power obtained with COMSOL. ^{8}Li and ^{9}Li yields were regrouped in two groups, one where the maximum target temperature was around 1700 °C and the other with a maximum temperature around 1800 °C (Fig. 4.33).

As expected, a φ^2 trend like in Fig. 4.32a was not observed in any of the groups in Fig. 4.33, but the yield measurements populating them were scarce. Nevertheless, note that the ^{8}Li and ^{9}Li intensities increase in all the cases (Fig. 4.33 top) even though the corresponding temperature predicted with the ISAC model (Fig. 4.33 bottom) reduces at increasing proton beam current, suggesting that even if the target is colder the release would be enhanced with proton current; however, this is unlikely given that the hottest zone of

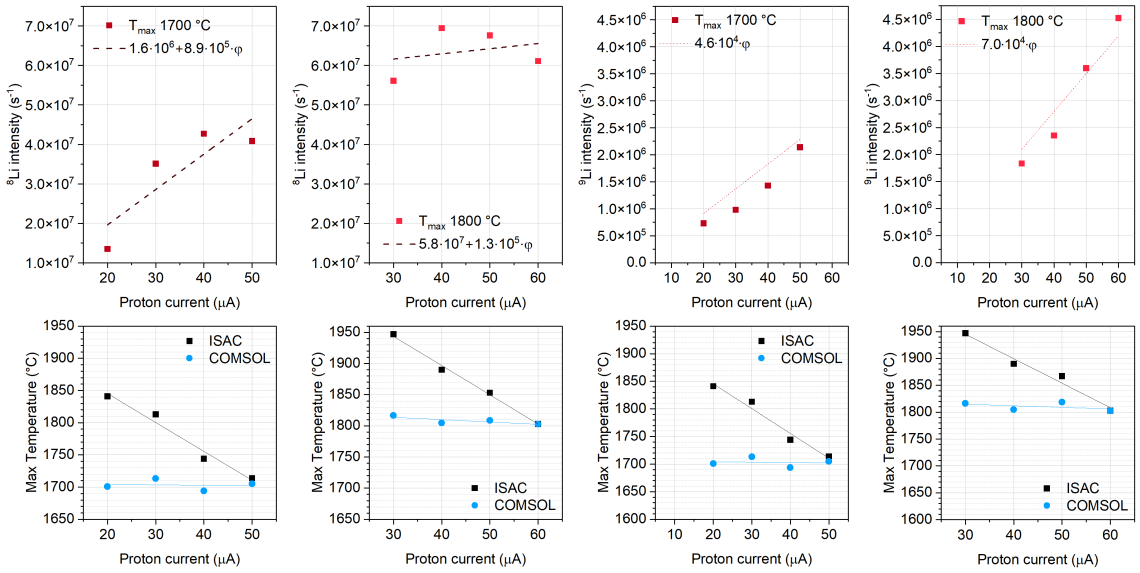

(a) ^{8}Li 1700 °C **(b)** ^{8}Li 1800 °C **(c)** ^{9}Li 1700 °C **(d)** ^{9}Li 1800 °C

Figure 4.33: ^{8}Li yields regrouped by maximum temperature. The temperature was estimated with the ISAC model evaluated with the COMSOL electrical power.

the target is expected to shrink at increasing proton current. Instead, if the operational temperature reduces during irradiation, the yield would most likely reduce, so the results of regrouping the yields suggest that the non-linear behaviour observed in Fig. 4.32a might be because the target temperature at increasing proton current was not fixed during irradiation, but rather higher at each electric proton-beam current combination.

Both sets of ^{8}Li and ^{9}Li yields increase with proton beam current (Fig. 4.33). Even though the ^{8}Li yields at 1800 °C (Fig. 4.33b) are higher than those at 1700 °C (Fig. 4.33a), the slope corresponding to ^{8}Li yields at the latter temperature is steeper. In fact, the ^{8}Li yields at 1800 °C have a negligible increase with proton intensity. In contrast, yields of ^{9}Li at 1800 °C (Fig. 4.33d) have higher yields and a similar slope to the corresponding to ^{9}Li yields at 1700 °C (Fig. 4.33c). Since both ^{8}Li and ^{9}Li are isotopes of the same element, it is not expected for them to react differently with the target material, so the chemical interaction of ^{8}Li with graphite does not explain its poor yield increment at 1800 °C. ^{8}Li and ^{9}Li differ however, in their half-life; ^{8}Li has a half-life of 838.7 ms while ^{9}Li half-life is 178.2 ms. The longer half-life of ^{8}Li allows a larger number of isotopes to escape the target before decaying, resulting in a yield of an order of magnitude larger than the corresponding to ^{9}Li (Fig. 4.33); therefore, it is unexpected for the ^{8}Li yield to have a negligible slope at 1800 °C. The reason for the flat slope of ^{8}Li at 1800°C is unknown, more yield measurements should be taken to observe the yield tendency, but the operational temperature should be predicted with the ISAC model evaluated with a better measured electrical power or with the electrical power obtained from COMSOL simulations.

According to the FE simulations, even though the volume of the target material at 1700 °C reduces with proton beam current (Fig. 4.25), the rise in isotope production due to it compensates the shrinkage of the hot zone up to 40 µA (Fig. 4.27), matching with the ^{8}Li intensity fall at 50 µA (Fig. 4.33a); however, this is not the case for ^{9}Li yields at the same temperature, suggesting that the ^{8}Li decrease at 50 µA is not an indication of the maximum target temperature volume shrinkage, but just random variation. More yields must be taken at different electrical combinations to determine the yield trends at fixed temperature and increasing proton-beam current.

The non-linear increase in the ^{8}Li and ^{9}Li intensity is most likely an artifact associated with the estimated temperature, and not radiation enhancement diffusion (RED). Larger sets of yield measurements need to be taken, but the temperature should be calculated with the ISAC model evaluated with a more accurate experimental electrical power or with the electrical power obtained with FE simulations. Nonetheless, it must be taken in consideration that the thermal properties of the target material that are used in the FE model have not been verified experimentally; also, they are fixed even though they are temperature dependent. Carrying on experiments in the CHI stand [34] would allow the characterization of the target materials, and it will provide information to run more reliable simulations that could be used to operate the targets optimally, resulting in more productive irradiating campaigns, and the possibility of extracting more exotic isotopes.

4.6.3 Lithium overall release from graphite target

The graphite target release efficiency (Eq. 1.2) of ^{8}Li and ^{9}Li was investigated. To observe the temperature's influence on the isotope release, the graphite-composite target was irradiated with a fixed proton beam current while the electrical current was increased. This procedure was repeated for proton beam currents between 10 µA and 80 µA. The temperature corresponding to each electric and proton-beam current combination was estimated with the ISAC model evaluated with the empirical electrical power (Section 4.5).

The target's lithium yields were normalized by proton-beam current, and divided by their respective in-target production (Section 4.3). As expected, given that the isotope diffusion is enhanced with heat, the release curves grow as function of the temperature (Fig. 4.34); however, considering that the yields are normalized per µA, curves corresponding to the same isotope should have the same yield at the same temperature, yet, at increasing proton beam currents, the normalized yield curves show higher yields for the same temperature (Fig. 4.34a). This behaviour could suggest either Radiation Enhancement Diffusion (RED), or an inaccurate estimation of the operational temperature as explained in the previous section (Section 4.6.2).

Most of the ^{8}Li and ^{9}Li release curves overlap when plotted as a function of the temperature obtained when evaluating the ISAC model with the FE electrical power (Fig. 4.34b).

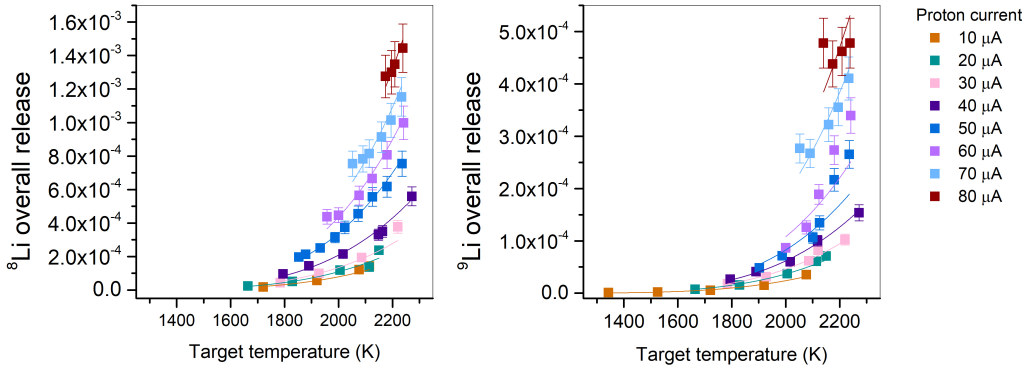

(a) Operational temperature

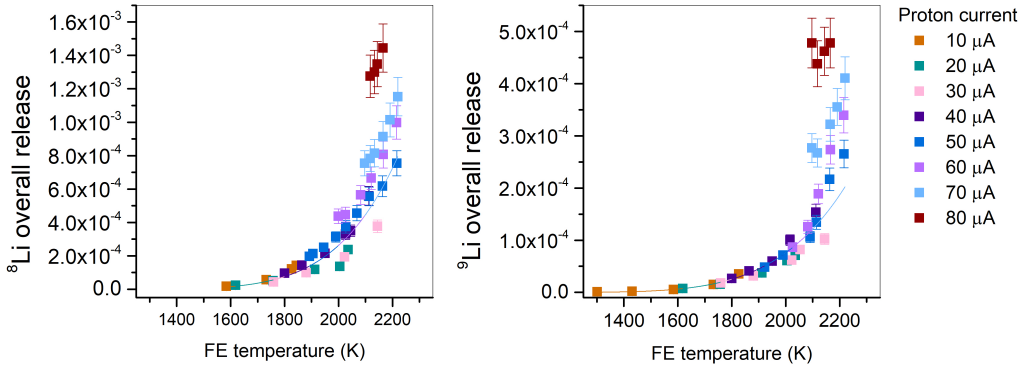

(b) FE electrical power derived temperature.

Figure 4.34: ^{8}Li and ^{9}Li overall release as function of operational temperature estimated with ISAC model evaluated with empirical (a) and FE (b) electrical power.

The amount of ^{8}Li and ^{9}Li yield measurements gives the confidence to discard a RED effect and justify, with a discrepancy between the operating temperature and the actual target temperature during irradiation, the non-linear yield increment observed when increasing the proton-beam current at an alleged fixed temperature (Fig. 4.32). It seems like the ISAC model evaluated with the empirical electrical power overestimates the target temperature (Fig. 4.18b). The oven's legs are indirectly water-cooled, so the electrical power corresponding to them might not be contributing to the target material heating; however, the empirical electrical power takes into consideration the voltage drop through the whole oven. The voltage drop through the oven body, excluding its legs, should be measured experimentally and compared to reconcile the analytical model with the FE simulations.

Larger target temperature gradients are expected at increasing proton-beam currents (Fig. 4.19). According to FE simulations, at a proton-beam and electrical current of 80 µA and 250 A, the target is around 2200 K (2000 °C), but it has a temperature gradient of ≈500 K (Fig. 4.24d), and only 20% of the target volume promotes diffusion at maximum temperature (Fig. 4.25); thus, isotope release enhancement due to temperature is not expected under these operational conditions, suggesting that the higher release at this proton current is due to RED. The 60 µA and 70 µA release curves also drift apart (Fig. 4.34), but to a lesser

extent than the 80 µA curve. At these proton-beam and respective electric currents, the target material is also expected to have temperature gradients, so these proton-beam and electric combinations are not supposed to favour isotope release over combinations at lower proton-beam currents. Again, RED could be leading to increased release; however, it has to be considered that instead of temperature-dependent properties, the model used to calculate the corrected temperature uses fixed material properties.

The release curves overlapping suggest that the corrected temperature is closer to the real target operational temperature. Given that the ^{8}Li and ^{9}Li release curves at proton currents above 60 µA do not fully overlap with the rest, further investigations in the target material and oven properties are advised. Further analysis of the lithium release, together with more thermal simulations, would allow the estimation of a temperature-dependent effective emissivity for the oven and graphite target combination. Also, it has to be considered that the target is not expected to have a uniform temperature but a gradient. The ISAC model estimates the target's maximum temperature, establishing the limit to operate the target without vaporization; in contrast, temperature gradients are available with FE simulations, so the irradiation campaigns should be planned based on FE simulation results, and the isotopes yields must be used as feedback to evaluate the simulations accuracy. The lithium release curves drifting away at higher proton-beam currents most likely indicate a discrepancy between the estimated and the operational temperature. If even with new temperature estimations the release curves of the same element do not overlap, radiation enhancement diffusion (RED) would be an alternative justification for the behaviour of the release curves corresponding to proton currents above 60 µA.

The activation energy Q and the preexponential D_0 of ^{8}Li and ^{9}Li isotope diffusing from a graphite-composite target were estimated. The release efficiency curves plotted against the corrected temperature (Fig. 4.34b) were fitted with

$$\varepsilon = \frac{6}{\pi^2} \frac{\frac{t_{1/2}}{ln(2)} \frac{\pi^2 D_0}{r^2} e^{-Q/R \cdot T}}{\left(\frac{ln(2)}{t_{1/2}} + \frac{\pi^2 D_0}{r^2} e^{-Q/R \cdot T} \right)}, \tag{4.30}$$

an equation for the release of radioactive species described in Section 1.1.1. In Eq. 4.30, $t_{1/2}$ is the isotope half-life (s), D_0 (m^2/s) is the diffusion preexponential, r is the diameter of the target material particles (m), Q is the activation energy of diffusion in J/mol, R is the gas constant (8.31 J/K·mol), and T is the maximum temperature of the target (K).

Both lithium isotopes are expected to have the same value for Q and D_0. The ^{8}Li and ^{9}Li release curves (Fig. 4.34b) were globally fitted with Origin [137] using Eq. 4.30, sharing Q and the term $\pi D_0/r^2$. The radius of the graphite particles should also be the same since all the measurements were collected from the same target. The resulting activation energy and D_0/r^2 values for ^{8}Li and ^{9}Li are consistent between each other within one sigma (Table 4.4).

Table 4.4: Compendium of activation energy Q and D_0/r^2 values for ^{8}Li and ^{9}Li released from a graphite-composite target.

Isotope	Q **(kJ/mol)**	D_0/r^2 **(1/s)**	D_0 **(cm^2/s)**
^{8}Li	186±12	2±1	$(4\pm2)\times10^{-5}$
^{9}Li	165± 9	4±2	$(8\pm4)\times10^{-5}$

The activation energy corresponding to the release of lithium from a graphite composite target differs from values reported in the literature, ranging from 5 kJ to 15 kJ [138, 139]. Given the wide variations between graphite grades, their microstructure, and the conditions at which are tested (e.g. at ambient temperature) it is not surprising that the activation energy obtained for the graphite-composite target is an order of magnitude larger than the values reported in the literature.

The activation energy and diffusion coefficient of lithium releasing from the graphite target presented here will become a precedent for future targets. Since the material microstructure of this target is characterized, its release properties can be associated with its microstructure and become a reference for future material improvements. What is more, the methodology followed to characterize the lithium release from graphite-composite targets could be followed to also characterize other target materials (e.g. UC_x, SiC, Ta), and work towards the optimization of old and new targets.

4.6.4 Graphite-composite target aging

A decline in the isotope production is often observed in ISAC targets throughout their irradiation campaign. To study this phenomenon in the graphite-composite target, yield measurements of ^{8}Li, ^{9}Li, and ^{11}Be were reassessed at the end of the irradiation campaign (Fig. 4.35). Since the measurements were taken at the same electrical and proton-beam current combinations, the temperature corrections associated with the ISAC model's electrical power are not taken into consideration because in case of a temperature offset (Fig. 4.18b), both sets should be affected in the same manner.

While ^{8}Li and ^{9}Li yield measurements were taken above 1900 °C, ^{11}Be measurements were taken below that temperature. Regardless of the temperature range, the yield intensities of the lithium and beryllium isotopes are lower at the end in comparison to the beginning of the irradiation campaign (Fig. 4.35) despite the irradiation conditions being the same.

All the lithium yields are in the same order of magnitude (Fig. 4.35a and 4.35b). On the other hand, the ^{11}Be yields at 20 µA and 30 µA are one order of magnitude lower at the end than at the beginning of the irradiation campaign (Fig. 4.35c). Among the isotopes measured, ^{11}Be with a half-life of 13.81 s, has the longest hal-life when compare to ^{8}Li (838 ms) and ^{9}Li (178 ms). Therefore, it is expected that a larger number of ^{11}Be isotopes

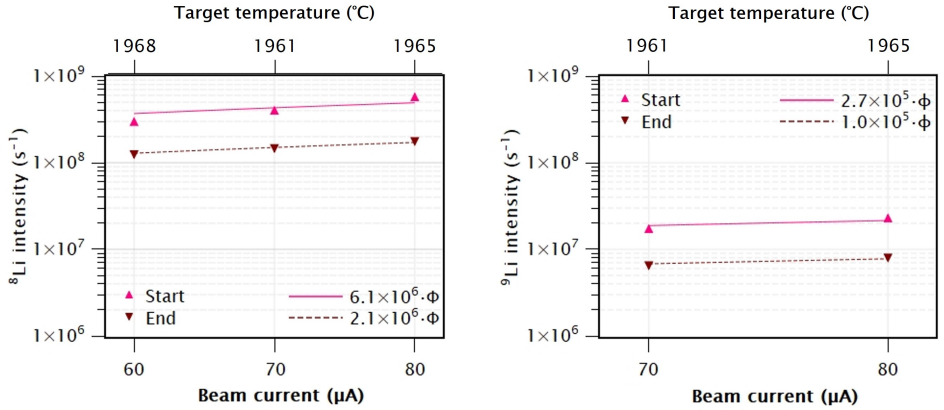

(a) ^{8}Li intensity **(b)** ^{9}Li intensity

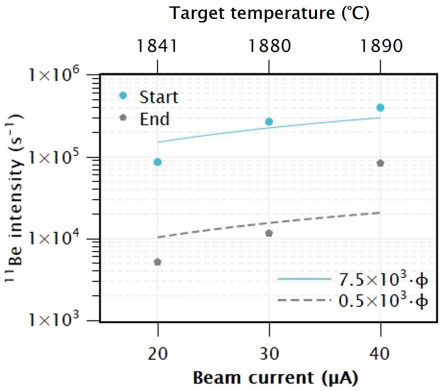

(c) ^{11}Be intensity

Figure 4.35: Comparison of ^{8}Li, ^{9}Li, ^{11}Be intensities at same irradiating conditions at beginning and end of irradiation campaign.

can diffuse out of the target before decaying.. Nonetheless, the ^{11}Be intensities are several orders of magnitude lower than lithium yields (Fig. 4.35), indicating the relevance of the target temperature on the isotope release. Furthermore, the ^{11}Be yield at 40 µA is five times smaller at the end in comparison to the beginning of the irradiation campaign; this might be an anomaly, considering that, even though the temperature is higher at consecutive proton currents, there is only 10 °C difference between the 30 µA and 40 µA yields; in any case, a lower intensity would be expected for the 20 µA as observed in the yield measurements taken at the beginning of the irradiation campaign (Fig. 4.35c).

The intensity of all the isotopes increases with increasing proton-beam current in agreement with the linear increment expected (Eq. 1.1). However, at the end irradiation campaign, the slopes of the lithium isotopes yield are three times smaller, while the ^{11}Be slope is seven times smaller. The slopes might be less steep if the temperature of the target is not the same at the end of the irradiation campaign, which is possible since carbon penetrates the tantalum in the oven, changing its properties (Section 3.1).

Limited by carbon penetration in the tantalum oven (Section 3.1) and by the target material's vapour pressure, most ISAC composite targets are operated below 1900 °C even though the isotope release is enhanced with increasing temperature. To investigate the graphite-composite target performance at high temperature without compromising the rest of the irradiation campaign, the target temperature was heated to above 2000 °C at the end of the irradiation campaign. With the target at 1965 °C, ^{8}Li and ^{9}Li yield measurements were taken at 70 µA, 80 µA and 90 µA proton beam current. Ten days after, yield measurements of the same isotopes were reassessed at the same proton currents, but at higher electrical current; two sets of measurements were taken, one with the target at 2100 °C and the other at 2200 °C. As expected, the ^{8}Li and ^{9}Li yields at 2200 °C are higher than those at 2100 °C (Fig. 4.36). However, both sets had a lower yield in comparison to the yields taken at the beginning of the irradiation campaign with the target at 1965 °C.

The yields and increasing slopes of all isotopes were higher at the beginning of the irradiation campaign in both cases, where the target was irradiated at the same conditions, and when it was irradiated at a higher temperature but same proton current. The drop in intensity at the end of the irradiation campaign might be due to changes in the target material, while the flattening of the intensity slope could be related to the corrosion of the tantalum oven.

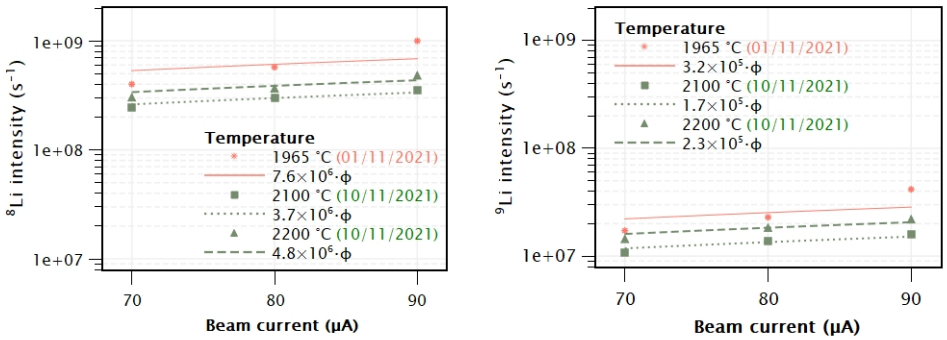

(a) ^{8}Li intensity **(b)** ^{9}Li intensity

Figure 4.36: Comparison of ^{8}Li and ^{9}Li intensities at same irradiating conditions at beginning and end of irradiation campaign.

Given that the isotope release from the target material particles is governed by diffusion (Eq. 1.12), it is evident that increasing the particle size would diminish the isotope release. Since the target material is operated at high temperatures, the graphite particles could grow due to sinterization, but it is unlikely. Because of its lack of structural stability, graphite target material has not been analyzed after irradiation; however, UC_x targets have been observed under SEM before and after irradiation, the graphite particles do not present signs of sinterization. On the other hand, according to the literature [47] and in agreement with offline tests (Section 3.1), the graphite foils undergo sublimation when heated at 2000 °C

under vacuum, so it would be expected for the graphite composite target to sublimate during irradiation; this is backed up by the embrittlement due to carbon penetration observed in the ovens after irradiation. Thus, changes in the target material porosity are expected due to graphite sublimation. In offline release experiments carried out in CHI (Section 4.1) it was observed that differences in quantity and morphology of the porosity have a drastic impact on the release of ^{7}Be (Fig. 4.8), so the decline in isotope release from the graphite-composite target might be justified by a decrease in effusion due to porosity changes. Further morphology characterization of the graphite-composite target before and and after irradiation are necessary to assess the effects of the online operation in the material.

Even though the same electrical and proton-beam current combinations were replicated, the target material temperature at the beginning and end of the irradiation campaign might have been different. As discussed in Section 3.1.1, the electrical resistance of the tantalum oven changes when heated in presence of graphite at high temperatures due to carbon penetration. Therefore, at the end of the irradiation campaign the same electrical current value used at the beginning does not raise the target temperature to the same value as it would do at the beginning when the oven is pristine. If the temperature is the only factor affecting the yield, it means that the temperature offset between the beginning and the end of the irradiation campaign is larger than 200 °C.

The model that predicts the operational temperature does not implicitly take in consideration the electrical resistance change in the oven that is caused by carbon penetration, but it considers the electrical power. A first step towards improving the temperature regulation during irradiation is to monitor the electrical power (P) of the target (Eq. 4.31); in this way, the electrical resistance (R) of the target can also be monitored and analyzed while operating the target online (Eq. 4.32).

$$P = V \cdot I \tag{4.31}$$

$$R = I^2/P. \tag{4.32}$$

In this work the change in electrical resistance was identified and correlated with heating time at a fixed electrical current, but during online irradiation, the target is not kept at a fixed electrical current, so the findings in Chapter 3 correspond to a specific case. The data analysis of the electrical resistance of all the targets containing carbon that have been irradiated online would show trends unavailable with offline experiments that cannot take into consideration the power deposited by the proton beam.

Changes in the emissivity of the oven cannot be assessed during target irradiation, but important differences in the temperature are expected if the material properties change (Fig. 4.27). Since the oven corrodes due to carbon, the surface finishing of the oven is expected to change with a corresponding emissivity change. Thus, not only the characterization of the target material but also the tantalum oven should be carried on the CHI

stand [34]. Furthermore, in offline experiments it has been observed that after heating the oven at 2000 °C under vacuum it becomes brittle and fails due to carbon penetration. Loss of structural stability and even fracture are therefore expected during irradiation. Lithium is a small element and it has been reported that it easily diffuses through graphene layers [139] of nanometric interlayer distance [140], so it would not be surprising for lithium isotopes to diffuse through micro (or macro) cracks in the tantalum ovens, justifying the lithium yield decline through the target irradiation campaign.

It must be considered that preventing the oven corrosion is the ideal case. Delaying the tantalum oven deterioration would allow longer irradiation campaigns, and it would also help on the regulating of the average temperature of the target for higher radioactive isotope intensity. Thus, further investigations on carbon diffusion barriers should be carried on. Rhenium is a promising coating material that could prevent carbon penetration. A methodology to apply it in the interior of an oven was developed for this work (Section 3.6). With this procedure, coatings of different thickness could be applied to tantalum samples in order to systematically study their effectiveness preventing the penetration of carbon in tantalum. On the other hand, target material post-irradiation characterization should be carried on, so changes in the microstructure could be correlated with the intensity trends.

4.7 UC_x target thermal analysis

A new analytical model was developed to predict the maximum temperature of a UC_x target. Conventionally, the UC_x targets were directly loaded into a tantalum oven, so their maximum temperature was calculated in the same way as the rest of the ISAC targets (Section 4.4). However, the UC_x targets made with the new method are loaded into a graphite container, and neither the target material nor the graphite container are in full contact with the oven (Fig. 3.4). Therefore, heat radiation becomes the dominant heat exchange mechanism between the graphite-container and the oven, and consequently their heat exchange cannot be described with the conduction-dominant ISAC model (Eq. 4.13). In contrast, the new analytical model accounts for the radiosity between the container and the oven; the temperature obtained with this model was compared with the results from the ISAC analytical model (Section 4.4), and with the maximum temperature of the target material obtained with COMSOL simulations (Section 4.7.2).

4.7.1 New analytical radiation model for 1-step casting targets

The new analytical model takes into consideration the power deposited by the proton beam and the electrical power given by joule heating as the heat sources for the target material. The new model assumes that the main heat exchange mechanism between the graphite container and the oven is radiation; therefore, it ignores the heat conduction through the

graphite container's belt and the oven. The model only considers the radiosity between the oven and the graphite container along the 12 cm of the tube over the graphite container (Fig. 4.38). Furthermore, the new model does not consider the dissipation of heat neither by conduction nor by radiation at the ends of the oven.

The new analytical model further considers the graphite container and the oven as two opaque concentric cylinders (Fig. 4.37a). The model assumes that the the internal and external wall of the graphite insert have the same temperature because the graphite-container wall is thin enough (0.125 cm) to consider its temperature gradient negligible. Also, the model assumes that the target-material rim has the same temperature as the graphite-container wall. These two assumptions allow considering the graphite container and the target material as one cylinder with the bulk properties of the target material, but the surface properties of the graphite container.

Like the ISAC model, the new one also ignores the radiosity within the dome formed between the D-shaped composite-discs stack and the graphite container. However, the D-shape of the discs is taken in consideration in the new model to calculate the temperature gradient from the axial centre of the target-material stack to its rim.

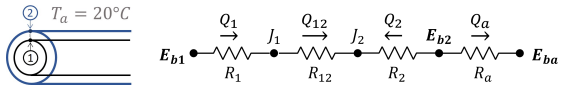

Figure 4.37: (a) Diagram of tantalum oven in blue (2) surrounding a graphite container in black (1), depicting the blackbody emitted power of the oven wall (E_{b2}) and the emissive power of the graphite-container surface (E_{b1}). (b) The net radiation transferring from and between surfaces are represented as Q_1, Q_2, and Q_{12}; the corresponding surfaces' and space resistance against radiation is illustrated by R_1, R_2 and R_{12}. E_{ba} is the blackbody emitted power corresponding to the vacuum, Q_a is the net radiation transferring from the outer surface of the tantalum oven.

The heat transfer between the graphite container, tantalum oven, and ambient is represented as an electric network (Fig. 4.37b). In the network approach, the black body emitted power E_{bi} and the radiosity J_i of a surface i are analogous to the voltage in a circuit [128]. The emitted power of the tantalum oven and graphite container is their corresponding black body emitted power, and is given by

$$E_{b1} = \sigma T_1^4 \tag{4.33}$$

$$E_{b2} = \sigma T_2^4 \tag{4.34}$$

where σ is the Stefan Boltzmann constant, and T_2 and T_1 are the temperature of the oven and graphite-container walls respectively. The emitted power of the ambient is given by [128]

$$E_{ba} = \sigma T_a^4 \tag{4.35}$$

where T_a is the ambient temperature.

On the other hand, the radiosity J_i is the total radiation energy leaving a surface per unit time and unit area, and J_i is given by [128]

$$J_i = \varepsilon_i E_{bi} + (1 - \varepsilon_i) G_i \tag{4.36}$$

where ε_i is the emissivity of the surface i, G_i is the incident radiation, and E_{bi} is the black body emitted power.

The emissivity of the surfaces and the space between them is taken in consideration in their resistance to radiate (R_i). R_2, is the resistance to radiation of the oven's interior wall, R_1 is the one corresponding to the graphite-container surface, and R_{12} is the resistance to radiation of the space between them

$$R_1 = \frac{1 - \varepsilon_1}{A_1 \varepsilon_1}, \tag{4.37}$$

$$R_2 = \frac{1 - \varepsilon_2}{A_2 \varepsilon_2}, \tag{4.38}$$

$$R_{12} = \frac{1}{A_1 F_{12}}, \tag{4.39}$$

where ε_2 and ε_1 are the emissivity of the internal face of the tantalum oven, and the emissivity of external surface of the graphite container respectively. A_2 and A_1 are the areas of the oven wall and graphite container that are facing each other, and F_{12} is the view factor between them (0.785 from Fig. 12.8 in [128]). The resistance corresponding to the external surface of the oven is given by

$$R_a = 1/A_o \varepsilon_o, \tag{4.40}$$

where ε_o is the emissivity of the external face of the oven and A_o its area.

The net rate of radiation heat transfer Q_i from a surface i to a surface area A_i is analogous to the current passing through the circuit. Q_i is given by the difference between the emitted power and the radiosity over the resistance, so from the circuit (Fig. 4.37b) the net rate of radiation heat from the graphite-container surface Q_1, and from the oven's interior wall Q_2 are given by:

$$Q_1 = \frac{E_{b1} - J_1}{R_1}, \tag{4.41}$$

$$Q_2 = \frac{E_{b2} - J_2}{R_2}. \tag{4.42}$$

Furthermore, since the graphite container is contained in the oven, the system is considered an enclosure. The radiosity between the graphite container and the oven is considered in the net rate of radiation heat transfer Q_{12} that is given by the difference in radiosity $(J_1 - J_2)$ over R_{12}:

$$Q_{12} = \frac{J_1 - J_2}{R_{12}}. \tag{4.43}$$

Finally, since the system is under vacuum, it follows that Q_a is dissipated to the ambient through radiation [128]

$$Q_a = \sigma \varepsilon_o A_o (T_2^4 - T_a^4). \tag{4.44}$$

An expression for the graphite-container temperature is obtained by solving Eq. 4.41 and Eq. 4.42 for J_1 and J_2, and substituting them in Eq. 4.43:

$$Q_{12} = \frac{E_{b1} - Q_1 R_1 - E_{b2} + Q_2 R_2}{R_{12}}, \tag{4.45}$$

solving for E_{b1}

$$E_{b1} = Q_{12} R_{12} + Q_1 R_1 - Q_2 R_2 + E_{b2}, \tag{4.46}$$

and substituting $E_{b1} = \sigma T_1^4$ (Eq. 4.33) in Eq. 4.46

$$T_1^4 = \frac{1}{\sigma}(Q_{12} R_{12} + Q_1 R_1 - Q_2 R_2 + E_{b2}). \tag{4.47}$$

Substituting $E_{b2} = \sigma T_2^4$ (Eq. 4.34) in Eq. 4.44 gives

$$Q_a = \varepsilon A_0 (E_{b2} - \sigma T_a^4); \tag{4.48}$$

then, solving Eq. 4.48 for E_{b2}:

$$E_{b2} = \frac{Q_a}{\varepsilon_o A_o} + \sigma T_a^4. \tag{4.49}$$

Substituting Eq.4.49 in Eq. 4.47 gives an expression for the temperature of the graphite container given by the net heat radiation corresponding to the surfaces of the graphite-container, the oven, and the space between them

$$T_1^4 = \frac{Q_{12} R_{12} + Q_1 R_1 - Q_2 R_2}{\sigma} + \frac{Q_a}{\sigma \varepsilon_o A_o} + T_a^4. \tag{4.50}$$

The power deposited by the proton beam q_p is assumed to be dissipated by conduction from the target-material axial centre to the graphite container wall. Therefore, the net rate heat transfer going from the graphite-container wall to the tantalum oven (Q_1) is equal to q_p. Also, the net heat transfer between the graphite container and the oven wall Q_{12} is equal to Q_1 by energy conservation. Furthermore, the net rate heat transfer from the oven's internal wall to the graphite container has the same magnitude as q_p, but the opposite direction to Q_1, so

$$Q_1 = Q_{12} = -Q_2 = q_p. \tag{4.51}$$

The total power deposited in the target is dissipated to the ambient. Thus, Q_a is the addition of the electrical power q_e and the power deposited by the proton beam q_p

$$Q_a = q_e + q_p. \tag{4.52}$$

Substituting q_p and $Q_a = q_p + q_e$ in Eq. 4.50 allows expressing the temperature of the graphite container as a function of the power deposited by the proton current and the electrical power

$$T_1 = \left(\frac{q_p}{\sigma}(R_{12} + R_1 - R_2) + \frac{q_p + q_e}{\sigma \varepsilon_o A_o} + T_a^4 \right)^{1/4}. \tag{4.53}$$

Nevertheless, to only consider the electrical power corresponding to the tantalum tube that is facing towards the graphite container, the electrical power is scaled by multiplying it by the ratio of the graphite-container length l_g over the full oven's length l_o

$$T_1 = \left(\frac{q_p}{\sigma}(R_{12} + R_1 - R_2) + \frac{q_p + q_e(l_g/l_o)}{\sigma \varepsilon_o A_o} + T_a^4 \right)^{1/4}. \tag{4.54}$$

The heat transfers from the axial centre of the target material to the graphite-container wall mainly by conduction. Due to the material's D-shape, some heat would be exchanged between the material and the graphite container by radiation, but here it is assumed that the conduction dominates, so the radiation contribution is ignored. Also, the model considers that the target material is isotropic, and that it dissipates heat from the target-material stack axial centre radially. The temperature of the target-material area in contact with the graphite container is estimated with the Fourier law for conduction (Eq. 4.55 [128])

$$q_p = -k A_m \frac{dT}{dr}. \tag{4.55}$$

In Eq. 4.55, q_p is the power deposited by the proton beam current, k is the thermal conductivity of the target material, dT/dr is the temperature gradient through the radius of the target material, and A_m is the area of the target material in contact with the oven wall:

$$A_m = L \left(r\theta + 2r \sin \frac{\theta}{2} \right). \tag{4.56}$$

In Eq. 4.56, L is the length of the target material, and the term in parenthesis corresponds to the perimeter of a circular segment, where r and θ are its corresponding radius and angle encompassing its cord.

Substituting Eq. 4.56 in Eq. 4.55, and integrating from the half width at half maximum of the Gaussian beam r_0 to the edge of the circular segment r, and from the temperature of the target material axial centre (T_c) to the temperature in of the target-material outer surface (T_1):

$$\int_{r_0}^{r} \frac{dr}{r} = -\frac{kL}{q_p}\left(\theta + 2\sin\frac{\theta}{2}\right)\int_{T_c}^{T_1} dT, \tag{4.57}$$

$$\ln\left(\frac{r}{r_0}\right) = \frac{kL}{q_p}\left(\theta + 2\sin\frac{\theta}{2}\right)[T_c - T_1] \tag{4.58}$$

gives an expression for the temperature difference between the centre and the target-material edge:

$$T_c - T_1 = \frac{q_p}{kL}\left(\frac{1}{\theta + 2\sin\theta/2}\right)\ln\left(\frac{r}{r_0}\right). \tag{4.59}$$

Solving Eq. 4.59 for T_c and substituting T_1 (Eq.4.54) provides an analytical model to obtain the maximum temperature of the target material as a function of the proton power deposited, the electrical power, and the emissivity values of the graphite container, and the oven:

$$\begin{aligned} T_c = \left(\frac{q_p}{\sigma}(R_{12} + R_1 - R_2) + \frac{q_p + q_e(l_g/l_o)}{\sigma\varepsilon_o A_o} + T_a^4\right)^{1/4} \\ + \frac{q_p}{kL}\left(\frac{1}{\theta + 2\sin\theta/2}\right)\ln\left(\frac{r}{r_0}\right). \end{aligned} \tag{4.60}$$

The new analytical model (Eq. 4.60) was compared with the ISAC model (Eq. 4.13), and with the results of FE simulations. The three models were evaluated using the same conditions compiled in Table 4.5. The power deposited by the proton beam current was calculated with FLUKA (Sec. 4.3), and assumed to be in the axial centre of the target material in the analytical models. In contrast, the distribution of the power deposited by the proton beam was used in the simulation; nevertheless, its global magnitude was the same as the one used in the analytical models. Moreover, the analytical models were evaluated with the electrical power (P_e) obtained from the COMOSL simulations; the P_e values obtained with COMSOL were plotted against electrical current and the resulting curves were fitted. In addition, the ISAC model was evaluated with the empirical electrical power obtained when joule heating an oven loaded with an empty graphite container in the non-actinide furnace (Fig. 2.3b).

4.7.2 Numerical and analytical model results comparison

For this work, an FE model has been developed with COMSOL to estimate the temperature of the new UC_x target. The results of the simulation were compared with those obtained with the ISAC model for UC_x targets, and with the new analytical model developed in this work. Unlike the previous UC_x targets, the new ones are loaded in a graphite container that is inserted in a target oven; the graphite container is in contact with the oven only through a narrow belt (Fig. 3.4). Instead of conduction, heat radiation is the expected heat transfer

Table 4.5: Parameters used in the COMSOL thermal simulation, and analytical models of a UC_x target in container.

Parameter		Value
q_p	Total power deposited by p+ beam	51.8 W/µA
A_1	Graphite-container external area	57.3 cm^2
A_2	Oven internal area	68.9 cm^2
A_0	Oven external area	72.0 cm^2
F_{12}	Graphite-container - oven view factor	0.785
ε_1	Graphite-container emissivity	0.75
ε_2	Oven internal emissivity	0.73
ε_o	Oven effective emissivity	0.12
θ	Circular segment central angle	272.8°
R_1	Graphite container surface resistance to radiation	0.0058 cm^{-1}
R_2	Oven's interior wall resistance to radiation	0.0053 cm^{-1}
R_{12}	Oven-graphite container space resistance to radiation	0.0222 cm^{-1}
l_g	Graphite-container length	12.0 cm
l_o	Oven length	18.8 cm
k	UC_x thermal conductivity	0.22 W/cm·K

mechanism to dominate due to the gap between the graphite container and the oven. The FE simulation considers heat transfer by conduction and radiation.

A simplified geometrical CAD (Computer-Aided Design) model of the UC_x target was drawn in SolidWorks® [108] (Fig. 4.38), and imported in COMSOL. The tantalum oven shown had the same diameter, thickness, and length as the target oven (1.91 cm, 0.038 cm, and 18.8 cm respectively); however, aiming at a lower computational load, no legs nor ion source were included in the FE model. Similar to the one used online, the graphite container only touches the oven through its belt in the centre; furthermore, the target material geometry consisted of a D-shaped cylinder centred in the graphite container.

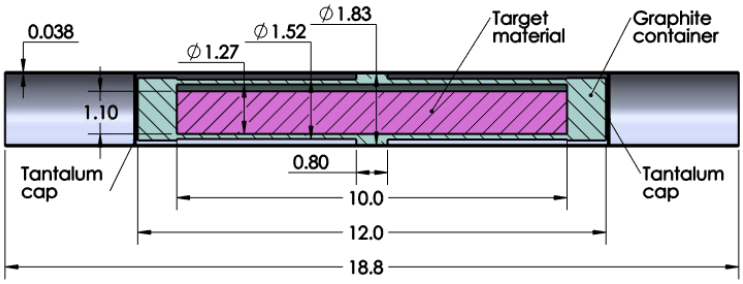

Figure 4.38: Section view of simplified target oven loaded with a graphite container and target material. To ease the computation time for its thermal simulations, this simplified oven does not have legs nor an ion source.

The heat sources for the FE model were the electric power, and the driver beam power deposition. For the electric power, the simulation included joule heating; the terminal and ground were set on the circular edges of the oven. Encompassing the electrical current range

used during target irradiation online, the current values were 100 A, 340 A, and 580 A. On the other hand, the power deposited per µA in the 10 cm long UC_x target was obtained with FLUKA (Section 4.3), and scaled for 10 µA, 20 µA, and 40 µA, corresponding to the proton currents routinely used to irradiate a UC_x target. The power deposited was assigned to the volume corresponding to the target material in the COMSOL model (Fig. 4.38). Since the proton beam passes through the graphite container caps, the power deposited in the graphite container was also obtained with FLUKA, and it was assigned to the corresponding geometry. Similar to the ISAC model, the power deposited in the tantalum oven and caps is ignored in the COMSOL and new analytical models.

The contact between target material and graphite container, and between the graphite-container belt and oven (Fig. 4.38) were considered ideal. Since the target material is D-shaped, in the simulation the target-material volume transfers heat by conduction and radiation; the area of the target-volume in contact with the container is set for conduction, while the area that is not in contact is set to transfer heat through radiation. The graphite container and oven exchange heat by conduction over the graphite-container's belt, and by radiation through the rest of its area. Furthermore, the oven is set to dissipate heat to the ambient by radiation through its exterior wall; also, the internal wall of the oven exchanges heat by surface to surface radiation with itself, and with the graphite container.

The emissivity of any material is temperature dependent [128]. However, a COMSOL simulation was run with fixed emissivity values to compare it with the new analytical model and with the ISAC model. Another simulation was run with temperature-dependent values to determine the target-material maximum temperature when accounting for temperature-dependent emissivity.

The emissivity values assigned to the geometry's faces were obtained from COMSOL's library, literature, or experiments. An effective emissivity of 0.12 was assigned to the external wall of the oven; this experimental value corresponds to target ovens routinely wrapped with three heat shields[1] (Appendix A.4). Furthermore, taking its TaC coating in consideration, the internal face of the oven was assigned with an average emissivity of 0.73 corresponding to TaC [130]. On the other hand, the emissivity value assigned to the graphite container and target material was 0.75 [141]; this last emissivity value corresponds to extruded graphite as the one used for the graphite container, but it was also assigned to the target material because the UC_x composite has a high carbon content, including the graphite foil, and the stoichiometric and excess graphite. Ballan et al. [142] reports an emissivity of 0.8 for UC_x pellets; however, the overall emissivity of the UC_x composite might be very different because, in contrast with the pellets reported by Ballan et al. [142], the UC_x composites have a backing graphite foil.

[1]The UC_x targets are submitted online with three heat shields to reduce the effective emissivity of the oven, allowing the target material to reach higher temperatures and better heat homogeneity with less electrical power.

The thermal conductivity values assigned to the FE simulations matched with those used in the ISAC model, or were obtained from COMSOL's library. The thermal conductivity assigned to the tantalum oven was 60 W/m·K [132], corresponding to solid-annealed tantalum available in COMSOL's library. The thermal conductivity of the graphite container was set to 105 W/m·K as per its material's specifications [88]. On the other hand, the thermal conductivity of the UC_x composite was set to 22 W/m·K, corresponding to the value used for online targets; this thermal conductivity was estimated using Eq. 4.15 with a thickness fraction of 0.65 and 0.35 for the UC_x slip-cast and graphite foil correspondingly, and 4.7 W/m·K [78] and 55 W/m·K [35] for their respective thermal conductivity.

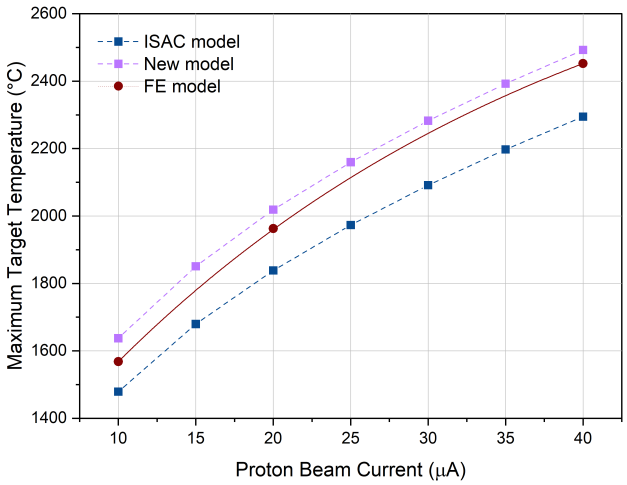

Figure 4.39: Comparison of the maximum temperature in the UC_x material with proton power deposited as only heat source. The temperature results were obtained with COMSOL simulations, and with the new analytical model (Eq. 4.60) and the ISAC model modified for the UC_x target (Eq. 4.13).

An FE simulation with fixed emissivity values was run with the power deposited by the proton beam as the only heat source. The maximum temperature results for the target material obtained with this simulation were compared with those from the ISAC and the new analytical models. The ISAC model (Eq. 4.13) only accounts the difference in geometry of the UC_x target with the electrical power P_e, so it was expected to not match with the FE simulation results. The difference in temperature between the FE and the ISAC model increases with the proton beam current (Fig. 4.39). At low beam currents, conduction has not been overcome by the radiosity between the graphite container and the oven, so the ISAC analytical model only differs by 89 °C; on the other hand, for 40 µA, when radiation dominates, the difference between the simulated temperature and ISAC is 157 °C. In contrast, the new model ignores the conduction between the graphite container and the oven, so it overestimates the temperature; however, the largest difference is 69 °C at 10 µA. The new model temperature results are in general agreement with the premise that radiation becomes dominant at higher beam currents when the temperature is higher.

FLUKA considers the density and length of the target material, so the FE simulation temperature maps depict the combined effects of power-deposition and heat transfer gradients throughout the target material. Since the proton beam was set to strike the target from left to right in the FE simulation, the first half of the target is expected to be hotter due to proton beam scattering (Fig. 4.40). The highest temperature is localized in the first half of the target material for the evaluated proton currents (10 µA, 20 µA, and 40 µA) (Fig. 4.40). Moreover, the temperature maps present more contours of 32 °C increments as the proton beam current increases, indicating a larger temperature gradient in the axial cross section of the target material. This is confirmed by the difference between the global maximum and minimum temperature in the target-material volume that increases with the proton beam intensity; when irradiating with 10 µA the difference between maximum and minimum temperature is only ∼125 °C, while it is ∼300 °C for 40 µA (Fig. 4.41).

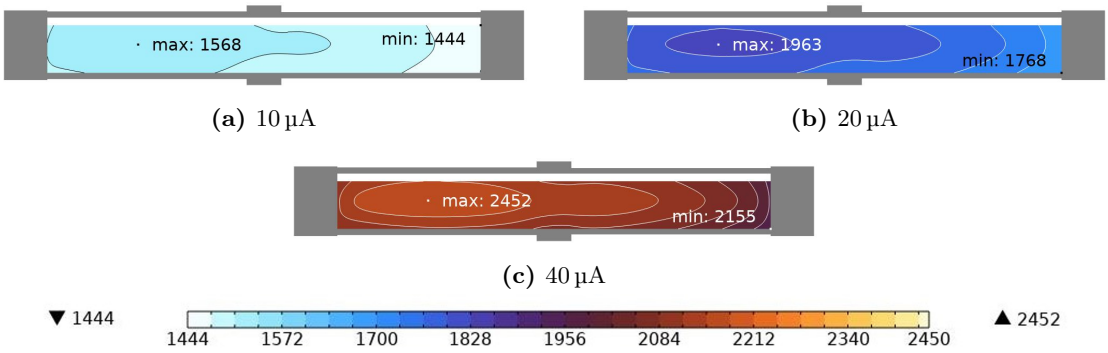

(a) 10 µA **(b)** 20 µA **(c)** 40 µA

Figure 4.40: Target-material temperature maps for a 10 cm long UC_x target with proton-beam power deposited as only heat source. Each contour represents a bin of 32 °C.

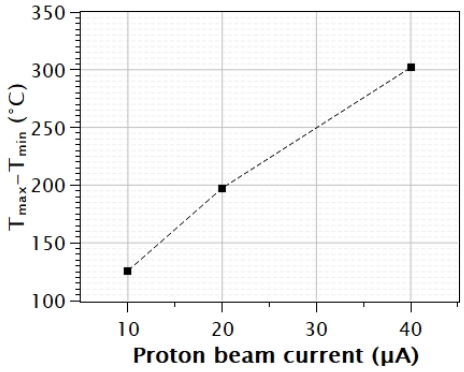

Figure 4.41: Difference between the maximum and minimum target-material temperature. According to a FE simulation of a 10 cm UC_x target, the difference between maximum and minimum temperature increases with increasing proton current.

Following the same operational methodology, the oven is joule-heated to generate a uniform temperature along the target material. To observe the target-material temperature gradient due to joule heating alone, an FE simulation was run with electric power as only

source of heat. Similarly to the graphite FE simulation with a simplified geometry, the resulting electrical power for the UC_x FE model does not match with the power used in the ISAC model for UC_x targets (Eq. 4.19) that includes the voltage drop from the whole oven (Fig. 4.42a).

The experimental electrical power was compared with a COMSOL simulation of a complete oven geometry. Emulating the UC_x target experimental set up to obtain the electrical power and emissivity of the UC_x target (Appendix B), the CAD imported in COMSOL consisted of the complete geometry of a target oven, including ion source, legs, and an empty graphite container. The simulation of the oven with a complete geometry had the same material properties as the simulation for the simplified geometry; the simulations differ in that the oven legs and the ions source terminals were water cooled, and the ion source terminals were set at nominal electrical current (230 A).

The tantalum-cap temperature obtained with the COMSOL simulations was compared with the experimental one, as the caps are the only accessible measuring area in the experimental set up. The temperature in the experimental set up was measured at the tantalum caps, so the tantalum-caps temperature was compared with the corresponding temperature obtained from the COMSOL simulations. The maximum tantalum-cap temperatures obtained with both, the simplified and complete geometry simulations, were in general agreement between simulations and with the experimental results (Fig. 4.42b). Therefore, the electrical power obtained with the FE simulation (with simplified geometry Fig. 4.38), was used in the analytical models to calculate the target-material temperature because they share the same ideal geometry. Both, the ISAC and the new models ignore the oven legs and ion source, so the results from all three models are consistent for comparison. Hereafter, the results of the simplified oven geometry simulations are presented.

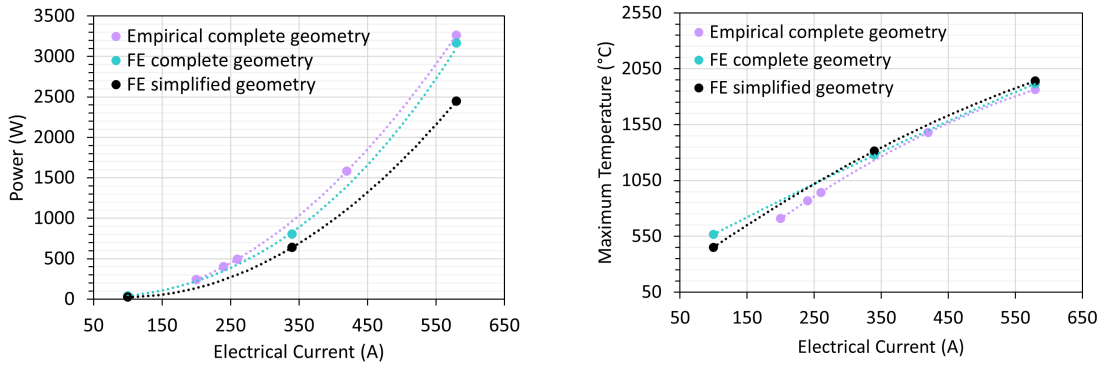

(a) Electrical power **(b)** Maximum oven temperature

Figure 4.42: The empirical power corresponding to an oven with ion source and legs, is in general agreement with the power resulting from COMSOL for an analogous geometry (a). The COMSOL electrical power for an oven of simplified geometry (no ion source, nor legs) is smaller than that of the complete geometry, but it results in identical oven's maximum temperature (b). Lines for guiding the eye only.

The resulting temperature map from COMSOL for a joule heated UC_x target is symmetric. The target material is slightly hotter in the centre and colder at the extremes (Fig. 4.43). Within the range of electrical current to resistively heat the ISAC targets during irradiation (100 A to 580 A), the largest difference between maximum and minimum temperature is only 3 °C for 100 A, and 58 °C for 580 A (Fig. 4.44). Given the asymmetric temperature gradient due to the proton beam power deposited, the symmetric temperature gradient due to joule heating is unlikely to promote a uniform temperature throughout the target material.

(a) 0 µA and 100 A **(b)** 0 µA and 580 A

Figure 4.43: Target temperature maps for a 10 cm long UC_x target being joule heated with an electric current of 100 A (a) and 580 A (b).

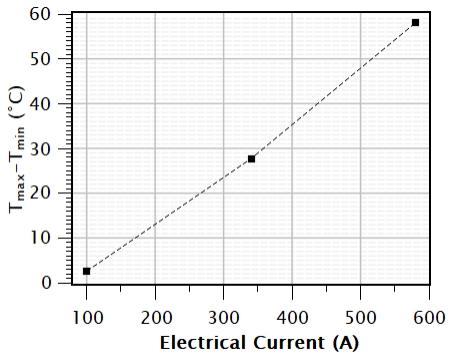

Figure 4.44: Difference between maximum and minimum temperature in the target material when joule heated at 100 A, 340 A, and 580 A.

A COMSOL simulation was run with a combined power deposited by the proton beam and joule heating as heat sources. Comprising the operational parameters routinely used during online irradiation, the FE simulation was evaluated for proton beam currents of 10 µA, 20 µA, and 40 µA, and electrical currents of 100 A, 340 A, and 580 A. The ISAC and the new analytical models were evaluated with the electrical power obtained with the FE simulations; the resulting maximum temperature values for the target material were compared with those from the FE simulations.

In contrast with the ISAC model, the new analytical model takes into consideration the radiosity between the graphite-container and the oven. Thus, it predicts temperature values closer to those calculated with COMSOL, being the largest difference 53 °C (Fig. 4.45). Nonetheless, the new analytical model ignores the heat dissipation by conduction between the graphite-container belt and the oven, so it predicts higher temperatures than the FE model at combinations of low proton currents and low electrical current (Fig. 4.45).

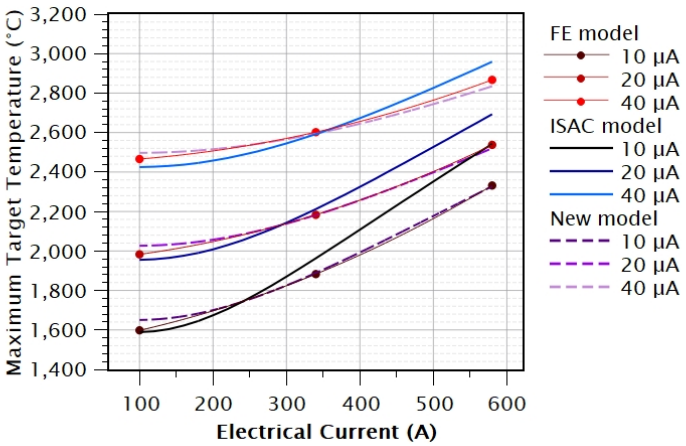

Figure 4.45: Comparison of the maximum temperature obtained with COMSOL simulation, ISAC model, and the new model. The ISAC model evaluated with the COMSOL results for the electrical power does not result in matching temperature; in contrast, the new model has a closer shape because it takes in consideration the radiosity in the system.

The temperature-current curves predicted with the ISAC model do not have a general match with the COMSOL simulation results (Fig. 4.45). The ISAC model temperature-current curves match better for all the proton-beam currents at electrical currents below 340 A (Fig. 4.45). The ISAC model (Eq. 4.13) was also evaluated with the experimental electrical power (Eq. 4.19) (Fig. 4.46). When evaluated with the electrical power obtained with COMSOL, the ISAC model overestimates the temperatures up to ≈200 °C, and up to to ≈333 °C when evaluated with the empirical electrical power.

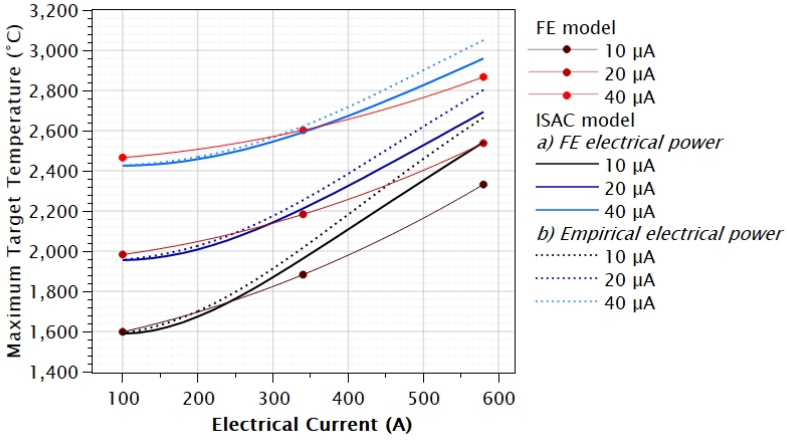

Figure 4.46: Comparison of the maximum temperature obtained with an FE model, the ISAC model evaluated with the empirical electrical power and the electrical power obtained with COMSOL. The results correspond for the temperature at different proton beam currents, and increasing electrical currents.

By making the resistance to radiation $(R_{12} + R_1 - R_2)$ equal to zero and ignoring the electrical power scaling l_g/l_0 in the new model, Eq. 4.60 becomes identical to the ISAC

model (Eq. 4.13). Conversely, scaling the electrical power in the ISAC model results in temperature-current curves in better agreement with the COMSOL results (Fig. 4.47), but now underestimating the temperature because the radiosity within the oven and graphite container is ignored. These results indicate that for the UC_x target system, the electrical power has a more drastic effect for predicting the temperature than the resistance to radiation ($R_{12} + R_1 - R_2$). Therefore, the experimental electrical power of the targets must be fully characterized.

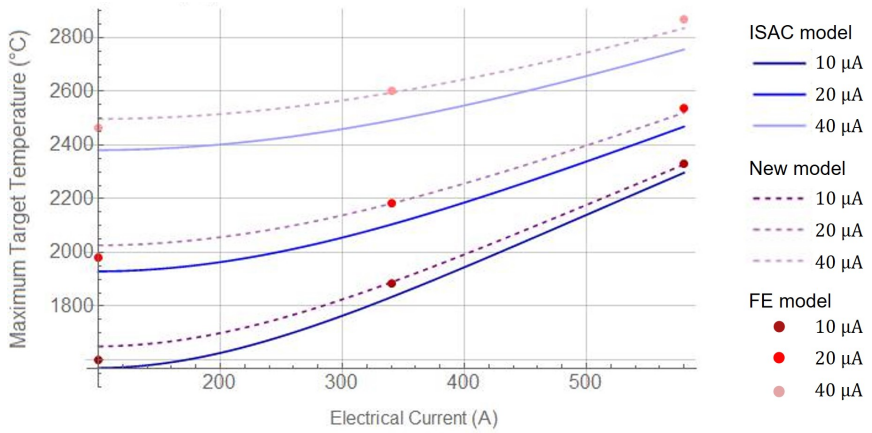

Figure 4.47: Comparison of the maximum temperature obtained with COMSOL simulation, ISAC model, and the new model. The ISAC model evaluated with the COMSOL results for the electrical power does not result in matching temperature; in contrast, the new model shows better agreement because it takes in consideration the radiosioty in the system.

During the online irradiation of all UC_x targets, their temperature is sought to be kept at 2000 °C or below. The UC_x target temperature is regulated by joule heating its oven, the necessary electrical current values are obtained with the ISAC analytical model evaluated with the empirical power. Assuming that the COMSOL temperature is closer to the real one, then the maximum temperature of the UC_x targets irradiated online was underestimated at low electrical currents, and overestimated at high electrical currents (Fig. 4.46).

In contrast with the analytical models, the temperature gradient in the target material is available with the FE simulations. The temperature maps resulting from the COMSOL simulations of a joule heated UC_x target and irradiated with proton currents were investigated. As expected, due to the symmetry of the electrical power thermal gradient (Fig. 4.43) and the asymmetry of the thermal gradient of the proton-beam power deposited (Fig. 4.40), for all the combinations of electrical and proton beam currents, the maximum temperature zone is located in the left side of the target, matching with the entrance of the proton beam (Fig. 4.48).

The simulation results for the global maximum and minimum temperature in the target-material volume were studied. Within the evaluated range, the minimum difference between the maximum and minimum temperature is 123 °C and corresponds to the case where the

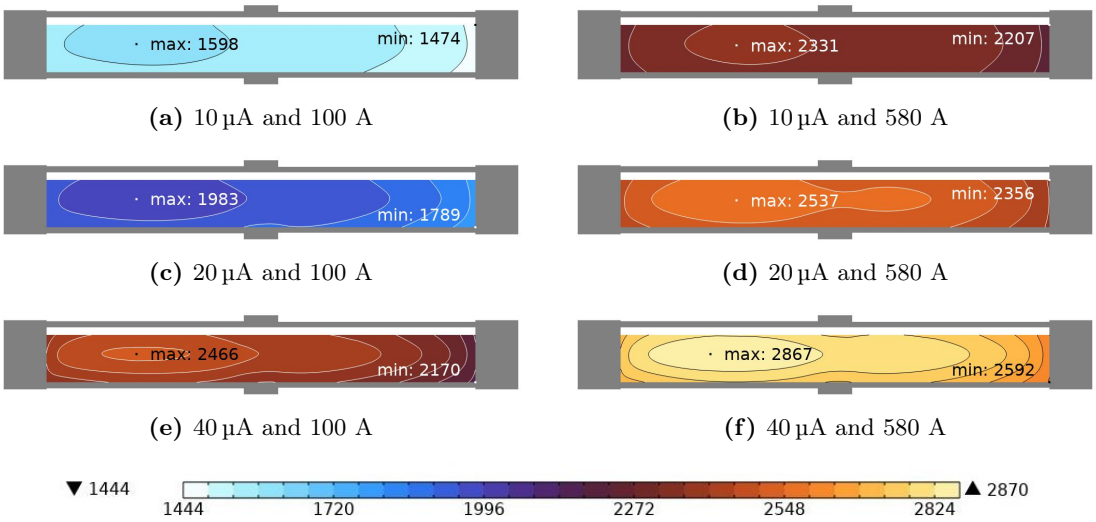

(a) 10 µA and 100 A **(b)** 10 µA and 580 A

(c) 20 µA and 100 A **(d)** 20 µA and 580 A

(e) 40 µA and 100 A **(f)** 40 µA and 580 A

Figure 4.48: Target temperature map for a 10 cm long UC_x target irradiated with a proton beam of 480 MeV and a beam current of 10 µA, 20 µA and 40 µA; heated with an electrical current of 100 A and 580 A.

target is irradiated with a proton beam of 10 µA and is resistively heated with an electrical current of 340 A. The largest difference between maximum and minimum temperature corresponds to the case where the beam and electrical currents are 40 µA and 100 A, respectively (Fig. 4.49). With the exception of 10 µA-340 A, the tendency was to have a smaller temperature difference when irradiating at low proton beam current while heating with high electrical current.

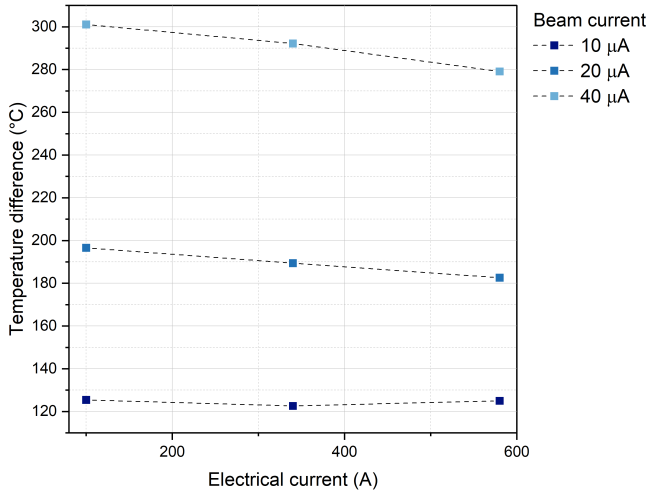

Figure 4.49: Difference between maximum and minimum temperatures in the UC_x target material volume obtained from COMSOL simulations.

Ideally, the target material would have uniform temperature. However, according to the simulations, the target-material volume develops a temperature gradient for all the proton-

beam current and electrical current combinations. A large temperature gradient in the target material is troublesome because its colder regions lower the isotopes diffusion rates such that the target volume is not optimally used in its entirety, or worse yet, cold spots would trap isotopes by propitiating their condensation. Although joule heating does not suppress the target temperature gradient, it reduces it. Thus, to have a lower temperature gradient is advisable to irradiate the target with low proton beam current and top up the temperature by joule heating the oven. Nevertheless, since the RIB intensity is linearly proportional to the proton-beam current (Eq. 1.1), irradiating at low proton currents would sacrifice isotope yield. Another option would be to simply shorten the target material length, reducing it from 10 cm to 5 cm; however this would reduce the fissible nuclei available and compromise the isotope production. An alternative to achieve more uniform temperature in a full-length target at high proton current would be to change the target's heat shields (Fig. A.3). Currently, the ovens are wrapped with single tantalum foils, covering the whole oven body; given that the hottest zone in the target material corresponds to the proton-beam entrance side, and that the number of heat shields modifies the effective emissivity of the outer oven wall, each half of the oven could have a different number of heat shields.

The maximum temperature in the target material was also obtained with a COMSOL simulation with temperature dependent emissivity. The results of this simulation were compared with those simulations with fixed emissivity. For these studies the external emissivity of the oven was set to Eq. 4.26 corresponding to annealed tantalum [143]. This emissivity function was chosen because it is the type of tantalum used for the target ovens, and its value above 2500 °C ($\varepsilon = 0.30$) is close to the effective emissivity found experimentally for a target oven without heat shields ($\varepsilon = 0.34$) [126]. As expected, the maximum temperature in the target material do not match. The simulation evaluated with temperature dependent emissivity results in higher temperatures than the simulations done with a fixed emissivity value for the tantalum oven (Fig. 4.50).

The results from FE simulations are not limited to fixed emissivity and thermal conductivity values as the analytical models. Furthermore, temperature maps and gradients become available with FE models. However, FE simulations as well as analytical models are limited by our knowledge of the target-material thermal properties. For instance, the estimated thermal conductivity assumed for the UC_x target material (Eq. 4.15), most likely will differ from that of the actual target material because of their specific density, porosity, microstructure, and the interface of the graphite foil-slip cast. Determining experimentally the UC_x thermal conductivity requires special precautions and authorizations because it is a radioactive target material. Nonetheless, the CHI stand (Chamber for Heating Investigations) has been designed and developed by Mia Au and Luca Egoriti [34] with the purpose of investigating the emissivity and conductivity of target materials; when commissioned for temperature investigations, CHI will allow the in-house characterization of our current tar-

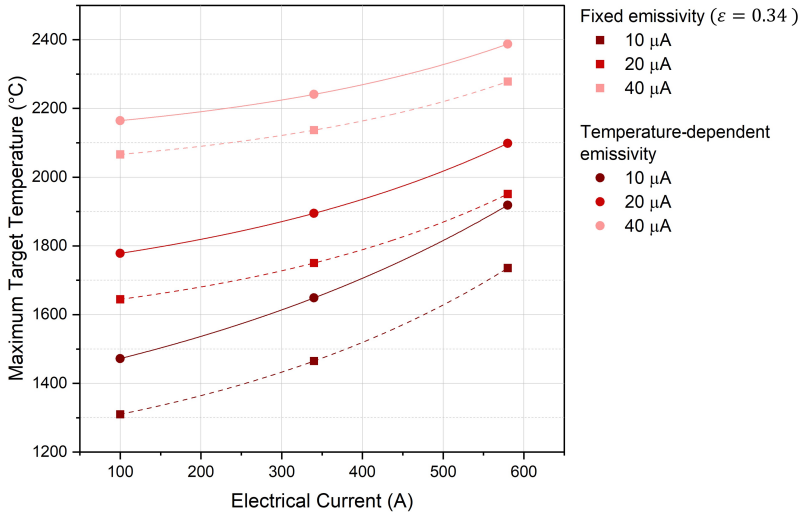

Figure 4.50: UC_x maximum temperature obtained with FE simulations using fixed ($\varepsilon = 0.34$) and temperature-dependent (Eq. 4.26) emissivity values for tantalum.

get materials. CHI will be an important tool for the study of current target materials, and for the development of new materials with enhanced properties to reach higher and homogeneous temperature. CHI results will also be a starting point for inputting experimental properties to the materials simulated with FE analysis, and obtaining results closer to the ISAC and ARIEL target materials, aiming at their characterization and optimal operation during irradiation.

4.8 UC_x release properties

UC_x targets have been irradiated at TRIUMF since 2010 but until 2018, they had been produced with the 2-step casting method [6]. In December of 2018, the first UC_x produced with the 1-step casting was submitted online to deliver isotopes to experiments. Currently, 1-step casting targets have substituted the labour-intensive 2-step casting targets. As per February of 2023, twelve UC_x targets made with the new method have been irradiated. In this section, the yield results of the first three successful targets are presented (UC_x 26, UC_x 29, and UC_x 30)[2].

In contrast with the graphite target, the UC_x targets made with the new method have not had a week long experimental run dedicated to their yields' characterization because UC_x targets are highly demanded for delivering isotopes to experiments, so providing RIB to users is prioritized over development. However, despite the time constraint, francium and radium have been systematically extracted from 1-step casting UC_x targets at a minimum of two proton-beam currents and increasing temperature. Also, at the beginning of each target's Radioactive Isotope Beam (RIB) delivery, the intensity and composition of the RIB

[2] UC_x 27 failed during irradiation due to impurities in the material (Fig. 2.55). UC_x 28 failed during irradiation due to an electrical short unrelated to the target material.

are assessed; this evaluation consists on measuring the yield of the isotopes before delivering them to experiments. The RIB intensity of the targets made with the new method was contrasted with that of the targets made with the old method by comparing their isotopic yield or overall efficiency (Eq. 4.5).

The activation energy (Q) and diffusion coefficient (D_0/r^2) of francium and radium releasing from the 1-step casting UC_x targets were obtained with a similar methodology as that used for the graphite-composite target (Section 4.6.3). The francium and radium resulting overall efficiency (ε) curves corresponding to different proton currents (Eq. 4.5) were fitted with Eq. 4.30 sharing Q or D_0/r^2. Also, a temperature offset between the ε curves was investigated with the fit. In addition, with the expectation that the corresponding yields would increase linearly with proton current (Eq. 4.25), the UC_x targets were irradiated with an increasing proton current while keeping the same temperature. For both cases, fixed proton current but increasing temperature and fixed temperature but increasing proton current, the referential temperature used during irradiation was estimated with the established ISAC model [120] (Section 4.4) evaluated with the empirical electrical power (Eq. 4.19) [78] despite its limitations.

4.8.1 First 1-step casting UC_x target performance

UC_x 26 was the first target synthesized with the new method (Sec. 2.3) to be submitted online. ^{214}Fr, ^{214}Ra, ^{213}Fr, ^{212}Fr, and ^{212}Ra yields were systematically extracted from the UC_x 26 at increasing target temperature. In contrast with the rest of the 1-step casting UC_x targets, the UC_x 26 was coupled with an ion guide laser ion source (IGLIS) instead of a rhenium-surface ion source (SIS) (Appendix C). IGLIS is not the ideal ion source for extracting francium or radium, so the UC_x 26 target results are not compared with the rest 1-step casting targets. Nevertheless, the overall efficiency (ε) (Eq. 4.5) of these isotopes was analyzed.

The UC_x 26 target was irradiated at 14 µA and 20 µA, and resistively heated to ramp its temperature and promote isotope release. According to the ISAC model (Eq. 4.13), the UC_x 26 maximum temperature ranged from 2173 K (1900 °C) to 2443 K (2168 °C). While the maximum operational temperature for UC_x targets is ≈2200 K, the UC_x 26 was operated hotter because the yield measurements were taken at the end of the irradiation campaign, so the experiments receiving its RIBs would have not been compromised in case of target failure.

The overall efficiency of all the isotopes extracted from the UC_x 26 at 20 µA does not follow the same trend like when extracted at 14 µA. Since the isotopes' yields are normalized per proton current, it is expected for their overall efficiency to change in accordance to target temperature changes. Instead, when compared with the 14 µA curves, all the isotopes extracted at 20 µA have a lower overall efficiency at higher temperature (Fig. 4.51, 4.52, and 4.53).

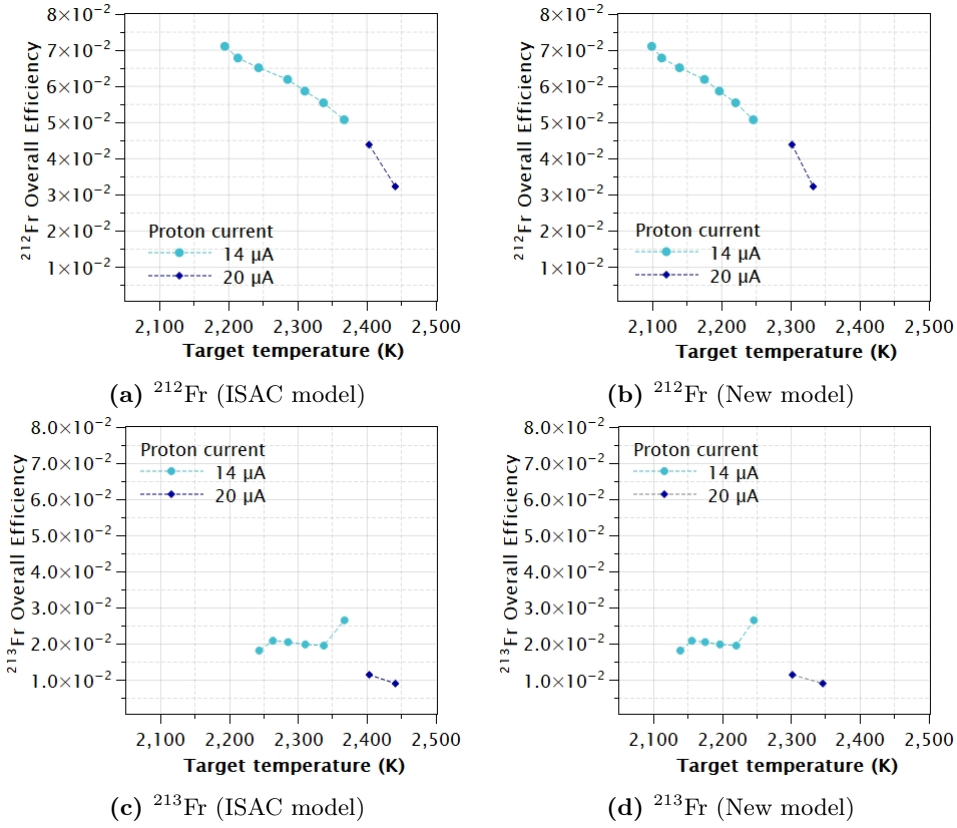

(a) ^{212}Fr (ISAC model) **(b)** ^{212}Fr (New model)

(c) ^{213}Fr (ISAC model) **(d)** ^{213}Fr (New model)

Figure 4.51: ^{212}Fr ($t_{1/2}$=20 min) and ^{213}Fr ($t_1/2$=34.14 s) overall efficiency from UC$_x$ 26.

According to the ISAC model (Eq. 4.13), the UC$_x$ 26 maximum temperature was above the maximum operational temperature (2200 K) during irradiation at 14 µA (Fig. 4.51a, 4.51c, 4.52a, 4.53a, and 4.53c), so target material vaporization was expected. Neither uranium nor carbon were detected in large quantities during the irradiation of the UC$_x$ 26 at 14 µA, so it is unlikely that the target temperature was above 2200 K at that proton current. A maximum temperature of 2240 K, only ≈40 K above the operational limit, is estimated with the new model for a target irradiated at 14 µA (Fig. 4.51b, 4.51d, 4.52b, 4.53b, and 4.53d), meaning that the temperature estimated with the new model might be closer to the true target temperature.

The overall efficiency of all the radium and francium isotopes extracted at 20 µA appears lower than the one for 14 µA (Fig. 4.53, 4.52, and 4.51) even when plotted against the target temperature estimated with the new model (Eq. 4.60). Based on the ^{238}U counts during the UC$_x$ 26 irradiation at 20 µA (192 pA/s), it is suspected that the target was in fact above 2200 K. The increase of uranium vapour, would have contributed to an increment of neutrals in the ion source, saturating it and decreasing its efficiency [66]; then, even if larger yields of francium and radium isotopes were being released, just a small fraction would have been ionized efficiently.

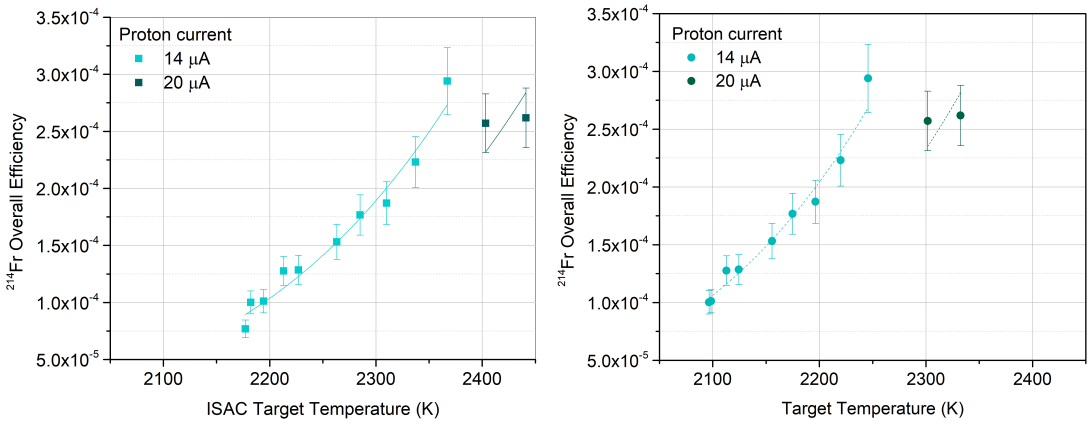

(a) ^{214}Fr (ISAC model) **(b)** ^{214}Fr (New model)

Figure 4.52: ^{214}Fr overall efficiency for UC_x 26 target plotted against maximum temperature. In (a) temperature is estimated with the ISAC model (Eq. 4.13), and in (b) with the new model (Eq. 4.60). Curves are fitted with Eq. 4.6.

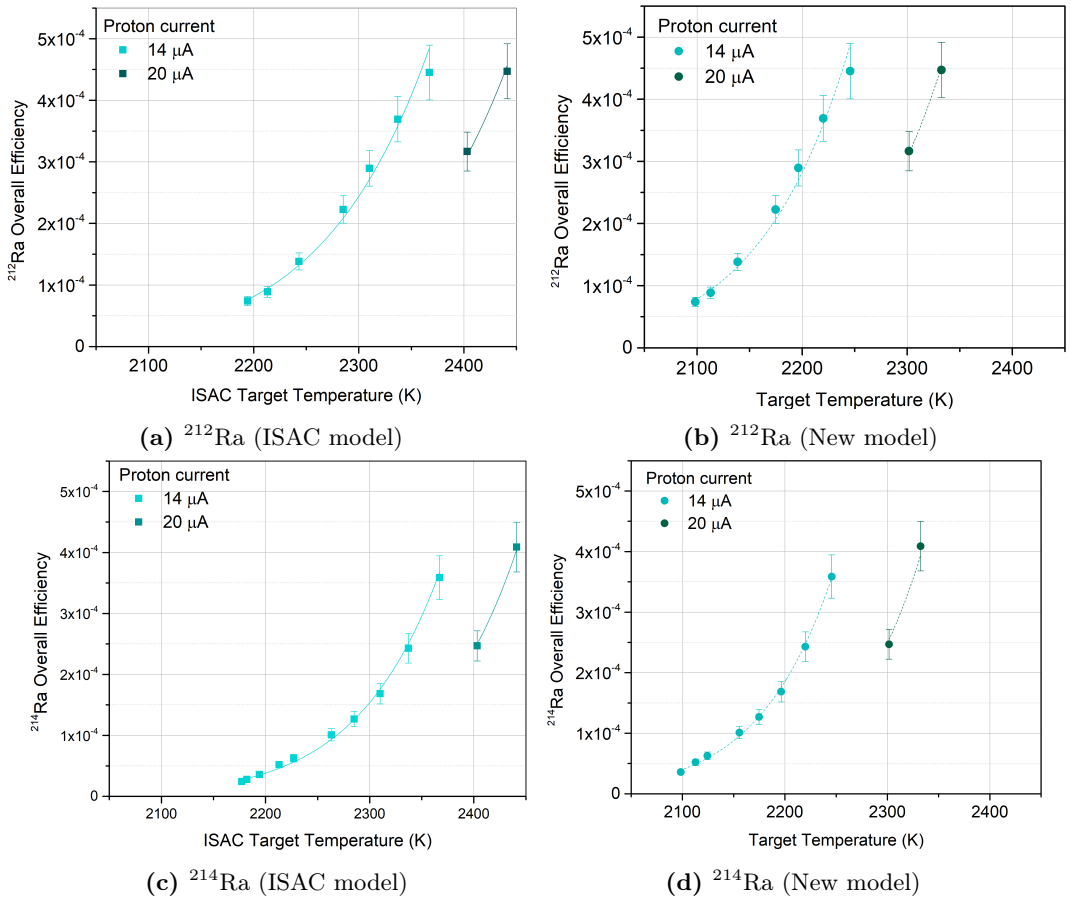

(a) ^{212}Ra (ISAC model) **(b)** ^{212}Ra (New model)

(c) ^{214}Ra (ISAC model) **(d)** ^{214}Ra (New model)

Figure 4.53: Radium overall efficiency for UC_x 26 target plotted against maximum temperature. (a) and (c) temperature is estimated with the ISAC model (Eq. 4.13), and (b) and (d) with the new model (Eq. 4.60). Curves are fitted with Eq. 4.6.

Alternatively, the overall efficiency at 20 µA would appear lower than expected if both, the ISAC and the new model, are overestimating the target temperature at that proton current. Most likely the UC_x properties assumed in the models do not match with the UC_x target material properties, so even if the new model and the FE simulations have the capacity of describing the UC_x targets' maximum temperature and gradient, the results could be in disagreement with the real temperature during irradiation. As done with the graphite target (Sec. 4.6.3), additional sets of radium and francium irradiation at different proton beam currents are required to identify their overall release trend and the target temperature properties. For better results when investigating these isotopes, instead of an IGLIS, an SIS should be coupled to UC_x target.

The ^{212}Fr overall efficiency from UC_x 26 reduces with increasing target temperature (Fig. 4.51a and 4.51b). The ^{212}Fr overall efficiency from the UC_x 26 irradiated at 14 µA is in the same order of magnitude at minimum and maximum temperature, but it is reduced almost in half at the maximum temperature. Although the reduction is small, it is unexpected because heat should promote isotope release. The cause of the ^{212}Fr overall efficiency reduction with temperature at 14 µA is unknown. The target might not be at the estimated temperature, but it must be relatively hotter at consecutive measurements since the proton current is fixed and the electrical current is increased to joule heat the target. Given that the ^{212}Fr half-life is 20 minutes it is possible to reach a maximum overall efficiency and plateau despite increasing the temperature, but the ^{212}Fr overall efficiency reduced instead. If the target temperature was in agreement with the ISAC model predictions (Fig. 4.51a), a drop in overall efficiency would be expected due to target material evaporation, but this would affect all the isotope yields, which is not the case. On the other hand, the ^{212}Fr yield measurements were taken at the end of the irradiation campaign. A drop in the ^{212}Fr yield would be expected with temperature if the oven's structural integrity was compromised due to carbon penetration (being the graphite container and the carbon in the target material itself the carbon sources), leading to the formation of microcracks where ^{212}Fr could have escaped; however, ^{212}Ra and ^{212}Fr yields were measured simultaneously and ^{212}Ra increases with temperature as expected (Fig. 4.53a).

In comparison with ^{212}Fr, the ^{213}Fr overall efficiency is lower as its half-life is shorter ($t_{1/2}$ =34.1 s) and the isotopes have more chances of decaying before escaping the target (Fig. 4.51). While the ^{212}Fr overall efficiency reduces with temperature, at 14 µA the ^{213}Fr overall efficiency has almost null change with a temperature increment of 100 K (≈2250 K-2350 K). Given the relatively long half-life of ^{213}Fr, it is possible for it to plateau, with the last data point at 2246 K being an outlier.

The overall efficiency of ^{214}Fr, ^{212}Ra, and ^{214}Ra, isotopes with a half-life of 5 ms, 13 s, and 2.435 s respectively, increases as the target gets hotter (Fig. 4.52 and 4.53), so their diffusion coefficient (D_0/r^2) and activation energy (Q) were obtained by fitting their overall efficiency

curves. The curves of each isotope were globally fitted with Eq. 4.30, sharing D_0/r^2 and Q, assuming that the temperatures corresponding to 14 µA were correctly determined by the temperature models. The average temperature offset obtained for the overall efficiency curves at 20 µA were (-73±4) °C and (-84±3) °C for the ISAC (Eq. 4.13) and the new model (Eq. 4.60) respectively.

Since ^{212}Ra and ^{214}Ra are isotopes of the same element, it is expected for them to have the same Q and D_0/r^2. The activation energy values obtained by fitting the overall efficiency of ^{212}Ra and ^{214}Ra are consistent between isotopes and are also similar when fitting the curves plotted against the temperature obtained with both models. In contrast, the D_0/r^2 obtained by fitting the curves plotted against the temperature estimated with the new model is one order of magnitude larger than the D_0/r^2 estimated by fitting the curves plotted against the ISAC model temperature (Table 4.6 and 4.7). Moreover, the D_0/r^2 for ^{214}Ra is several orders of magnitude larger than for ^{212}Ra; despite the half-lives difference between the ^{212}Ra and ^{214}Ra such a great difference in D_0/r^2 is unexpected.

Table 4.6: Activation energy Q and diffusion coefficient values for ^{212}Ra, ^{214}Ra, and ^{214}Fr released from $\mathrm{UC_x}$ 26. Results obtained by fitting overall efficiency curves plotted against temperature estimated with ISAC model (Eq. 4.13).

Isotope	$t_{1/2}$ (s)	Q (J/mol)	D_0/r^2 (s^{-1})
^{212}Ra	13.0	$(4.63 \pm 0.19) \times 10^5$	$(0.37 \pm 0.35) \times 10^4$
^{214}Ra	2.435	$(5.87 \pm 0.18) \times 10^5$	$(4.52 \pm 3.97) \times 10^7$
^{214}Fr	0.005	$(2.62 \pm 0.22) \times 10^5$	$(5.57 \pm 6.41) \times 10^5$

Table 4.7: Activation energy Q and diffusion coefficient values for ^{212}Ra, ^{214}Ra, and ^{214}Fr released from $\mathrm{UC_x}$ 26. Results obtained by fitting overall efficiency curves plotted against temperature estimated with new model (Eq. 4.60).

Isotope	$t_{1/2}$ (s)	Q (J/mol)	$\mathrm{D_0/r^2}$ (s^{-1})
^{212}Ra	13.0	$(4.91 \pm 0.20) \times 10^5$	$(6.02 \pm 6.51) \times 10^4$
^{214}Ra	2.435	$(5.89 \pm 0.18) \times 10^5$	$(2.39 \pm 2.22) \times 10^8$
^{214}Fr	0.005	$(2.60 \pm 0.20) \times 10^5$	$(1.00 \pm 1.10) \times 10^6$

The radium yields collected from the $\mathrm{UC_x}$ 26 are not enough to identify the reason for the difference between the ^{212}Ra and ^{214}Ra D_0/r^2. The suspected overheating of the $\mathrm{UC_x}$ 26 target during yield measurements at 20 µA, leaves the 14 µA curves as the only reliable data for analyzing D_0/r^2; any inconsistency between the irradiation conditions during these measurements could have shifted the curves. More systematic measurements at different proton currents are necessary to identify these isotopes' overall efficiency trends. Also, given that the $\mathrm{UC_x}$ 26 was coupled with an IGLIS, it is futile to compare the diffusion

coefficient results obtained here with those corresponding to targets coupled with SISs, so it cannot be determined if either the D_0/r^2 corresponding to ^{212}Ra or ^{214}Ra is closer to an overall value for radium, but the results presented stay as reference for future studies.

The ^{214}Fr results for Q and D_0/r^2 are consistent between the ISAC and the new model. Since ^{214}Fr was the only francium isotope to have an increasing yield with increasing temperature, a comparison with other francium isotopes results is not available. As with the radium isotopes, the ^{214}Fr Q and D_0/r^2 obtained constitute a reference for future studies.

4.8.2 UC_x 29 and UC_x 30 performance investigations

The activation energy (Q) and the diffusion coefficient (D_0/r^2) corresponding to the ^{211}Fr and ^{211}Ra releasing from the UC_x 29 and UC_x 30 were estimated. These isotopes were extracted from both targets at fixed proton currents and increasing target temperature. The results for the isotopes' overall efficiency (Eq. 4.5) at increasing temperature were fitted with Eq. 4.30. Moreover, yields of ^{211}Fr and ^{211}Ra were measured at fixed temperature and increasing proton current to investigate their expected lineal increment (Eq. 1.1). In addition, actinium was extracted from target UC_x 29.

The ^{211}Fr and ^{211}Ra yields from the UC_x 30 target increase when increasing proton-beam current at fixed temperature (2173 K±8 K) (Fig. 4.54). This suggests that the temperature estimated for this target is similar at each proton-beam electrical current combination, and not increasing as suspected for the graphite-composite target (Fig. 4.32).

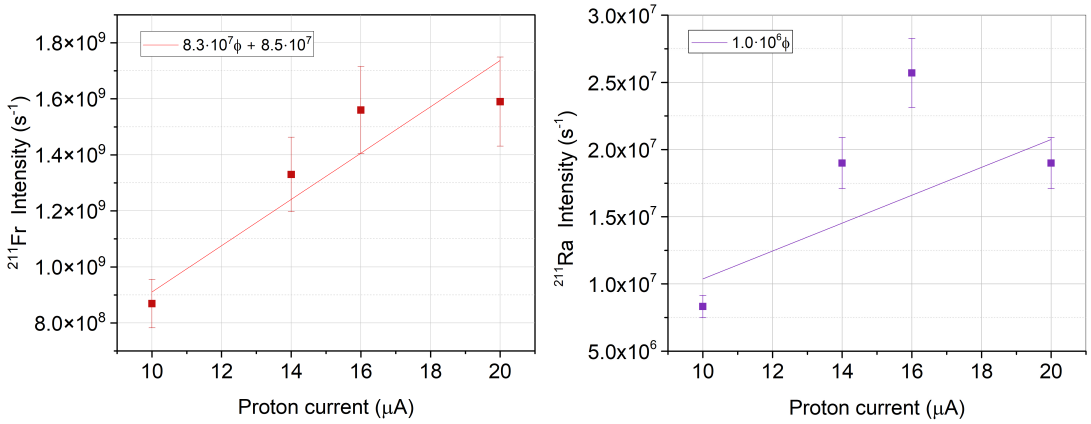

(a) ^{211}Fr release from UC_x 30 **(b)** ^{211}Ra release from UC_x 30

Figure 4.54: ^{211}Fr and ^{211}Ra intensity curves at increasing proton-beam current but fixed temperature (≈2200 K). The target temperature used as reference during irradiation was calculated with the ISAC model.

At increasing temperature but fixed proton current, for both the UC_x 29 and UC_x 30 targets, the ^{211}Fr overall efficiency increases with temperature up to ≈1900 K; afterwards, the release plateaus (Fig. 4.55a and 4.55b). The ^{211}Fr release saturation could be explained

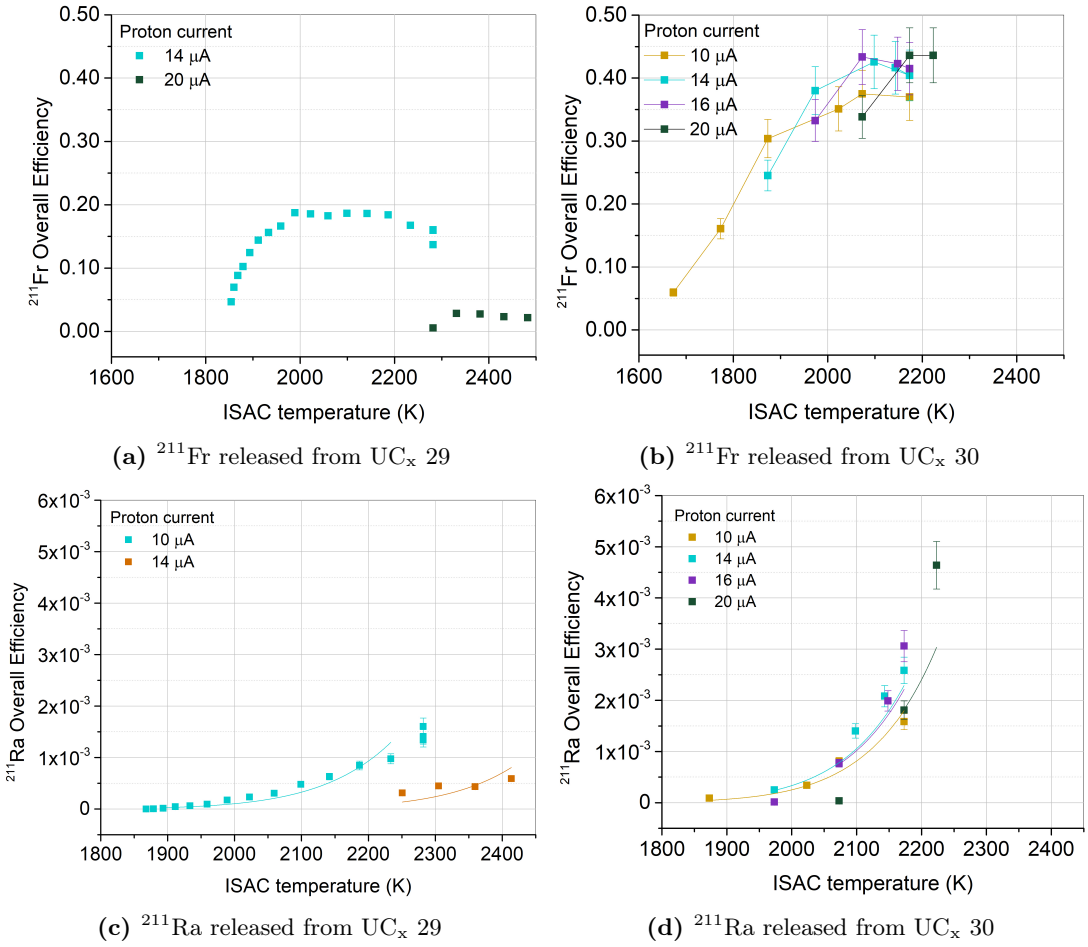

(a) ^{211}Fr released from UC$_x$ 29 **(b)** ^{211}Fr released from UC$_x$ 30

(c) ^{211}Ra released from UC$_x$ 29 **(d)** ^{211}Ra released from UC$_x$ 30

Figure 4.55: Overall efficiency of ^{211}Fr and ^{211}Ra released from UC$_x$ 29 and UC$_x$ 30. Curves fitted with Eq. 4.30

by the relatively long half life of this isotope ($t_{1/2}$=3.10 min). In contrast with short-lived isotopes that rely on fast thermal-promoted diffusion to escape on time before decaying, long-lived isotopes will approach a constant release since their diffusion times are shorter than their half-life and their probability of escaping maximizes (Eq. 1.4). Above ≈1900 K, most ^{211}Fr isotopes might be able to escape before decaying, so changes in temperature are negligible for their release.

The overall efficiency curves of ^{211}Fr released from the UC$_x$ 30 at different proton-beam currents overlap (Fig. 4.55b), suggesting that the target temperature estimated with the ISAC model is correct. On the other hand, the overall efficiency curves of ^{211}Fr released from UC$_x$ 29 do not overlap. Several ^{211}Fr measurements were taken with the UC$_x$ 29 target above 2200 K at 14 μA and 20 μA. The results indicate that the overall efficiency at both proton currents reduces despite the increasing temperature (Fig. 4.55a). This trend implies that uranium vaporization, expected at T >2200 K, was hindering the ion source efficiency as was also speculated for UC$_x$ 26 (Section 4.8.1). The overall efficiency reducing with

increasing temperature suggests that the ISAC model estimations were correctly predicting the temperature of this target as well.

The ^{211}Ra overall efficiency increases with temperature in both UC_x 29 and UC_x 30 targets (Fig. 4.55). Given that the ^{211}Ra yields are normalized per µA, it would be expected for their overall efficiency curves to be overlapped at similar temperatures; however, the curves corresponding to UC_x 29 do not overlap (Fig. 4.55c). As hypothesized for the ^{211}Fr overall efficiency at 20 µA, the ^{211}Ra overall efficiencies at 10 µA are most likely lower than expected because the corresponding yields were taken at T>2200 K and this caused target material vaporization and consequently a decline in the ionization efficiency. In contrast with the UC_x 29, all the overall efficiency curves of ^{211}Ra released from UC_x 30 at different proton-beam currents are overlapping (Fig. 4.55d).

For both targets, the temperature estimated with the ISAC model seems correct. The overall efficiency curves of ^{211}Fr and ^{211}Ra released from UC_x 30 at different proton currents overlap, confirming that the temperature estimated for this target is consistent. In addition, despite the fact that the UC_x 29 overall efficiency curves do not overlap, they seem to be lower at temperatures over the operational limit, agreeing with the assumption that uranium vaporization reduces the ion source efficiency. The temperature of the very first 1-step casting UC_x target (UC_x 26) was estimated with the ISAC model [120] assuming a conservative effective emissivity value of 0.10 [78], that was later on corrected to 0.15 for consecutive UC_x targets (UC_x 29 and UC_x 30) [78].

The ISAC model temperature estimations are close to those obtained with FE simulations at electrical currents bellow 300 A (Fig. 4.45). The temperature agreement between models is better when the ISAC model is evaluated with the electrical power obtained with COMSOL (Fig. 4.46). Nevertheless, the maximum electrical current allowed to keep the target below the maximum operational temperature of ≈2200 K is 350 A, so most of the proton-beam and electrical current combinations are within the range of agreement between models. Since yield measurements are not taken with proton-beam and electrical current combinations in the range where the ISAC model drifts away from the FE model, the electrical power functions cannot be validated with the isotopes' yields. However, given the difference between the UC_x 29, UC_x 30, and UC_x 26 targets it can be concluded that the effective emissivity is crucial for the estimation of the target temperature, and that it most likely ≈0.15. Experimentally, an effective emissivity of 0.12 was found for a target oven with three heat shields loaded with a graphite container; however, the container was empty because the experiment was performed in the non-actinide furnace. Thus, it is possible for the effective emissivity to be different than 0.12 for a target loaded with a graphite container filled with UC_x discs. An experimental campaign for the determination of the effective emissivity of the UC_x targets made with the 1-step casting method is advised.

The Q and D_0/r^2 for ^{211}Ra releasing from UC_x 29 and UC_x 30 targets were obtained by fitting their overall efficiency curves with Eq. 4.6. The temperatures of the UC_x 29

and UC_x 30 at 14 µA were considered correct, so an offset between the overall efficiency corresponding to this proton-beam current and the rest was estimated. Since the activation energy for ^{211}Ra should be identical for both UC_x targets, the Q obtained from fitting the overall effcicency curves of UC_x 30 was used as a boundary when fitting the overall efficiency curves of ^{211}Ra released from UC_x 29. The UC_x 30 results were set as reference because yields of ^{211}Ra were extracted from this target at several proton-beam currents and, in contrast with the UC_x 29, the UC_x 30 was not operated above the temperature limit. Also, the overall efficiency values above 2200 K were not included when fitting the 14 µA curve of the UC_x 29 because it was assumed that above that temperature the ion source efficiency was diminished due to uranium evaporation.

The diffusion coefficient D_0 for ^{211}Ra should be similar for both UC_x targets. The resulting D_0/r^2 from the fits is in the same order of magnitude for both targets, but it is smaller for UC_x 29. Assuming that the average diameter of the targets' cross sections (Table 4.8) would determine the isotope diffusion, a D_0 is obtained. The D_0 of ^{211}Ra diffusing from UC_x 30 is almost twice than the UC_x 29 D_0, but is within one sigma (Table 4.9). The isotope diffusion would be determined by the particle size distribution of the target with a corresponding distribution of diffusion coefficients. However, for comparison between these and future targets, the average particle size in the target material's cross section could be a reference.

Table 4.8: Open porosity, and maximum, minimum and average particle size of UC_x 29 and UC_x 30 (Section 2.3).

		Particle size (µm)					
	Open porosity (%)	Surface			Cross section		
Target		Min	Max	Ave	Min	Max	Ave
UCx29	49	0.8	6.2	1.8	0.8	3.0	1.7
UCx30	40	0.5	4.8	1.8	0.7	2.8	1.3

UC_x 30 had a better performance than UC_x 29 (Fig. 4.55). The difference in overall efficiency between the UC_x 29 and UC_x 30 targets is within the same order of magnitude. However, the maximum overall efficiency of ^{211}Fr and ^{211}Ra released from UC_x 30 is almost double than that of UC_x 29 (cyan curves in Fig. 4.55). While the UC_x 29 has higher open porosity (Table 4.8), the higher UC_x 30 overall efficiency indicates that diffusion from grains has a larger influence in the release of ^{211}Fr and ^{211}Ra. This is in agreement with Carraz et.al. [23], which found that the release of elements of groups 1A and 2A (as francium and radium are respectively) are diffusion and not effusion dominated. The difference in overall efficiency between targets highlights the importance of particle size. While there is no commercially available UO_2 with smaller particle size, modifying the milling methodology and optimizing the UO_2 carbothermal reduction will deliver smaller UC_x particle size.

Table 4.9: Activation energy Q and diffusion coefficient values for ^{211}Ra released from UC_x 29 and UC_x 30. Results obtained by fitting with Eq. 4.30 the overall efficiency curves plotted against temperature estimated with the ISAC model (Eq. 4.13).

Target	Q (J/mol)	D_0/r^2 (s^{-1})	D_0 (cm^2/s)
UC_x 29	$(4.01 \pm 0.39) \times 10^5$	$(0.14 \pm 3.13) \times 10^3$	$(4.15 \pm 1.67) \times 10^{-5}$
UC_x 30	$(4.02 \pm 0.50) \times 10^5$	$(0.47 \pm 1.28) \times 10^3$	$(7.98 \pm 5.08) \times 10^{-5}$

4.8.3 Yield comparison of UC_x targets synthesized with new and old method

The UC_x 29 and UC_x 30 targets were coupled to a rhenium surface ion source[3], so their isotope release results were comparable to historic targets. The isotopes measured in common among UC_x targets made with the new and old methods (Section 2.3) were ^{29}Mg, ^{31}Mg and ^{33}Mg, and ^{25}Na, ^{26}Na, ^{27}Na and ^{28}Na, as well as several francium isotopes. Since each UC_x target was irradiated at different proton-beam currents, their yields were normalized with the proton beam current used during their irradiation. The variation in yields or overall efficiency among targets is depicted as error bars. To obtain the overall efficiency (ε) (Eq.1.2), the normalized yields were averaged and divided by the expected nominal production rates obtained with FLUKA for the 1-step and 2-step casting target respectively (Section 4.3). The overall efficiency is fitted with Eq. 4.8 [121], but the data is insufficient for a reliable fit; the curves are left as guides to compare the 1-step casting overall release results with that of other targets.

In comparison with the average francium yields measured from several targets synthesized with the old method, the 1-step casting UC_x targets have a lower extraction yield but are still within the standard deviation (Fig. 4.56a). The intensity of the francium isotopes varies significantly for the UC_x targets. This is in part because a reliably stable RIB yield is sought during the yield evaluation preceding RIB delivery. To avoid compromising the target oven performance (Chapter 3) and to prevent sintering the UC_x particles (Section 2.3), the target might not be submitted to its limiting temperature; consequently, the yield measurements reported might not always correspond to the maximum yield available. Further investigations in the target materials to find their electrical and thermal properties will expand the simulations capabilities of the targets to determine their temperature and optimize their operation. Moreover, further development of barriers to stop carbon from penetrating the ovens will contribute to extend their lifetime, having its prime properties through all its operation.

The UC_x targets performance is also affected by variations in their microstructure. Furnace malfunctions and variations in the carbothermal reduction and conditioning during the

[3]At TRIUMF, the SIS has the same structure as the RILIS (C.2); when required, lasers were aimed at the UC_x 29 and UC_x 30 SISs to operate them as RILISs.

production of the targets leads to variations in their particle size and porosity (Section 2.3). Moreover, the yield fluctuation might also be associated with the artisanal nature of the UC_x targets. While their production process is standardized, variations in the composite thickness are expected since the slip cast is done manually. Darwin Ortiz (ISAC chemist) has successfully implemented a slip-casting methodology using a Micrometer Adjustable Film Applicator to homogenize the thickness of non-actinide slip castings; implementing this technique for casting UC_x targets is under consideration.

The overall efficiency of most of the francium isotopes' obtained from the 1-step casting is either within one standard deviation or within the same order of magnitude as the corresponding overall release from 2-step casting targets. Furthermore, to gauge the new UC_x targets' performance within the ISOL community, a comparison is made with the ISOLDE yields (Fig. 4.56b); overall, the francium yields obtained with the new UC_x targets are lower than those of ISOLDE except for ^{214}Fr with a half-life of $t_{1/2}$=5 ms, signalling the potential gain of the new target material synthesis for short lived isotopes.

Ideally, the overall release of the 1-step casting targets would be equal or higher than the traditional method, so further developing of the UC_x targets is advised. Improvements in the milling and carbothermal reduction methods will deliver UC_x targets with smaller particle size to enhance isotope release. This development is feasible thanks to the manufacturing time reduction gained with the new UC_x production method (Section 2.3).

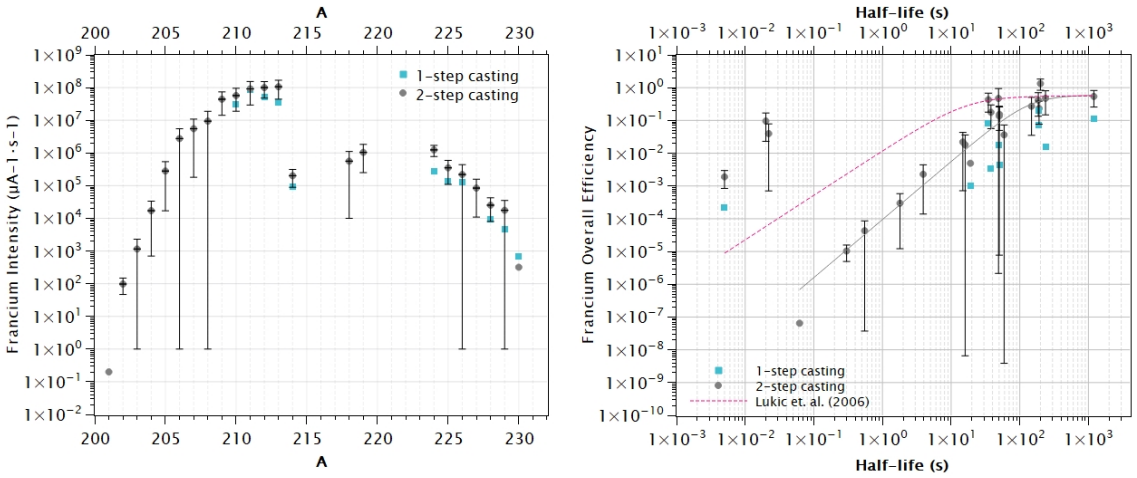

(a) Yield **(b)** Overall release

Figure 4.56: Francium yield and overall release from 1-step and 2-step UC_x targets. The 2-step casting error bars correspond to the yields standard deviation among several 2-step casting UC_x targets.

The magnesium yields from the 2-step casting UC_x targets are consistently higher than the 1-step casting ones (Fig. 4.57a). Nonetheless, the UC_x 1-step casting target performance for all three magnesium isotopes is within the same order of magnitude as the 2-step casting targets. For both, the 1-step and the 2-step casting targets, the magnesium overall release is

larger for magnesium isotopes with longer half-lives as expected given that long-lived isotopes have a larger chance to escape the target before decaying. However, the slope corresponding to the 2-step casting targets is smaller than the 1-step casting one. On the other hand, the magnesium overall efficiency obtained with the new UC_x target is several orders of magnitude higher than the one reported in [121] (Fig. 4.57b). This higher performance can be attributed to the ion source; while the ion source of all the targets compared was originally a SIS (Appendix C.1), the 1 and 2-step casting targets' ion source was operated with a Resonant Ionization Laser Ion Source (Appendix C.2), resulting in a higher ionization efficiency. This superior overall efficiency demonstrates how important is the ion source - target material match for the extraction of certain isotopes.

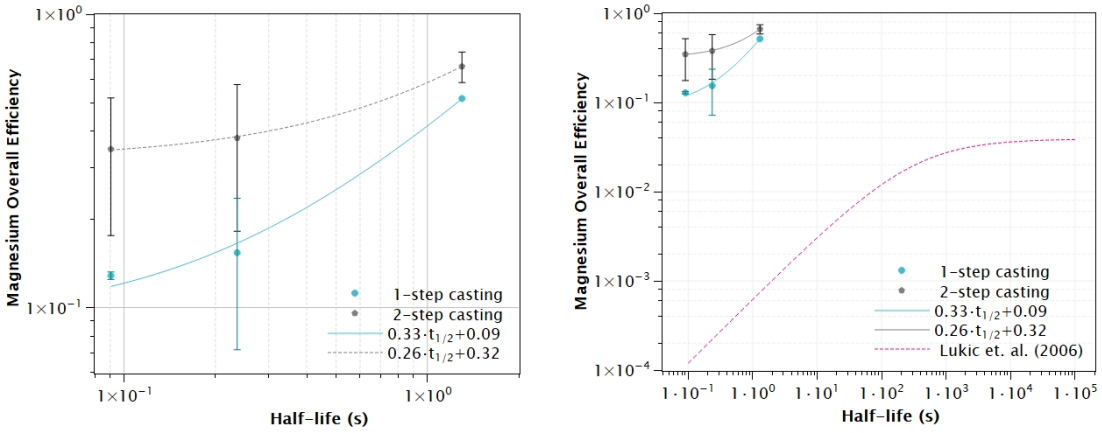

Figure 4.57: Magnesium overall release from 1-step and 2-step UC_x targets (a), and their comparison with ISOLDE [121] (b). The 2-step casting error bars correspond to the standard deviation among several targets.

The sodium release of the 1 and 2-step casting targets is identical. Comparing the sodium release of TRIUMF UC_x targets to the one of the ISOLDE targets [121] (Fig. 4.58), it is observed that the overall release of the short lived one is higher while the release of the sodium isotopes with loger half-lives is similar as their overall efficiency approaches one. All the UC_x targets compared, including the ISOLDE ones, were coupled with surface ion sources, so a direct comparison between overall release is viable.

The francium, magnesium, and sodium overall release from 1-step casting UC_x targets is of the same order of magnitude as the traditional UC_x targets. Furthermore, the overall release of the UC_x targets developed in this work is also competitive to that of other ISOL facilities. Moreover, thanks to the accelerated manufacturing method of the new UC_x targets, continuous investigations and development of UC_x is feasible. Extensive irradiation campaigns are advised for the complete characterization of the UC_x targets' release.

Yield measurements campaigns should be dedicated to the characterization of UC_x targets made with the new method. Despite their adequate performance, continuous investiga-

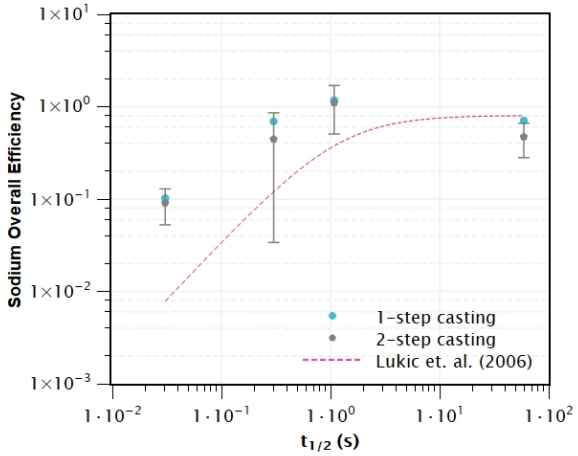

Figure 4.58: Sodium isotopes measured from UC_x targets synthesized with the one and the two step casting methods.

tions of their isotope release will provide trends to guide the development and consequential improvement of UC_x targets. The Chamber for Heating Investigations will also be a powerful tool for the characterization of the release and thermal properties of the UC_x, but online experiments will still be required to account for the thermal gradients due to power deposited by the proton beam. The 1-step casting has relieved resources and allowed the accelerated production of a larger number of UC_x targets per season, this should seized as an opportunity for the continuous development of the UC_x target.

Chapter 5

Conclusions

Target materials are an essential component of the ISOL method. Isotopes are produced when a high-energy beam impacts a target, inducing nuclear reactions. The efficiency of the isotopes released from the target is the main limitation of the ISOL method; tailoring the target materials' microstructure and operating them at high temperatures account for the isotopes' release. In this work, target materials with microparticle size, high porosity, and the ability to withstand high temperatures have been synthesized and characterized.

TRIUMF's target collection has been expanded by developing three new targets, contributing to delivering more diverse and intense beams to experiments through the ISOL method. To expand the quality and duration of the targets' irradiation campaign, tantalum embrittlement due to carbon penetration has been investigated. Furthermore, the temperature of the target has been studied and better understood by combining modelling and online isotope-release experiments, resulting in a comprehensive characterization of the target's isotope release.

LaC_2/C, UC_x, and graphite-composite targets have been developed in this work. LaC_2/C has been synthesized as a rehearsal for UC_x. Even though LaC_2/C targets cannot be irradiated at ISAC because of their promptness to oxidation, this target material will be part of ARIEL's repertoire since its resulting porosity and micro morphology are competent for isotope release. This target is projected to deliver cesium and barium isotopes with no isobaric contamination. By improving the methodology for the successful carbothermal reduction of LaC_2/C over graphite foil in a single step, the UC_x targets are synthesized eight times faster than conventionally.

The new accelerated methodology for synthesizing UC_x targets developed in this work liberates personnel and resources to pursue research and development. The new UC_x targets have a similar particle size to those synthesized before; also, their isotope release is within one standard deviation of the average yields corresponding to the targets made with the traditional methodology. The new UC_x target is part of the ISAC target collection and it

will be part of ARIEL's collection in the future. To improve the performance and purity of the new UC_x targets, it is proposed to reduce the milling time by using commercially available precursors with smaller particle sizes, consequently minimizing the tungsten and cobalt content that has been detected with post-irradiation studies of UC_x targets. This change in milling methodology will further shorten the production length, which has already allowed the development of a new target that is the graphite-composite target.

The graphite-composite target developed in this work has become part of ISAC's target collection, supplying beryllium and lithium isotopes at competitive rates. In contrast with the preceding targets used to deliver these light isotopes, the graphite-composite target has a lower gas exhaust during irradiation, alleviating ISAC's radioactive inventory. The graphite-composite target open porosity is ≈41% higher than that of the commercially available graphite foil (Table 2.14), and its ^{7}Be offline release is ten times larger than that of the graphite foil. These materials release have been compared offline in CHI, giving insight into the targets' performance before submitting them online. Continuous offline studies with the current and upgraded equipment and methods endorse improving existing target materials and promote developing new ones. Together, offline and online studies allow a complete characterization of target materials isotope release.

The three targets developed in this work have high carbon content. The tantalum ovens used for resistively heating the targets online are prone to embrittlement due to carbon penetration, consequently modifying their thermal and electrical properties, impairing their performance, and ultimately hindering the targets' isotope release. In this research, the embrittlement mechanism of the target oven and the TaC coating conventionally used to protect them have been investigated, concluding that TaC does not prevent carbon penetration. Rhenium has been proposed as an alternative coating material. Furthermore, a methodology to coat tantalum with rhenium has been developed and tested in-house. Additional trials with simultaneous characterization should be carried on to quantify the effectiveness of rhenium as a carbon diffusion barrier. Also, an alternative to a diffusion barrier is proposed, consisting of injecting an inert gas in the oven during operation to increase the internal pressure of the oven such that the graphite's vaporization temperature is higher than the target operational temperature. Increasing the ovens' resistance against carbon embrittlement shifts the performance of the target towards the target material that is often qualified to withstand longer and more intense irradiation campaigns than those to which it is submitted.

Heating the target material enhances the isotope release. Measuring the targets' temperature during irradiation is currently unattainable, so operating them at a proper temperature relies on models. Two new finite element models have been developed for the UC_x and the graphite-composite targets. In contrast with previous analytical models, the new FE model for the UC_x target accounts for heat exchange by radiation within the target oven. However,

the temperature properties of the house-made target materials should be experimentally obtained to improve the FE results. The new model for the graphite-composite target indicates that the ^{8}Li and ^{9}Li release from the graphite-composite do not present a RED effect as initially suspected, and suggests that these isotope trends are due to a thermal gradient that is not taken into consideration during irradiation. Characterizing the thermal properties of the graphite-composite target is also recommended. Moreover, all targets should be characterized in pursuit of optimal operation during irradiation and maximum isotope release.

Finally, new targets have been included in ARIEL and ISAC collections, broadening TRIUMF's scientific capacity. Furthermore, with the new accelerated UC_x synthesis method, resources can be dedicated to keep developing the target repertoire. The unprecedented characterization performed in this work, including microstructure, thermal modelling, post-irradiation analysis, and target longevity marks the beginning of a systematic research and development targetry era for TRIUMF's RIB factory essential when both ISAC and ARIEL run experiments simultaneously.

Bibliography

[1] J. Dilling, R. Krücken, and G. Ball. ISAC overview. *ISAC and ARIEL: The TRIUMF Radioactive Beam Facilities and the Scientific Program*, (225):1–7, 2014.

[2] P. G. Bricault. Thick target for high-power ISOL facilities. *Nuclear Instruments and Methods in Physics Research B*, 376:3–7, 2016.

[3] T.I. Meyer, B. K. Jennings, R. Kruecken, M. Baluk, J. Gagné, and M. McLean. Five-year plan 2015–2020: Realizing the vision. pages 1–484, 2013.

[4] J. Dilling, R. Krücken, and L. Merminga. ARIEL overview. *ISAC and ARIEL: The TRIUMF Radioactive Beam Facilities and the Scientific Program*, (225):253–262, 2014.

[5] A. Gottberg. Target materials for exotic ISOL beams. *Nuclear Instruments and Methods in Physics Research B*, 376:8–15, 2016.

[6] P. Kunz, P. Bricault, M. Dombsky, N. Erdmann, V. Hanemaayer, J. Wong, and K. Lützenkirchen. Composite uranium carbide targets at TRIUMF: Development and characterization with SEM, XRD, XRF and L-edge densitometry. *Journal of Nuclear Materials*, 440(1-3):110–116, 2013.

[7] S. Carturan, M. Tonezzer, L. Piga, P. Zanonato, P. Colombo, A. Andrighetto, L. Biasetto, P. Di Bernardo, G. Maggioni, F. Gramegna, and G. Prete. Synthesis and characterization of lanthanum dicarbide-carbon targets for radioactive ion beams generation via the carbothermal reaction. *Nuclear Instruments and Methods in Physics Research A*, (583):256–263, 2007.

[8] M. Cervantes, P. Fouquet-Mètivier, P. Kunz, Laura L., A. Mjøs, T. Day Goodacre, J. Wong, and A. Gottberg. UC_x target production at TRIUMF in the ARIEL era. *Nuclear Instruments and Methods in Physics Research Section B*, 463:367–370, 2019.

[9] Igor L. Shabalin. *Ultra-High Temperature Materials II. Refractory Carbides I (Ta, Hf, Nb and Zr Carbides)*. Springer, Dordrecht, 2019.

[10] G.D. Alton, J.R. Beene, and Y. Liu. Criteria for selection of target materials and design of high-efficiency-release targets for radioactive ion beam generation. *Nuclear Instruments and Methods in Physics Research A*, 438:190–209, 1999.

[11] U. Köster. Intense radioactive-ion beams produced with the ISOL method. *European Physical Journal A*, 15:255–263, 2002.

[12] Walter D. Loveland, David J. Morrissey, and Glenn T. Seaborg. *Modern Nuclear Chemistry*. John Wiley & Sons, Inc., Hoboken, New Jersey, 2006.

[13] D. W. Stracener, G. D. Alton, R. L. Auble, J. R. Beene, P. E. Mueller, and J. C. Bilheux. Targets used in the production of radioactive ion beams at the HRIBF. *Nuclear Instruments and Methods in Physics Research A*, 521:126–135, 2004.

[14] U. Köster. ISOLDE target and ion source chemistry. *Radiochimica Acta*, 89(11-12): 749–756, 2001.

[15] ISAC's Simulation Data Search. https://yield.targets.triumf.ca/search/simulation/data.

[16] Rahaman M. N. *Ceramic processing and sintering*. Marcel Dekker, Inc., New York, Basel, 2003.

[17] ISAC's target index.

[18] J. Ramos. *Titanium carbide-carbon porous nanocomposite materials for radioactive ion beam production: processing, sintering and isotope release properties*. PhD thesis, Ecole Polytechnique Federale De Lausanne, 2017.

[19] R. Kirchner. On the release and ionization efficiency of catcher-ion-source systems in isotope separation on-line. *Nuclear Instruments and Methods in Physics Research B*, 70:186–199, 1992.

[20] Mehrer Helmut. *Diffusion in Solids*. Springer Berlin Heidelber, 2007.

[21] J. Crank. *The mathematics of diffusion*. Clarendon press Oxford, 1975.

[22] S. Corradetti, L. Biasetto, D. Manzolaro, M.and Scarpa, S. Carturan, A. Andrighetto, G. Prete, J. Vasquez, P. Zanonato, P. Colombo, C. U. Jost, and D. W. Stracener. Neutron-rich isotope production using a uranium carbide - carbon Nanotubes SPES target prototype. *Neutron-rich isotope production using a uranium carbide - carbon Nanotubes SPES target prototype*, 49:1–10, 2013.

[23] L. C. Carraz, I. R. Iialdorsen, H. L. Ravn, M. Skarestad, and L Westgaard. Fast release of nuclear reaction products from refractory matrices. *Nuclear Instruments and Methods*, 148:217–230, 1977.

[24] Karl Jousten. *Handbook of Vacuum Technology*. Wiley-VCH, second edition, 2016.

[25] O. Bajeat, M. Cheikh Mhamed, S. Essabaa, and Y. Huguet. UC_x target developments for the ALTO and the SPIRAL 2 projects. *Nuclear Instruments and Methods in Physics Research A*, 562:44–53, 2006.

[26] L. Biasetto, P. Zanonato, S. Carturan, P. Bernardo, P. Colombo, A. Andrighetto, and G. Prete. Developing uranium dicarbide – graphite porous materials for the SPES project. *Journal of Nuclear Materials*, 404(1):68–76, 2010.

[27] P. Hoff, O. C. Jonsson, E. Kugler, and H. L. Ravn. Release of nuclear reaction products from refractory compounds. *Nuclear Instruments and Methods In Physics Research*, 221:313–329, 1984.

[28] TRIUMF. Annual Report Scientific Activities 2001. pages 1–263, 2002.

[29] TRIUMF. Annual Report Scientific Activities 2002. pages 1–322, 2003.

[30] M. Dombsky and P. Kunz. ISAC targets. *Hyperfine Interactions*, (225):17–24, 2013.

[31] M. Dombsky and V. Hanemaayer. Method of forming composite targets. (Patent-20060040064.).

[32] V. Hanemaayer, P. Bricault, and M. Dombsky. Composite ceramic targets for high power proton irradiation. *Nuclear Instruments and Methods in Physics Research B*, 266:4334–4337, 2008.

[33] Xing Hai Wei, Lang Liu, Jin Xi Zhang, Jing Li Shi, and Quan Gui Guo. Mechanical, electrical, thermal performances and structure characteristics of flexible graphite sheets. *Journal of Materials Science*, 45:2449–2455, 2010.

[34] Mia Au. Thermal Conductivity in ISOL Target Materials: Development of a numerical approach and an experimental apparatus. Master's thesis, University of British Columbia, 2020.

[35] Technical data sheet graphite foil. CeraMaterials. https://www.ceramaterials.com/wp-content/uploads/2021/10/GRAPHITE_FOIL_TDS_CM_10_21.pdf. Accessed: 2020-01-27.

[36] Laura Lambert, private communication.

[37] Argonne National Laboratory. EPICS. Experimental Physics and Industrial Control System. https://epics.anl.gov/.

[38] O. Alyakrinskiy, K. Gubin, P. Martyshkin, and L. Tecchio. Influence of grain size and porosity on the release of radioactive isotopes from target materials with high open porosity. *Nuclear Instruments and Methods in Physics Research, Section B*, 267: 2554–2558 Contents, 2009.

[39] David R. Lide. *Handbook of chemistry and physics*. CRC Press, 2003-2004.

[40] D. William and Jr. Calister. *Materials Science and Engineering an Introduction*. John Wiley & Sons, Inc., 1997.

[41] Goldstein Joseph I., Newbury Dale E., Michael Joseph R., W.M. Ritchie Nicholas, Scott John Henry J., and Joy David C. *Scanning Electron Microscopy and X-Ray Microanalysis Theory, Practice, & Procedures*. Springer, 2018.

[42] Dunlap Michael and J. E. Adaskaveg Dr. *Introduction to the Scanning Electron Microscope Theory, Practice, & Procedures*. Facility for advanced instrumentations, 1997.

[43] Regie Sacdalan. Equipment | Electron Microscopy Laboratory. http://emlab.mtrl.ubc.ca/.

[44] Putz, H. and Brandenburg GbR, K. Match! - Phase Analysis using Powder Diffraction, Crystal Impact, version 3.x. https://www.crystalimpact.de/match.

[45] COD - Crystallography Open Database. http://www.crystallography.net/cod/.

[46] Gschneidner K.A. and Calderwood F.W. *Bull. Alloy Phase Diagr*, 7:86, 1986.

[47] Richard E. Honig. *Radio Corporation of America*. Princeton, N. J., 1965.

[48] D. Yosifov and I. Sekachev. ISAC target vacuum system. *Journal of Vacuum Science and Technology. A, International Journal Devoted to Vacuum, Surfaces, and Films*, 24(4), 7 2006.

[49] C. A. Stearns and F. J. Kohl. Vaporization thermodynamics of the lanthanum carbon system. Mass spectrometric determination of the dissociation energy of LaC_2, LaC_3, and LaC_4. *The Journal of Chemical Physics*, 54:5180–5187.

[50] M. J. Joung, J. W. Jeong, W Hwang, S. G. Hong, J. Y. Kim, S. J. Park, H. J. Woo, B. H. Kang, and S. H. Na. A study of the high-temperature characteristics of a lanthanum dicarbide-carbon composite for RAON. *Nuclear Instruments and Methods in Physics Research B*, 456:97–102, 2019.

[51] J. Guillot. Synthèses et caractérisations de pastilles de carbure de lanthane. Master 2 Recherche en Matériaux pour les Structures et l'Energie, Université Paris Sud, 2014.

[52] H. L. Ravn, T. Bjørnstad, P. Hoff, O. C. Jonsson, E. Kugler, S. Sundell, and B. Vosički. Use of refractory oxides, carbides and borides as targets for on-line mass separation. *Nuclear Inst. and Methods in Physics Research, B*, 26:183–189, 1987.

[53] L. Biasetto, S. Carturan, G. Maggioni, P. Zanonato, P. Di Bernardo, P. Colombo, A. Andrighetto, and G. Prete. Fabrication of mesoporous and high specific surface area lanthanum carbide-carbon nanotube composites. *Journal of Nuclear Materials*, 385:582–590, 2009.

[54] Alfa Aesar. Lanthanum(III) hydroxide. https://www.alfa.com/en/catalog/043123/. Accessed: 2023-03-09.

[55] Alfa Aesar. Graphite powder. https://www.alfa.com/en/catalog/040798/. Accessed: 2022-09-28.

[56] The ISOLDE Yield Database, Version 0.2. Target types containing Lanthanum - Yield Overview. https://isoyields2.web.cern.ch/YieldBasic.aspx?targetTypeZ=57, 2021. [Online; accessed 17.06.2022].

[57] A. Neumann and D. Walter. The thermal transformation from lanthanum hydroxide to lanthanum hydroxide oxide. *Thermochimica Acta*, 445:200–204, 2006.

[58] N. N. Greenwood and A. J. Osborn. 345. chemical and magnetic properties of lanthanum dicarbide and sesquicarbide. *Journal of the Chemical Society*, page 1775, 1961.

[59] American Elements. *Lanthanum Carbide*, 5 2021.

[60] M. Atoji, A.H. Daane, K.A.jr. Gschneidner, R.E. Rundle, and Spedding F.H. The structures of lanthanum dicarbide and sesquicarbide by X-ray and neutron diffraction. *Crystal Structures*, 80:1084–1808, 1958.

[61] R. W. G. Wyckoff. Structure of Crystals. Second edition. *Chemical Catalog Company, INC*, 80:237–241, 1931.

[62] H. Schumann, K. Zietzke, and R. Weimann. Organometallic compounds of the lanthanides, 99. Synthesis and crystalstructure of bis(cyclopentadienyl)rare earth acetates $(Cp_2LnO_2CCH_3)_2$ (Cp = C_5H_5, C_5HMe_4, C_5Me_{55}. *European Journal of Solid State and Inorganic Chemistry*, 33:122–144, 1996.

[63] Reynolds . Plastic wrap with slide cutter | reynolds brands . https://www.reynoldsbrands.com/products/other-products/plastic-wrap.

[64] Andrew Peacock. *Handbook of polyethylene : structures: properties, and applications*. Boca Raton, FL : CRC Press, first edition edition, 2000.

[65] J. Fayos. Possible 3D carbon structures as progressive intermediates in graphiteto diamond phase transitionNote: mathematical model. *Journal of Solid State Chemistry*, 148:278–285, 1999.

[66] R. Kirchner. On the thermoionization in hot cavities. *Nuclear Inst. and Methods in Physics Research, A*, 292:203–208, 1990.

[67] J. P. Hiernaut, J. Y. Colle, R. Pflieger-Cuvellier, J. Jonnet, J. Somers, and C. Ronchi. A knudsen cell-mass spectrometer facility to investigate oxidation and vaporisation processes in nuclear fuel. *Journal of Nuclear Materials*, 344:246–253, 2005.

[68] International Bio-Analytical Industries, Inc. Uranium Dioxide. https://ibilabs.com/uranium-uranyl-thorium-compounds/https-ibilabs-com-msds-uranium-compounds/uranium-oxide-di-uo2/.

[69] AmScope ©, 2003-2020, Version x64, 4.11.17864.20201020.

[70] Edmund K. Storms. *Refractory Materials: The Refractory Carbides (A Series of Monographs, Volume 2)*. Academic Press, 1967.

[71] A.E. Austin. Carbon positions in uranium carbides. *Acta Crystallographica (1,1948-23,1967)*, 12:159–161, 1959.

[72] D.W. Jones, I.J. McColm, J. Yerkess, and N.J. Clark. *J. Solid State Chem*, 74.

[73] R. W. G. Wyckoff. Second edition. Interscience Publishers, New York, New Yorkrock-salt structure. *Crystal Structures*, 1:85–237, 1963.

[74] Ph. Dehaudt, L. Bourgeois, and H. Chevrel. Activation energy of UO_2 and UO_{2+x} sintering. *Journal of Nuclear Materials*, 299:250–289, 2001.

[75] R. W. G. Wyckoff. Second edition. Interscience Publishers, New York, New YorkFluorite structure. *Crystal Structures*, 1:239–444, 1963.

[76] S. Lambert, H. Leligny, and D. Grebille. Three forms of the misfit layered cobaltite (Ca2 Co O3) (Co O2)1.62. A 4D structural investigation. *Journal of Solid State Chemistry*, 160:322–331, 2001.

[77] Q. H. Wang, Z. D. Huang, J. L. Ni, W. Xiong, and J. R. Li. A novel force rendering approach for virtual assembly of mechanical parts. *International Journal of Advanced Manufacturing Technology*, 86:977–988, 2016.

[78] TRIUMF's internal documentation.

[79] J. Leciejewicz. A note on the structure of tungsten carbide. *Acta Crystallographica*, 14(2):200, 1961.

[80] T. Epicier, J. Dubois, C. Esnouf, P. Convert, and G. Fantozzi. Neutron powder diffraction studies of transition metal hemicarbides M2C1-x - II. In situ high temperature study on W2 C1-x and Mo2 C1-x. *Acta Metallurgica*, 36:1913–1921, 1988.

[81] Igor L. Shabalin. *Ultra-High Temperature Materials I. Carbon (Graphene/Graphite) and Refractory Metals*. Springer, Dordrecht, 2019.

[82] G. Hörz, K. Lindenmaier, and R. Klaiss. The influence of carbon on the electrical resistivity of niobium and tantalum. *Journal of The Less-Common Metals*, 35:77–84, 1974.

[83] Paul Rossiter. *The Electrical Resistivity of Metals and Alloys*. Cambridge University Press, 1987.

[84] A. Mjøs. Power loss in target heater transmission lines. *TRIUMF documents*, pages 1–5, 2016.

[85] CeraMaterials. graphite foil. https://www.ceramaterials.com/graphite-foil/. Accessed: 2022-09-28.

[86] G. Hörz, K. Lindenmaier, and R. Klaiss. High-temperature solid solubility limit of carbon in niobium and tantalum. *Journal of The Less-Common Metals*, 35:97–105, 1974.

[87] M. Bischof, S. Mayer, H. Leitner, H. Clemens, P. Staron, E. Geiger, A. Voiticek, and W. Knabl. On the development of grain growth resistant tantalum alloys. *Nuclear Instruments and Methods*, 24:437–444, 2006.

[88] SGL carbon SIGRAFINE®R7510. https://www.sglcarbon.com/pdf/SGL-Datasheet-SIGRAFINE-R7510-EN.pdf.

[89] Charles Kittel. *Introduction to Solid State Physics*. John Wiley & Sons, Inc., 2005.

[90] P. Lejček. *Grain Boundary Segregation in Metals*. Springer, Berlin, Heidelberg, 2010.

[91] Christian Herzig and Yuri Mishin. *Diffusion in Condensed Matter: Methods, Materials, Models*. Springer Berlin Heidelber, 2005.

[92] H. Bhadeshia and R. Honeycombe. *Steels : Microstructure and properties*. Elsevier Science & Technology, 2017.

[93] D. R. Askeland, P. P. Fulay, and W. J. Wright. *The Science and Engineering of Materials*. Cengage Learning, Stamford, CT, 2011.

[94] Plansee. tantalum. https://www.plansee.com/en/materials/tantalum.html.

[95] J.A. Jacobs and Kilduff T. F. *Engineering materials technology*. Prentice-Hall Inc., New Jersey, 1985.

[96] Paul Shewrnon. *Diffusion in Solids. Fundamentals,Methods,Materials, Diffusion-Controlled Processes*. Springer, 2007.

[97] W. F. Hosford. *Physical Metallurgy*. CRC Press Taylor & Francis Group, Boca Raton, FL, 2010.

[98] TRIUMF. Annual Report Scientific Activities 2003. pages 1–331, 2004.

[99] M. Dombsky, P. Bricault, and V. Hanemaayer. Increasing beam currents at the TRIUMF-ISAC Facility; techniques and experiences. *Nuclear Physics A*, (746):32c–39c, 2004.

[100] Dominique Cotton. *Etude de formation d'hémicarbure de tantale (Ta_2C) par l'intermédiaire d'un procédé de cémentation sous pression réduite*. PhD thesis, Universite de Bourgogne, 2015.

[101] L. Carette, Ph. Jacquet, D. Cotton, V. Vignal, and S. Faure. (TaC/Ta_2C) bilayer formed on carburized and annealed tantalum; development of a numerical growth model. *Applied Surface Science*, 467-468:84–88, 2019.

[102] E. A. Juarez-Arellano, B. Winkler, A. Friedrich, D. J. Wilson, M. Koch-Müller, K. Knorr, S. C. Vogel, J. J. Wall, H. Reiche, W. Crichton, M. Ortega-Aviles, and M. Avalos-Borja. Reaction of rhenium and carbon at high pressures and temperatures. *Zeitschrift fur Kristallographie*, 223:492–501, 2008.

[103] J. E. Boyd and B. S. Lenient. Investigation of diffusion barriers for refractory metals. *Technical documentary report NR ASD-TDR-62-432*, 1962.

[104] J. Li and R. H. Zee. Interdiffusion of rhenium and poco graphite. *Journal of The Less-Common Metals*, 420:381–385, 1998.

[105] Eagle Alloys. Global Materials Supplier. Pure Tantalum Metal & Tantalum Alloy Suppliers. https://www.eaglealloys.com/tantalum/.

[106] T. Gladman. *Grain size control*. Routledge, New York, NY, 2017.

[107] COMSOL Multiphysics® v. 6.0. COMSOL AB, Stockholm, Sweden. www.comsol.com.

[108] SOLIDWORKS® Professional 2020 SP5.0. https://www.3ds.com/products-services/solidworks/.

[109] E. R. Plante and R. Szwarc. Vapor pressure and heat of sublimation of rhenium. *JOURNAL OF RESEARCH of the National Bureau of Standards - A. Physics and Chemistry*, 70:175–179, 1965.

[110] G. Zschornack. *Handbook of X-Ray Data*. Springer, Berlin, Heidelberg, 2007.

[111] A. Réal Couture and D. Drouin. CASINO, monte CArlo SImulation of electroN trajectory in sOlids, Version 2. 2000.

[112] B. Hy, N. Barré-Boscher, and A. Özgümüs. An off-line method to characterize the fission product release from uranium carbide-target prototypes developed for SPIRAL2 project. *Nuclear Instruments and Methods in Physics Research, B*, 288:34–41, 2012.

[113] S. Tusseau-Nenez, B. Roussière, N. Barré-Boscher, and A. Gottberg. Characterization of uranium carbide target materials to produce neutron-rich radioactive beams. *Nuclear Instruments and Methods in Physics Research, Section B: Beam Interactions with Materials and Atoms*, 370:19–31, 2016.

[114] ed. Chan, H. E. *Graphene and Graphite Materials*. Nova Science Publishers, Incorporated, New York, Basel, 2009.

[115] Miriam Rossi. How can graphite and diamond be so different if they are both composed of pure carbon? *Scientific American*, 2007.

[116] D. D.L. Chung. A review of exfoliated graphite. *Journal of Materials Science*, 51: 554–568, 2015.

[117] M. Bonnissel, L. Luo, and D. Tondeur. Compacted exfoliated natural graphite as heat conduction medium. *Carbon*, 14:2151–2161, 2001.

[118] D. D.L. Chung. Exfoliation of graphite. *Journal of Materials Science*, 22:4190–4198, 1987.

[119] Anwar Kamal. *Nuclear Physics*. Springer, 2014.

[120] P. Kunz. Design note TRI-DN-14-10 ThO_2/nb target - beam power and thermal conductivity calculations. *TRIUMF Documents*, (111623):1–9, 2014.

[121] S. Lukić, F. Gevaert, A. Kelić, M. V. Ricciardi, K. H. Schmidt, and O. Yordanov. Systematic comparison of ISOLDE-SC yields with calculated in-target production rates. *Nuclear Instruments and Methods in Physics Research A*, 565:784–800, 2006.

[122] L. C. Carraz, I. R. Iialdorsen, H. L. Ravn, M. Skarestad, and L Westgaard. Fast release of nuclear reaction products from refractory matrices. *Nuclear Instruments and Methods*, 148:217–230, 1978.

[123] J. Daw, J. Crepeau, J. Rempe, D. Knudson, K. Condie, and C. Wilkins. Initial results from investigations to enhance the performance of high temperature irradiation-resistant thermocouples. *Journal of Power and Energy Systems*, 2:854–863, 2008.

[124] R. Skifton, J. Palmer, and A. Hashemian. Optimized high-temperature irradiation-resistant thermocouple for fast-response measurements. *EPJ Web of Conferences*, 253: 1–4, 2021.

[125] L. Michalski, K. Eckersdorf, J. Kucharski, and J. McGhee. *Temperature Measurement. Second Edition.* John Wiley Sons Ltd, 2001. ISBN 0-471-86779-9.

[126] M. Dombsky, P. Bricault, P. Schmor, and M. Lane. ISAC target operation with high proton currents. *Nuclear Instruments and Methods in Physics Research, Section B*, 204:191–196, 2003.

[127] P. Bricault, M. Dombsky, A. Dowling, and M. Lane. High power target developments at ISAC. *Nuclear Instruments and Methods in Physics Research B*, 204:319–324, 2003.

[128] Yunus A. Cengel. *Heat and Mass Transfer: Fundamentals and Applications.* McGraw-Hill Global Education Holdings, LLC., Oklahoma, USA, 2002.

[129] SRIM - The Stopping and Range of Ions in Matter. http://www.srim.org/index.htm.

[130] The thermal properties of twenty-six solid materials to 5000F or their destruction temperatures. (ASD-TDR-62-765), 1962.

[131] O.H. Olson and Morris J.C. WADC Technical Report 56-222, part 2, supplement 1, ASTIA Document No. 202494. 1958.

[132] C.Y. Ho, R.W. Powell, and P.E. Liley. Thermal Conductivity of the Elements. *Journal of Physical and Chemical Reference Data*, 1(2):279, 1972.

[133] A. Cezairliyan. High Temperatures-High Pressures. 4:541, 1972.

[134] ITW-TM2-C_2-LP-SIS Heating Curves (TRIUMF internal documentation). https://documents.triumf.ca/docushare/dsweb/View/Collection-29656. Accessed: 2023-05-25.

[135] Luca Egoriti. *Transport Phenomena in Radioisotope Beam Production Targets*. PhD thesis, Universite of British Columbia, 2023.

[136] TRIUMF Yield Database. https://yield.targets.triumf.ca/search/yield/data.

[137] Origin(Pro), Version 2022. OriginLab Corporation, Northampton, MA, USA.

[138] P. Yu, B. N. Popov, J. A. Ritter, and R. E. White. Determination of the lithium ion diffusion coefficient in graphite. *Journal of The Electrochemical Society*, 146:8–14, 1999.

[139] L. Mandeltort and J. Yates. Rapid atomic Li surface diffusion and intercalation on graphite: A surface science study. *Journal of Physical Chemistry C*, 116:24962–24967, 2012.

[140] V. Kumar, A. Kumar, D. Lee, and S. Park. Estimation of number of graphene layers using different methods: A focused review. *Materials*, 14:4590, 2021.

[141] M. Manzolaro, S. Corradetti, A. Andrighetto, and L. Ferrari. A steady-state high-temperature method for measuring thermal conductivity of refractory materials. *Review of Scientific Instruments*, 84, 2013.

[142] M. Ballan, M. Manzolaro, G. Meneghetti, A. Andrighetto, A. Monetti, G. Bisoffi, and G. Prete. A combined experimental and numerical approach for the control and monitoring of the SPES target during operation at high temperature. *Nuclear Instruments and Methods in Physics Research B*, 376:28–32, 2016.

[143] N. D. Milošević, G. S. Vuković, D. Z. Pavičič, and K. D. Maglić. Thermal properties of tantalum between 300 and 2300 K. *International Journal of Thermophysics*, 20: 1129–1136, 1999.

[144] Polyethylene glycol 400. https://www.alfa.com/en/catalog/B21992/.

[145] DI-PAK®Purification Pack (Large) CPDI000L1. https://www.emdmillipore.com/CA/en/product/DI-PAK-Purification-Pack-Large,MM_NF-CPDI000L1?ReferrerURL=https%3A%2F%2Fwww.google.com%2F&bd=1.

[146] City of Vancouver. City of vancouver waterworks utility annual report 2021. https://vancouver.ca/files/cov/water-quality-utility-report-2021.pdf.

[147] Ammonium Citrate Dibasic, Honeywell Fluka^{TM}. https://www.fishersci.ca/shop/products/ammonium-citrate-dibasic-honeywell-2/p-7071747.

[148] Glycerol, ReagentPlus. https://www.sigmaaldrich.com/CA/en/product/sigald/g7757.

[149] 1-Butanol, ACS. https://www.alfa.com/en/catalog/031068/.

[150] Methanol, ultrapure, HPLC Grade. https://www.alfa.com/en/catalog/022909/.

[151] Materion. Inorganic Chemicals Catalog. Tantalum Carbide. https://materion.com/electronic-materials/about/inorganic-chemicals-catalog/123590. Accessed: 2022-09-14.

[152] Methyl Ethyl Ketone (ACS), Fisher Chemical^{TM} . https://www.fishersci.ca/shop/products/methyl-ethyl-ketone-certified-acs-fisher-chemical-6/p-216191.

[153] UBC. Solvent Dispensing. Ethanol. https://www.chem.ubc.ca/solvent-dispensing.

[154] Sigma-Aldrich. Mineral Oil. https://www.sigmaaldrich.com/CA/en/product/sial/330779.

[155] Acros Organics. Butvar®B-98 Poly(vinyl butyral) resin. https://www.acros.com/DesktopModules/Acros_Search_Results/Acros_Search_Results.aspx?search_type=CAS&SearchString=63148-65-2.

[156] V. N. Panteleev, A. E. Barzakh, L. Kh. Batist, D. V. Fedorov, V. S. Ivanov, F. V. Moroz, P. L. Molkanov, S. Yu. Orlov, M. D. Seliverstov, and Yu. M. Volkov. Highly efficient ion source for surface and laser ionization. *Nuclear Instruments and methods in Physics Research Section B*, 463:364–366, 2020.

[157] F. Ames, P. Bricault, H. Heggen, P. Kunz, Lassen, A. Mjøs, and S. Raeder. Ion source developments for the production of radioactive isotope beams at TRIUMF. *Review of Scientific Instruments*, 85:02B912–1 – 02B912–3, 2014.

[158] J. P. Bricault, Lavoie P., and J. Lassen M. R. Pearson. Segmented linear radiofrequency quadrupole/laser ion source project at TRIUMF. *Hyperfine Interactions*, 174:33–39, 2007.

[159] M. Mostamand, R. Li, J. Romans, F. Ames, P. Kunz, A. Mjøs, and J. Lassen. Production of clean rare isotope beams at TRIUMF Ion Guide Laser Ion Source. *Hyperfine Interactions*, 241:1–9, 2020.

[160] Fernando Maldonado Millan. *Comprehensive Ionization Model Development for the FEBIAD Ion Source and Its Application for TRIUMF's Radioactive Ion Beam Program*. PhD thesis, Universite of Victoria, 2022.

[161] P. Kunz, C. Andreoiu, P. Bricault, and M. Dombsky. Nuclear and in-source laser spectroscopy with the ISAC yield station. *Review of scientific instruments*, 85:190–209, 2014.

Appendix A

Materials and methods

A.1 Substances in target materials slurries

LaC_2/C, UC_x, and graphite targets have been synthesized for this work (Chapter 2) with $La(OH)_3$, UO_2 and graphite powders (Table A.1) as precursors, respectively. In the case of the LaC_2/C (Section 2.2) and UC_x (Section 2.3), $La(OH)_3$ or UO_2 have been mixed with graphite powder to carbothermally reduce them; the graphite powder used for these targets is the same used to synthesize the graphite-composite target (Section 2.4). The powders have been suspended in slurries and then slip cast over a graphite foil (Table A.2).

Table A.1: LaC_2/C, UC_x, and graphite targets precursors.

Target agent	**Particle size (μm)**	**Purity**	**CAS#**	**Supplier**
$La(OH)_3$	20	99.95%	14507-19-8	Alfa-Aesar [54]
Graphite	<44	99.9995%	7782-42-5	Alfa-Aesar [144]
UO_2	<297	>99%	1344-57-6	International Bio-Analytical Industries Inc. [68]

The $La(OH)_3$, graphite, and UO_2 slurries contain the same substances (Table A.3). All of them are commercially available, and their purity and corresponding supplier are listed in Table A.3. The slurries also contain deionized water, supplied by a DI-PAK® Purification Pack [145]. This device removes chlorine, colloids and ionic contaminants from tap water. Table A.4 lists the Maximum Acceptable Concentrations of metals in Vancouver's tap water according to the Guidelines for Canadian Drinking Water Quality [146].

Organic impurities from the slurries' plastizicers do not represent an issue because the target materials are thermally treated at ≥1700 °C. This temperature is above the vaporization temperature of most impurities, so they would evaporate during heating. From the metals in tap water, iron (Fe) has the highest vaporization temperature (≈1027 °C [47] at 10^{-6} Torr [48]). As the target with the highest amount of water (28 g), the graphite-

Table A.2: Graphite foils characteristics.

Characteristic	Value
Thickness (mm)	0.129 ± 0.004
Bulk density (g/cm^3)	1.15 ± 0.04
Apparent density (g/cm^3)	2.03 ± 0.01
Total porosity	0.49 ± 0.02
Open porosity	0.44 ± 0.01
Closed porosity	0.05 ± 0.02
Provider	CeraMaterials [35]

Table A.3: Substances in $La(OH)_3$/C, UC_x, and graphite slurries.

Substance	Function	Purity	CAS#	Supplier
Ammonium citrate dibasic	Emulsifier	≥99%	3012-65-5	Honeywell-Fluka [147]
Glycerol	Dispersant	>99%	56-81-5	Sigma-Aldrich [148]
Polyethylene glycol 400	Plasticizer	>95%	25322-68-3	Alfa-Aesar [144]
Polyvinyl alcohol	Plasticizer	>87-89%	9002-89-5	Sigma-Aldrich [148]
η-Butanol	Surfactant	>99.4%	71-36-3	Alfa-Aesar [149]
Methanol	Surfactant	>99.8%	67-56-1	Alfa-Aesar [150]

Table A.4: Maximum Acceptable Concentration of metals in drinkable/tap water of Vancouver city according to Guidelines for Canadian Drinking Water Quality [146].

Metals	Guideline (g/ml)
Copper	$\leq 1.0\times10^{-6}$
Iron	$\leq 0.3\times10^{-6}$
Lead	$\leq 0.005\times10^{-6}$
Zinc	$\leq 5.0\times10^{-6}$

composite would have a maximum amount of iron of 1.4×10^{-4} g if the water purificator fails filtering the Fe and the target is heated below ≈1027 °C. This amount of Fe represents a 9×10^{-6}% of the graphite-composite's slip-cast mass; such a small concentration of Fe wouldn't be detectable with XRD analysis [16], and it would be unlikely to cause problems during irradiation.

A.2 Pre-milling graphite procedure

The targets developed in this work, i.e. LaC_2/C (Section 2.2), UC_x (Section 2.3), and graphite composite (Section 2.4), contain pre-milled graphite powder (Table A.1). As purchased, the graphite powder particle size is <44 µm (-325 mesh) [55]. To reduce and homogenize its particle size, the graphite powder is pre-milled.

A batch of 50 g of graphite is combined with 5 mL of deionized water in a tungsten carbide (WC) jar with eight WC balls, and milled with the planetary ball mill Pulverisette 5 for three rounds at 400 RPM, each round lasting five minutes. The resulting powder is

left in a fume hood partially covered to allow the evaporation of the water.

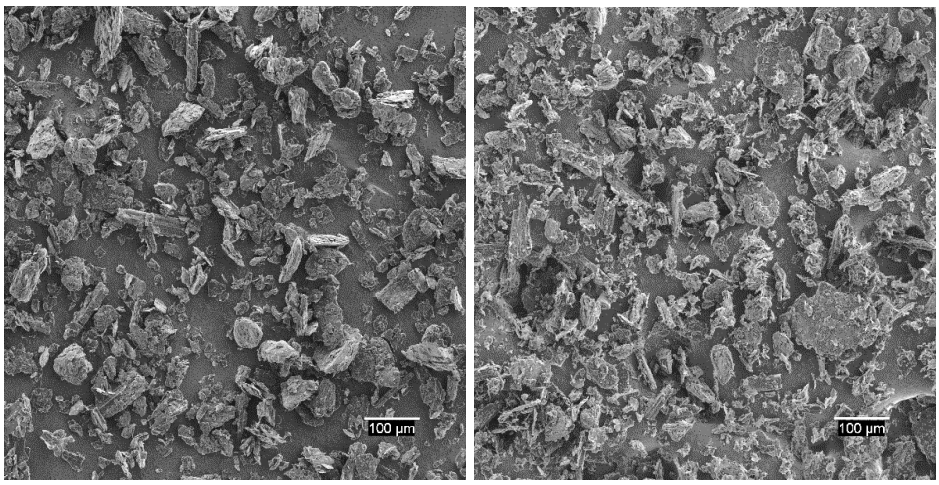

(a) **(b)**

Figure A.1: Graphite powder before (a) and after (b) pre-milling.

The pre-milling reduces the graphite's average particle size from ∼44 µm to ∼35 µm. However, milling wears the WC jars and introduces WC in the graphite (Fig. 2.64). To avoid pre-milling, the graphite powder currently purchased will be substituted with a commercially available one with smaller particle size.

A.3 Tantalum sample preparation

Thirty two samples have been cut from tantalum tubes of 19.1 cm outside diameter, and 18.3 cm interior diameter (Section 3.3). The tubes were sectioned with a pipe cutter, and samples were cut from the sections with metal scissors. Sixteen of the samples were prepared for analyzing their microstructure surface, and the other sixteen were prepared for analyzing their cross section (Fig. A.2). Besides washing, no additional preparation was required for the former samples. On the other hand, the samples that were appointed for cross-sections analyses were polished because the pipe cutter and scissors smear their edges, consequently distorting the samples cross-sections.

A set of three cross-section samples was set in a sample holder to polish them (Fig. A.2). All sixteen cross-section samples were polished at the same time to guarantee that all have same height and polishing finish. The samples were polished at MEML [43] with the Buehler Phoenix Beta polisher, using sandpaper of four grades. To start smoothing the highly rough surface of the cross-section samples, they were polished with sandpaper of 400 µm, following by a 600 µm, 800 µm, and 1200 µm. The samples were polished with each sandpaper during 10 min, with a force of 40 N, and 100 RPM.

The last polishing steps to reduce scratches were semi-manual. One sample-holder with

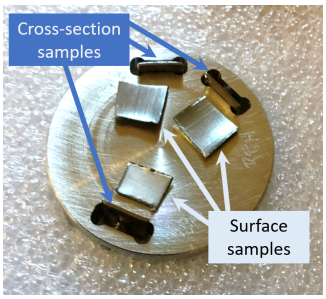

Figure A.2: Sample holder with three cross-section samples and three surface samples.

three samples was polished at a time. The holder was held against a rotatory cloth of 6 µm and 1 µm damped in a diamond solution of 6 µm and 1 µm respectively. The samples were polished for 10 min with each cloth; halfway through the polishing time and at the end, the samples were observed with an optical microscope to spot scratches. If the samples were not smooth, they would be further polished to remove remaining scratches.

The samples and sample holders were washed to get rid of impurities that they could have got during their cutting or polishing. The samples were sonicated with deionized water for five minutes. The water excess of the samples was blown with air, and the remaining water was evaporated by placing the samples in an oven at 100 °C for 10 min. When the samples and the sample holders were dry, clean, and at ambient temperature, the cross section samples were fastened in the holders with a set screw, and the unpolished samples were adhered to the centre of the sample holders with double side carbon tape.

A.4 TaC coating procedure

The internal face of the target ovens and tubes are coated in-house with a TaC coating to prevent carbon penetration during target irradiation. The coating procedure consists of suspending the TaC powder (Table A.5) in a slurry (Table A.6), coating the oven or tube with the slurry, letting the coating dry, and heating the tube or oven to sinter the coating.

Table A.5: Specifications of TaC powder.

Target agent	Particle size (µm)	Purity	CAS#	Supplier
Tantalum carbide	<44	99.5%	12070-06-3	Materion [151]

Table A.6: Specifications of the plasticizer and solvents in the TaC slurry.

Substance	Purity	CAS#	Supplier
Methyl Ethyl Ketone	≥99%	78-93-3	Fisher Scientific [152]
Ethanol	100%	NS	UBC Chemistry Stores [153]
Mineral oil	100%	8042-47-5	Sigma-Aldrich [154]
Polyethylene glycol 400	>99%	25322-68-3	Sigma-Aldrich [148]
Poly(vinyl butyral)	98%	63148-65-2	Acros Organics [155]

To prepare the TaC slurry, first TaC powder is milled in a WC jar with eight WC balls at 400 RPM for 25 min three times, pausing for three minutes between each repetition. Next methyl ethyl ketone, ethanol and mineral oil (Table A.7) are added to the jar and milled at 140 RPM for 2 hours. Then, poly(vinyl butyral) and polyethylene glycol 400 (Table A.7) are added; next, the slurry is mixed at 140 RPM for 2 hours.

Table A.7: Function of the substances used to prepare the TaC slurry.

Substance	**Function**	wt.%
TaC powder	Coating agent	53.7
Methyl Ethyl Ketone	Solvent	15.4
Ethanol	Solvent	23.2
Mineral oil	Surfactant	1.3
Poly(vinyl butyral)	Plasticizer	3.2
Polyethylene glycol 400	Plasticizer	3.2

To apply the TaC slurry, one side of the oven (Fig. 1.7b) or tube (Fig. 2.59c) is sealed with masking tape, and the ion source (in the case of the ovens) is blocked with a rolled-paper rod. Then, around 10 ml of slurry is poured into the oven's open side which is thereafter also sealed with tape. The oven is tilted and rotated to distribute the slurry and coat the oven walls; immediately after, one of the seals is removed, and the excess slurry is poured out. Finally, the oven is left in a fume hood for the slurry to dry.

In preparation for sintering the TaC coating, the body of the oven is wrapped with three tantalum foils (25.4 µm thickness, 18.8 cm× 6.0 cm) that render as heat shields (Fig. A.3b). The tantalum foils are dimpled in advance (Fig. A.4) to prevent them to sinter between each other. To prevent the tantalum foils from sintering with the tube, tantalum wire is wrapped around the oven body (Fig. A.3a). Additionally, each foil is fastened with 0.5 mm thick tantalum wires that, beside fixing the foils in place, keep them apart, and also help to prevent them from sintering (Fig. A.3b).

The TaC is sintered in the non-actinide furnace (Fig. 2.3b). The pressure is kept under 3×10^{-5} Torr while the tantalum oven is resistively heated at 1800 °C for four hours. The oven temperature is increased slowly to avoid the binders boiling and generating bubbles that could leave pores on the coating which would act as paths for carbon penetration.

The TaC coating had only been characterized before its sintering. For this work, the internal face of a cold-rolled tantalum tube has been TaC coated and sintered. A sintered TaC coated sample has been analyzed under SEM. Also, two samples have been heated under vacuum at 2000 °C; one of them in the presence of carbon, and the other by itself. Both samples have been analyzed under SEM (Section 3.5.2).

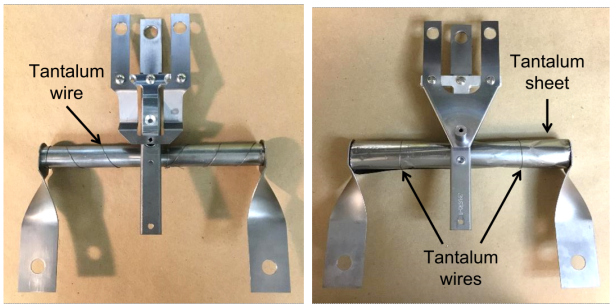

(a) **(b)**

Figure A.3: Heat shields on tantalum oven (b). First Ta wire is wrapped on the oven body (a), then three Ta sheets are wrapped over tube fastening each sheet with Ta wire (b).

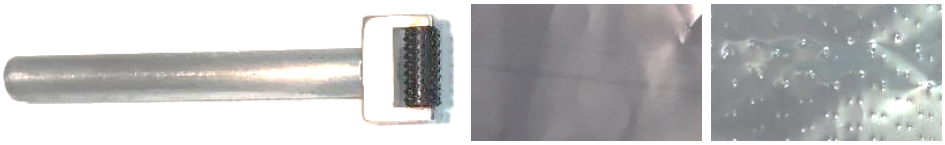

(a) Dimpler **(b)** Ta foil **(c)** Dimpled Ta foil

Figure A.4: The tantalum foils used as heat shield are dimpled to prevent them from sintering. The indent roller (a) is rolled manually over a tantalum foil (b), the depth of the dimples (c) varies depending on the force applied when rolling the indent roller.

A.5 Particle size measurements

The target-materials developed in this work have been synthesized with powders as precursors. All of the powders have amorphous particles, but they are assumed spherical. Powders or slip-casts have been observed under SEM, and their micrographs have been analyzed with Amscope [69] to estimate the particles' dimensions. The material particles have been circled with this software, considering the circle's diameter as the particle's size. Several micrographs have been measured this way, but for brevity, only one micrograph of each material is included in this document.

Since the particles' shape and arrangement are not uniform or periodic through the micrographs, they cannot be selected automatically with the Amscope software [69]. Instead, the particles are circled manually, selecting them along a diagonal through the micrographs, aiming at obtaining a representative sample. At least ten particles are circled from each micrograph. The global average, maximum and minimum diameter are collected per micrograph.This methodology is not accurate, but it gives a referential particle size to compare between specimens. $La(OH)_3$, UO_2, and UC_x particles have been measured; LaC_2 target particles have not been measured with this methodology because this material oxidizes and is not representative of LaC_2. Graphite particles have only been measured in the micrographs of the graphite-composite target.

A.5.1 $La(OH)_3$ dry and suspension milled powder

The $La(OH)_3$ particles are <0.9 µm, but they agglomerate (Fig. A.5b). Since the agglomerates' size influences the LaC_2-target particle size, the size of the agglomerates has been included in the calculation of the average, and maximum $La(OH)_3$ particle size.

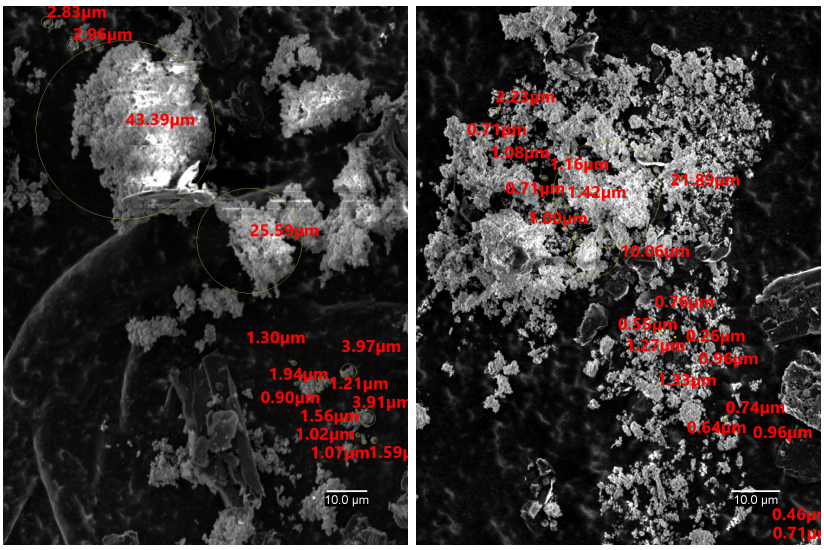

(a) Dry milled $La(OH)_3$ **(b)** Suspension milled $La(OH)_3$

Figure A.5: $La(OH)_3$ powder dry and suspension milled (Section2.2). The $La(OH)_3$ particles were circled with Amscope; the circles diameter is indicated in red.

A.5.2 UC_x two-step casting micrographs

Discs made with the 2-step casting, but unconventionally conditioned (p. 45) have been analyzed under SEM (Fig. A.6b). The UC_x particle size has been determined with the same methodology described above.

A.5.3 UC_x one-step casting micrographs 11% molar excess carbon

The UO_2 particle size is smaller than its agglomerates. UO_2 powder has been suspended and slip-cast; a fragment of the slip cast has been observed under SEM (Fig. A.7a). Since the agglomerate size influences the UC_x-target particle size, the size of the agglomerates has been included in the calculation of the average, and maximum UO_2 particle size (Table 2.11).

After carbothermal reduction, fragments of UC_x discs made with the 1-step casting method have been analyzed under the SEM. Most particles have been measured through the diagonal, but additional particles are selected nearby in highly sintered zones. The discs of the batch B3 are highly sintered, so no boundaries could be used to delimit a particle (Fig. 2.37c), and no particles were measured in micrographs corresponding to this batch.

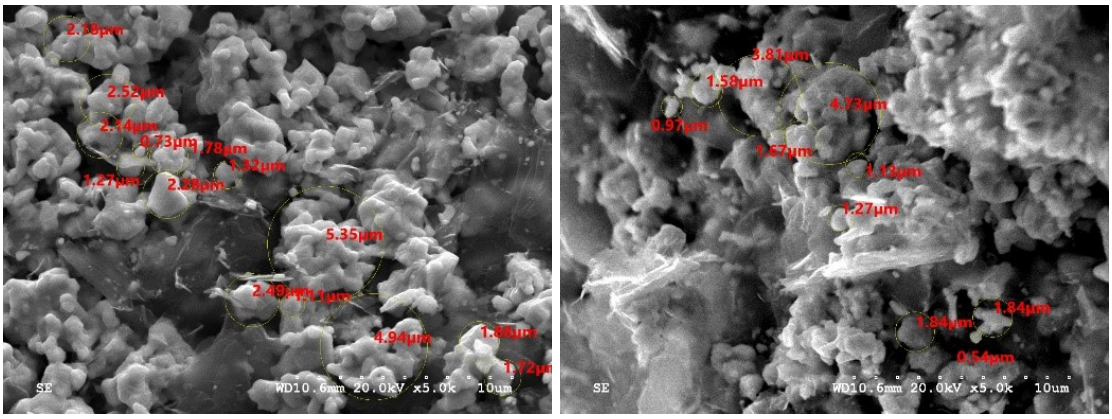

(a) 2-step casting surface **(b)** 2-step casting cross section

Figure A.6: Micrographs of the surface of a discs made with 2-step casting method. The UC_x particles were circled with Amscope; the circles diameter is indicated in red.

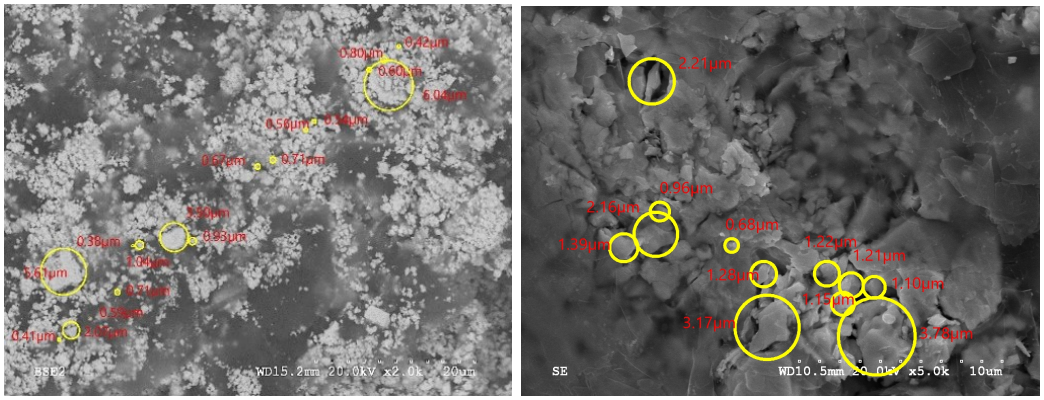

(a) Micrograph of UO_2/C disc surface. **(b)** B1 surface

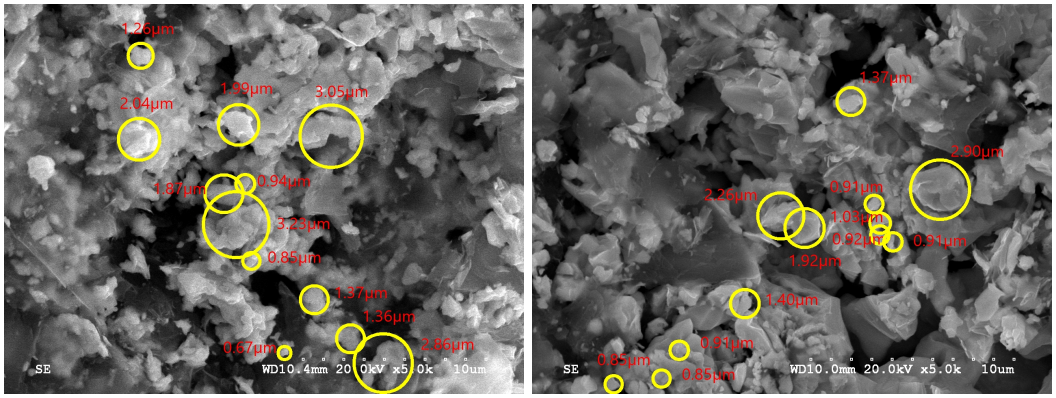

(c) B2 surface **(d)** B7 surface

Figure A.7: Micrographs of UC_x batches with circled UC_x particles, and diameter indicated in red.

A.5.4 UC_x one-step casting micrographs 31% molar excess carbon

The UO_2 agglomerates in the UO_2 slip cast are larger than the particles, and their size is taken in consideration on the average and maximum UO_2 particle size reported.

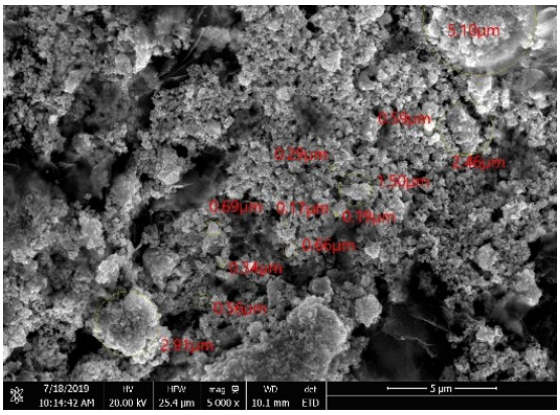

Figure A.8: Micrograph of UO_2/C disc with circled UO_2 particles, and diameter indicated in red.

The UC_x discs' surface and cross section have been explored, so a pair of micrographs is presented per specimen. In the case of micrographs of highly sintered discs, like UCx28 (Fig. A.11a), the size of the UC_x monolith has not been taken in consideration for calculating the average UC_x particle size of the surface. Furthermore, particles not completely sintered are considered particles even when presenting necking (e.g. Fig. A.12a).

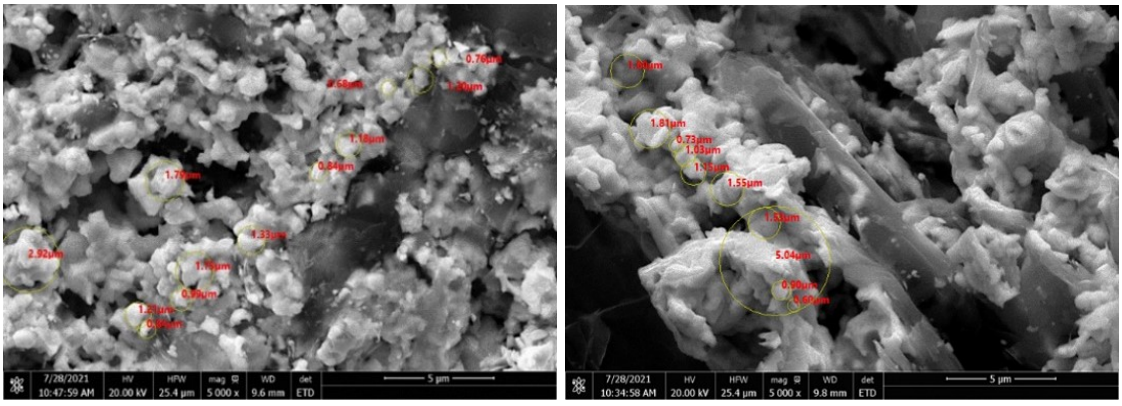

(a) UCx26 surface **(b)** UCx26 cross section

Figure A.9: Micrographs of UCx26 with circled UC_x particles, and diameter indicated in red.

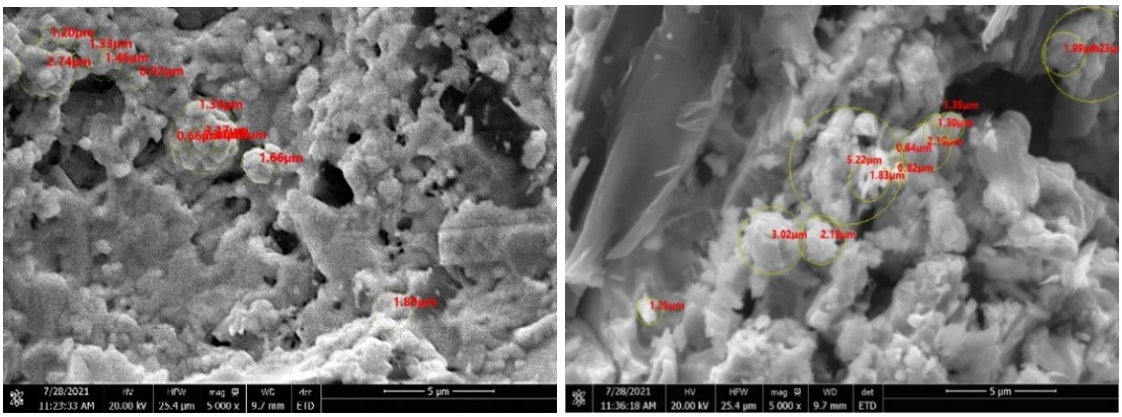

(a) UCx27 surface **(b)** UCx27 cross section

Figure A.10: Micrographs of UCx27 with circled UC_x particles, and diameter indicated in red.

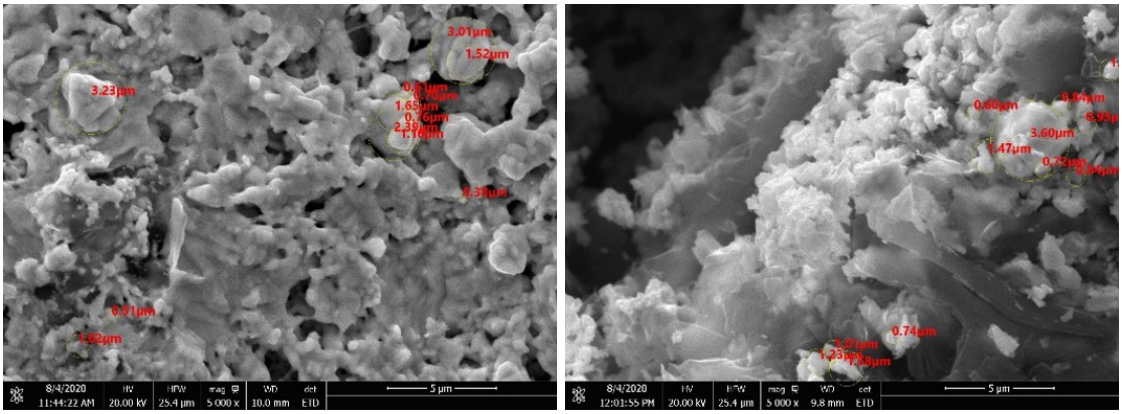

(a) UCx28 surface **(b)** UCx28 cross section

Figure A.11: Micrographs of UCx28 with circled UC_x particles, and diameter indicated in red.

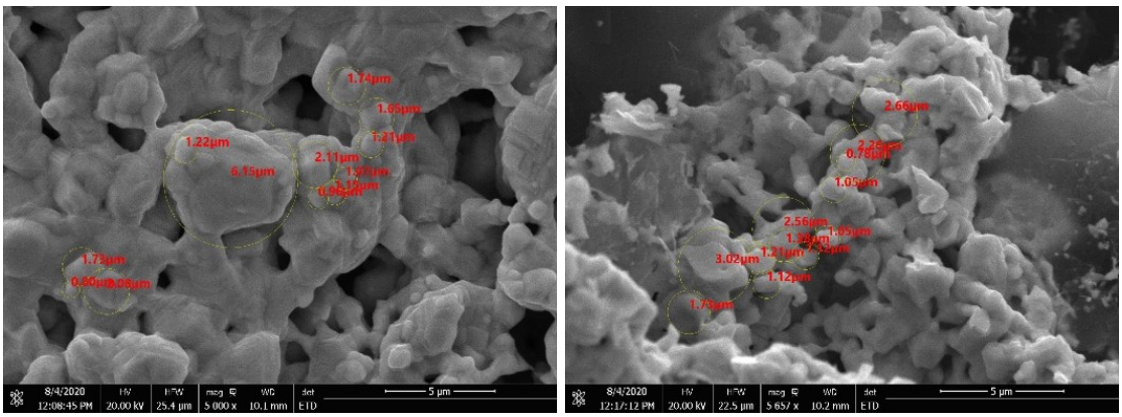

(a) UCx29 surface **(b)** UCx29 cross section

Figure A.12: Micrographs of UCx29 with circled UC_x particles, and diameter indicated in red.

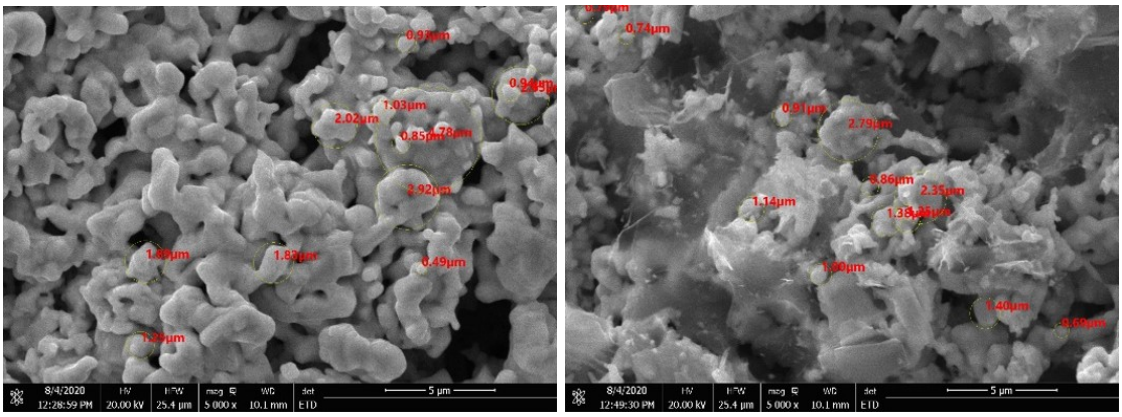

(a) UCx30 surface **(b)** UCx30 cross section

Figure A.13: Micrographs of UCx30 with UC_x particles circled and diameter indicated in red.

A.5.5 Graphite-composite target

The graphite composite discs' surface has been explored with SEM before and after thermal treatment (Fig. A.14). Before thermal treatment (green) the particles look overexposed due to the plasticizers in the slip-cast (Fig. A.14a). After thermal treatment, the particles shape and size do not present important changes, suggesting that this target material do not undergo sinterization.

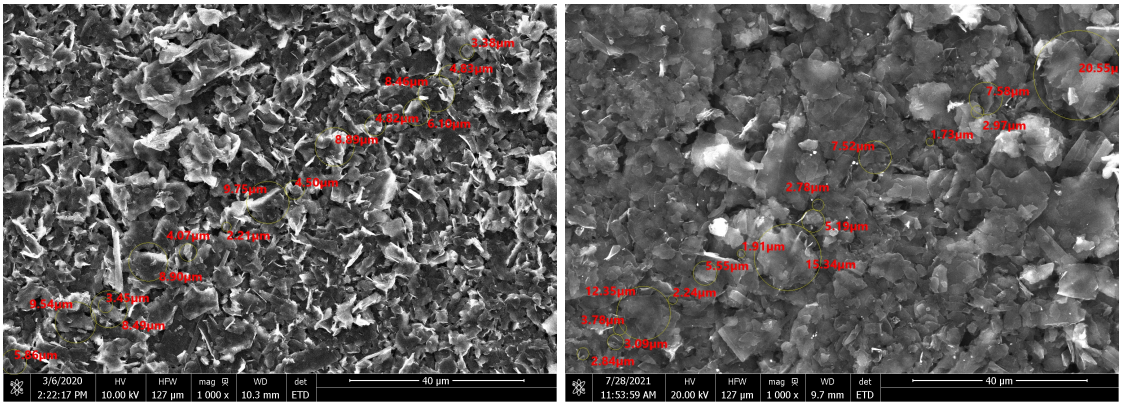

(a) Green graphite composite **(b)** Conditioned graphite composite

Figure A.14: Micrographs of graphite-composite surface with graphite particles circled, and diameter indicated in red.

Appendix B

Empirical effective emissivity

The emissivity is a temperature dependent property. However, the analytical models for predicting the target temperature during irradiation use an effective emissivity value (ε_{eff}) for the target ovens (Fig. 1.7b) [127]. To estimate the oven's ε_{eff}, a target-oven is set up in the non-actinide furnace and resistively heated under vacuum [126]. In preparation for the experiment, the internal face of the target-oven is TaC coated (A.4), and its body is wrapped with tantalum sheets. Depending on the target, the oven would be loaded with an empty graphite container or with target-material discs; next, the oven is sealed with tantalum-caps. While joule heating the oven, its electrical current I, voltage drop V, and temperature are registered; the cap and oven temperatures are assumed to be identical, so the temperature is measured in one of the tantalum caps with a two-colour pyrometer. The power passing through the oven is corrected with the power lost in the non actinide furnace (Eq. B.1) [84]

$$P_{tot} = VI - (8.04 \times 10^{-3} I^2 - 3.01 \times 10^{-1} I). \tag{B.1}$$

According to the Boltzmann's law [128], the net rate of radiation heat transferred (Q_{tot}) between a surface of temperature T_s and a surrounding (black) surface of temperature T_a is given by

$$Q_{tot} = \sigma \varepsilon A_s (T_s^4 - T_a^4), \tag{B.2}$$

where $\sigma = 5.67 \times 10^{-12}$ W·cm^{-2}·K^{-4} is the Stefan Boltzmann constant, and ε and A_s are the emissivity and area of the surrounded surface, respectively. In the experiment to find ε_{eff}, the net radiation heat transfer Q_{tot} is the power passing through the oven (P_{tot}) (Eq. B.1), T_s is the temperature of the cap, and T_a is the temperature of the water-cooled assembly surrounding the oven (Fig. 2.60) assumed to be 300 K. The effective emissivity of the oven is calculated by plotting the oven's temperature against the corresponding power, and fitting the curve with the Boltzmann equation (Eq. B.2) solved for T_s [127].

Appendix C

Ion sources overview

Isotopes released from the target effuse in the oven until reaching the ion source, where ionization takes place. The isotopes lose an electron becoming ions, such that they can be extracted, accelerated, separated by mass, and sent to experiments.

A universal ion source does not exist, so there are different ion sources to efficiently ionize different elements. At ISAC, four types of ion sources are used: Surface Ion Source (SIS), Resonant Ionization Laser Ion Source (RILIS), Ion Guide Laser Ion Source (IGLIS), and Forced Electron Beam Induced Arc Discharge Ion Source (FEBIAD). This last ion source was not used with the targets presented in this work.

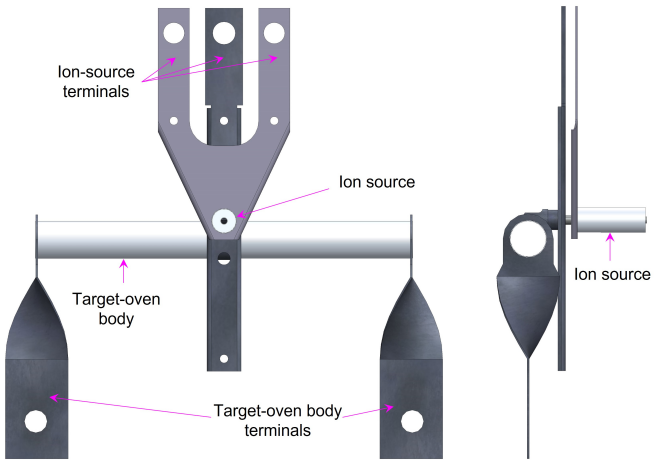

(a) Front SIS **(b)** Side

Figure C.1: Front and side views of target oven. The target ovens consist of a body and an ion source. This target oven has a Surface Ion Source (SIS).

All ion sources require an extraction system to extract the isotopes from the ion source. At ISAC an extraction electrode (Fig. C.2) is situated in front of the ion source, and the difference in voltage between them extracts the ions.

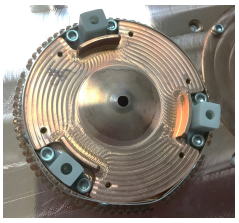

Figure C.2: ISAC extraction electrode.

C.1 Surface Ion Source (SIS)

Upon contact with a hot, high-work function metal, an atom is adsorbed into the metal and is thermally desorbed as an ion [156]. The Surface Ion Source (SIS) ionizes neutrals elements with ionization potential $W \leq 6$ eV [157]. The SIS is composed by a tantalum transfer line (Fig. C.3). The ion source is made out of tantalum, a refractory metal [81] with a high work function (ϕ) of 4.25 eV [39]. Since rhenium has a work function of 4.72 eV [39], a foil of this metal is introduced in the SIS transfer line to increase its efficiency.

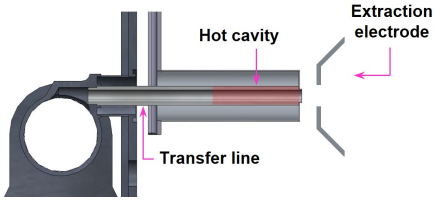

Figure C.3: Cross-section of Surface ion source (SIS). This ion source is composed by a transfer line, and a hot zone called hot cavity.

C.2 Resonant Ionization Laser Ion Source

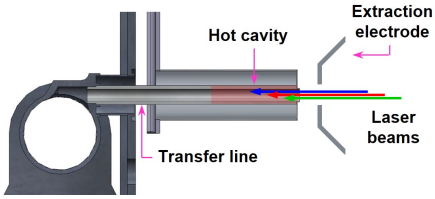

Figure C.4: Cross-section of Resonant Ionization Laser Ion Source (RILIS). The structure is identical to the SIS, but in addition to surface ionization the RILIS ionize neutrals with laser beams.

The Resonant Ionization Laser Ion Source (RILIS) has the same structure as the Surface Ion Source (Fig. C.4). They differ in that up to three laser beams are aimed at the transfer line of the RILIS; the wavelength of the laser beams matches with the energy level of the atoms' outer shell electrons [157]. The RILIS ionizes elements with ionization potential ≤ 10 eV [158]. Despite the RILIS chemical selectivity due to the ionization mechanism, surfaced ion ionized species are still present in the ion beam delivered by this ion source.

C.3 Ion Guide Laser Ion Source

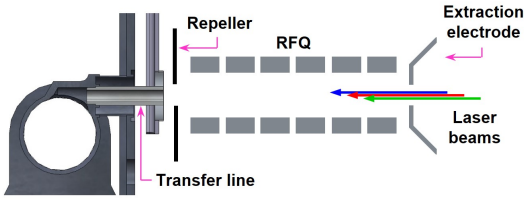

Figure C.5: Cross-section of Ion Guide Laser Ion Source (IGLIS). The IGLIS laser resonant ionization occurs in a Radio Frequency Quadrupole (RFQ) instead of the hot cavity. ISAC's IGLIS hot cavity was shortened to allow space for the RFQ.

The Ion Guide Laser Ion Source (IGLIS), has a higher selectivity than the RILIS. This ion source has achieved isobar suppression of up to 10^6 [159]. The higher selectivity of the IGLIS is because it blocks surface ionized isotopes. This ion source has a repulsive electrode that repels the ions coming from the hot cavity, allowing only neutral isotopes to pass towards a Radio Frequency Quadrupole (RFQ) where they are ionized with laser beams (Fig. C.5). The ions are guided towards the extraction electrode by means of the RFQ potential gradient [157].

C.4 Forced Electron Beam Induced Arc Discharge Ion Source

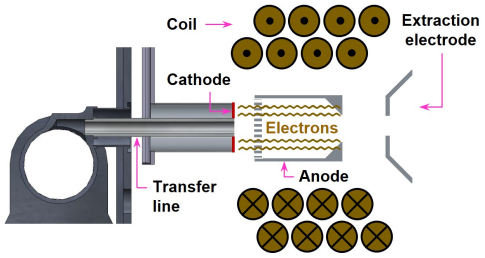

Figure C.6: Cross-section of Forced Electron Beam Induced Arc Discharge Ion Source (FEBIAD).

The Forced Electron Beam Induced Arc Discharge Ion Source (FEBIAD) ionizes neutrals elements with ionization potential $\geq$ 10 eV [157]. In the FEBIAD the neutrals are ionized in an anode by electron impact ionization (Fig. C.6) [160]. Electrons are generated in the cathode by thermionic emission, that in ISAC's case, is the front face of the ion-source nozzle [157] (Fig. C.1a and C.6). Furthermore, an electric field between the anode and the cathode accelerates the electrons, and a magnetic filed generated with a coil focuses and confines them in the axial direction. The ions are extracted from the FEBIAD by the extraction electrode.

Appendix D

ISAC yield station

Before delivering them to experiments, the RIBs are characterized at the ISAC yield station where the RIBs' yield are measured. The ISAC yield station consists of a tape station with a detector system under vacuum ($< 10^{-7}$ mbar). The RIB implants on an aluminized Mylar tape on the tape station where plastic scintillators detect β particles, PIN diodes detect α particles, and an HPGe detector detects γ particles [161].

The RIB yield Y is a function of the production rate P over the number of implantation cycles n, the detection efficiency ϵ, and the decay channel b [161]:

$$Y = \frac{P}{n\epsilon b}. \tag{D.1}$$

The production rate, depends on the isotope decay constant λ, the implantation time $t_{collect}$ (RIB ON), the decay time t_{decay} (RIB OFF), and on the number of counts N accumulated during t_{decay} [161]:

$$P = \frac{\lambda}{(1 - e^{-\lambda t_{collect}})} \frac{N}{(1 - e^{-\lambda t_{decay}})}. \tag{D.2}$$